Generation and shaping of ultra-short, ultra-high contrast pulses for high repetition rate relativistic optics

Lorenzo Canova

THÈSE DE DOCTORAT DE L'ÉCOLE POLYTECHNIQUE

Spécialité:

Physique

Présentée par:

Lorenzo CANOVA

Pour obtenir le grade de:

Docteur de l'École Polytechnique

Titre de la thèse

Generation and shaping of ultra-short, ultra-high contrast pulses for high repetition rate relativistic optics

Soutenue le 30 septembre 2009 devant le jury composé de:

M. Joffre	Président du jury
R. Lopez Martens	Directeur de thèse
M. Nisoli	Rapporteur
F. Druon	Rapporteur
D. Kaplan	Examinateur

Thèse de doctorat de l'École Polytechnique

Spécialité :

Physique

Présentée par :

Lorenzo CANOVA

Pour obtenir le grade de :

Docteur de l'École Polytechnique

Titre de la thèse :

Generation and shaping of ultra-short, ultra-high contrast pulses for high repetition rate relativistic optics.

Soutenue le 30 septembre 2009 devant le jury composé de :

M. Joffre	Président du jury
R. Lopez Martens	Directeur de thèse
M. Nisoli	Rapporteur
F. Druon	Rapporteur
D.Kaplan	Examinateur

Remerciements

Ce manuscrit synthétise le travail que j'ai réalisé pendant mes trois années de thèse au Laboratoire d'Optique Appliquée (LOA). Une thèse c'est avant tout un travail en collaboration et je souhaite donc remercier toutes les personnes qui ont contribué à la réussite de mon travail.

Mon premier remerciement va tout naturellement à mon directeur de thèse Rodrigo Lopez Martens. Sans lui cette thèse n'aurait pas vu le jour. Quand je suis venu la première fois au LOA en août 2005, j'ai été tout de suite impressionné par son enthousiasme pour la physique attoseconde et par sa bonne humeur. (Je me rappelle encore la phrase " si on a ces intensités on peut faire des impulsions attosecondes même dans un bout de fromage "). Nos nombreuses discussions et échanges (plus au moins acharnés) ont été la base de la réussite de mon travail. Je souhaite ensuite remercier tous les autres membres du groupe PCO : Un grand merci à Alex pour le travail ensemble et pour tout le temps qu'il a passé à réaligner le Femtopower pour me permettre de faire les mesures XPW. A great thanks to Xiaowei for all the time spent together working on the laser system and on the CEP stabilization (and I'm sorry if we walked too much in Munich). Je tiens à remercier également Antonin et Arnaud surtout pour avoir supporté le désordre sur mon bureau. Un grand merci va également à Olivier et Aurélie pour leur encadrement sur la partie XPW (et pour m'avoir logé au début à Berkeley), à Brigitte, Aurélien et Jean Philippe. Je veux aussi remercier tous les autres membres du laboratoire qui ont contribué directement ou indirectement à mon travail. Un grand merci en particulier à Greg pour sa sympathie et pour les nombreuses discussions de foot du lundi matin.

Une thèse c'est aussi un travail de collaboration entre laboratoires. I really want to thank Stoyan and Nikolai for all the time spent together doing beta-scans in "salle rose". Thank you also to Solomon for all his help on the XPW generation theory and in general for his enthusiasm. His sudden death in last march really shocked me. His passion for research will always remain a model for me. I want to thank also Wim Leemans and all the members of the LOASIS group. I really had a great experience in Berkeley. Je tiens aussi à remercier M. Joffre, F. Druon et M. Nisoli pour avoir accepté de faire partie de mon jury de thèse en tant que président du jury et rapporteurs.

Last but not least je veux remercier tous les "industriels" de Fastlite et Amplitude Technologies pour la très fructueuse collaboration qu'on a eu au cours de ma thèse (et aussi pour toutes les fois qu'ils m'ont invité au restaurant pendant les conférences). En particulier je souhaite faire un hommage spécial à Nicolas Forget. Son aide a été fondamental tout au long de ma thèse (jusqu'à la relecture du manuscrit). J'espère ne pas avoir trop gâché sa productivité avec toutes les questions que je lui ai posé à travers Skype. Un grand merci aussi à D. Kaplan pour avoir accepté de faire partie de mon jury de thèse. Je tiens également à remercier G. Riboulet pour avoir accepté mes services en tant que doctorant-conseil et Pierre Mary pour tout le temps passé sur les mesures XPW haute énergie.

Enfin, dans un cadre plus personnel, je remercie et dédie ce travail à ma famille et à Gilda. Sans leur soutien tout ceci n'aurait pas été possible.

Contents

Chapter 1

Introduction

1.1 Introduction

The field of laser physics has seen tremendous growth since the first practical realization of laser light in 1960 [9]. The first laser pulses were produced by gain switching and Q-switching also known as giant pulse formation. In the following years lasing action was reported from He-Ne gas mixture [6] and from Nd^{3+}-doped solid state laser material [15]. Population inversion in semiconductor materials was also demonstrated in GaAs-junctions in 1962 [3]. Shorter pulses were later produced by mode-locking techniques with dye lasers. These lasers were later replaced by Ti:sapphire laser [11]. This material proved to be one of the best amplifying media at 800 nm: it combines a high damage threshold and a high fluence saturation with excellent thermal conductivity and a very large gain bandwidth (650 nm 1100 nm). The characteristics of this material together with the possibility of Kerr lens "magic" mode-locking allow generating and amplifying ultra-short pulses at a high repetition rate. Another important breakthrough towards the generation of ultra-intense pulses has been the introduction in 1985 by D. Strickland and G. Mourou of the Chirped Pulse Amplification (CPA) [16]. This technique enables working at a high fluences, for a good extraction of the energy while minimizing the intensity to avoid nonlinear effects, destructive for the amplifier and optics. The idea is to generate an initial ultra-short pulse with a low energy, to stretch it in temporal domain with a spectral phase modulation and then to amplify it keeping the intensity low enough to avoid nonlinear effects. The pulse is finally recompressed compensating the spectral phase modulation. (Fig. 1.1)

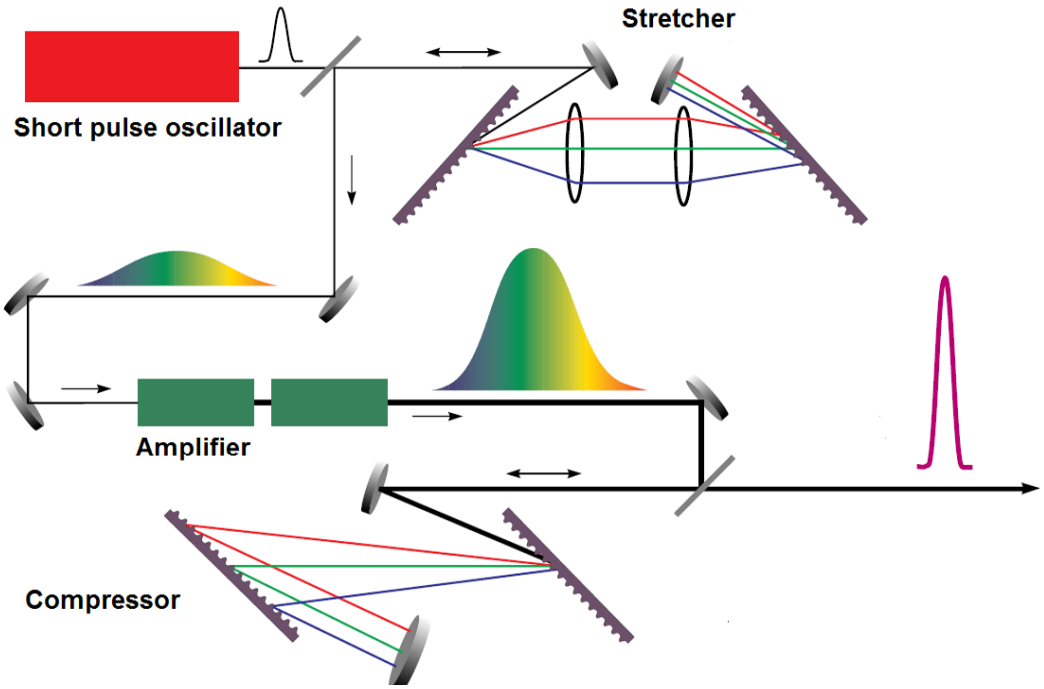

Figure 1.1: Illustration of the CPA principle: the pulse is at first stretched by adding a spectral phase modulation, then it is amplified and finally it is compressed by adding a spectral phase modulation opposite to the initial one. Reprinted from [2]

A CPA laser system can then be decomposed in four parts: a laser oscillator, a stretcher, one or more amplifying stages and a compressor. Most currently operating high-intensity laser systems use this technique which allows reaching a peak power of hundreds of Terawatts (1 TW=$10^{12}W$) with a relatively compact system. Fig. 1.2 shows the evolution of the focused intensity together with the different kind of laser-matter interaction regimes.

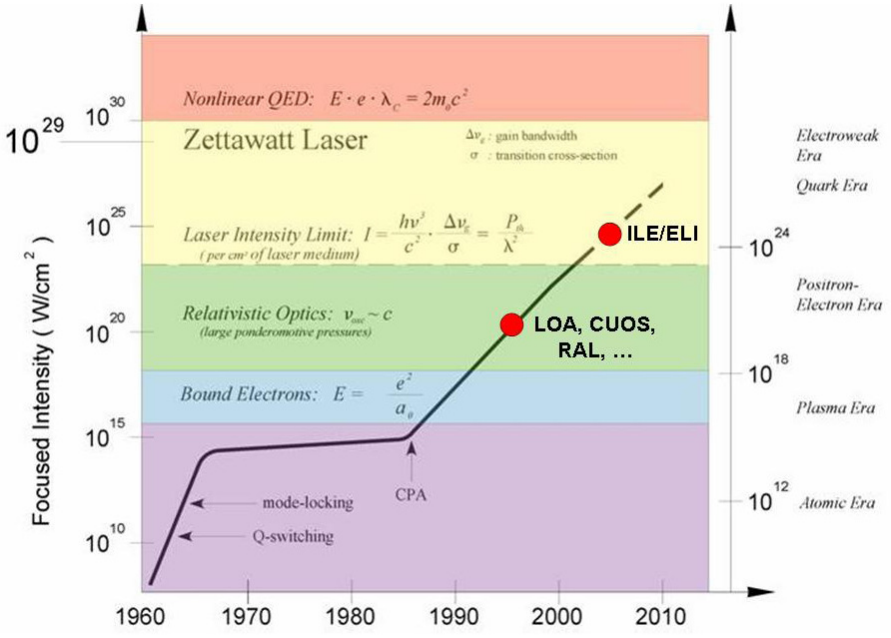

Figure 1.2: Chronology of the temporal intensity after the invention of the laser and corresponding focused intensity for the more powerful installations. Reprinted from [17]

Even with the combination of the CPA technique and the Ti:sapphire lasing medium the shortest pulse duration obtained at the mJ level is around 18 fs [14, 4, 21, 20]. This is due to the gain narrowing during pulse amplification which reduces the spectral bandwidth and thus increases the temporal duration. To obtain shorter pulses down into the few-cycle regime (one optical cycle is equal to 2.6 fs at 800 nm) various techniques based on nonlinear effects have been used: gas filled hollow-core fiber [13], filamentation [5] or Optical Parametric Chirped Pulse Amplification (OPCPA) [18].
During my Ph.D I concentrated on the hollow-core fiber technique. State of art pulse shortening in hollow-core fibers enables the generation of pulses as short as 3.8 fs [1]. This corresponds practically to the optical cycle of the infrared radiation. To decrease the pulse duration further the central wavelength needs to be shifted to the XUV. This is possible by generating high order harmonics (HHG) of the fundamental frequency in a gas target [10] or by relativistic reflection from an overdense plasma [19]. The generation and phase matching of these harmonics allows generating pulses with temporal duration in the attosecond regime (1 as=$10^{-18}s$) which can then be used to probe ultra-fast dynamic of matter [7]. According to the laws of quantum mechanics the classical motion of an electron corresponds to the temporal evolution of a coherent superposition of electronic atomic states. When the electron is in a non-stationary state, the corresponding wave function shows an evolution with a time scale ranging from attoseconds to microseconds (in the case of Rydberg states). For example, if the 1s electron of an hydrogen atom is partially excited to the 2s state, a coherent superposition of the two states can be generated. The corresponding electron density oscillates between the two states with a period $T = \frac{2\pi\hbar}{\Delta E} = 0.4\ fs$ ($\Delta E = 10.2\ eV$ is the energy difference between the 1s and 2s states). On the basis of this argument, it can be concluded that the essence of attosecond science is the investigation of the electronic processes on the atomic time scale. Fig. 1.3 shows the evolution over time of the pulse duration down to the attosecond regime. In the last few years a dramatic progress has been achieved in the field of attosecond technology, mainly because of the breakthroughs in laser science and due to the introduction of new techniques for temporal characterization of XUV attosecond pulses.

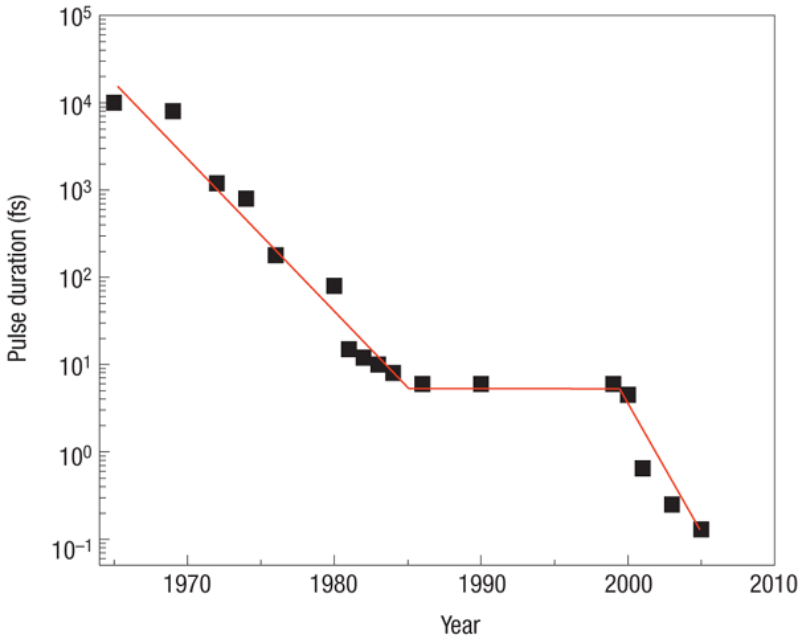

Figure 1.3: Evolution of the pulses temporal duration function of time. Reprinted from [8]

Harmonics generated from a multi-cycle pulse (for example with a temporal duration of 25 fs) correspond in time domain to a train of attosecond pulses. For many applications it is important to have a single attosecond pulse. Using a few-cycle pulse a single attosecond pulse can be generated. When the incident pulse is short enough, the highest frequency component is generated only at the highest peak power, where the intensity is significantly higher than the other part of the pulse. Filtering out the highest frequency part of the spectrum will lead to a single attosecond pulse. Theoretical simulations also show that there is a particular regime, named λ^3, which occurs when few-cycle pulses are focused into a focal spot with dimensions close to the laser wavelength [12]. All the laser energy is therefore concentrated inside a volume corresponding to the cube of the wavelength. In this regime single attosecond pulses are reflected by the overdense plasma with an efficiency that can reach 10^{-1}.

The "Physique du Cycle Optique" (PCO) group at the Laboratoire d'Optique Appliquée (LOA, Palaiseau, France) was created just before the beginning of my Ph.D to study this λ^3 regime and in general the possibility of building a kHz, attosecond source based on HHG from solid targets. To reach this goal it is necessary to have a laser source that delivers few-cycle pulses with an energy $\geq$ 1 mJ. The 1 kHz repetition rate of the laser facilitates detection and characterization of the generated harmonics. This source must also satisfy two other important requirements. The first is the temporal contrast (section 2.2.2) which needs to be high enough to prevent uncontrolled pre-ionization of the solid target. The second is the stabilization of the carrier envelope phase (CEP) between successive pulses. The CEP is the shift between the electric field and the envelope of the pulse and influences highly nonlinear effects like HHG process. This kind of source was not commercially available at the beginning of my thesis.

The work during my Ph.D was articulated around these requirements. It consisted of using nonlinear pulse shaping to generate high-contrast, few-cycle pulses and to develop new solutions for the CEP stabilization at high energy. The results of this work, done in collaboration with several laser companies like Fastlite, Amplitude Technologies and Femtolasers, are presented in the following chapters. After an introduction to ultra-short pulses and their characterization (chapter 2), in chapters 3, 4 and 5 I present theoretical and experimental results on the third order non linear process called cross-polarized wave (XPW) generation. This nonlinear process is used for generating high contrast, ultra-short pulses. Chapter 6 deals with the development of the CEP stabilized, few-cycle, mJ level laser source (Salle Noire). In chapter 7 I present how this source can be used for high order harmonic generation. In the last chapter (8) I give the prospects for future laser developments in "Salle Noire" with the integration of an XPW filter in a double CPA configuration and the generation of high contrast, few-cycle, mJ level, CEP stabilized laser pulses.

Bibliography

[1] A. L. Cavalieri, E. Goulielmakis, B. Horvath, W. Helml, M. Schultze, M. Fiess, V. Pervak, L. Veisz, V. S. Yakovlev, M. Uiberacker, A. Apolonski, F. Krausz, and R. Kienberger. Intense 1.5-cycle near infrared laser waveforms and their use for the generation of ultra-broadband soft-x-ray harmonic continua. *New Journal of Physics*, 9(7):242, 2007.

[2] Science and Technology review (1995)

[3] R. N. Hall, G. E. Fenner, J. D. Kingsley, T. J. Soltys, and R. O. Carlson. Coherent light emission from GaAs junctions. *Phys. Rev. Lett.*, 9(9):366–368, Nov 1962.

[4] C. P. Hauri, M. Bruck, W. Kornelis, J. Biegert, and U. Keller. Generation of 14.8-fs pulses in a spatially dispersed amplifier. *Opt. Lett.*, 29(2):201–203, 2004.

[5] C. P. Hauri, A. Trisorio, M. Merano, G. Rey, R. B. Lopez-Martens, and G. Mourou. Generation of high-fidelity, down-chirped sub-10 fs mj pulses through filamentation for driving relativistic laser-matter interactions at 1 kHz. *Appl. Phys. Lett.*, 89(15):151125, Oct 2006.

[6] A. Javan, W. R. Bennett, and D. R. Herriott. Population inversion and continuous optical maser oscillation in a gas discharge containing a He-Ne mixture. *Phys. Rev. Lett.*, 6(3):106–110, Feb 1961.

[7] F. Krausz and M. Ivanov. Attosecond physics. *Reviews of Modern Physics*, 81(1):163, 2009.

[8] J. Levesque and P.B.Corkum Attosecond science and technology. *Can.J.Phys*, 84:1-18, 2006.

[9] T. H. Maiman. Stimulated optical radiation in ruby. *Nature*, 187:493–494, 1960.

[10] A. McPherson, G. Gibson, H. Jara, U. Johann, T. S. Luk, I. A. McIntyre, K. Boyer, and C. K. Rhodes. Studies of multiphoton production of vacuum-ultraviolet radiation in the rare gases. *J. Opt. Soc. Am. B*, 4(4):595–601, 1987.

[11] P. F. Moulton. Spectroscopic and laser characteristics of $Ti : Al_2O_3$. *J. Opt. Soc. Am. B*, 3(1):125–133, 1986.

[12] N. M. Naumova, J. A. Nees, I. V. Sokolov, B. Hou, and G. A. Mourou. Relativistic generation of isolated attosecond pulses in a λ^3 focal volume. *Phys. Rev. Lett.*, 92(6):063902, 2004.

[13] M. Nisoli, S. De Silvestri, and O. Svelto. Generation of high energy 10 fs pulses by a new pulse compression technique. *Appl. Phys. Lett.*, 68(20):2793–2795, 1996.

[14] S. Sartania, Z. Cheng, M. Lenzner, G. Tempea, Ch. Spielmann, F. Krausz, and K. Ferencz. Generation of 0.1-Tw 5-fs optical pulses at a 1-kHz repetition rate. *Opt. Lett.*, 22(20):1562–1564, 1997.

[15] E. Snitzer. Optical maser action of Nd^{3+} in a barium crown glass. *Phys. Rev. Lett.*, 7(12):444–446, Dec 1961.

[16] D. Strickland and G. Mourou. Compression of amplified chirped optical pulses. *Opt. Commun.*, 56(3):219–221, 1985.

[17] T. Tajima and G. Mourou. Zettawatt-exawatt lasers and their applications in ultrastrong-field physics. *Phys. Rev. ST Accel. Beams*, 5(3):031301, Mar 2002.

[18] F. Tavella, A. Marcinkevicius, and F. Krausz. 90 mJ parametric chirped pulse amplification of 10 fs pulses. *Opt. Express*, 14(26):12822–12827, 2006.

[19] G. D Tsakiris, K. Eidmann, J. Meyer ter Vehn, and F. Krausz. Route to intense single attosecond pulses. *New Journal of Physics*, 8(1):19, 2006.

[20] K. Yamakawa, M. Aoyama, S. Matsuoka, H. Takuma, C. P. J. Barty, and D. Fittinghoff. Generation of 16-fs, 10-tw pulses at a 10-Hz repetition rate with efficient ti:sapphire amplifiers. *Opt. Lett.*, 23(7):525–527, 1998.

[21] E. Zeek, R. Bartels, M. M. Murnane, H. C. Kapteyn, S. Backus, and G. Vdovin. Adaptive pulse compression for transform-limited 15-fs high-energy pulse generation. *Opt. Lett.*, 25(8):587–589, 2000.

Chapter 2

Introduction to ultra-short pulses

2.1 Introduction

I start this chapter by giving an introduction to the basic concepts relative to ultra-short pulses. In particular I define the concepts of temporal contrast and Carrier Envelope Phase that are fundamental to understand the work presented in this manuscript. I then introduce the main techniques for the temporal characterization of ultra-short pulses such as second order autocorrelation, SPIDER and FROG. I also introduce a new pulse characterization device (Phazzler) that combines, in a same instrument, all these characterization techniques. I conclude this chapter by presenting the third order correlation technique that is used to characterize the pulses with a high temporal dynamic range.

2.2 Ultra-short laser pulses

The electric field of a linearly polarized optic wave is a real function varying with time, solution of the Maxwell equations. This function $\mathcal{E}(t)$ can be decomposed into frequencies by making a Fourier transform to obtain:

$$\tilde{\mathcal{E}}(\omega) = \int_{-\infty}^{+\infty} \mathcal{E}(t) exp(i\omega t) dt. \tag{2.1}$$

A complex temporal analytic signal can also be defined as:

$$E(t) = 2 \int_{0}^{+\infty} \tilde{\mathcal{E}}(\omega) exp(-i\omega t) \frac{d\omega}{2\pi}, \tag{2.2}$$

with an associated Fourier transform spectral decomposition:

$$\tilde{E}(\omega) = \int_{-\infty}^{+\infty} E(t) exp(i\omega t) dt = \left|\tilde{E}(\omega)\right| exp(i\varphi(\omega)) \tag{2.3}$$

This field is zero for negative frequencies and equal to $2\tilde{\mathcal{E}}(\omega)$ for positive frequencies. The basic idea behind working with analytic signals is that the negative frequency components of the

Fourier transform (or spectrum) of a real-valued function are superfluous, due to the Hermitian symmetry of such a spectrum. They can be discarded with no loss of actual information. The quantity $I(\omega) = \frac{\epsilon_0 c}{2}\left|\tilde{E}(\omega)\right|^2$ is the spectral intensity and $\varphi(\omega)$ is the spectral phase. The spectral phase is typically expanded in a Taylor series around the central frequency ω_0:

$$\varphi(\omega) = \sum_{k=0}^{n} \frac{\varphi^{(k)}}{k!}(\omega - \omega_0)^k \tag{2.4}$$

Where $\varphi^{(2)}$ is the linear chirp (also named Group Delay Dispersion GDD or second-order phase dispersion) and $\varphi^{(3)}$ the quadratic chirp. In the temporal domain a temporal phase $\varphi(t)$ is also defined and the complex temporal field is written as: $E(t) = |E(t)|\, exp(i(\varphi_0 + \varphi(t) - \omega_0 t))$. $|E(t)|$ is the temporal envelope. Assuming $\varphi(0) = 0$, φ_0 is the phase shift between the electric field and the envelope. This term is also called carrier envelope phase (CEP). $I(t) \propto |E(t)|^2$ is the cycle-averaged radiation intensity. For a Gaussian pulse the intensity is $I(t) = E_0 exp\left(\frac{-2t^2}{\tau^2}\right)$ with τ the width at $1/e^2$ in intensity. The Full Width at Half Maximum (FWHM) in intensity, Δt, is related to τ by: $\Delta t = \tau\sqrt{2ln(2)}$. Fig. 2.1 shows the electric field (red) and the envelope (blue) for two pulses having a FWHM of 25 fs and 5 fs at a central wavelength of 800 nm. Pulses as short as 5 fs contain just 3 optical cycles at $\lambda = 800nm$.

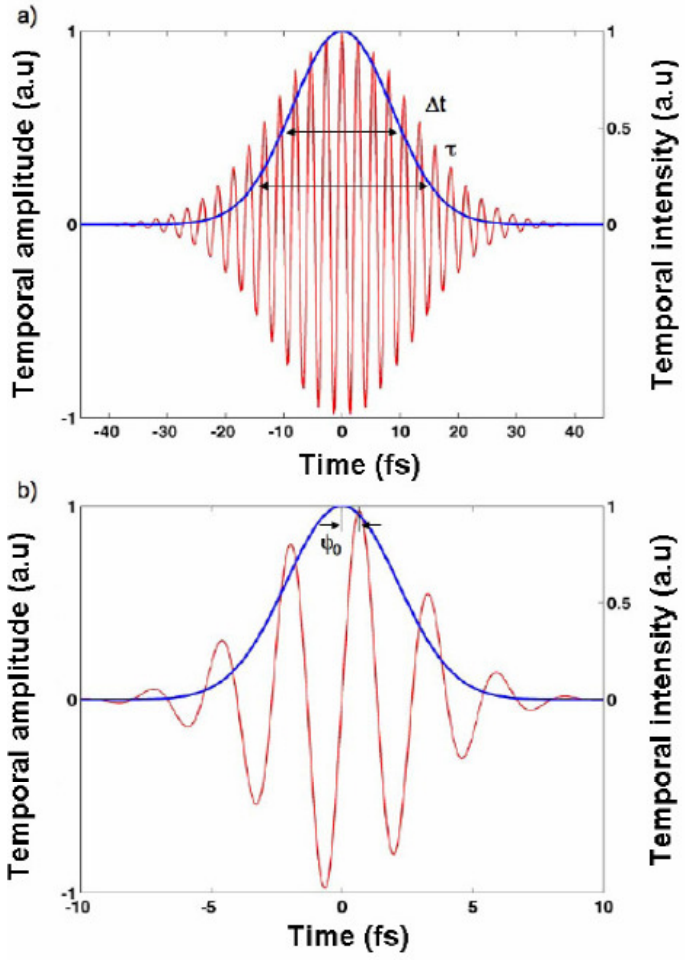

Figure 2.1: Electric field (red) and associated temporal intensity (blue) for pulses with a FWHM of: 25 fs (a) and 5 fs (b)

2.2.1 CEP and its stabilization

A more detailed description of the CEP measurement and stabilization in a laser system with a fast and a slow feedback loop is given with the description of the development of the laser source (chapter 6). Here I just want to derive the CEP off-set between successive output pulses of an oscillator and how to stabilize it. Inside the laser cavity, together with the Ti:sapphire crystal, there are other dispersive elements. All together they are responsible for the variation of the off-set between the carrier wave and the envelope of the pulses. This variation is caused by the difference between the phase velocity $v_f = \frac{\omega}{k_0}$ (where $k_0 = 2\pi/\lambda$ is the constant of propagation) of the carrier wave and the group velocity $v_g = \frac{\partial\omega}{\partial k_0}$ of the pulse envelope. In dispersive media the group and phase velocity are different and there is a shift between the envelope and the carrier inside the cavity. The consequence is that the CEP varies between successive pulses at the output of the oscillator. Without any perturbation the CEP, φ_0, varies by a fixed quantity $\Delta\varphi_0$ between two successive pulses. This phase difference contains typically some hundreds of times 2π, plus a significant term between 0 and 2π. This value is defined $\Delta\varphi_0$ [1]. Considering a cavity length L, $\Delta\varphi_0$ is given by the expression:

$$\Delta\varphi_0 = 2\pi \int_0^{2L} \frac{dn(z)}{d\lambda_0} dz \tag{2.5}$$

where n(z) is the index of refraction of the materials inside the cavity. In reality φ_0 varies between successive pulses by the quantity $\Delta\varphi_0$ plus a random variation due to perturbations of the laser cavity and fluctuations of the energy of the pump pulses.
The variation of the CEP, $\Delta\varphi_0$, is the quantity that can be experimentally measured and used for the stabilization. The stabilization is realized in frequency domain. In frequency domain, the frequency comb of the oscillator is shifted compared to the repetition frequency, f_{rep}, by an offset frequency, f_{ceo}, which is a direct function of $\Delta\varphi_0$ (Fig. 2.2). The value of f_{ceo} is given by the relation:

$$f_{ceo} = (\Delta\varphi_0/2\pi) f_{rep} \tag{2.6}$$

Measuring f_{ceo} and making it constant implies that successive pulses of the cavity have a fixed $\Delta\varphi_0$. A self-referenced interferometer for measuring f_{ceo} is presented in section 6.2.1

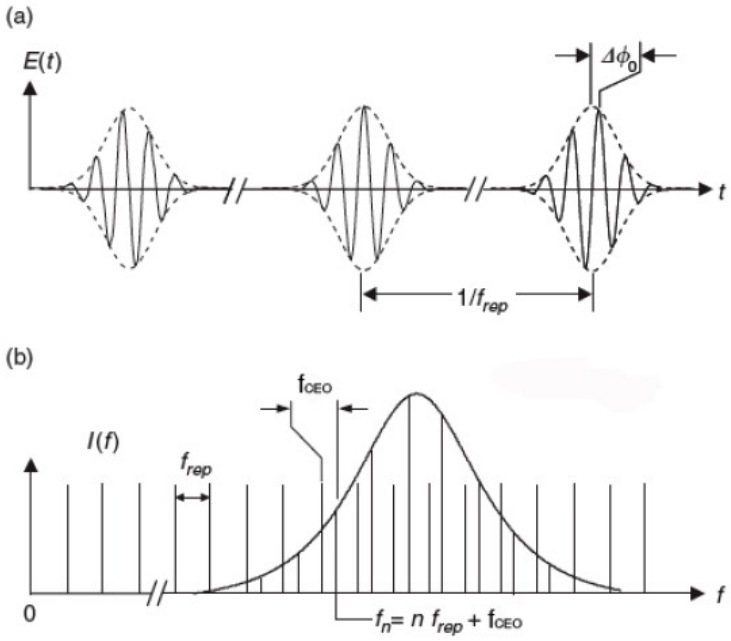

Figure 2.2: Correspondence between the temporal and frequency domain. (a) In the temporal domain φ_0 varies by a quantity $\Delta\varphi_0$. (b) In the frequency domain there is a frequency comb with a frequency f_{rep}. This comb is translated by the integer multiple frequencies by an offset f_{ceo}. Its amplitude is given by the Fourier transform of the temporal amplitude of the pulse at ω_0. Reprinted from [1]

2.2.2 Temporal contrast of a short pulse

Every process of amplification introduces a certain amount of noise on the amplified signal and causes some distortion. This is true for electronic amplification and it is also verified for optical amplification. For ultra-intense sources, the temporal quality of the pulses and, in particular, the ratio between the peak intensity and the intensity at a delay Δt, is defined as the temporal contrast of the pulses at this delay. This quantity has a fundamental importance in laser-matter interaction. Focusing a 25 fs pulse with an energy > 1 mJ in a spot size of 1 μm (limit of diffraction at 800 nm) produces a peak intensity higher than $10^{18} W/cm^2$. With a temporal contrast of 6 orders of magnitude the intensity of the background pedestal, $\approx 10^{12} W/cm^2$, is high enough to pre-ionize the target (for example fused silica) before the arrival of the main, ultra-short pulse [15]. If the plasma is generated before the main pulse arrives, it will expand hydrodynamically and the main pulse will no longer interact with a clean, steep plasma density. This deformation of the plasma-vacuum interface has a strong influence on processes such as high-order harmonic generation from solid surfaces [17] and ion acceleration [7]. To better understand the concept of contrast Fig. 2.3 shows, on logarithmic scale, the typical temporal profile of a short pulse. Four types of contributions can be distinguished:

- A long pedestal (>100ps);
- A short pedestal (some tens of time the pulse duration);

- pre-pulses: replicas situated in front of the pulse

- post-pulses: replicas situated after the pulse.

These structures have different physical origins. The long pedestal corresponds to the incoherent noise introduced by the amplified spontaneous emission (ASE) and for this reason it is called incoherent contrast. The ASE is mainly generated in the first, high gain, amplification stages. The short pedestal comes from an imperfect recompression after the stretcher/compressor and amplification and is called the coherent contrast. Finally pre-pulses and post-pulses are replicas of the main pulse due to reflection or diffusion from optical surfaces and from non linear effects such as four-wave mixing [9].

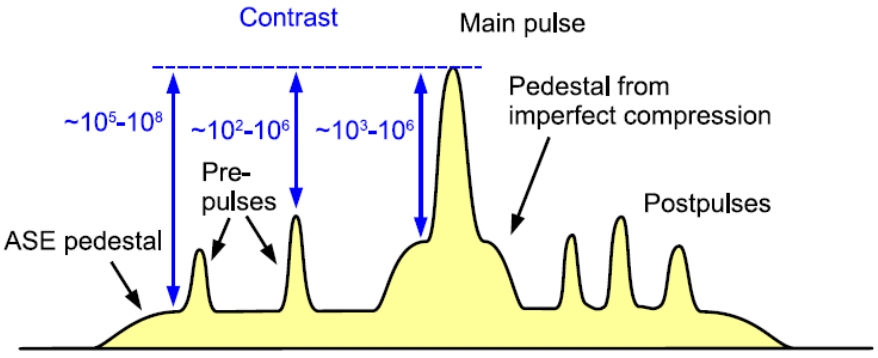

Figure 2.3: Typical temporal profile of the output pulse of a (CPA) laser. Aside from the main pulse, it generally has pre- and post-pulses. The underlying pedestal comes from ASE (ns) and imperfect compression (ps). Reprinted from [12]

2.3 Temporal characterization of femtosecond pulses

This section presents a brief review of the main solutions for the temporal characterization of femtosecond pulses. As discussed in the previous section, imperfections in the temporal compression influence not only the temporal width of the pulse but also affect its coherent contrast. During my Ph.D I contributed to the development of a temporal characterization device named Phazzler (Fastlite) that makes it possible to carry out several temporal characterization techniques using the same instrument. A presentation of this device is given at the end of this section.

2.3.1 Second order autocorrelator

One of the first techniques for the temporal characterization of femtosecond pulses is the second order autocorrelation [2]. For some particular temporal profiles, the FWHM of the temporal intensity and of the autocorrelation are linked. With an assumption of the temporal profile, the corresponding FWHM is retrieved measuring the FWHM of the second order autocorrelation. A schematic of this device is shown in Fig. 2.5. The input pulse is split into two temporally delayed replicas in a Michelson interferometer and the two replicas are focused into a non linear crystal. The signal is detected with a photodiode or a photomultiplier and visualized with an oscilloscope. The result of the nonlinear interaction of the beams from the two arms depends on the delay. This signal is named autocorrelation function. There are two types of autocorrelations:

- Interferometric autocorrelation: when the beams incident on the crystal are collinear (can not be distinguished).
- Intensity autocorrelation: for non collinear beams.

Interferometric autocorrelator

For the interferometric autocorrelator the measured signal is given by the expression:

$$S_{col}(\tau) \propto \int_{-\infty}^{+\infty} \left|(E(t) + E(t-\tau))^2\right|^2 dt \tag{2.7}$$

where τ is the delay between the pulses. This signal is the sum of three components function of τ: $S_{col}(\tau) \propto I_{back} + I_{int}(\tau) + I_{\omega}(\tau) + I_{2\omega}(\tau)$ with:

$$I_{back} = \int_{-\infty}^{\infty} (|E(t-\tau)|^4 + |E(t)|^4) dt = 2\int_{-\infty}^{\infty} I^2(t) dt \tag{2.8}$$

$$I_{int}(\tau) = 4\int_{-\infty}^{\infty} (|E(t-\tau)|^2 |E(t)|^2 = 4\int_{-\infty}^{\infty} I(t-\tau) I(\tau) dt \tag{2.9}$$

$$I_{\omega}(\tau) = 4\int_{-\infty}^{\infty} Re[(I(t) + I(t-\tau))E^*(t)E(t-\tau)exp(i\omega_0\tau)]dt, \tag{2.10}$$

$$I_{2\omega}(\tau) = 2\int_{-\infty}^{\infty} Re[(E(t)^2(E^*(t-\tau))^2 exp(i2\omega_0\tau)]dt \tag{2.11}$$

I_{back} is a background signal independent of τ, $I_{int}(\tau)$ is the intensity autocorrelation, $I_{\omega}(\tau)$ and $I_{2\omega}(\tau)$ are named coherence term oscillating respectively at ω_0 and $2\omega_0$. There is a ratio 8 between the maximum ($\tau = 0$) and the minimum signal. When the delay is large enough to avoid temporal overlap between the pulses the measured signal is twice the one measured with a single beam. When the delay is zero the signal is equal to $2^4 = 16$. The ratio between the two is then equal to 8. An example of an interferometric trace is shown in Fig. 2.5. Even if there are algorithms for extracting the spectral phase from an interferometric trace, for example PICASO, (Phase and Intensity from Cross Correlation and Spectrum Only) this reconstruction is not robust and does not always converge.

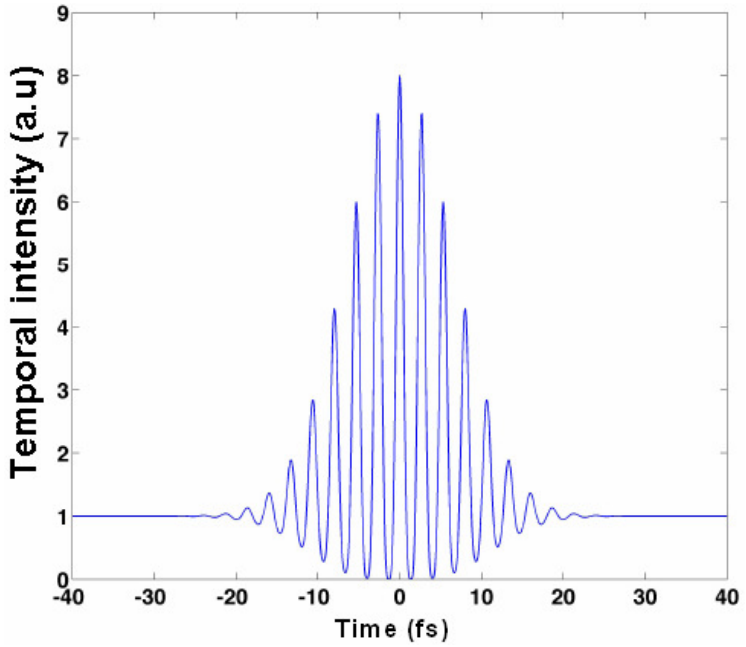

Figure 2.4: Calculated interferometric autocorrelation for a 10 fs pulse

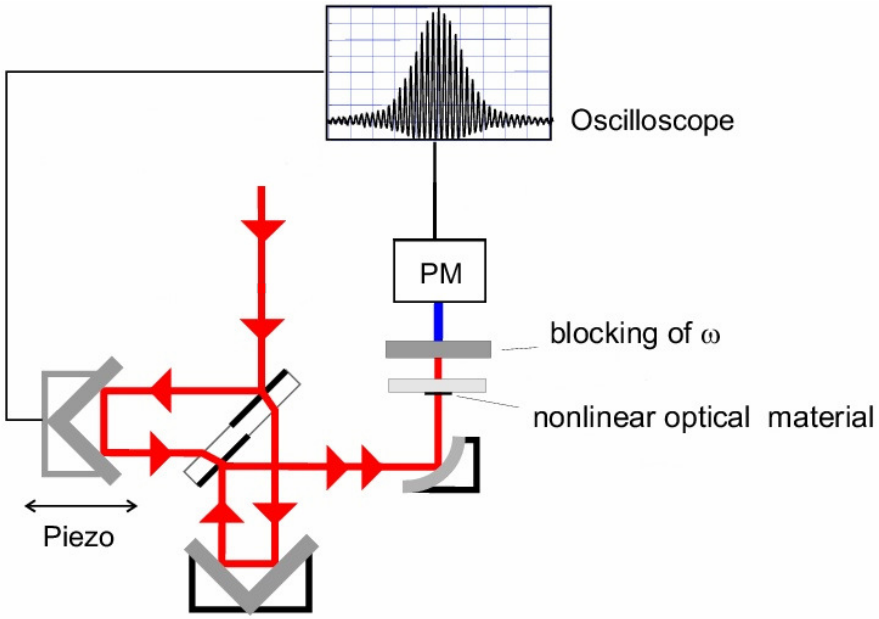

Figure 2.5: Schematic of a second order autocorrelator. The detector can be a photomultiplier (MHz detection) or a photodiode (kHz detection). Reprinted from [4]

Intensity autocorrelator

For the intensity autocorrelator the measured signal is given by the expression:

$$S_{non-col}(\tau) = I_{int}(\tau) \propto \int_{-\infty}^{+\infty} |E(t)E(t-\tau)|^2 \, dt = \int_{-\infty}^{+\infty} I(t)I(t-\tau)dt \tag{2.12}$$

The signal is measured in the direction corresponding to the addition of the wave vectors of the two arms. The intensity autocorrelation does not contain full information about

the electric field of the pulse, since the phase of the pulse in the time domain is completely lost. The only information that can retrieved is the FWHM and basic shape of the input pulses.

Two main techniques have been developed to measure the spectral phase of femtosecond pulses: SPIDER and FROG.

2.3.2 SPIDER technique

Spectral Phase Interferometry for Direct Electric-field Reconstruction (SPIDER) [6, 5] uses spectral shearing interferometry to retrieve the spectral phase of an incident pulse. This form of interferometry measures the interference between two pulses separated in time which are identical except for their central frequencies. This pulse pair is said to be spectrally sheared. Nonlinear optics provides a general approach to globally shearing two pulses by a frequency Ω. This can be done by sum frequency generation between a monochromatic frequency, Ω, and the field we want to shear, $\tilde{E}(\omega)$, resulting in a sheared field, $\tilde{E}(\omega+\Omega)$. It is convenient to obtain the monochromatic frequency from a strongly chirped ultrashort pulse for which the instantaneous frequency, which is approximately a linear function of time, does not vary during the nonlinear interaction with the short pulse(Fig. 2.6). The magnitude of the spectral shear generated in this manner is then a function of two parameters: the delay between the pulses and the amount of chirp of the stretched pulse. The exact value of the shear is equal to: $\Omega = -\frac{\tau}{2\varphi_2}$ where τ is the delay between the pulses and φ_2 is the second order dispersion present on the chirped pulse.

The interference of the two sheared pulses (SPIDER signal) is given by:

$$I_{SPIDER}(\omega) = \left|\tilde{E}(\omega)\right|^2 + \left|\tilde{E}(\omega+\delta\omega)\right|^2 + 2\left|\tilde{E}(\omega)\tilde{E}(\omega+\delta\omega)\right| \times cos(\phi(\omega+\delta\omega) - \phi(\omega) + \omega\tau) \quad (2.13)$$

The phase difference between the two spectrally sheared replicas can be extracted algebraically using methods taken from Fourier Transform Spectral Interferometry (FTSI) [14]. The extraction of the phase difference $\phi(\omega+\delta\omega) - \phi(\omega) + \omega\tau$ is performed using a Fast Fourier Transform, a filtering of one of the interference terms, and a Fast Fourier Transform back to the initial experimental points.

A possible schematic of a SPIDER device is presented in Fig. 2.7. The pulse to be characterized is separated into two replicas with different intensities. The first arm (low intensity) is composed of an interferometer for producing and delaying two replicas by τ. The second arm (high intensity) is constituted of a device for introducing a fixed amount of dispersion in order to stretch the pulse. The beams from the two arms are focused into a non linear crystal (BBO) for the sum frequency generation (SFG). The SPIDER signal is measured with a spectrometer.

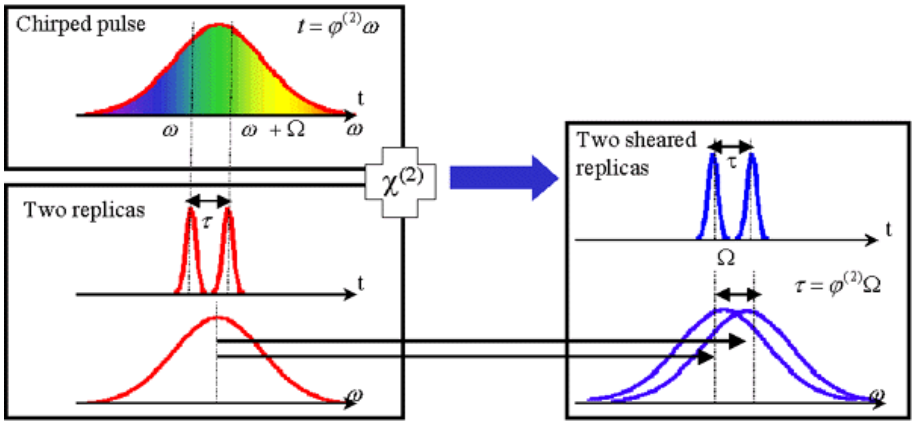

Figure 2.6: Generation of two sheared replicas of the input pulse by non-linear interaction with a chirped pulse. Reprinted from [3]

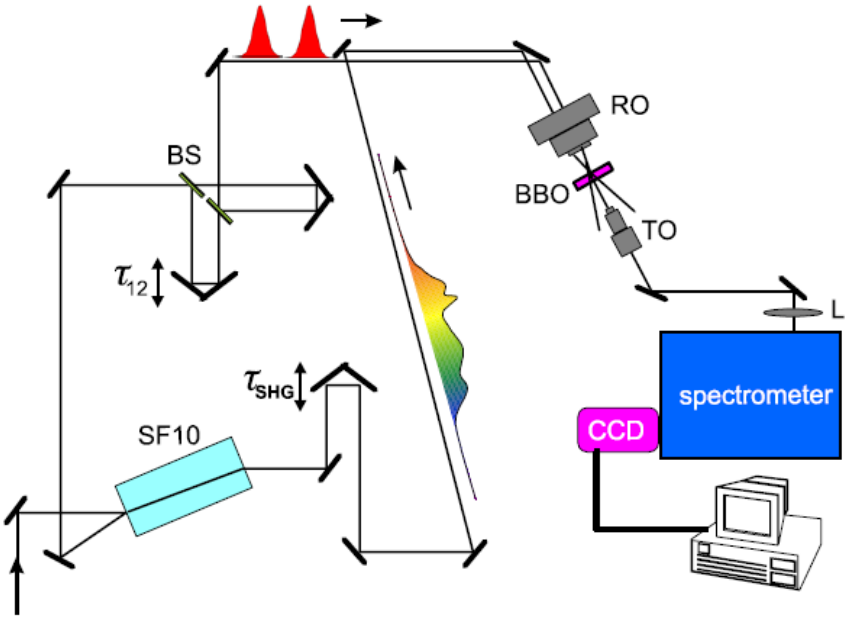

Figure 2.7: Example of SPIDER schematic. SF 10: glass block, BS: beam splitter, τ: adjustable delay between unchirped replica, τ_{SHG}: delay between unchirped pulses and strongly chirped pulse, RO: focusing lens, TO: collecting lens

2.3.3 FROG technique

Another technique for the complete pulse characterization is the FROG (Frequency Resolved Optical Gating) [8, 16]. This technique can be understood as a spectrally resolved autocorrelation. The result of the measurement is a time-frequency spectrogram and the spectral phase

and amplitude is extracted using an iterative algorithm. A schematic of a FROG device is shown in Fig. 2.8. The FROG measurement can use second or third order nonlinearity. The pulse to be measured with an electric field $E(t)$ interacts, in the non linear medium, with a temporal gate $G(t-\tau)$, being τ the delay between the pulses. The signal generated by the nonlinear interaction can be expressed as: $E_{signal}(t,\tau) = E(t)G(t-\tau)$. A spectrometer enables to measure the spectral intensity $I_{FROG}(\omega)$ for different delays τ. The mathematical expression of the measured spectrogram is:

$$I_{FROG}(\omega,\tau) = \left| \int_{-\infty}^{+\infty} E(t)G(t-\tau)exp(-i\omega t)dt \right|^2 \tag{2.14}$$

Considering the case with SHG (non collinear geometry) as the nonlinear process, the gate function is the pulse to be measured delayed by τ. The FROG trace (Fig. 2.9) can then be expressed as:

$$I^{SHG}_{FROG}(\omega,\tau) = \left| \int_{-\infty}^{+\infty} E(t)E(t-\tau)exp(-i\omega t)dt \right|^2 \tag{2.15}$$

With an iterative algorithm the spectral phase and amplitude is extracted from the trace.

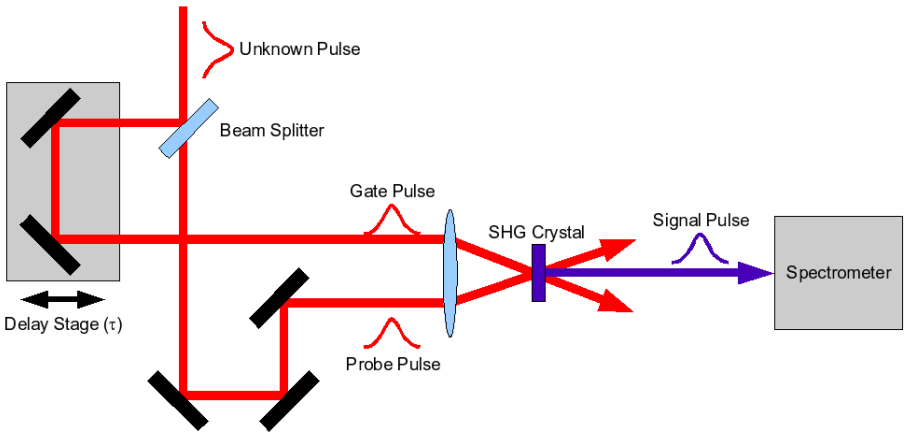

Figure 2.8: Schematic of a typical FROG (multishot SHG) setup.

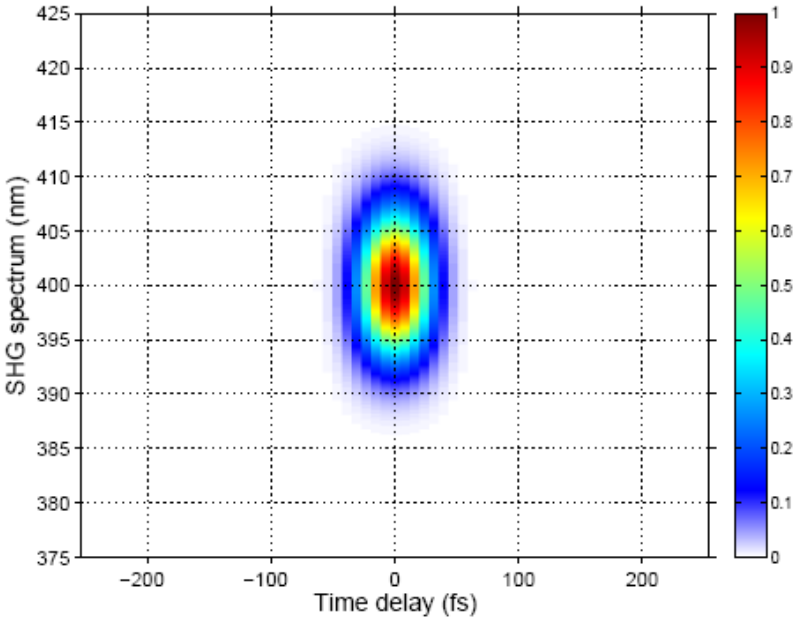

Figure 2.9: Example of a measured SHG FROG trace. The spectral phase and amplitude is extracted from this trace with an iterative algorithm

2.3.4 Phazzler

All the previous solutions for characterizing ultra-short pulses are made up by the same blocks. A linear interferometer, a non linear process and a detector. In particular it can be demonstrated that for the measurement of a pulse with an integrating detector (it is always the case for fs pulses) a non linear process is needed. As it will be shown in section 6.2.3, an Acousto-Optical Programmable Dispersive Filter (AOPDF, Dazzler) acts as a linear filter. In particular if $\left|\tilde{E}_{in}(\omega)\right|$ is the input spectral amplitude of an optical pulse, the spectral amplitude at the output of the programmable dispersive filter, $\left|\tilde{E}_{out}(\omega)\right|$, is equal to the product of $\left|\tilde{E}_{in}(\omega)\right|$ with the spectral transfer function $H(\omega)$:

$$\left|\tilde{E}_{out}(\omega)\right| = H(\omega)\left|\tilde{E}_{in}(\omega)\right| \tag{2.16}$$

The AOPDF can then substitute the linear interferometer of a pulse measurement device. This idea is implemented in the device for pulse shaping and characterization named Phazzler (Fastlite) [11] (Fig. 2.10). The main advantage of this solution is the extreme flexibility of the device: a FROG, a SPIDER and an autocorrelation measurement can be done with the same device without changing the elements inside and the alignment. Furthermore working in a collinear configuration makes the alignment extremely easy (there are two external pin-holes for the alinement). Generating two delayed replicas of the pulse with the pulse shaper opens also some new interesting features [10]. For example, scanning the delay between the two replicas can be realized, first, by shifting simultaneously the envelope and CEP as is the case for a mechanical delay line (for example moving one arm of a Michelson interferometer). In this case the spectral transfer function is $H(\omega) = exp(i(\omega - \omega_0)\tau)$, with ω_0 the carrier frequency. We

define this optical delay. The second option is to shift only the envelope keeping the CEP fixed. In this case the spectral transfer function is $H(\omega) = exp(i(\omega\tau))$ and we define this pure delay. Any intermediate carrier envelope phase shift between the two extremes is also possible.

The spectral transfer function to produce to replicas delayed by τ (symmetric respect to t=0) is than given by the expression:

$$H(\omega) = \frac{1}{2}(exp(i(\omega - (1-\gamma)\omega_0))\tau/2 + exp(-i(\omega - (1-\gamma)\omega_0)\tau/2 \tag{2.17}$$

The CEP remains unchanged for $\gamma = 1$ (pure delay) and shifts together with the envelope for $\gamma = 0$ (optical delay).

When the two delayed pulses are generated for an interferometric autocorrelation measurement, changing the value of γ changes the period of oscillation of the trace. In particular for $\gamma = 1$ the trace presents no oscillations and only the envelope is visible. This may seem surprising given the fact that the two wave propagate collinearly, but beautifully demonstrates the ability to control the CEP. This control of the CEP with the Dazzler will be discussed more precisely in section 6.9. When $\gamma = 1$ we define this as a base-band measurement. For $\gamma < 1$ oscillations appear and their periodicity can be adjusted at will through a choice of γ. While for $\gamma = 0$ the oscillation frequency matches the carrier frequency, for $\gamma = 0.5$ the oscillation frequency is reduced by a factor of two. For this reason this interferometric autocorrelation made with the Phazzler is called Pseudo Interferometric Autocorrelation (PIAC).

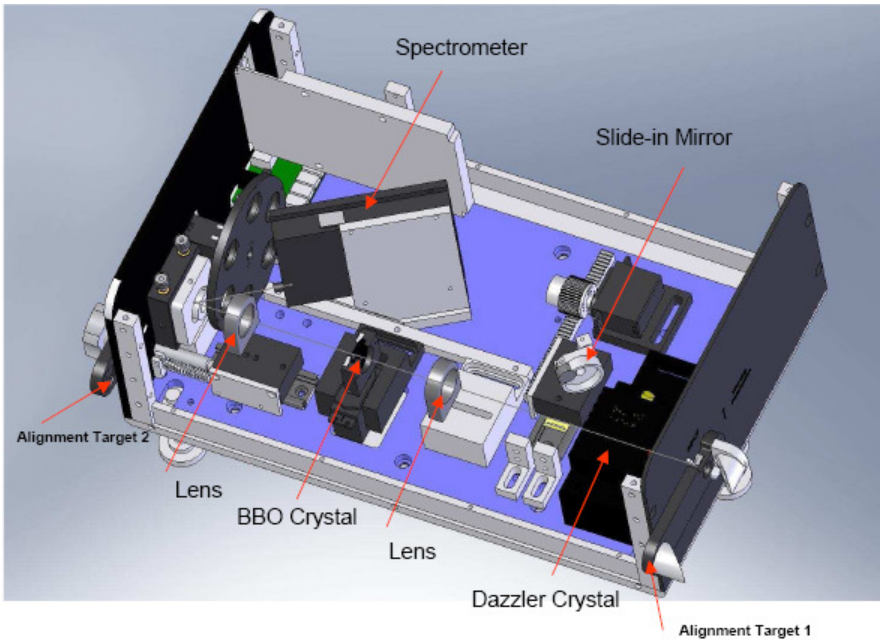

Figure 2.10: CAD drawing of the internal view of the Phazzler optical module. Reprinted from [11].

Phazzler FROG

I have previously presented that a SHG FROG measurement is a frequency resolved interferometric autocorrelator. The expression for the FROG trace with collinear beams gives [13]:

$$I_{iFROG}^{SHG}(\omega,\tau) = \left| \int_{-\infty}^{+\infty} (E(t) + E(t-\tau))^2 exp(-i\omega t) dt \right|^2 \tag{2.18}$$

The Phazzler configuration for a FROG measurement is shown in Fig. 2.11. Changing the value of γ affects the FROG trace. In particular when $\gamma = 1$ we obtain a baseband FROG trace (Fig. 2.12) and when $\gamma < 1$ an interferometric FROG trace (Fig. 2.13). As for a standard FROG, the spectral phase and amplitude are extracted from the FROG traces with an iterative algorithm.

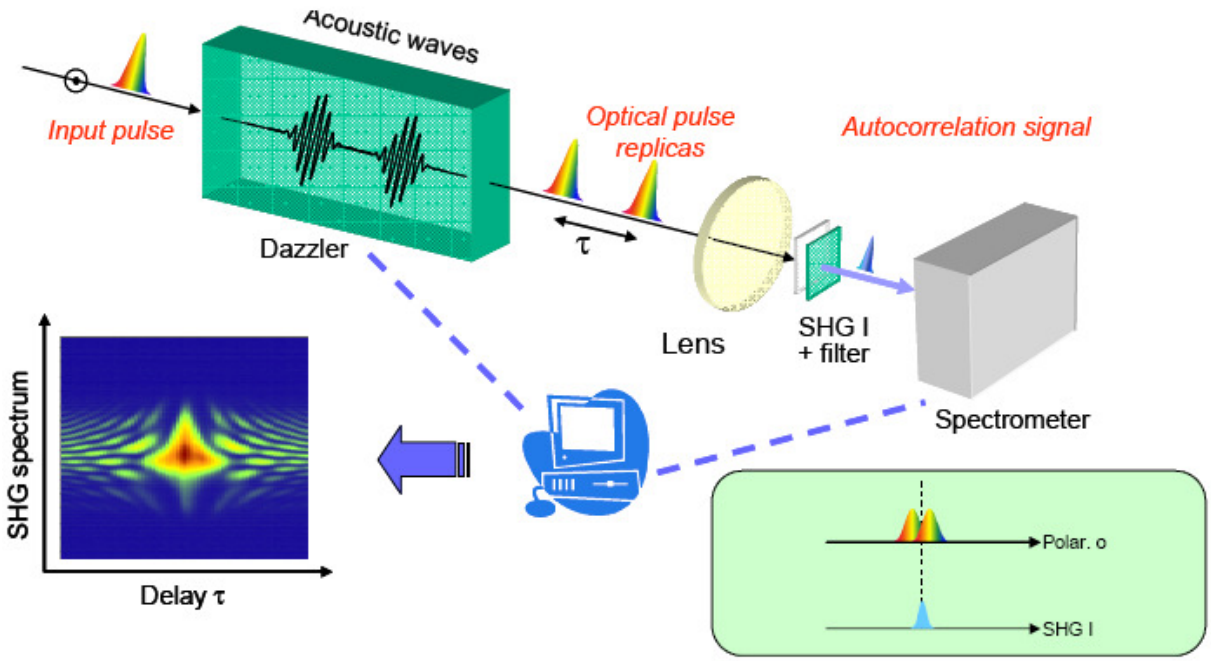

Figure 2.11: Schematic of a Phazzler FROG measurement

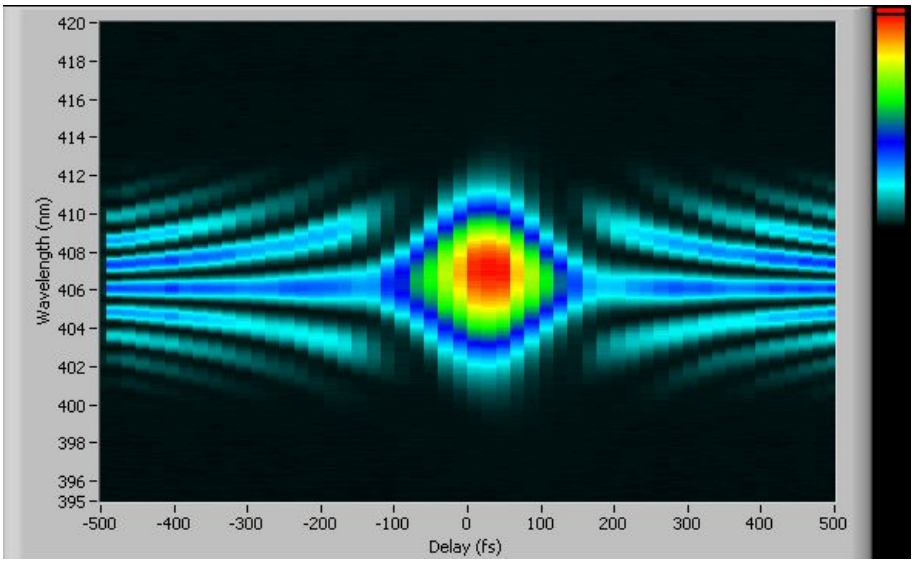

Figure 2.12: Experimental baseband ($\gamma = 1$) SHG FROG trace measured with the Phazzler. The pulse duration is 100 fs

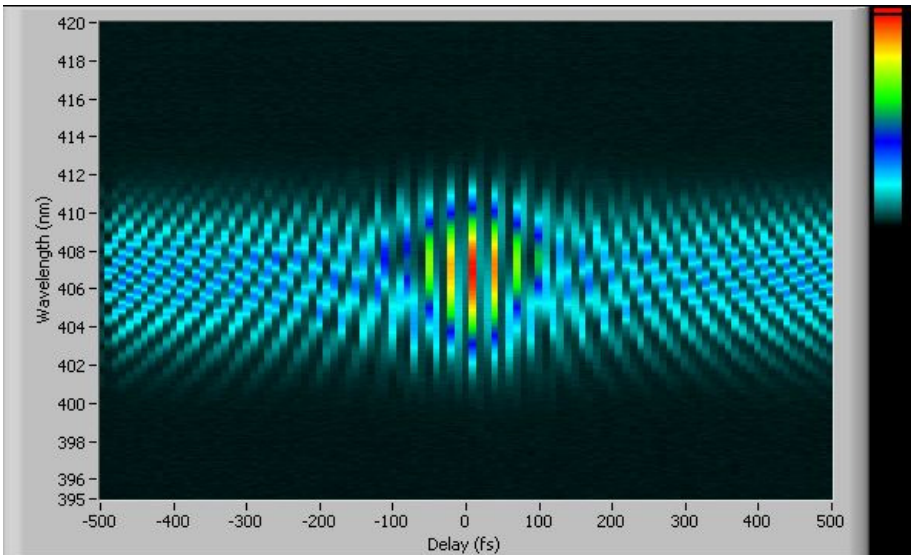

Figure 2.13: Experimental interferometric ($\gamma = 0.75$) SHG FROG trace measured with the Phazzler. The pulse duration is 100 fs

Until now I have only considered SHG FROG. Using this nonlinear effect has the drawback that there is an ambiguity in the temporal axis of the reconstructed temporal pulse and it is not possible to distinguish between the front and the back of the pulse. To avoid this ambiguity several third order non linear processes have been used (third harmonic generation, self diffraction, polarization gating...). XPW generation can also be a good candidate because it is a collinear process and the generated beam is easily separable from the fundamental using

a polarizer. As it will be clearly presented later, XPW generation has the other advantage of being achromatic and degenerate in wavelength. This means that the generated pulse is at the same wavelength as the fundamental. This is very important if we want to measure pulses in the UV where generating multiples of fundamental frequency (second, third harmonic generation) is not possible. The application of an XPW FROG for measuring UV pulses is one of the motivations for extending the study of the XPW process to shorter wavelengths(section 4.10). A Phazzler for measuring UV pulses using the XPW generation as a nonlinear process is under development. Fig. 2.14 shows an example of a baseband XPW FROG trace for a compressed pulse at 800 nm. The mathematical expression of the FROG trace in that case is given by:

$$I_{iFROG}^{XPW}(\omega,\tau) = \left| \int_{-\infty}^{+\infty} (E(t) + E(t-\tau))^3 exp(-i\omega t) dt \right|^2 \tag{2.19}$$

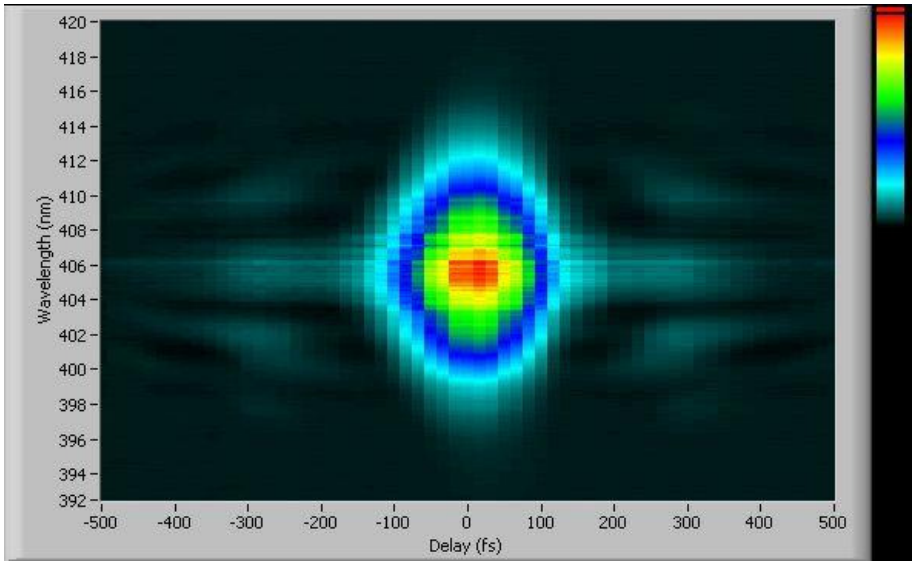

Figure 2.14: Experimental baseband ($\gamma = 0$) XPW FROG trace measured with the Phazzler

Phazzler SPIDER

Working with a pulse shaper as a substitute for the linear interferometer has several advantages also concerning the SPIDER measurement. The technique can be made totally collinear, the interpulse delay is accurately known (without any need for external calibration), the spectral shear is also known with an accuracy equal to the spectral resolution of the pulse shaper and all the parameters can be changed at will. When a type I SHG crystal is used this measurement is called a phase cycling SPIDER (cSPIDER). This variant is multi-shot (as it will be clear later 4 shots are needed for the reconstruction) but the optical setup is single beam and reduced to the same number of elements : the AOPDF, a type I SHG crystal and the spectrometer.
In this variant of the SPIDER there is a combination of three collinear pulses in the same

polarization state: two well separated time-delayed replicas $(E(t-\tau/2), E(t+\tau/2))$ and one chirped pulse with the time-dependent complex envelope $F(t)$:

$$E_{++}(t) = E(t-\tau/2) + E(t+\tau/2) + F(t) \tag{2.20}$$

In time domain and for perfect phase matching over the full spectrum, the type I SHG signal is proportional to the square of $E_{++}(t)$. If the interpulse delay τ is much larger than the pulse duration, the cross-terms between the pulse replicas vanishes and the only remaining cross-term corresponds to the SPIDER signal. Unfortunately, the only physical quantity experimentally accessible is the spectral intensity of the SHG spectrum $I_{++}(\omega)$, that is the square modulus of the Fourier Transform of $E^2_{++}(t)$. As a result, the experimental signal contains several parasitic signals together with the SPIDER signal. Phase cycling can be used to eliminate the parasitic terms by linear combination of several measurements. More precisely, given the SHG signals of the four following pulse combinations (obtained by changing the sign of the transfer function of the AOPDF):

$$E_{++}(t) = \pm E(t-\tau/2) \pm E(t+\tau/2) + F(t) \tag{2.21}$$

the SPIDER signal is extracted by the following combination:

$$I_{SPIDER}(\omega) = I_{++}(\omega) + I_{++}(\omega) - I_{+-}(\omega) - I_{-+}(\omega) \tag{2.22}$$

The input spectral phase is retrieved from this SPIDER signal with the same method presented in section 2.3.2.

2.3.5 Third order correlator

In section 2.2.2 I showed that to characterize the temporal quality of a femtosecond pulse it is not sufficient to measure its temporal duration but also its temporal contrast. The device used to measure this temporal contrast with a high dynamic range (>10 orders of magnitude) is a third order correlator. The schematic of this measurement is shown in Fig. 2.15. In this device the beam passes thought a variable attenuator and is then separated into two different paths. In the first the beam is frequency doubled. In the other the fundamental beam passes through a motorized delay line. The fundamental and the second harmonic interact in a BBO crystal for the generation of the third harmonic by sum frequency generation. The third harmonic is then separated from the other pulses and is detected with a photomultiplier. The third order correlation signal is given by the expression:

$$S_{3\omega}(\tau) = \int_{-\infty}^{+\infty} I_{2\omega}(t) I_{\omega}(t-\tau) dt \tag{2.23}$$

The temporal contrast of the input beam is estimated by measuring the temporal contrast of the correlation trace. This trace has a high temporal dynamic because the parasitic sources of third harmonic are limited to the third harmonic generation generated directly by the fundamental beam.

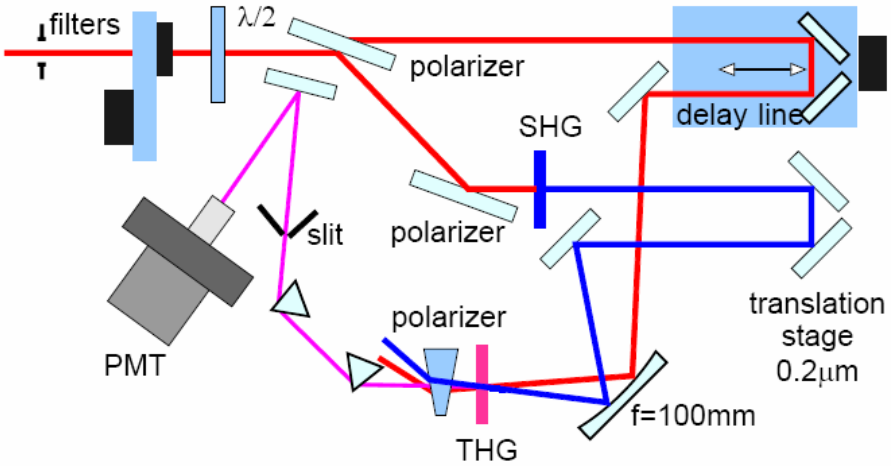

Figure 2.15: Schematic for a high dynamic third order correlator

Bibliography

[1] A. Apolonski, A. Poppe, G. Tempea, Ch. Spielmann, Th. Udem, R. Holzwarth, T. W. Hänsch, and F. Krausz. Controlling the phase evolution of few-cycle light pulses. *Phys. Rev. Lett.*, 85(4):740–743, 2000.

[2] J-C. M. Diels, J. J. Fontaine, I. C. McMichael, and F. Simoni. Control and measurement of ultrashort pulse shapes (in amplitude and phase) with femtosecond accuracy. *Appl. Opt.*, 24(9):1270–1282, 1985.

[3] http:ultrafast.physics.ox.ac.uk.

[4] http:nanooptics.uni-graz.at

[5] C. Iaconis and I. A. Walmsley. Spectral phase interferometry for direct electric-field reconstruction of ultrashort optical pulses. *Opt. Lett.*, 23(10):792–794, 1998.

[6] C. Iaconis and I. A. Walmsley. Self-referencing spectral interferometry for measuring ultrashort optical pulses. *IEEE J. Quantum Electron.*, 35(4):501–509, 1999.

[7] M. Kaluza, J. Schreiber, M. I. K. Santala, G. D. Tsakiris, K. Eidmann, J. Meyer-ter Vehn, and K. J. Witte. Influence of the laser prepulse on proton acceleration in thin-foil experiments. *Phys. Rev. Lett.*, 93(4):045003–, July 2004.

[8] D. J. Kane. Single-shot measurement of the intensity and phase of an arbitrary ultrashort pulse by using frequency-resolved optical gating. *Opt. Lett.*, 18(10):23–25, 1993.

[9] X. Liu, R. Wagner, A. Maksimchuk, E. Goodman, J. Workman, D. Umstadter, and A. Migus. Nonlinear temporal diffraction and frequency shifts resulting from pulse shaping in chirped-pulse amplification systems. *Opt. Lett.*, 20(10):1163–1165, 1995.

[10] T. Oksenhendler PhD manuscript.

[11] Phazzler manual.

[12] Y. Nomura PhD manuscript.

[13] G. Stibenz and G. Steinmeyer. Interferometric frequency-resolved optical gating. *Opt. Express*, 13(7):2617–2626, 2005.

[14] M. Takeda, H. Ina, and S. Kobayashi. Fourier-transform method of fringe-pattern analysis for computer-based topography and interferometry. *J. Opt. Soc. Am.*, 72(1):156–160, 1982.

[15] C. Thaury, F. Quere, J.-P. Geindre, A. Levy, T. Ceccotti, P. Monot, M. Bougeard, F. Reau, P. d'Oliveira, P. Audebert, R. Marjoribanks, and Ph. Martin. Plasma mirrors for ultrahigh-intensity optics. *Nat Phys*, 3(6):424–429, June 2007.

[16] R. Trebino, A. Baltuska, M. S. Pshenichnikov, and D. A. Wiersma. *Few-Cycle Laser Pulse Generation and Its Applications*, volume 95, chapter Measuring Ultrashort Pulses in the Single-Cycle Regime: Frequency-Resolved Optical Gating, pages 231–264. Springer-Verlag, 2004.

[17] M. Zepf, G. D. Tsakiris, G. Pretzler, I. Watts, D. M. Chambers, P. A. Norreys, U. Andiel, A. E. Dangor, K. Eidmann, C. Gahn, A. Machacek, J. S. Wark, and K. Witte. Role of the plasma scale length in the harmonic generation from solid targets. *Phys. Rev. E*, 58(5):R5253–R5256, Nov 1998.

Chapter 3

Theoretical introduction to cross-polarized wave generation

3.1 Introduction

This paragraph introduces theoretically the process of cross-polarized wave generation. An historical introduction is presented in section 4.3.
XPW generation is a four-wave mixing process, governed by the anisotropy of the real part of the crystal third-order nonlinearity tensor $\chi^{(3)}$, where an intense linearly polarized incident wave generates a new linearly polarized wave in the orthogonal direction. This process has important applications as a nonlinear filter to increase the temporal contrast of ultra-short laser pulses and to broaden their spectrum (section 4.2).

In the first section I derive the system of differential equations governing XPW generation and analyze the contribution from different terms. Due to the fact that this nonlinear process is generated in a crystal lattice, these terms depend on the angles of propagation of the waves with respect to the crystal axis. This analysis continues in the second section with the derivation of the system in Hamiltonian form and the analysis of the trajectories in phase space. All these results are derived for monochromatic plane waves. This analysis is then extended for ultra-short pulses. One of the most interesting properties of XPW generation is that the process is automatically phase-matched and is therefore adapted for applications involving ultra-short pulses. For this kind of pulses temporal compression is not trivial and it is interesting to understand the influence of quality of the recompression on the efficiency of the process and on the generated spectrum. This will be presented in the third section for pulses as short as 10 fs. To describe correctly the process for sub-10 fs pulses the propagation in the crystal needs to be taken into account. In this case a system of nonlinear partial differential equations needs to be solved. This is done using a numerical method called the split-step Fourier method and it is the subject of the fourth section.

3.1.1 Cross-polarized wave generation

I start the theoretical description of XPW generation with the wave propagation equation in a dielectric, linearly isotropic, non-magnetic nonlinear medium [12].

$$\Delta\vec{\mathcal{E}} - \frac{n^2}{c^2}\frac{\partial^2\vec{\mathcal{E}}}{\partial t^2} = \mu_0\frac{\partial^2\vec{P}^{NL}}{\partial t^2}, \tag{3.1}$$

where $\vec{\mathcal{E}}$ is the electric field, n the linear index of refraction, c is the vacuum speed of light, μ_0 vacuum permittivity, and $\vec{P}^{NL}\left(\vec{\mathcal{E}}\right) = \varepsilon_0\chi^{(2)}\vec{\mathcal{E}}\vec{\mathcal{E}} + \varepsilon_0\chi^{(3)}\vec{\mathcal{E}}\vec{\mathcal{E}}\vec{\mathcal{E}} + \cdots$ is the nonlinear dielectric polarization. Only the contribution of the third-order susceptibility tensor $\chi^{(3)}$ is considered to obtain:

$$\vec{P}^{NL}\left(\vec{\mathcal{E}}\right) = \varepsilon_0\chi^{(3)}\vec{\mathcal{E}}\vec{\mathcal{E}}\vec{\mathcal{E}}. \tag{3.2}$$

In a Cartesian coordinate system for a plane wave traveling in z-direction it results:

$$\frac{\partial^2\mathcal{E}_i}{\partial z^2} - \frac{n^2}{c^2}\frac{\partial^2\mathcal{E}_i}{\partial t^2} = \varepsilon_0\mu_0\frac{\partial^2}{\partial t^2}\sum_{j,k,l}\chi^{(3)}_{ijkl}\mathcal{E}_j\mathcal{E}_k\mathcal{E}_l, \tag{3.3}$$

where indices i, j, k, l take x, y, z-values. The plane wave for linearly isotropic medium ($k_x = k_y = k_z \equiv k$) in complex notation is written as

$$\begin{aligned}\mathcal{E}_i(z,t) &= \frac{1}{2}E_i(z)\exp\left[-i\left(\omega t - kz\right)\right] \\ &\quad + \frac{1}{2}E_i^*(z)\exp\left[+i\left(\omega t - kz\right)\right].\end{aligned} \tag{3.4}$$

From Eqs. (3.3) and (3.4) and using the slowly-varying envelope approximation the following system of ordinary differential equations can be derived

$$\begin{aligned}\frac{dE_i(z)}{dz} &= i\frac{2\pi}{8n\lambda}\sum_{j,k,l=x}^{z}\chi^{(3)}_{ijkl}[E_j(z)E_k(z)E_l^*(z) \\ &+ E_j(z)E_k^*(z)E_l(z) + E_j^*(z)E_k(z)E_l(z)].\end{aligned} \tag{3.5}$$

In Eq. (3.5) terms corresponding to third harmonic generation are omitted since I consider degenerate third order processes (the other processes are not phase matched and therefore with a very low efficiency). The relation $2\pi/n\lambda = \varepsilon_0\mu_0\omega^2/k$ is used. The third-order susceptibility $\chi^{(3)}_{ijkl}$ is a fourth-rank tensor and has in general 81 elements. Due to the symmetries of the medium most of these terms vanish. The crystals used for XPW generation are cubic crystals (BaF_2, CaF_2, LiF) with m3m cubic symmetry. It is also assumed that the photon energy is below the half band-gap and the two-photon absorption is then neglected. In this case $\chi^{(3)}_{ijkl}$ is a purely real tensor. The $\chi^{(3)}_{ijkl}$-components are usually given in a coordinate system connected with crystalline axes so we assume that (x, y, z) coincide with the corresponding crystalline axes. Components of the electric field of a wave that propagates in the k-direction are however given in a different Cartesian coordinate system (A, B, k). In general (A, B, k) does not coincide with (x, y, z) basis. For definition of angles between the axes of the two coordinate systems see Fig. 3.1. Further I shall refer to the wave E_A with polarization along A-axis as pump or

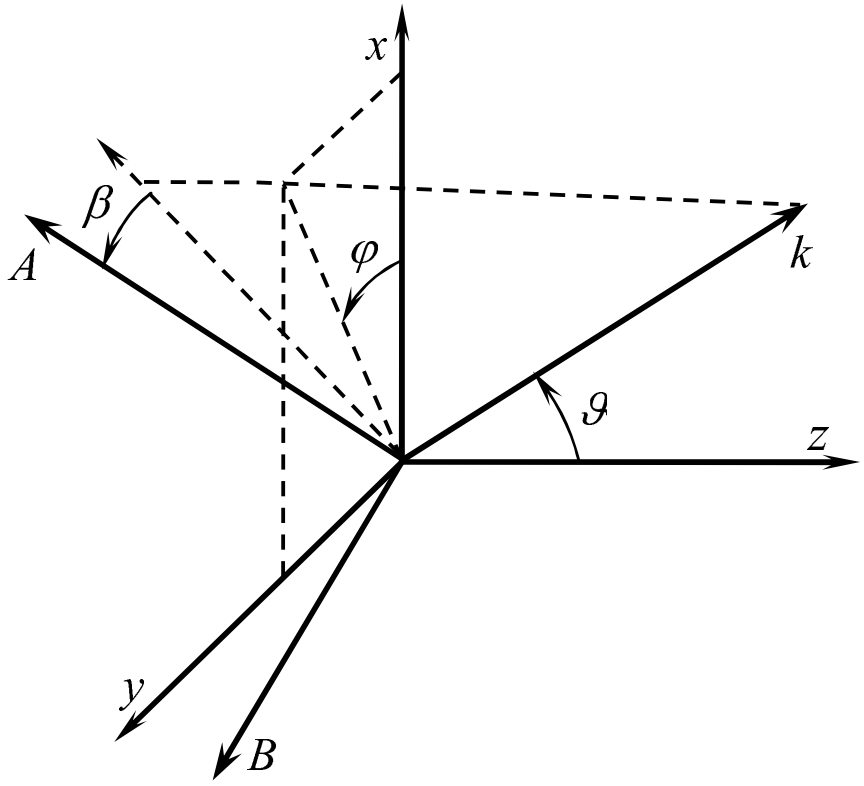

Figure 3.1: Definition of angles. (x, y, z) – basis of the nonlinear crystal, (A, B, k) – light propagation basis. The coordinate system (A, B, k) can be obtained from (x, y, z) by rotating (x, y, z) first around the z-axis by an angle φ, then around the new y axis by θ, and finally by β around the k-axis.

fundamental wave (FW), and to the wave E_B polarized along B-axis (orthogonal to A) as probe wave or XPW. Transformation of coordinates from (x, y, z) to (A, B, k) is given by

$$\begin{pmatrix} E_A \\ E_B \\ E_k \end{pmatrix} = \mathbf{T}(\varphi, \vartheta, \beta) \begin{pmatrix} E_x \\ E_y \\ E_z \end{pmatrix}, \tag{3.6}$$

where the transformation matrix $\mathbf{T}(\varphi, \vartheta, \beta)$ is

$$\mathbf{T}(\varphi, \vartheta, \beta) = \begin{pmatrix} \cos\beta\cos\vartheta\cos\varphi - \sin\beta\sin\varphi & \cos\beta\cos\vartheta\sin\varphi + \sin\beta\cos\varphi & -\cos\beta\sin\vartheta \\ -\sin\beta\cos\vartheta\cos\varphi - \cos\beta\sin\varphi & -\sin\beta\cos\vartheta\sin\varphi + \cos\beta\cos\varphi & \sin\beta\sin\vartheta \\ \sin\vartheta\cos\varphi & \sin\vartheta\sin\varphi & \cos\vartheta \end{pmatrix}. \tag{3.7}$$

First, using the inverse matrix $\mathbf{T}^{-1}$, the components of E_A and E_B waves are derived in (x, y, z)-basis by

$$\begin{pmatrix} E_x \\ E_y \\ E_z \end{pmatrix} = \mathbf{T}^{-1}(\varphi, \vartheta, \beta) \begin{pmatrix} E_A \\ E_B \\ E_k \end{pmatrix} \tag{3.8}$$

and then are substituted in the right-hand side of Eq. (3.5). There is no k-component of the field thus $E_k = 0$ is set. Next, using Eq. (3.7) the derivatives in the left-hand side of Eq. (3.5)

are combined to get back to the system connected with E_A and E_B waves. The following system of differential equations is obtained:

$$\frac{dA(\zeta)}{d\zeta} = i\gamma_1 AAA^* + i\gamma_2 AAB^* + 2i\gamma_2 ABA^* + 2i\gamma_3 ABB^* + i\gamma_3 BBA^* + i\gamma_4 BBB^*, \tag{3.9a}$$

$$\frac{dB(\zeta)}{d\zeta} = i\gamma_5 BBB^* + i\gamma_4 BBA^* + 2i\gamma_4 ABB^* + 2i\gamma_3 ABA^* + i\gamma_3 AAB^* + i\gamma_2 AAA^*. \tag{3.9b}$$

ζ is the longitudinal coordinate in the light propagation direction $\vec{k}$. Polarization of the medium along the k-axis does not generate an electromagnetic wave therefore in Eqs.(3.9) the expression for $dE_k/d\zeta$ is omitted. In Eqs. (3.9) E_A and E_B are denoted simply as A and B, respectively. The γ-coefficients in Eqs. (3.9) depend on the orientation and on the components of the $\chi^{(3)}$-tensor. In the case of crystals with m3m cubic symmetry there are only two independent components [10]: $\chi^{(3)}_{xxxx}$ and $\chi^{(3)}_{xxyy}$. The relation between them is usually defined [10] as $\sigma = \left(\chi^{(3)}_{xxxx} - 3\chi^{(3)}_{xxyy}\right)/\chi^{(3)}_{xxxx}$ and is referred to as the anisotropy of the $\chi^{(3)}$-tensor. For z-orientation, due to the symmetry with respect to rotation around z-axis, there are only three independent nonlinear coupling coefficients since $\gamma_5 = \gamma_1$ and $\gamma_4 = -\gamma_2$. For arbitrary orientation of the nonlinear crystal such relations between coefficients are no longer valid. Instead, the following general relations for the coefficients in the full system (9) may be written

$$\gamma_5(\beta, \varphi, \vartheta) = \gamma_1(\beta + \pi/2, \varphi, \vartheta), \tag{3.10a}$$

$$\gamma_4(\beta, \varphi, \vartheta) = -\gamma_2(\beta + \pi/2, \varphi, \vartheta). \tag{3.10b}$$

The above expressions (3.10) do not convey new physical information. They simply mean that rotating β by 90°, the B-wave would become A, and the A-wave would become B. They could thus serve as a check for the correctness of the derivation of γ coefficients.

Coefficients γ_1 and γ_5 are responsible for self-phase modulation, γ_3 for cross-phase modulation and γ_2 and γ_4 govern the XPW conversion process from A to B and from B to A waves through the last terms in (3.9b) and (3.9a), respectively. This will be shown more clearly in the next section using an Hamiltonian formalism for the XPW generation equations. Note that generally self-phase modulation and XPW generation are not the same for the A and B waves except for z crystallin orientation.

Even in the relatively simple case of cubic crystals explicit expressions for the γ-coefficients as a function of β, φ, and ϑ are quite cumbersome. Here I prefer to take advantage of the transformation matrix $\mathbf{T}$ given in Eq. (3.7) and its inverse matrix $\mathbf{T}^{-1}$ to give more compact expressions for the γ-coefficients:

$$\gamma_1 = \gamma_0 \sum_{j,k=1}^{3} [\delta_{jk} + (1 - \delta_{jk})(1 - \sigma)] T_{1j} T_{j1}^{-1} \left(T_{k1}^{-1}\right)^2, \tag{3.11a}$$

$$\gamma_2 = \gamma_0 \sum_{j,k=1}^{3} [\delta_{jk} + (1 - \delta_{jk})(1 - \sigma)] T_{2j} T_{j1}^{-1} \left(T_{k1}^{-1}\right)^2, \tag{3.11b}$$

$$\gamma_3 = \gamma_0 \sum_{j,k=1}^{3} \left\{ \left[\delta_{jk} + \frac{2}{3}(1-\delta_{jk})(1-\sigma) \right] T_{j2} T_{k1}^{-1} T_{k2}^{-1} + \frac{1}{3}(1-\delta_{jk})(1-\sigma) T_{j1}^{-1} \left(T_{k2}^{-1} \right)^2 \right\} T_{1j}, \tag{3.11c}$$

$$\gamma_4 = \gamma_0 \sum_{j,k=1}^{3} [\delta_{jk} + (1-\delta_{jk})(1-\sigma)] T_{1j} T_{j2}^{-1} \left(T_{k2}^{-1} \right)^2, \tag{3.11d}$$

$$\gamma_5 = \gamma_0 \sum_{j,k=1}^{3} [\delta_{jk} + (1-\delta_{jk})(1-\sigma)] T_{2j} T_{j2}^{-1} \left(T_{k2}^{-1} \right)^2, \tag{3.11e}$$

where $\gamma_0 = 6\pi\chi^{(3)}_{xxxx}/8n\lambda$. δ_{jk} is the Kronecker delta-symbol.

Investigation of Eq. (3.11b) shows that $\gamma_2(\beta, \varphi, \vartheta)$ reaches its global maxima (with equal absolute values of γ_2) when $\varphi = 2n\pi/4$ and $\vartheta = 2(m+1)\pi/4$, or when $\varphi = 2(n+1)\pi/4$ and $\vartheta = 2m\pi/4$ where $m, n = 0, 1, \ldots$. This means that, to reach the maximum of $|\gamma_2|$ for specific values of β-angle, the light propagation direction k should lie in the (x, y), (x, z), or (y, z) plane just between (at 45 degrees) the corresponding crystalline axes. In this respect there are twelve equivalent optimal orientations of the NLC: [110], [$\bar{1}$10], [1$\bar{1}$0], [$\bar{1}\bar{1}$0], [101], [$\bar{1}$01], [10$\bar{1}$], [$\bar{1}$0$\bar{1}$], [011], [0$\bar{1}$1], [01$\bar{1}$], and [0$\bar{1}\bar{1}$], also known as holographic-cut orientations. For the eight equivalent to [111] propagation directions $\gamma_2 = \gamma_4 = 0$ for any angle β and the orthogonal generation term is always zero regardless of the polarization state or orientation, and the medium shows isotropic behavior.

3.1.2 Numerical results

In the non-depleted regime, the efficiency of XPW generation is proportional to the square of γ_2 ([8, 9]). The dependence of this coefficient on angle β is plotted on Fig. 3.2 for three orientations: the most efficient one [101] (holographic-cut), [001] (z-cut), and for the polarization preserving orientation [111] (Fig. 3.3). In calculations $\gamma_0 = 1$ and $\sigma = -1.2$ (typical values for the BaF_2 anisotropy [6]) were used. All the firsts experiments of XPW generation were done using z-cut crystals. This was an academic choice because in this case the k-axis is along the z or equivalent axis. This theoretical analysis demonstrates that the maximum absolute value of γ_2 for [101]-cut is 12% greater than the maximum for z-cut and this corresponds to an almost 26% increase in the XPW efficiency. This advantage does not depend on the particular choice of the values of γ_0 and σ since γ_2 depends linearly on them for arbitrary crystal orientation i.e $\gamma_2 \propto \gamma_0\sigma$.

Calculated values for the coefficients γ_1 and γ_5 for z-cut and holographic-cut crystals are presented in Fig. 3.4. Knowing these coefficients is important since the phase mismatch induced by self-phase modulation impedes efficient XPW generation.

In order to determine the XPW-generation efficiency, the system of differential equations (3.9) is numerically solved. This can be done using standard programs like Matlab, Mathematica, Maple. Analytical information from the equations will be extracted in the next section looking for the trajectories in phase space. In the case of plane-wave propagation the efficiency is defined as the ratio of the intensities of the XPW and the input fundamental wave. The

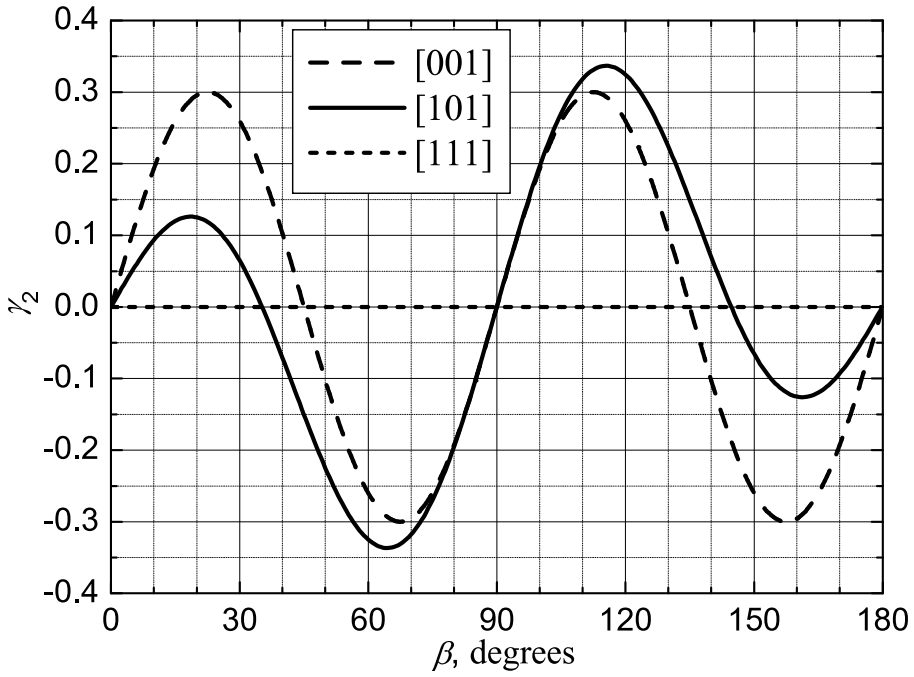

Figure 3.2: Calculated values of γ_2 as function of angle β for different crystal orientations. $\sigma = -1.2$ and $\gamma_0 = 1$.

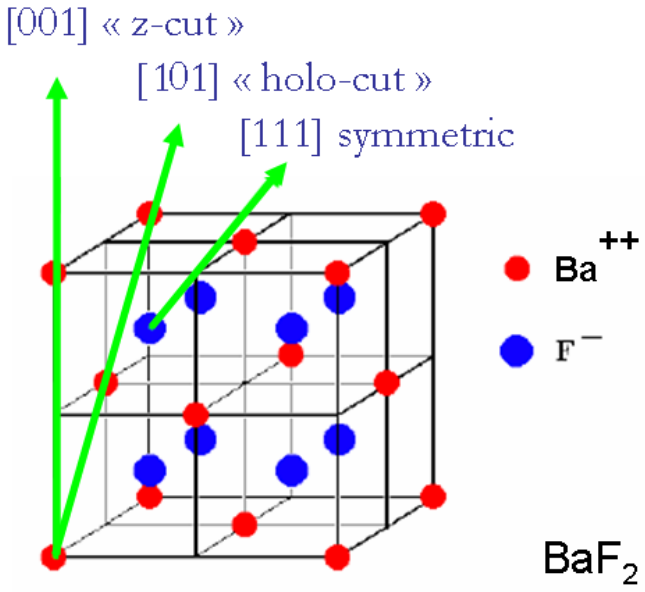

Figure 3.3: Representation of the three different orientations in BaF_2 crystal

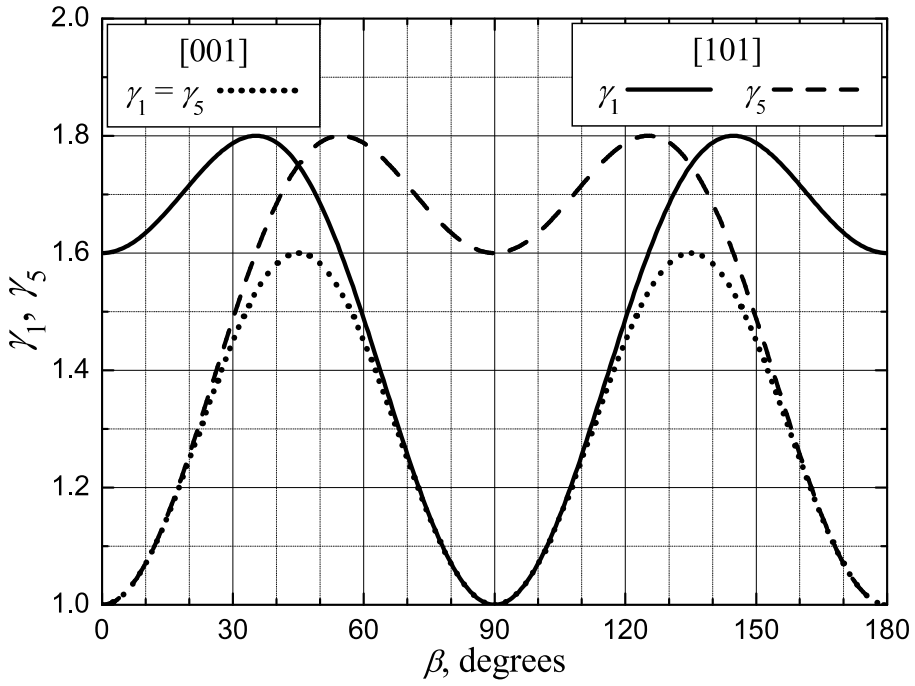

Figure 3.4: Calculated values of γ_1 and γ_5 as function of angle β for z-cut ([001]) and holographic-cut ([101]) crystal orientations. $\sigma = -1.2$ and $\gamma_0 = 1$.

calculated XPW efficiencies for the [101]-cut and for the [001]-cut (z-cut) are shown in Fig. 3.5 along with phase shifts between the fundamental wave and the generated XPW. The dimension-

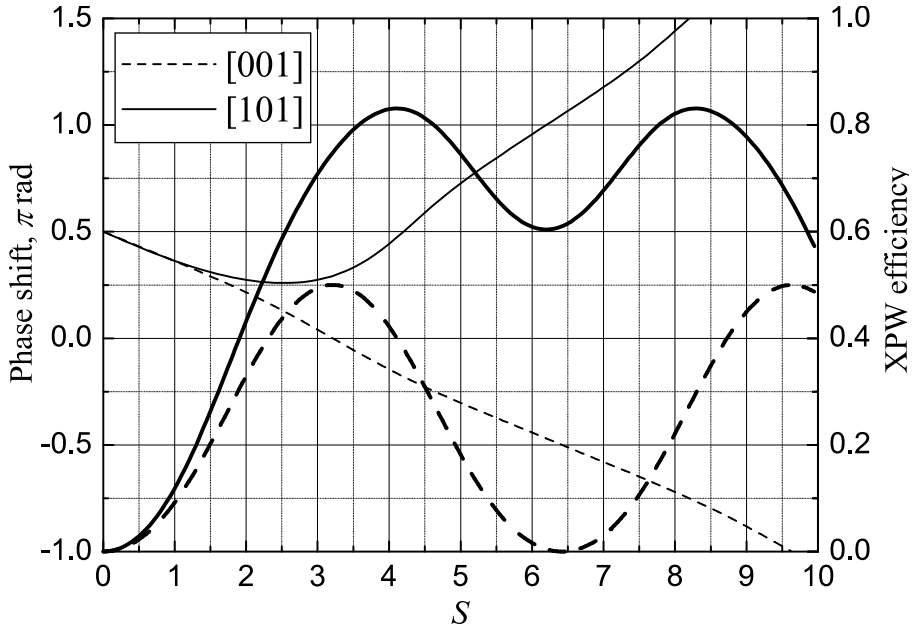

Figure 3.5: Numerically calculated plane-wave XPW efficiency (right scale, thick lines), and phase shift between the fundamental and XPW (left scale, thin lines) for [001] (z-cut) and [101] (holographic-cut) directions of light propagation. $\sigma = -1.2$; $\beta = 22.5°$ for [001] and $\beta = 115.5°$ for [101]-orientation, respectively.

less argument $S = \gamma_0 |A_0|^2 L$, where $A_0 = A(\zeta = 0)$ and L is the crystal length, is proportional to the product of nonlinearity × input intensity × crystal length. The initial condition for the

B-wave is $B(0) = 0$. β-angles used in calculations correspond to the angles at which $|\gamma_2|$ is maximum for each cut (see Fig. 3.2). These angles are optimal for XPW generation at low input intensity.

For z-cut crystals the optimum β depends on the input intensity[9]. This is illustrated in Fig. 3.6(a). At first, it should be noticed that for z-cut crystals there are eight equal maxima

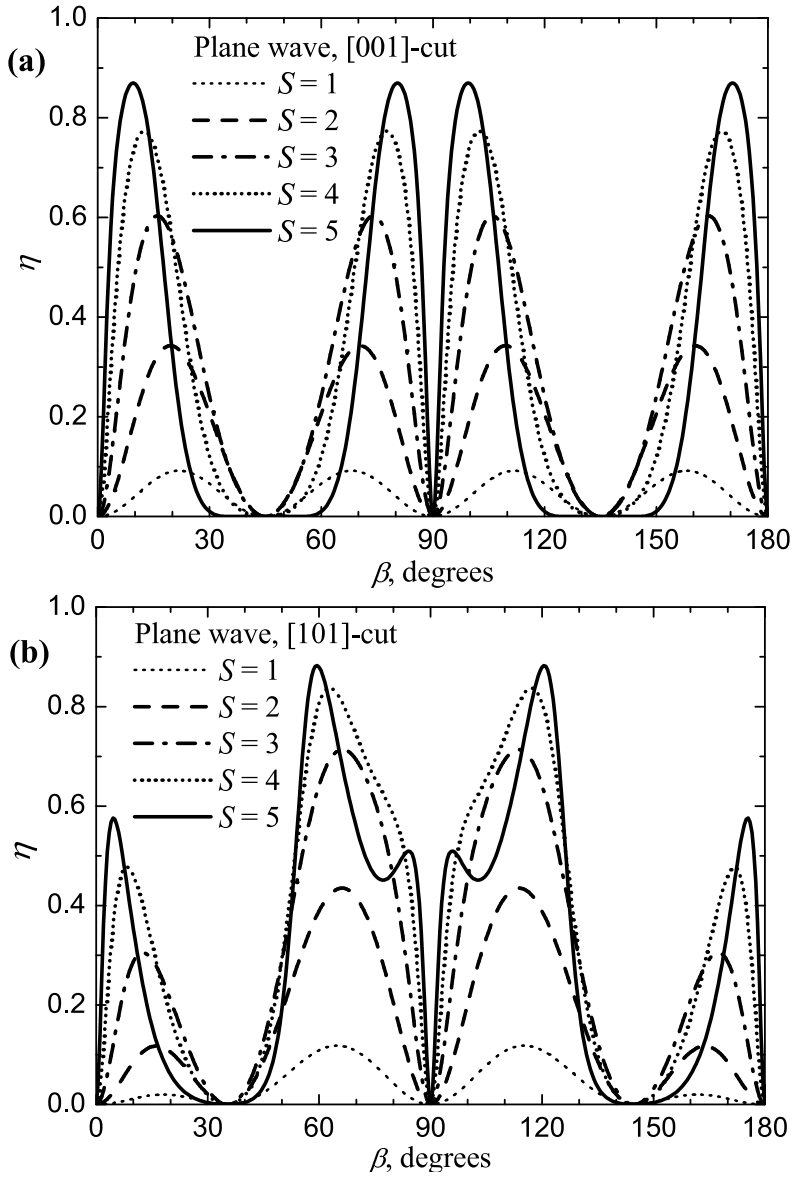

Figure 3.6: Plane-wave XPW efficiency η: (a) for [001]-orientation, and (b) for [101]-orientation as function of angle β for different input intensities. See text for definition of S. $\sigma = -1.2$.

of the generated XPW within 360° rotation of input linear polarization. For any other crystal orientation there are still eight maxima but they are no longer equal – two higher are succeeded by two lower. From Fig. 3.6 it is visible that increasing the input intensities up to $S \approx 5$, the optimal β is shifted by as much as 13 degrees for the z-cut while, for the higher maxima of the [101]-cut, this shift does not exceed 5 degrees. At a slightly lower intensity the shift for [101]-cut becomes very small. The origin of this shift is that the phase mismatch between the fundamental and XPW beam induced by SPM is partly compensated by the shift of β. The

practical experimental limit for the S parameter, $S \approx 5$, [7] can be estimated considering a BaF_2 crystal of few millimeters and a maximum intensity I_0 of $10^{12} W/cm^2$. This maximum intensity corresponds to the threshold for white-light continuum generation [11] for numerical apertures < 0.05 (typical experimental condition). In conclusion, with holographic-cut orientation, the optimum β is almost insensitive to the changes in the intensity for the whole reasonable range of input intensities, which is in contrast to the strong dependence observed with the z-cut. This feature of the holographic-cut orientation together with the higher efficiency make this orientation the most suitable for applications.

The insensitivity of optimum β to the input intensity for holographic-cut orientation is explained by the fact that, compared to the z-cut case, the phase matching conditions for optimal phase shift between the two waves ($\pi/2$) are maintained over a bigger range of input intensities (see Fig. 3.5 left scale, thin lines). The deviation from the optimal phase shift for the holographic-cut is less than $\pi/2$ up to $S = 6$, while at the same conditions the deviation from the optimal phase shift for z-cut is almost π. This insensitivity also means less distortions of the temporal and spatial pulse shape.

Efficiencies shown in Fig. 3.6 are obtained by direct solution of the system (3.9) and are relevant to monochromatic plane waves only. In experiments Gaussian femtosecond pulses are used. Considering the temporal and spatial shapes enables to obtain the energy efficiency of the XPW process. The input beam is assumed with Gaussian spatial and temporal profiles of the form $A(r, t, \zeta = 0) = A_0 \exp(-r^2) \exp(-t^2)$. Diffraction, dispersion, and self-focusing propagation effects are not included in the model. The results for XPW energy efficiencies for [001] and [101] cuts are shown in Fig. 3.7. These curves confirm the advantage of the

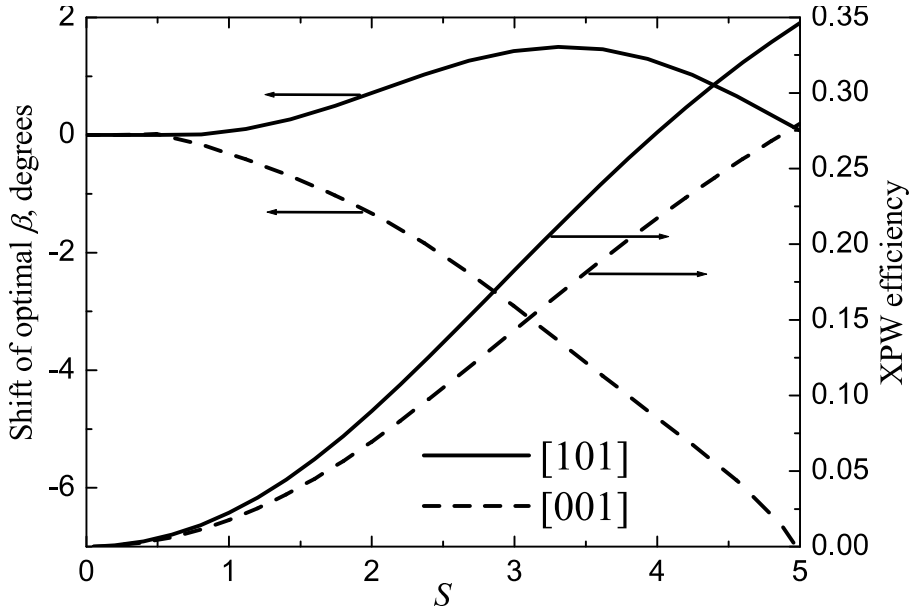

Figure 3.7: XPW efficiencies (right scale) for [001] and [101] orientations assuming Gaussian spatial and temporal profiles of the input beam. Angle β is always optimized for maximum efficiency. The shift of optimum β from its value β_0 for very low input intensity is also shown (left scale). β_0 is 22.5° for [001] and 64.5° for [101] orientation, respectively, and $\sigma = -1.2$.

holographic cut over the z-cut. The ratio of [101] XPW efficiency to [001] XPW efficiency in the range $S = 1 \ldots 5$ is between 1.24 and 1.29, reaching the maximum for $S \approx 1.9$. On the same figure the shift of optimum β from the low-intensity value is also shown. With $S = 5$ an XPW efficiency of more than 30 % can be obtained with the [101] cut. As it will discussed in section 4.4, this efficiency cannot be achieved experimentally in a single crystal but with a two crystals configuration.

3.2 Hamiltonian approach

3.2.1 Introduction

The motivation behind this alternative formulation of the XPW generation system of equations is to extract as much information as possible from the system without solving it numerically. The approach is to start from the general complex system of XPW equations (3.9)(or some simplified version) and to separate the real and imaginary part to obtain the real evolution equations for the amplitude of the two waves and their phase difference. From this system of equations we can derive two quantities that are conserved (first integrals) which are the energy and the momentum. These conserved quantities can be used to solve the problem analytically with some simplifying hypothesis. The conserved momentum is the Hamiltonian of the system and so the real XPW system can be expressed in Hamiltonian form for two conjugate quantities. This is very useful because, as in classical mechanics, the Hamiltonian can be plotted in phase space to derive topological information about the solutions of the differential system of equations without solving it. Furthermore an arbitrary polarization state can be considered. A comparison between z-cut and holographic cut is then made.

3.2.2 Simplified version : only γ_2

I start working with a simplified version of the system (3.9) where I consider just γ_2. In this approximation I just allow the conversion of energy from the fundamental to the XPW beam without any contribution of the self and cross phase modulation (γ_1, γ_5, γ_3). Neglecting γ_4 the system is made fundamentally asymmetric because there is no energy flux if the fundamental is initially zero (no back conversion). Even if this system is simplified it is close to the experimental condition at low intensity (initial condition with just the fundamental beam as input, thin crystals) and the form of the equation is very similar to that used to treat three-wave interactions hence a comparison can be made [2, 4, 3, 5]. To obtain a real system of equations I define the input field A and the XPW field B as: $A = r_1 e^{i\varphi_1}$, $B = r_2 e^{i\varphi_2}$ and $\theta = \varphi_1 - \varphi_2$. Substituting in (3.9) and considering just γ_2 it results:

$$\begin{aligned} \dot{r_1} &= r_1^2 r_2 \gamma_2 sin(\theta) \\ \dot{r_2} &= -r_1^3 \gamma_2 sin(\theta) \\ \dot{\theta} &= 3\gamma_2 r_1 r_2 cos(\theta) - \frac{r_1^3}{r_2}\gamma_2 cos(\theta) \end{aligned} \tag{3.12}$$

with the notation $\frac{dr_i}{d\zeta} = \dot{r}_i$. This system of equation has two constants: the first $r_1^2 + r_2^2 = const$ is the Manley-Rowe relation and it expresses the conservation of the photon flux. Working with normalized quantities the constant is equal to 1. The second is the Hamiltonian of the system $\Gamma = \gamma_2 r_1^3 r_2 cos(\theta)$. Here and in the following calculations the expression for the Hamiltonian is obtained starting with a guess expression and than verifying that the condition $\dot{\Gamma} = 0$ is satisfied. The use of the term 'Hamiltonian' immediately suggests that the conserved quantity is energy, as in classical mechanics. However an analogy is being used when the coupling equations are recognized as being in "Hamiltonian form": the space variable ζ here plays the role of time in the classical mechanics formalism. Since time invariance leads to conservation of energy, it is not surprising that the Hamiltonian in this case is momentum since the conservation of momentum is related to system property invariance in the spatial coordinate [1].

The most typical configuration for XPW generation consists of a single beam (fundamental beam) incident on the nonlinear medium (cubic crystal). In this case the initial condition is $r_1^2 = 1$ and $r_2^2 = 0$ and so $\Gamma = 0$. But $\Gamma = 0$ is a first integral of the system so it will remain zero also when r_1^2 and r_2^2 will be different from zero. The consequence is that $\theta = \pm\pi/2$. In this case $\sin(\theta) = \pm 1$ and the system (3.12) can be further simplified:

$$\dot{r_1} = r_1^2 r_2 \gamma_2 \tag{3.13}$$

$$\dot{r_2} = -r_1^3 \gamma_2 \tag{3.14}$$

and has solutions of the form: $r_1(\zeta) \propto \sqrt{\frac{1}{1+\zeta^2}}$ and $r_2(\zeta) \propto \sqrt{\frac{\zeta^2}{1+\zeta^2}}$. These solutions, derived analytically, have the same asymptotic behavior as the well-known hyperbolic tangent and secant solutions for the SHG process in the case of perfect phase matching. (Fig. 3.8) [2].

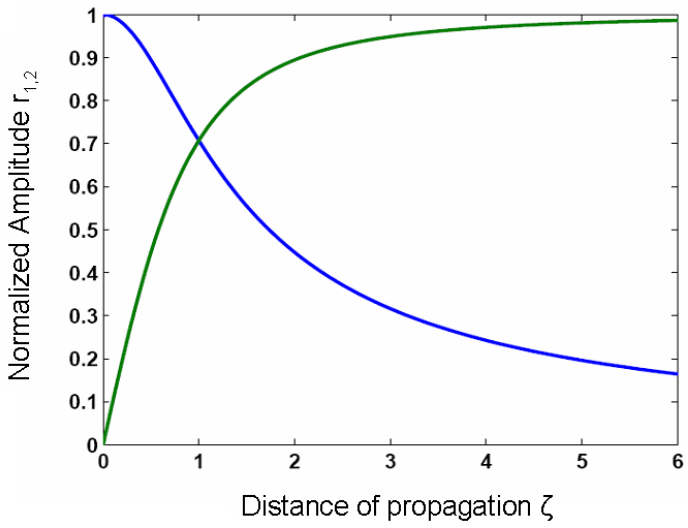

Figure 3.8: Aperiodic energy exchange between the fundamental (blue) and cross-polarized beam (green)

The equation for θ can be expressed using Γ to obtain:

$$\dot{\theta} = 3\gamma_2 \frac{\Gamma}{r_1^2} - \gamma_2 \frac{\Gamma}{r_2^2} \tag{3.15}$$

and so for $\Gamma = 0$, confirmation is given that $\theta(\zeta) = const = \pm\pi/2$. There is an aperiodic transfer of energy between the fundamental and the XPW beam with constant phase difference. The same occurs for r_1^2 and r_2^2 different from zero and $\theta = \pm\pi/2$. For a more general situation the system (3.12) can be written in the form :

$$\zeta = \int_{r_2^2(0)}^{r_2^2(\zeta)} \frac{d(r_2^2)}{(r_2^2(1-r_2)^3 - \Gamma^2)^{1/2}} \tag{3.16}$$

which is an elliptical integral of the first type. The solutions can be expressed in terms of Jacobi elliptic function and are in general periodic (we have seen previously a particular situation where this is not true). It is not very interesting to enter into the mathematical details of these solutions because more can be understood by working with the system in Hamiltonian form. Defining $\eta = r_1^2$ and using the Manley-Rowe relation (const=1) the system (3.12) is written in Hamiltonian form:

$$\frac{d\eta}{dz} = -2\frac{\partial \Gamma}{\partial \theta} \tag{3.17}$$

$$\frac{d\theta}{dz} = 2\frac{\partial \Gamma}{\partial \eta} \tag{3.18}$$

with $\Gamma = \gamma_2 \eta^{3/2}(1-\eta)^{1/2} cos(\theta)$. η and θ are conjugate variables and a phase space can be defined (Fig. 3.9). For this plot it is assumed a propagation with an angle β corresponding to a maximum of γ_2 at low intensity. The observation of the trajectories in phase space highlights some of the more general properties of the solutions. No information function of z can be extracted because the differential system of equations is not solved. Due to the Manley-Rowe relation, information about the XPW signal is directly extracted from the variation of η ($r_2^2 = 1-\eta$). We see that in phase space there are two separatrix (vertical trajectories) for $\theta = \pm\pi/2$; these correspond to the solutions we have derived in the case of $\eta = 1$ as input, where there is an exchange of energy between the two waves with constant phase difference. Separatrix illustrate the aperiodic nature of the conversion. Between this two separatrix we have closed orbits where η and θ are periodic functions. These correspond to the Jacobi elliptical functions. The center of the closed orbits are points where both η and θ remains constant, these are the eigensolution of the system and they can be obtained by imposing $\frac{d\eta}{dz} = \frac{d\theta}{dz} = 0$.

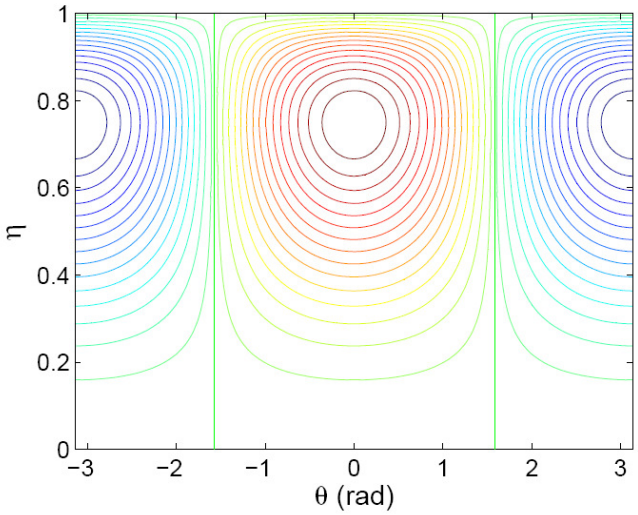

Figure 3.9: Hamiltonian in phase space for the simplified system (just γ_2). Trajectories $\Gamma(\eta, \theta) = const$ in phase space correspond to solutions of the differential system of equations for XPW generation.

3.2.3 Extension of the analysis

This analysis can then be extended including one by one the missing terms for the complete description of the XPW process. The first step is to work with a symmetric system and so consider the presence of both γ_2 and γ_4. Repeating the same procedure described in the previous section the same system of equations (3.18) is obtained with: $\Gamma = \gamma_2\eta^{3/2}(1-\eta)^{1/2}cos(\theta) + \gamma_4\eta^{1/2}(1-\eta)^{3/2}cos(\theta)$.

I start the phase space analysis of the trajectories by considering XPW generation in Z-cut crystals where $\gamma_4 = -\gamma_2$. As it can be seen from the trajectories reported in fig. 3.10 the form of the solution is equal to what I have discussed in the previous paragraph except from the fact that now the problem is perfectly symmetric between the fundamental and the XPW beam and only half of the energy can be at maximum transferred. When there is just one input beam, $\Gamma = 0$, and the solution moves along the separatrix with constant phase difference. Circular polarization ($\eta = 0.5, \theta = \pm\pi/2$) is an eigensolution of the system because it corresponds to a saddle point in phase space. Fig. 3.11 shows the trajectories in phase space for XPW generation in holo cut crystals $\gamma_4 \neq -\gamma_2$. As in the previous plot the propagation is assumed with an angle *beta* which maximizes γ_2 (this angle is different from previous one). The type of trajectories is the same that for Z-cut with the exception that circular polarization is not an eigensolution of the system. Furthermore the energy transfer between the to beam can reach 65%.

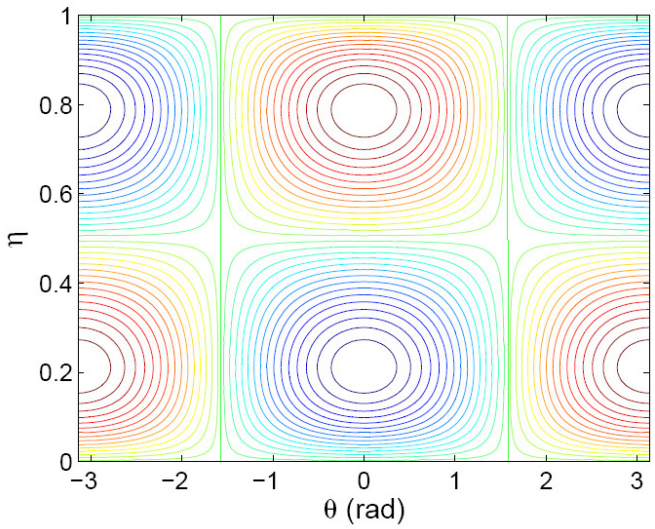

Figure 3.10: Hamiltonian in phase space and corresponding orbits for the system with γ_2 and γ_4 (Z-cut $\beta = \pi/8$).

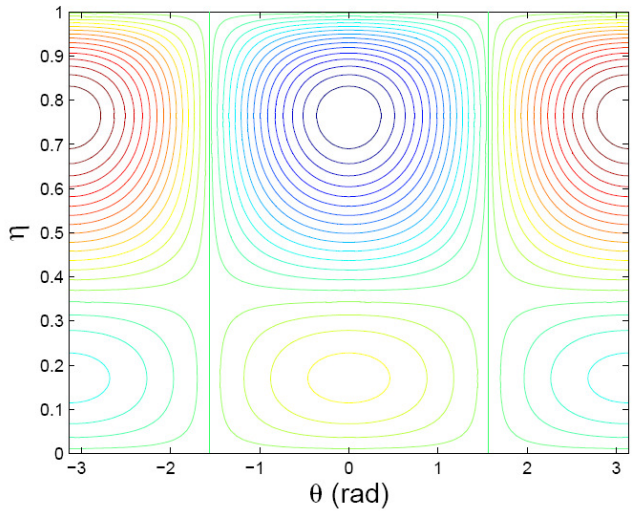

Figure 3.11: Hamiltonian in phase space and corresponding orbits for the system with γ_2 and γ_4 (Holo-cut $\beta = (115.5)$.

Including self-phase modulation of the fundamental beam means considering also the presence of γ_1 in the XPW system of equations. The Hamiltonian in this case is:

$$\Gamma = \gamma_2 \eta^{3/2}(1-\eta)^{1/2} cos(\theta) + \gamma_4 \eta^{1/2}(1-\eta)^{3/2} cos(\theta) + \frac{\gamma_1}{4}\eta^2 \tag{3.19}$$

Because there is no substantial difference between different cuts of the crystal, results about Z-cut only are presented. This problem can be solved analytically by neglecting depletion of the fundamental [9]. Fig. 3.12 shows the trajectories in phase space. There are two kind of trajectories: the closed orbits where the amplitude and the phase difference is periodic and the open orbits where the amplitude is periodic but the phase is not periodic. This new kind of solution is allowed in the system due to the presence of self phase modulation and this is

exactly the solution we have in practical experimental XPW generation at high intensity(just one input beam, $\theta_{in} = -\pi/2$). There is no longer the presence of separatrix and so transfer of energy with constant phase difference is not possible anymore. Comparing the Hamiltonian (3.19) to the one that can be derived for a Hamiltonian treatment of three-wave mixing, it is evident that the γ_1 term in XPW generation acts like the phase matching terms (except that here η is squared) with the generation of open orbits in phase space.

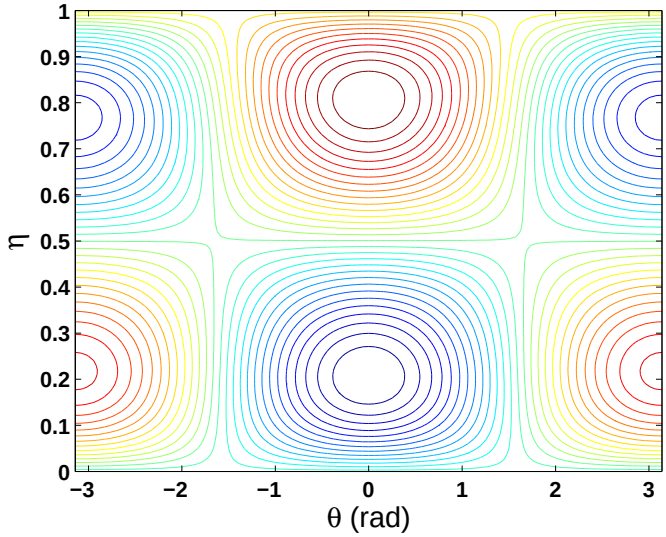

Figure 3.12: Hamiltonian in phase space and corresponding orbits for the system with γ_2 and γ_4 and γ_1 (Z-cut $\beta = \pi/8$).

The solutions of the complete problem expressed in (3.9) can now be addressed. The procedure to obtain the hamiltonian of the system consists, as previously presented, in obtaining the real system of equations starting from the complex system (separating the real and imaginary parts) and then finding the first integral (constant of motion) of the problem. The Hamiltonian is:

$$\begin{aligned} \Gamma = \gamma_2\eta^{3/2}(1-\eta)^{1/2}cos(\theta) + \gamma_4\eta^{1/2}(1-\eta)^{3/2}cos(\theta) + \\ +\gamma_3\eta(1-\eta)cos(2\theta)/2 + \frac{\gamma_1}{4}\eta^2 - \frac{\gamma_3}{2}(1-\eta)^2 - \frac{\gamma_3}{2}\eta^2 + \frac{\gamma_5}{4}(1-\eta)^2 \end{aligned} \tag{3.20}$$

where I have kept separated the contributions from different gamma. The plot of the trajectories in phase space is reported in Fig. 3.13 Fig. 3.14 for Z-cut and holo cut respectively. The same type of trajectories that I have discussed for the previous cases is present. In particular, depending on the relative (amplitude/phase) relation between the two orthogonal input waves, there are closed orbits with periodic oscillation of the amplitude and open orbits with periodic amplitude but not periodic phase. There are also different eigensolutions of the system (constant amplitude and phase) that can be divided into stable and unstable. Finding the stability of an eigensolution directly from the phase space plot is another advantage of the Hamiltonian approach. For example we can see that circular polarization is an eigensolution for Z-cut also in the presence of self and cross phase modulation but that this solution is unstable (saddle

point in phase space). For Holo cut we have the same kind of trajectories as discussed for Z-cut (but with a different angle β) and, due to the asymmetry in the η axis, circular polarization is not an eigensolution of the system.

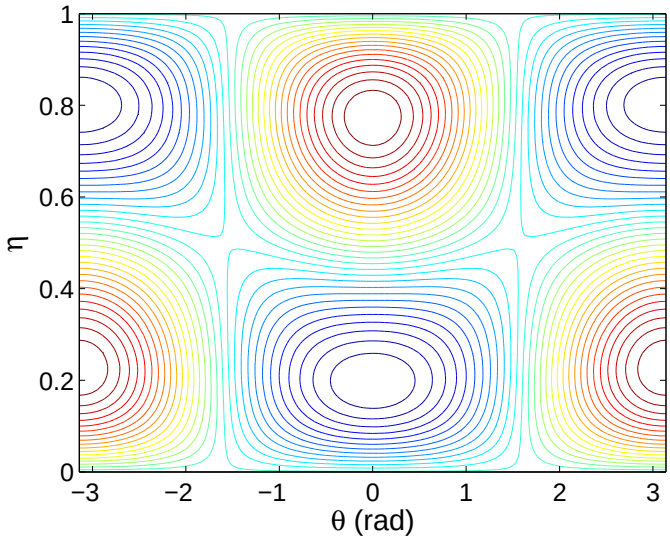

Figure 3.13: Hamiltonian in phase space and corresponding orbits for the complete system of equations and for Z-cut ($\beta = \pi/8$).

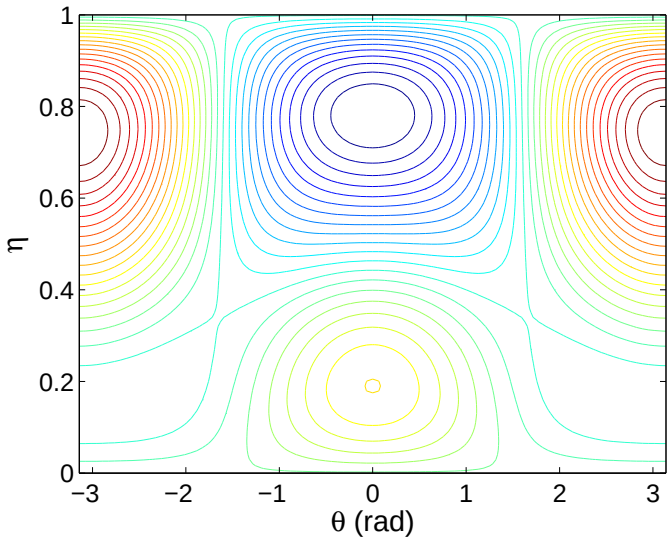

Figure 3.14: Hamiltonian in phase space and corresponding orbits for the complete system of equations and for Holo-cut ($\beta = (3/8 - 0.0168)\pi$).

Bibliography

[1] N. A. Ansari, C. Pask, and D. R. Rowland. Momentum in nonlinear optics. *Journal of Modern Optics*, 47(6):993–1011, 2000.

[2] J. A. Armstrong, N. Bloembergen, J. Ducuing, and P. S. Pershan. Interactions between light waves in a nonlinear dielectric. *Phys. Rev.*, 127(6):1918–1939, 1962.

[3] A. Bandilla, G. Drobný, and I. Jex. Phase-space motion in parametric three-wave interaction. *Optics Communications*, 128(4-6):353 – 362, 1996.

[4] A. Bandilla, G. Drobný, and I. Jex. The classical parametric approximation for three-wave interactions. *Optics Communications*, 156(1-3):112 – 122, 1998.

[5] N. Forget PhD manuscript.

[6] M. Dabbicco, A. M. Fox, G. von Plessen, and J. F. Ryan. Role of $\chi^{(3)}$ anisotropy in the generation of squeezed light in semiconductors. *Phys. Rev. B*, 53:4479–4487, 1996.

[7] A. Jullien, O. Albert, G. Chériaux, J. Etchepare, S. Kourtev, N. Minkovski, and S. M. Saltiel. Two crystal arrangement to fight efficiency saturation in cross-polarized wave generation. *Opt. Express*, 14:2760–2769, 2006.

[8] N. Minkovski, G. I. Petrov, S. M. Saltiel, O. Albert, and J. Etchepare. Polarization rotation induced by cascaded third-order processes. *Opt. Lett.*, 27:2025–2027, 2002.

[9] N. Minkovski, G. I. Petrov, S. M. Saltiel, O. Albert, and J. Etchepare. Nonlinear polarization rotation and orthogonal polarization generation experienced in a single-beam configuration. *J. Opt. Soc. Am. B*, 21:1659–1664, 2004.

[10] G. Petrocelli, E. Pichini, F. Scudieri, and S. Martellucci. Anisotropic effects in the third-harmonic-generation process in cubic crystals. *J. Opt. Soc. Am. B*, 10:918–923, 1993.

[11] Th. Schneider and J. Reif. Influence of an ultrafast transient refractive-index grating on nonlinear optical phenomena. *Phys. Rev. A*, 65(2):023801, Jan 2002.

[12] A. Yariv and P. Yeh. *Optical waves in crystals*. Wiley, New York, 1984.

3.3 XPW for short pulses

Introduction

In the previous sections XPW generation is treated in the time domain and using monochromatic plane waves equations. For the applications of this process as a contrast filter it is interesting to extend this analysis to ultra-short pulses. The quality of temporal pulse compression for ultra-short pulses is typically given in the frequency domain as a residual spectral phase that is expanded in a Taylor series around the central frequency. As is known for other nonlinear effects this spectral phase affects the output (efficiency, spectral width and spectral shape) of the process. It is thus interesting to express and solve the envelope equations of the process in the frequency domain. This is done by making some simplifications and is presented in the next sections. Before entering this subject I want to have a brief discussion about the response time of XPW generation. For optical frequencies non resonant with the optical medium, the response time of the nonlinear susceptibility is given by the time needed for an electron, excited by an oscillating electric field, to come back to the equilibrium position. If $\triangle\omega$ defines the difference in energy between the electromagnetic pulsation and the conduction band (or more generally the energy of the first ionization threshold), the life time τ of the electron out of equilibrium is given by the uncertainty relation:

$$\Delta E\tau \backsim \hbar \tag{3.21}$$

For all crystals used for XPW generation, $\triangle E \approx 10eV$ ($\triangle E_{BaF2} = 9.21$ eV, $\triangle E_{CaF2} = 9.92$ eV, $\triangle E_{LiF} = 11.6$ eV). It results that τ is <1 fs and thus much shorter than few-cycle optical pulses. XPW generation is then always considered an instant process.

3.4 Theoretical considerations: Spectral approach

3.4.1 Notations

For practical reasons linked to the fact that the XPW process leads to a strong pulse reshaping, the XPW spectrum is characterized by its statistic moments rather than central wavelength and FWHM spectral width. The following formulas are used to evaluate respectively the energy, spectral width and center of mass of a given spectral distribution $I(\omega)$:

$$E_{\mathrm{I}} = \int_{\mathbb{R}} I(\omega)d\omega \qquad \sigma_{\mathrm{I}}^2 = \frac{\int_{\mathbb{R}} \left(\omega - <\omega>_{\mathrm{I}}\right)^2 I(\omega)d\omega}{\int_{\mathbb{R}} I(\omega)d\omega} \qquad <\omega>_{\mathrm{I}} = \frac{\int_{\mathbb{R}} \omega I(\omega)d\omega}{\int_{\mathbb{R}} I(\omega)d\omega} \tag{3.22}$$

These parameters are not only universal and easy to define but also of first interest from an experimental point of view: the efficiency of the nonlinear process defines the output energy, the standard deviation defines the minimum available transform limited pulse duration and the spectral center of mass shift indicates whether the XPW spectrum still lies within the amplification bandwidth of a laser amplifier. More generally, the mean value of the spectral

function f(ω) with respect to the intensity I(ω) is defined by:

$$< f(\omega) >_{\mathrm{I}} = \frac{\int_{\mathbb{R}} f(\omega) I(\omega) d\omega}{\int_{\mathbb{R}} I(\omega) d\omega} \tag{3.23}$$

3.4.2 Propagation equation

The effect of spectral phase on a nonlinear process has been extensively studied theoretically for $\chi^{(2)}$ processes [15, 16, 17, 18, 19]. In this section this study is extended to $\chi^{(3)}$ processes and more specifically to XPW generation. The starting point is the plane wave propagation equations describing XPW generation (3.9) considering just the influence of γ_2. As previously ω_0 stands for the central angular frequency of the input pulse (fundamental pulse), n for the refractive index of the cubic crystal at ω_0, $\chi^{(3)}$ for the third order susceptibility tensor, β for the angle between the input polarization direction and the crystallographic axis x, $A(z,t)$ and $B(z,t)$ for the respective complex amplitude envelopes of the fundamental and XPW electric fields, $I_A(z,\omega)$ and $I_B(z,\omega)$ for the respective spectral intensity of the fundamental and XPW electric fields. Here the anisotropy factor of the third order susceptibility tensor is defined σ_x to avoid confusion with the second order momentum of a Gaussian function. The spectral phase function of the fundamental pulse will be referred as $\varphi(\omega)$ and, when required, $\varphi(\omega)$ will be expanded in a Taylor series around ω_0:

$$\varphi(\omega) = \sum_{k=0}^{n} \frac{\varphi^{(k)}}{k!} (\omega - \omega_0)^k . \tag{3.24}$$

In the frame of the moving pulse, the slowly varying envelope approximation leads to the following propagation equation for the complex amplitude of the XPW field:

$$\frac{\partial B(z,t)}{\partial z} = i\gamma_2 A(z,t) A^*(z,t) A(z,t) \tag{3.25}$$

$$\text{with } \gamma_2 = -\frac{3}{8}\frac{\omega_0}{n_0 c}\chi^{(3)}_{xxxx}\frac{\sigma_x}{4}\sin(4\beta) \tag{3.26}$$

Using the standard Fourier transform $B(z,t) = \int_{\mathbb{R}} \tilde{B}(z,\omega)\exp(i\omega t)d\omega$ and $A(z,t) = \int_{\mathbb{R}} \tilde{A}(z,\omega)\exp(i\omega t)d\omega$ and applying the reverse convolution theorem we obtain the following equation for the complex spectral amplitude of the XPW pulse:

$$\frac{\partial \tilde{B}(z,\omega)}{\partial z} = -i\gamma_2 \iint_{\mathbb{R}^2} \tilde{A}(z,\omega_1)\tilde{A}(z,\omega_2)\tilde{A}^*(z,\omega_1+\omega_2-\omega)d\omega_1 d\omega_2 \tag{3.27}$$

Equation (3.27) highlights the frequency-mixing process occurring during XPW generation: the XPW signal at a given angular frequency is proportional to some third order spectral autocorrelation function of the fundamental pulse. In the approximation of small conversion efficiency (undepleted regime) and of negligible dispersion, the fundamental pulse propagates unchanged ($A(z,t) = A(0,t) = A(t)$) and equation (3.27) can be solved analytically:

$$\tilde{B}(L,\omega) = -i\gamma_2 L \iint_{\mathbb{R}^2} \tilde{A}(\omega_1)\hat{A}(\omega_2)\tilde{A}^*(\omega_1+\omega_2-\omega)d\omega_1 d\omega_2 \tag{3.28}$$

3.4.3 Gaussian pulse with quadratic phase

For a fundamental pulse of Gaussian spectral intensity, the spectral amplitude is:

$$\tilde{A}(\omega) = \tilde{A}_0 \exp\left(-\frac{(\omega-\omega_0)^2}{2\sigma^2}\right) \exp\left[i\varphi(\omega)\right] \tag{3.29}$$

with the spectral phase defined as in (3.24). The right hand side of equation (3.28) can be solved analytically for the specific case of a quadratic phase. The result for the spectral intensity in this case is:

$$I_B(L,\omega) = \left(2\pi\sigma^2\tilde{A}_0^3\gamma_2 L\right)^2 \frac{\exp\left[-\frac{(\omega-\omega_0)^2}{3\sigma^2}\frac{\left(1+\sigma^4\left(\varphi^{(2)}\right)^2\right)}{\left(1+\sigma^4\left(\varphi^{(2)}\right)^2/9\right)}\right]}{\sqrt{\left(1+\sigma^4\left(\varphi^{(2)}\right)^2\right)\left(9+\sigma^4\left(\varphi^{(2)}\right)^2\right)}}. \tag{3.30}$$

This analytical result shows that for Fourier-transform limited input pulse ($\varphi^{(2)} = 0$) the XPW spectrum is $\sqrt{3}$ times broader than that of input pulse. For chirped pulses however ($\varphi^{(2)} \neq 0$), the XPW spectral width narrows with increasing $\varphi^{(2)}$ and is $1/\sqrt{3}$ smaller than the input spectrum for a high spectral chirp. Integrating (3.30) over the frequency domain, one can also obtain the dependence of the XPW pulse energy on the input second order spectral phase coefficient $\varphi^{(2)}$:

$$E_{\mathrm{XPW}}(L,\varphi^{(2)}) = \frac{E_{\mathrm{XPW},0}}{\left(1+\sigma^4\left(\varphi^{(2)}\right)^2\right)} \tag{3.31}$$

where $E_{\mathrm{XPW},0}$ is the XPW energy of the pure Fourier transform limited pulse. As can be seen, this dependence is Lorentzian. From Eq. (3.30) the spectral center of mass is calculated. Applying Eq. (3.22), leads to $<\omega>_{\mathrm{XPW}} = \omega_0$, demonstrating that there is no spectral shift.

From the previous results, two critical second order coefficient values can be defined corresponding respectively to the following conditions: the XPW efficiency is equal to half of the maximum conversion efficiency, the XPW spectrum is equal to the input spectrum. For a Gaussian input pulse, these critical coefficients are given by:

$$\varphi^{(2)}_{\mathrm{cr,Energy}} = \sqrt{3}/\sigma^2 \tag{3.32}$$

$$\varphi^{(2)}_{\mathrm{cr,Width}} = 1/\sigma^2 \tag{3.33}$$

For a Gaussian pulse of minimal pulse duration $\tau_0 = 30\,\mathrm{fs}$ the spectral width at $1/e$ is $\sigma = 55.5\,\mathrm{THz}$ and the corresponding critical second order phase coefficients are $325\,\mathrm{fs}^2$ and $562\,\mathrm{fs}^2$ respectively.

For the more general case of an input polynomial phase, the integration in Eq. (3.27) needs to be solved numerically. This is presented in section 3.4.5. Before doing this a simplified analytical model is derived to understand more easily some aspects of the solutions.

3.4.4 Asymptotic shapes and expressions for the XPW spectrum

Assuming a sufficiently regular and smooth input spectrum (i.e. not necessarily a Gaussian pulse), some features of the XPW spectrum can be described by applying the stationary phase

theorem to expression (3.28). This theorem leads, as I will discuss later, to two different results with two different and complementary ranges of validity. The goal of this model is to understand in a simple way the influence of the residual phase on the XPW spectrum and so to extract information about this phase from the shape of the spectrum. The results of the asymptotic model are confirmed more quantitatively by the numerical calculation. Before entering the heart of the matter, I recall the stationary phase theorem applied to a bidirectional complex function of modulus $a(x,y)$ and phase $\phi(x,y)$. According to the stationary phase theorem, the main contribution terms of the integral

$$\int_{\mathbb{R}^2} a(x,y)e^{i\phi(x,y)}dxdy \tag{3.34}$$

come from the angular frequencies x_0 and y_0 for which the phase of the integrand is locally stationary. If such stationary point exists in the $[x_0, y_0]$ ensemble for a particular value of ω_c, then the XPW spectrum will exhibit a local maximum at angular frequency ω_c. What is more, the theorem also gives the following asymptotic formula when the phase is locally stationary ($\phi'(x_0,y_0)=0$) but not critical ($\phi''(x_0,y_0)\neq 0$):

$$\int_{\mathbb{R}^2} a(x,y)e^{i\phi(x,y)}dxdy = 2\pi\frac{a(x_0,y_0)e^{i\phi(x_0,y_0)}}{\sqrt{|\phi_{x,x}\phi_{y,y}-\phi_{x,y}\phi_{y,x}|}}e^{i\frac{\pi}{4}\,\mathrm{sign}\,\phi''(x_0,y_0)}+O\left(h^2\right) \tag{3.35}$$

with $\phi_{i,j}$ i,j=x,y are partial derivative evaluated at $(x_0,y_0)=0$. Moreover, in this and in the following sections, the central angular frequency and spectral width of the cube of the input spectral intensity will be noted $<\omega>_{I_A^3}$ and $\sigma_{I_A^3}$ respectively.

Spectral phase with critical points

Mathematically, the stationary phase condition applied to the integrand of the right hand side of equation (3.28) is:

$$\exists\,(\omega_1,\omega_2)\ \mid\ \frac{d}{d\omega_{1,2}}\left[\varphi(\omega_1)+\varphi(\omega_2)-\varphi(\omega_1+\omega_2-\omega)\right]=f_{1,2}(\omega) \tag{3.36}$$

where $f_{1,2}(\omega)$ are two real functions. This condition of local maximum has a more natural expression using the group delays:

$$\begin{cases}\tau(\omega_1)-\tau(\omega_1+\omega_2-\omega)=f_1(\omega)\\ \tau(\omega_2)-\tau(\omega_1+\omega_2-\omega)=f_2(\omega)\end{cases} \tag{3.37}$$

Although the exact set of solutions of this equation system is unknown in the general case, there is one obvious solution: $\omega_1=\omega_2=\omega$. If this solution is the only solution, then, an asymptotic expression of the XPW spectrum is:

$$I_B(\omega)\simeq\frac{I_A(\omega)^3}{|\varphi"(\omega)|^2} \tag{3.38}$$

From a mathematical point of view, the range of validity of the stationary phase is limited to high phase values, that is to say for input pulses which are far from the Fourier-transform limit.

Nevertheless, this approximation proves to be useful. If the fundamental spectral phase exhibits a critical point (φ"$(\omega_c) = 0$), then the phase function of equation (3.28) is also critical at ω_c and formula (3.38) cannot be applied around ω_c, which is obvious since the formula diverges at ω_c. However, in such a case, the XPW spectrum can still be described by the sum of two contributions: a "local" contribution given by expression (3.38) (away from ω_c) and a "critical" contribution corresponding to a peak distribution located at ω_c.

An example of this is a spectral phase well described by a third order Taylor expansion around ω_0, then the XPW spectrum is expected to exhibit a maximum at the angular frequency which is solution of:

$$\varphi''(\omega) = \varphi^{(2)} + \varphi^{(3)}\,(\omega - \omega_0) = 0 \tag{3.39}$$

This analytical approach enables us to predict the following spectral behavior of the XPW spectrum: when there are strong residual second and third order phases on the fundamental pulse, the XPW spectrum is no longer symmetric even for a symmetric input. What is more, the XPW spectrum is the sum of the cube of the input spectrum and a peak at the position:

$$\omega = \omega_0 - \frac{\varphi^{(2)}}{\varphi^{(3)}} \tag{3.40}$$

Since the peak distribution is weighted by the amplitude factor I_A^3, the spectral center of mass is therefore expected to behave as follows:

$$< \omega >_{\mathrm{XPW}} = \omega_0 - \frac{\varphi^{(2)}}{\varphi^{(3)}} I_A^3(\omega_0 - \varphi^{(2)}/\varphi^{(3)})/I_A^3(\omega_0) \tag{3.41}$$

In this particular case, the range of validity of this approximation can be defined as $\sigma_{I_A}^3|\varphi^{(3)}| >> 1$ and $|\varphi^{(2)}| < |\varphi^{(3)}\sigma|$.

Spectral phase without critical points

The stationary phase theorem gives also some asymptotic expressions for the XPW spectrum when there are no critical points for the fundamental pulse. More precisely, if the group delay of the input pulse is monotonic (this is the case if the spectral phase is predominantly quadratic or quartic for example) and if the duration of the fundamental pulse is much longer than its transform-limit, then the XPW modulus of the spectral amplitude is approximately given by the solution in (3.38), over the whole spectral range.

From this result, one can compute, to the first order, the spectral center of mass and spectral width of the XPW spectrum for a chirped input pulse to which a perturbative third order phase has been added:

$$< \omega >_{\mathrm{XPW}} = \omega_0 - 2\frac{\varphi^{(3)}}{\varphi^{(2)}}\sigma_{I_A^3}^2 \tag{3.42}$$

$$\sigma_{\mathrm{XPW}}^2 = \sigma_{I_A^3}^2 - 2\frac{\varphi^{(3)}}{\varphi^{(2)}} < (\omega - \omega_0)^3 >_{I_A^3} \tag{3.43}$$

Applying this result to a linearly chirped pulse ($\varphi^{(3)} = 0$), leads to the same results found in section 3.4.3 for large chirps: the spectrum is narrowed by a factor $\sqrt{3}$, the conversion efficiency

decreases with $1/\left(\varphi^{(2)}\right)^2$. With a perturbative third order phase, the spectral center of mass is shifted proportionally to the $\varphi^{(3)}$ value. As far as the spectral width is concerned, it remains unchanged to the first order if the spectrum is symmetric with respect to the spectral center of mass. If the spectrum is not symmetric, then the spectrum may be broadened or narrowed depending on the relative signs of the phase coefficients.

Again, the range of validity of these approximations needs to be specified. The above results only apply for strongly chirped pulses. For a general cubic phase function, this means $\sigma_{I_A}^2|\varphi^{(2)}| >> 1$ and $|\varphi^{(2)}| >> |\varphi^{(3)}\sigma_{I_A}|$.

Synthesis

This simplified model predicts that, for a sufficiently regular spectrum with a large general cubic phase, the spectral center of mass varies linearly with $\varphi^{(3)}$ for large and constant values of $\varphi^{(2)}$ and linearly with $\varphi^{(2)}$ for large and constant values of $\varphi^{(3)}$. Such features are characteristic of a hyperbolic parabola surface, more widely known as a horse saddle surface and will be obtained experimentally in section 4.6. The saddle point is centered on $\varphi^{(2)} = \varphi^{(3)} = 0$ and can be implicitly defined by the equation $\varphi^{(2)}\varphi^{(3)} = const.$

The spectral width of the XPW spectrum is expected to be almost constant whenever the effects of $\varphi^{(2)}$ or $\varphi^{(3)}$ are dominant. In the first case, the spectral width is equal to that of the cube of the input spectrum. In the second case, it is related to the spectral width of the "critical" contribution. Last, this model confirms a general Lorentzian dependance of the XPW intensity as a function of $\varphi^{(2)}$.

3.4.5 Numerical calculation

In this paragraph I directly solve Eq. (3.28) and compute the XPW spectral intensity without any other assumptions than those stated in section 3.4.2. In order to verify the previous theoretical work, the effect of combined second and third order spectral phases are simulated. The input spectrum is Gaussian with a spectral width corresponding to a Fourier transform limited pulse of 30 fs. The energy, center of mass and spectral width of the XPW spectrum are shown in Fig. 3.15 and Fig. 3.16. For all these scans we choose approximatively $\triangle\varphi^{(2)} = \sigma_{I_A}^2 \triangle\varphi^{(3)}$ to have the same temporal effect for both phase terms.

The main conclusion from Fig. 3.15 is that the plots are symmetric with respect to the point where $\varphi^{(2)} = \varphi^{(3)} = 0$. At this point the XPW generation process exhibits maximum efficiency and the broadest spectrum without spectral shift. Efficiency and broadening decrease with residual spectral phase and one obtains numerically the same values for $\varphi^{(2)}_{\text{cr,Energy}}$ and $\varphi^{(2)}_{\text{cr,Width}}$ been derived analytically previously. As expected, the spectral center of mass of the XPW spectrum (Fig. 3.16 (a)) shifts when the contributions of second and third order phase coefficients are of the same order of magnitude. The numerical calculation provides realistic spectral shifts that can be used to compare with experimental data. For comparison,

Fig. 3.16 (b) presents the spectral shift behavior extracted from the analytical model for the same spectral phase range as Fig. 3.16 (a). They both behave the same, but the numerical calculation provides realistic spectral shifts for Gaussian laser spectra compared to the analytical model. Furthermore the analytical model is not valid at the saddle point in the center of the graph.

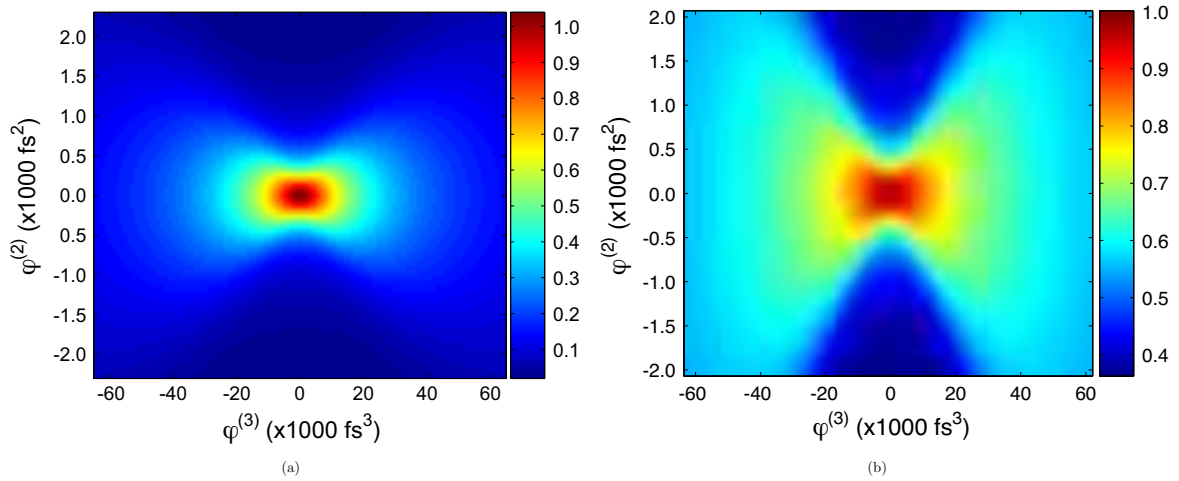

Figure 3.15: (a) normalized theoretical XPW efficiency function of the second and third order spectral phase for a 30 fs input pulse. The value 1 corresponds to a XPW efficiency of 5%. (b) theoretical prediction of XPW spectral width as a function of the second and third order spectral phases for a 30 fs pulse. The spectral width values are normalized to the XPW width value for the case of transform limited input pulse.

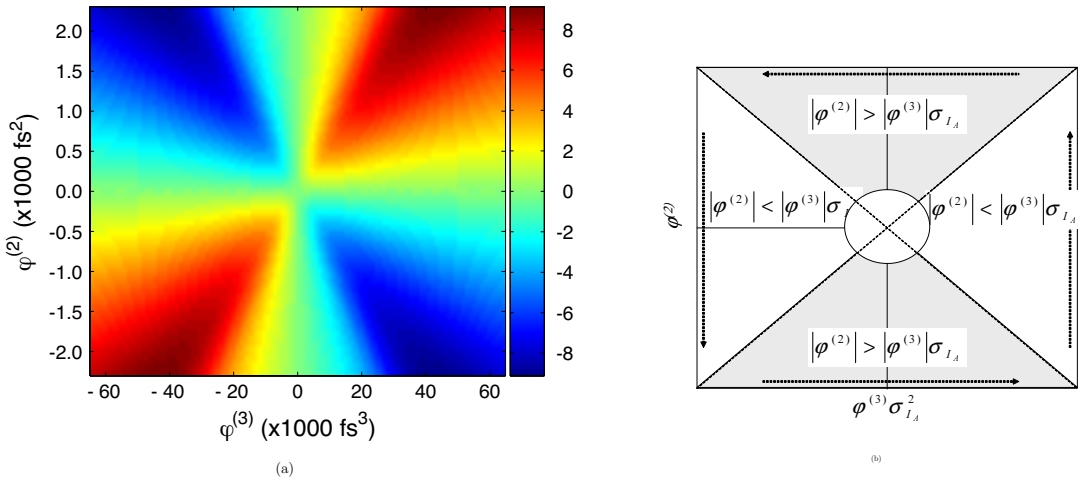

Figure 3.16: (a) theoretical prediction of the XPW spectral center of mass shift (in nm) as a function of the second and third order spectral phases for a 30 fs input pulse. (b) validity range of the two approximations in the $\left(\varphi^{(2)}(\omega_0), \varphi^{(3)}(\omega_0)\right)$ plane for the analytical model. The arrows show the direction of the spectral center of mass shift for a cubic spectral phase.

These theoretical predictions are verified experimentally in section 4.6.

3.4.6 XPW generation for sub-10 fs pulses

In the previous derivation the pulse dispersion during the propagation in the nonlinear medium has been neglected. For pulses shorter than 10 fs this is not valid anymore because dispersion and nonlinearity act together during propagation. This implies solving a nonlinear partial differential system of equations instead of a system of ordinary differential equations. The split-step Fourier method provides an approximate solution of this system by assuming that in propagating the optical field over a small distance h, the dispersive and nonlinear effects can be considered to act independently of each other. More specifically, propagation from z to z+h is carried out in two steps. In the first step the nonlinearity acts alone and the coupled nonlinear equations (3.9) are solved in time domain. In the second step dispersion acts alone and the spectral phase from material dispersion is applied in the frequency domain. Fig. 3.17 illustrates the dynamics of the XPW conversion process for three selected values for the residual chirp at the entrance of the crystal (1 mm) : 0 (a,b,c), -25 fs^2 (d,e,f), -60 fs^2 (g,h,i). Fig. 3.17 (a,d,g) shows the evolution of the temporal shape of the fundamental as it propagates through the crystal. For a short input pulse (8 fs in the simulation), the extremely wide bandwidth (we used a spectrum typical for spectral broadening in a hollow fiber) of the pulse results in a rapid broadening, even though the crystal is quite thin (Fig. 3.17a). For a slight negative input chirp ($-25f^2$), the pulse is temporally focused near the center of the crystal(Fig. 3.17d). If the input chirp is further decreased, the pulses compresses in the last 200 μm of the crystal(Fig. 3.17g). As the pulse compresses, the central wavelength of the shortest part of the pulse varies, resulting in a shift in the pulse peak, since the temporal window of the calculation moves at the group velocity of the 800 nm pulse. The moderate input intensity and rapid pulse broadening gives little self-phase modulation on the input spectrum. The remaining panels in Fig. 3.17 show the evolution of the XPW signal in the temporal (Fig. 3.17(b,e,h)) and spectral domains (Fig. 3.17(c,f,i)). The corresponding beam-integrated output spectra are shown in Fig. 3.18. Since the XPW pulse is initially quite short, it broadens over a very short distance (Fig. 3.17(b,e)). For the short pulse input, the conversion starts early in the crystal, and by the middle of the crystal the spectrum is very broad and smooth (Fig. 3.17(c)). Subsequent conversion takes place with a positively chirped pulse, leading to the evolution of the double humped output spectrum (Fig. 3.18). For a negatively-chirped input pulse, the pulse is temporally focused in the center of the crystal, there is some initial conversion on the initially chirped pulse, allowing a greater portion of the output energy to result from conversion of the short pulse. This results in a smoother output spectrum and better energy conversion (Fig. 3.17(f)). With the greater value of negative chirp ($-60fs^2$) (Fig. 3.17(i)) such that the temporal focus is near the exit face of the crystal, the output spectrum is somewhat narrower and the conversion efficiency is greatly reduced (Fig. 3.18). In this case, most of the conversion occurs with a negatively chirped pulse. Fig. 3.18 also shows the ideal output spectrum for dispersion free conversion calculated with a flat input spectral phase. Clearly the output spectra are limited by the crystal dispersion. Such very broad spectrum could be produced by using very thin crystals (< 100 μm), at the expense of the conversion efficiency.

The calculations suggest that a crystal thickness of 300-500 μm would give a good compromise between output spectrum and conversion efficiency.

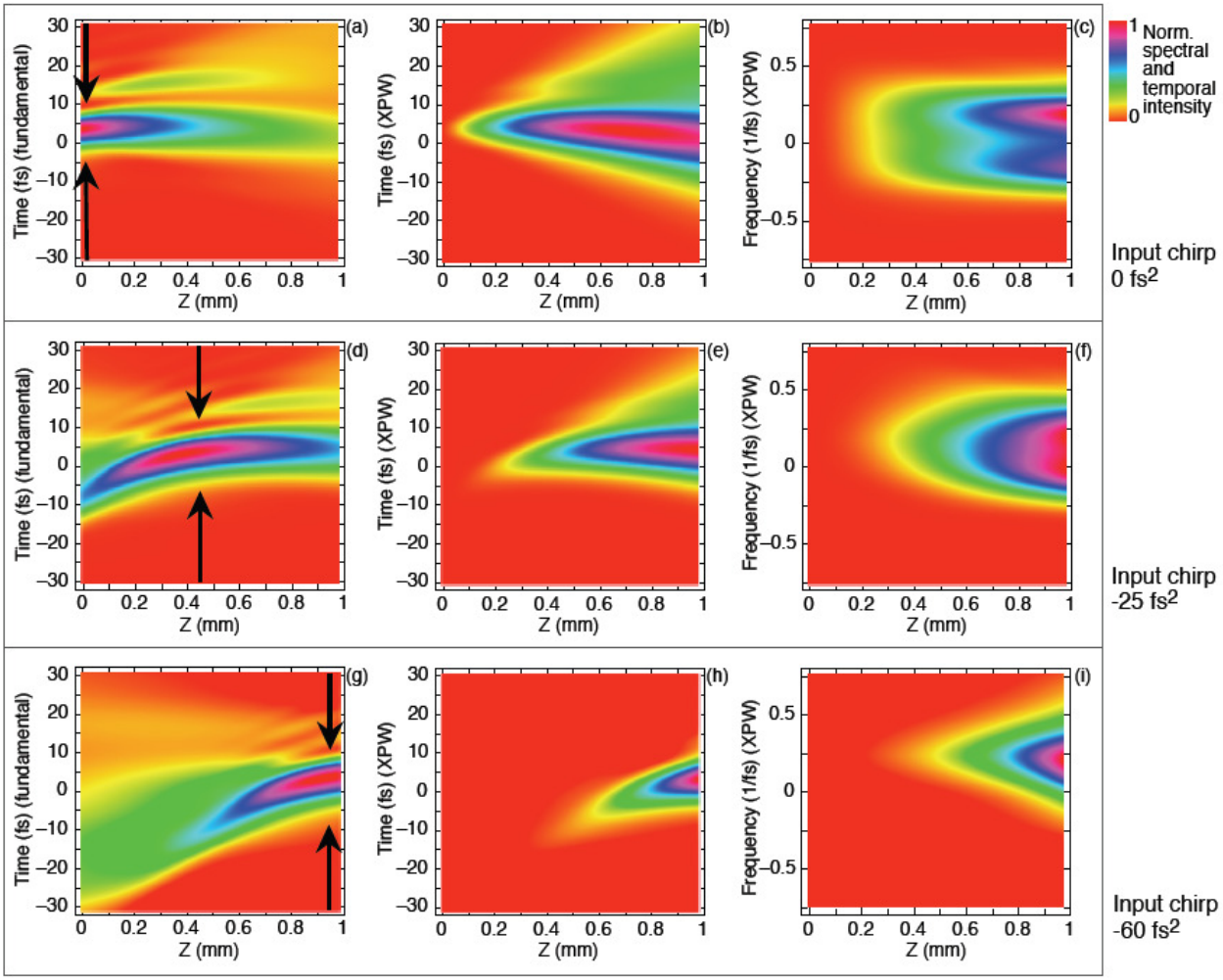

Figure 3.17: Calculated dynamics of XPW generation process. The temporal evolution of the fundamental (resp.XPW) pulse when propagating through the crystal is represented in Figs (a,d,g)(resp.(b,e,h). Figures (c,f,i) display the spectral evolution of the XPW signal within the crystal. Temporal and spectral intensities are normalized. The black arrows localize the area in the crystal where the fundamental beam is temporally the shortest. Panels (a,b,c) are calculated for no residual chirp (0 fs^2) at the entrance of the crystal. -25 fs^2 input chirp is taken into account for figures (d,e,f), and -60 fs^2 input chirp for figures (g,h,i). This values of the residual chirp are typical after hollow fiber spectral broadening and compression and comparison with experiments can thus be done.

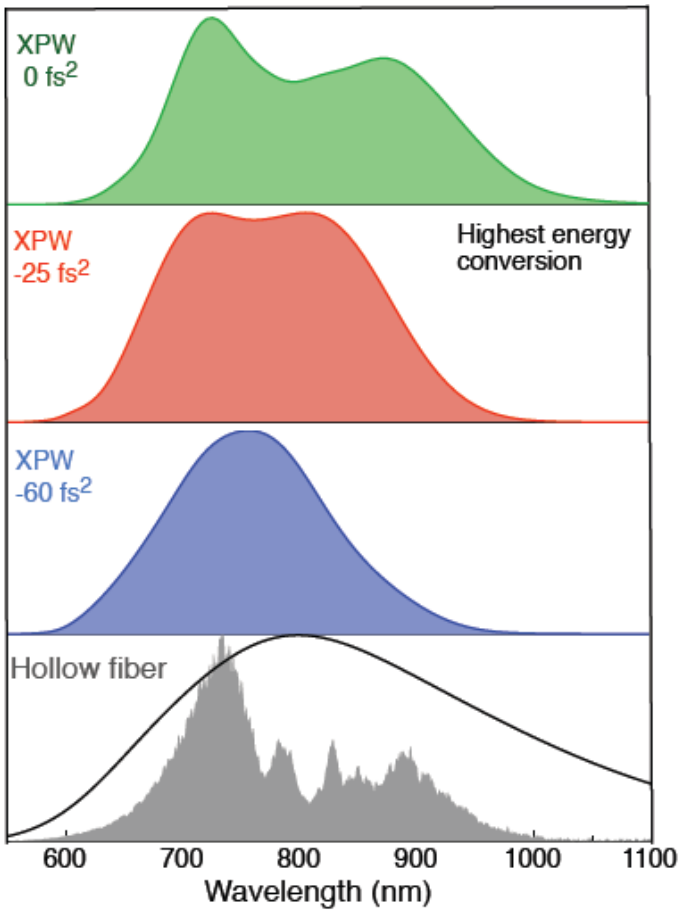

Figure 3.18: Calculated XPW spectra (extracted from Fig. 3.17(a,f,i)) for selected values of the input chirp. The experimental hollow fiber spectrum used for calculations is also shown (grey area, lower panel). The calculated XPW spectrum for a dispersion free conversion and flat input spectral phase is plotted in the lower panel (black line)

Up to now, all the theoretical equations discussed in this chapter have the SVEA approximation as a starting point. For short pulses this approximation implies that the envelope varies slowly over an optical cycle and this is certainly not verified for few-cycle pulses. For such short pulses it is not even evident that the separation of the electric field in a carrier and an envelope is acceptable. The validity of this assumption together with the slowly evolving wave approximation (SEWA) was discussed by Brabec and Krausz in [23]. In this approximation there are no conditions specifying the slowness of the temporal change of the envelope compared with the optical cycle time but it is required that the wave packet has small changing along a propagation distance equal to the wavelength. This can be extended to nonlinear frequency mixing as long as the difference between phase and group velocities of the waves involved in the interaction is small compared to the phase (or group) velocity of the fundamental. This is verified in the case of XPW generation. Within this approximation, a first-order propagation equation for the wave envelope, valid to the single cycle regime, is given by the expression:

$$[\partial_z - ik(\omega)]\,\tilde{E}(r,\omega) = \frac{i}{2k(\omega)}\nabla_\perp^2 \tilde{E}(r,\omega) - \frac{i\omega}{2\epsilon_0 n(\omega)c}\hat{F}\left[\tilde{P}_{nl}(r,t)\right] \tag{3.44}$$

Compared with the equation derived with SVEA it contains new terms which are responsible for effects like self-steepening and space-time focusing. This equation with the nonlinear contribution from XPW generation can be solved using the Fourier split step method presented previously. This falls within the frame of further investigations.

Bibliography

[1] N. Minkovski, G. I. Petrov, S. M. Saltiel, O. Albert, and J. Etchepare. Nonlinear polarization rotation and orthogonal polarization generation experienced in a single-beam configuration. *J. Opt. Soc. Am. B* **21**, 1659 (2004)

[2] A. Jullien, O. Albert, F. Burgy, G. Hamoniaux, J.-P. Rousseau, J.-P. Chambaret, F. Augé-Rochereau, G. Chériaux, J. Etchepare, N. Minkovski, and S. M. Saltiel. 10^{-10} temporal contrast for femtosecond ultraintense lasers by cross-polarized wave generation. *Opt. Lett.* **30**, 920 (2005)

[3] V. Chvykov, P. Rousseau, S. Reed, G. Kalinchenko, and V. Yanovsky. Generation of 10^{11} contrast 50 TW laser pulses. *Opt. Lett.* **31**, 1456 (2006)

[4] L. Canova, M. Merano, A. Jullien, G. Chériaux, R. Lopez-Martens, O. Albert, N. Forget, S. Kourtev, N. Minkovsky, and S. M. Saltiel. Coherent contrast improvement by cross-polarized wave generation. In Conference on Lasers and Electro-Optics/Quantum Electronics and Laser Science Conference and Photonic Applications Systems Technologies **JThD131** (2007)

[5] M. Kalashnikov, K. Osvay, and W. Sandner. High-power Ti:Sapphire lasers: Temporal contrast and spectral narrowing. *Laser and Particle Beams* **25**, 219 (2007)

[6] M. P. Kalashnikov, K. Osvay, I. M. Lachko, H. Schönnagel, and W. Sandner. Suppression of gain narrowing in multi-tw lasers with negatively and positively chirped pulse amplification. *Appl. Phys. B*, **81**, 1059 (2005)

[7] T. Oksenhendler, D. Kaplan, P. Tournois, G. M. Greetham, and F. Estable. Intracavity acousto-optic programmable gain control for ultra-wide-band regenerative amplifiers. *Appl. Phys. B*, **83**, 491 (2006)

[8] H. Takada and K. Torizuka. Design and construction of a tw-class 12-fs ti:sapphire chirped-pulse amplification system. *Selected Topics in Quantum Electronics, IEEE Journal of*, **12**, 201 (2006)

[9] I. Pastirk, B. Resan, A. Fry, J. MacKay, and M. Dantus. No loss spectral phase correction and arbitrary phase shaping of regeneratively amplified femtosecond pulses using miips. *Optics Express*, **14**, 9537 (2006)

[10] A. Jullien, L. Canova, O. Albert, D. Boschetto, L. Antonucci, Y.-H. Cha, J. P. Rousseau, P. Chaudet, G. Chériaux, J. Etchepare, S. Kourtev, N. Minkovski, and S. M. Saltiel. Spectral broadening and pulse duration reduction during cross-polarized wave generation: influence of the quadratic spectral phase. *Appl. Phys. B* **87**, 595 (2007)

[11] M. P. Kalashnikov, E. Risse, H. Schönnagel, and W. Sandner. Double chirped-pulse-amplification laser: a way to clean pulses temporally. *Opt. Lett.* **30**, 923 (2005)

[12] M. E. Anderson, L. E. E. de Araujo, E. M. Kosik, and I. A. Walmsley. The effects of noise on ultrashort-optical-pulse measurement using spider. *Appl. Phys. B* **70**, S85 (2000)

[13] D. N. Fittinghoff, K. W. DeLong, R. Trebino, and C. L. Ladera. Noise sensitivity in frequency-resolved optical-gating measurements of ultrashort pulses. *J. Opt. Soc. Am. B* **12**, 1955 (1995)

[14] G. Stibenz, C. Ropers, C. Lienau, C. Warmuth, A. S. Wyatt, I. A. Walmsley, and G. Steinmeyer. Advanced methods for the characterization of few-cycle light pulses: a comparison. *Appl. Phys. B*, **83**, 511 (2006)

[15] E. Sidick, A. Dienes, and A. Knoesen. Ultrashort-pulse second-harmonic generation. non-transform-limited fundamental pulses. *J. Opt. Soc. Am. B* **12**, 1713 (1995)

[16] A. C. L. Boscheron, C. J. Sauteret, and A. Migus. Efficient broadband sum frequency based on controlled phase-modulated input fields: theory for 351-nm ultrabroadband or ultrashort-pulse generation *J. Opt. Soc. Am. B*, **13**, 818 (1996)

[17] K. Osvay and I. N. Ross. Broadband sum-frequency generation by chirp-assisted group-velocity matching. *J. Opt. Soc. Am. B*, **13**, 1431 (1996)

[18] G. Veitas and R. Danielius. Generation of narrow-bandwidth tunable picosecond pulses by difference-frequency mixing of stretched pulses. *J. Opt. Soc. Am. B*, **16**, 1561 (1999)

[19] P. Baum, S. Lochbrunner, and E. Riedle. Generation of tunable 7-fs ultraviolet pulses: achromatic phase matching and chirp management. *Appl. Phys. B* **79**, 1027 (2004)

[20] C. Iaconis and I. A. Walmsley. Spectral phase interferometry for direct electric-field reconstruction of ultrashort optical pulses. *Opt. Lett.* **23**, 792 (1998)

[21] F. Verluise, V. Laude, Z. Cheng, Ch. Spielmann, and P. Tournois. Amplitude and phase control of ultrashort pulses by use of an acousto-optic programmable dispersive filter: pulse compression and shaping. *Opt. Lett.* **25**, 575 (2000)

[22] A. Baltuška, T. Fuji, and T Kobayashi. Controlling the carrier-envelope phase of ultrashort light pulses with optical parametric amplifiers. Phys. Rev. Lett., 88(13):133901

[23] T. Brabec and F Krausz. Intense few-cycle laser fields: Frontiers of nonlinear optics. *Rev. Mod. Phys.*, 72(2):545–591, Apr 2000.

Chapter 4

Experimental results on XPW generation

4.1 Introduction

In this chapter I present my experimental results about XPW generation and I compare them with the theory I derived. Before entering the heart of the matter I start giving a brief overview of the different non linear processes that can be used for the contrast cleaning together with an introduction of what where the results about XPW generation when I started my Ph.D.

4.2 Contrast filtering techniques

With the rapid increase of the achievable peak intensity at the output of table top TW laser systems, the temporal contrast of the generated pulses started to attract interest. The European research program named SHARP (Suppression over High dynamic range of ASE at the Rising edge of ultra intense femtosecond pulses) started for the theoretical and experimental investigation of the different solutions for measuring and increasing the temporal contrast in ns regime. This temporal contrast is determined by the ASE, mainly generated in the first, high gain, amplification stage (section 2.2.2).
All the filters that enhance the temporal contrast use a non linear process to exploit the different intensity between the main pulse and the background. A non linear filter is characterized by a relation: $I_{out} = f(I_{in}^n)$, with $n \geq 2$. Considering for example a relative ASE level of 10^{-6} and a second order nonlinear filter, the transmitted intensity is squared and the ASE pedestal is then rejected to a relative intensity of 10^{-12}. The transmitted pulse needs then to be discriminated from the input pulse using for example a difference in wavelength, polarization or phase.
Several nonlinear filters were tested and can be classified by their position in the laser system.

Filters at the beginning or in the middle of the laser system

When the filter is implemented inside the laser system the main non linear effects used are: nonlinear polarization rotation (NER) [9, 11] and cross-polarized wave (XPW) generation [6]. To work correctly these filters have to be seeded with a sufficiently intense, compressed pulse. This means to amplify the pulses in a first CPA to the $> 100\mu J$ level, to clean the pulses after the first compression and then to stretch them again for a further amplification that keeps the ASE constant (using low gain amplifiers).

If the XPW filter is implemented at lower energy, the first CPA can be substituted by an amplification in the fs regime and compensation of the dispersion accumulated during this amplification [1].
Another kind of filter uses a saturable absorber [5] to increase the temporal contrast of the pulse amplified in fs regime without the need to recompress it. This filter can not be applied to repetition rates higher than 10 Hz due to thermal problems.

Filters at the output of the laser system

The second solution is to clean the pulses directly at the the output of the CPA laser. This requires filters with a high transmission efficiency to limit the energy losses in the filtering process. The first non linear process that satisfies this requirement is SHG [13]. Furthermore SHG, dividing by two the wavelength, make it possible to focus the output beam into a smaller focal spot and thereby to maintain the same focused intensity with a lower input energy. The second process is ionization on a dielectric material. In this case the filter is named plasma mirror. Details of this filter will be given in section 7.5. Its drawback is that it is destructive and therefore not well adapted at high repetition rates.

4.3 Historical development of XPW generation

In general, light propagation through nonlinear crystals experiences nonlinear polarization rotation and induced ellipticity (XPW generation). Restricting the analysis to a nonlinear change of the polarization state in non-gyrotropic (without spatial dispersion of the $\chi^{(3)}$ optical nonlinearity) crystals, experiments and theoretical results showed that nonlinear polarization rotation is proportional the imaginary part of the $\chi^{(3)}$ anisotropy ,σ, whereas XPW generation is due to the real part [2, 12, 15, 3, 4]. XPW generation was observed in a range of highly transparent alkali-halide crystals of the m3m group namely NaCl, KBr_2, KCl, LiF, BaF_2. In their transparency range these crystals have $Im[\sigma] = 0$ and $Re[\sigma] \neq 0$.
XPW generation attracted at first interest as a nonlinear process for measuring the magnitude and sign of non linearity tensor's components and its anisotropy in crystals [14]. This non linear process was then extended at the end of the SHARP program as a technique for filtering contrast, in particular through the work of A. Jullien and O. Albert from LOA and N. Minkowski, S. Kourtev and S. Saltiel from the University of Sofia [6].

XPW generation benefits from several advantages in its implementation as a contrast filter: it is a third order nonlinear optical effect degenerate with respect to all frequencies and non degenerate with respect to the polarization vectors of the interacting waves. This means that the generated wave is at the same wavelength as the fundamental and can easily be discriminated using a polarizer with the optical axes orthogonal compared to the input beam. The increase in temporal contrast is defined by the extinction ratio of the polarizers (5-6 orders of magnitude). An impressive measurement of the temporal contrast before and after the XPW filter is shown in Fig. 4.1. Furthermore, as it is a third order nonlinear process, the temporal intensity of the XPW pulse is proportional to the cube of the input pulse intensity. This corresponds, in frequency domain, to a spectral broadening by a factor $\sqrt{3}$ (for Fourier transform Gaussian pulses). This can be very useful for the compensation of gain narrowing in the second CPA. Residual second order spectral phase decreases this broadening and the XPW spectrum becomes $1/\sqrt{3}$ narrower than the input one for large values of the second order phase [10]. This confirms the need to seed the XPW filter with adequately compressed pulses.

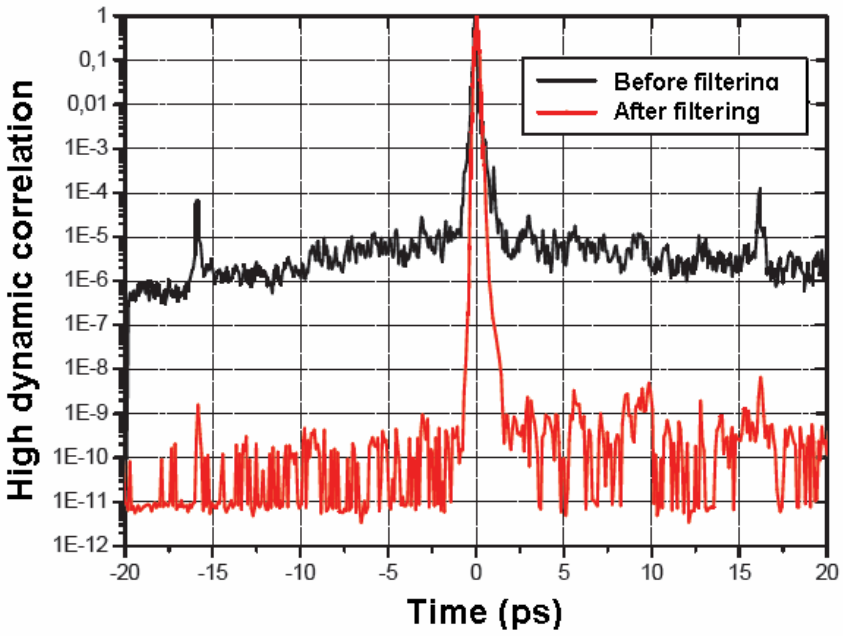

Figure 4.1: Temporal contrast before and after the XPW filter

4.3.1 Design of an efficient XPW generation

Several crystals were tested for efficient XPW generation. A good XPW crystal has to satisfy the following requirements. First it needs to have at least one isotropic plane in linear optics. This corresponds to cubic or tetragonal crystal symmetry. Along this plane the two orthogonally polarized waves propagate with the same group velocity. Crystals with cubic symmetry are preferred because in tetragonal crystals not all planes are isotropic. If the incident wave does not propagating exactly along the z axis of the crystal, a parasitic signal, generated by linear birefringence, is added to the XPW signal. The crystal needs also to be transparent from UV to IR, i.e. with a band-gap larger than 4 eV. This rules out the semiconductors and other

crystal like the Potassium Dihydrogen Phosphate (KDP) or the rutile TiO_2. For cubic crystals XPW generation efficiency depends on the product of the $\chi^{(3)}_{xxxx}$ component, the crystal length L, the input intensity and the anisotropy of $\chi^{(3)}$ -tensor, $\sigma = (\chi^{(3)}_{xxxx} - 3\chi^{(3)}_{xxyy})/\chi^{(3)}_{xxxx}$. Ideally an XPW crystal needs to have a high anisotropy for optimizing XPW generation efficiency and a small non linear index to limit SPM. In Tab. 4.2 I report a list of crystals with $\chi^{(3)}$ anisotropy that can be used for XPW generation. Following the previous considerations, the best crystals for XPW generation are BaF_2, CaF_2 and LiF. In particular, the best crystal for the infrared and visible is the BaF_2, while CaF_2 and LiF are more convenient in the UV (larger band-gap) where two-photon absorption starts to play an important role.

Crystals	Symmetry	Gap (eV)	n	σ
YVO_4	Tetragonal	6	16 [4.3]	+ 0.95 [4.3]
BaF_2	Cubic	9.21 [4.6]	2 [4.7, 4.8]	- 1.2 [4.5, 4.7]
CaF_2	Cubic	9.92 [4.6]	1.3 [4.7]	- 0.6 [4.7]
CdF_2	Cubic	9.54 [4.6]	11.7 [4.7]	+ 0.04 [4.7]
MgF_2	Tetragonal	11.27 [4.6]	0.7 [4.7]	
LiF	Cubic	11.60 [4.6]	0.7 [4.7]	- 0.35 [4.7]
NaCl	Cubic	7.21 [4.6]	4.7 [4.7]	- 0.29 [4.7]
MgO	Cubic	7.77 [4.6]	4.7 [4.7]	- 0.63 [4.7]

Figure 4.2: Table of candidate crystals for XPW generation

The firsts implementations of XPW generation were done using a single [100] (z-cut) crystal cut with a thickness of 1 or 2 mm. In this case the maximum efficiency saturates around 10 %. Increasing the thickness of the crystal does not increase the global efficiency. When the crystal is thicker than $\approx 3mm$, due to self-focusing in the crystal, the threshold for white-light continuum generation is reached before an efficient XPW generation. Furthermore the crystal needs to be thinner than the Rayleigh range of the focusing optics.
From the beginning intense research was made for increasing the efficiency of the process and thus the transmission of the XPW filter. A two-crystal setup was developed that enables reaching an overall efficiency higher than 20 % [8, 7]. The principle of this solution is to use the Kerr lensing in the first crystal in order to refocus the beam into the second crystal. Thanks to the different accumulation of the Gouy phase between the fundamental and the XPW waves by propagation in the space between the crystals, the XPW signals generated in the two crystals can interfere constructively and thus increase the efficiency. This two-crystal solution developed in LOA was patented together with Thales Laser (Patent, French, European and US- # 20060170858).

During my Ph.D I continued the development of the XPW filter with a particular interest in the following goals:

- to further increase the transmission efficiency
- to extend this process to shorter input pulse durations down to the < 10 fs regime.
- to extend this process to shorter wavelengths.

In chapter 3 I demonstrated that the global efficiency depends on the cut of the crystal. In particular it has been predicted theoretically that the [110] cut is the most efficient orientation. This will be confirmed experimentally in the third section of this chapter. Results with a two-crystal scheme to further increase the global efficiency are also presented.
The XPW filter needs to be implemented on compressed pulses. For pulse duration below 30 fs the presence of residual uncompensated higher order spectral phase terms after the first compression can no longer be neglected. It is important to quantify their effect on the XPW spectrum and efficiency. This systematic study is the subject of the fourth section. The extension of this study for sub-10 fs pulses is presented in the fifth section.
The spectrum corresponding to <10 fs pulses can extend over more than one octave and has tails down into the U.V. In all theoretical considerations I assumed a $\chi^{(3)}$ tensor independent of λ. This assumptions is no longer valid on such broad spectral ranges where the photon energy approaches half the band-gap. This motivated the study of the XPW generation in UV presented in the last section.

Bibliography

[1] V. Chvykov, P. Rousseau, S. Reed, G. Kalinchenko, and V. Yanovsky. Generation of 10^{11} contrast 50 TW laser pulses. *Opt. Lett.*, 31(10):1456–1458, 2006.

[2] M. G. Dubenskaya, R. S. Zadoyan, and N. I. Zheludev. Nonlinear polarization spectroscopy in gaas crystals: one- and two-photon resonances, excitonic effects, and the saturation of nonlinear susceptibilities. *J. Opt. Soc. Am. B*, 2(7):1174–1178, 1985.

[3] D. C. Hutchings. Nonlinear-optical activity owing to anisotropy of ultrafast nonlinear refraction in cubic materials. *Opt. Lett.*, 20(15):1607–1609, 1995.

[4] D. C. Hutchings, J. S. Aitchison, and J. M. Arnold. Nonlinear refractive coupling and vector solitons in anisotropic cubic media. *J. Opt. Soc. Am. B*, 14(4):869–879, 1997.

[5] J. Itatani, J. Faure, M. Nantel, G. Mourou, and S. Watanabe. Suppression of the amplified spontaneous emission in chirped-pulse-amplification lasers by clean high-energy seed-pulse injection. *Optics Communications*, 148(1-3):70 – 74, 1998.

[6] A. Jullien, O. Albert, F. Burgy, G. Hamoniaux, J.-P. Rousseau, J.-P. Chambaret, F. Augé-Rochereau, G. Chériaux, J. Etchepare, N. Minkovski, and S. M. Saltiel. 10^{-10} temporal contrast for femtosecond ultraintense lasers by cross-polarized wave generation. *Opt. Lett.*, 30(8):920–922, 2005.

[7] A. Jullien, O. Albert, G. Cheriaux, J. Etchepare, S. Kourtev, N. Minkovski, and S. M. Saltiel. Highly efficient temporal cleaner for femtosecond pulses based on cross-polarized wave generation in a dual crystal scheme. *Appl. Phys. B*, 84:409–414, 2006.

[8] A. Jullien, O. Albert, G. Cheriaux, J. Etchepare, S. Kourtev, N. Minkovski, and S. M. Saltiel. Two crystal arrangement to fight efficiency saturation in cross-polarized wave generation. *Opt. Express*, 14(7):2760–2769, 2006.

[9] A. Jullien, F. Augé-Rochereau, G. Chériaux, J.-P. Chambaret, P. d'Oliveira, T. Auguste, and F. Falcoz. High-efficiency, simple setup for pulse cleaning at the millijoule level by nonlinear induced birefringence. *Opt. Lett.*, 29(18):2184–2186, 2004.

[10] A. Jullien, L. Canova, O. Albert, D. Boschetto, L. Antonucci, Y.-H. Cha, J. P. Rousseau, P. Chaudet, G. Chériaux, J. Etchepare, S. Kourtev, N. Minkovski, and S. M. Saltiel. Spectral broadening and pulse duration reduction during cross-polarized wave generation: influence of the quadratic spectral phase. *Appl. Phys. B*, 87(4):595–601, 2007.

[11] M. P. Kalashnikov, E. Risse, H. Schönnagel, A. Husakou, J. Herrmann, and W. Sandner. Characterization of a nonlinear filter for the front-end of a high contrast double-cpa ti:sapphire laser. *Opt. Express*, 12:5088–5097, 2004.

[12] A.I. Kovrighin, D.V. Yakovlev, B.V. Zhdanov, and N.I. Zheludev. Self-induced optical activity in crystals. *Optics Communications*, 35(1):92 – 95, 1980.

[13] A. Marcinkevičius, R. Tommasini, G. D. Tsakiris, K. J. Witte, E. Gaižauskas, and U. Teubner. Frequency doubling of multi-terawatt femtosecond pulses. *Appl. Phys. B*, 79(5):547–554, 2004.

[14] N. Minkovski, G. I. Petrov, S. M. Saltiel, O. Albert, and J. Etchepare. Nonlinear polarization rotation and orthogonal polarization generation experienced in a single-beam configuration. *J. Opt. Soc. Am. B*, 21(9):1659–1664, 2004.

[15] R. S. Zadoyan, N. I. Zheludev, and L. B. Meysner. Nonlinear polarization spectroscopy of ions interaction potential in alkali halide crystals. *Solid State Communications*, 55(8):713 – 715, 1985.

4.4 Holocut vs z-cut

The theoretical analysis presented in chapter 3 shows that for cubic crystals the holographic cut ensures the highest efficiency with the added advantage that the position of optimal polarization of the fundamental beam is less sensitive to changes in the input intensity. The purpose of this section is:

- to present the experimental results for XPW generation with [011]-cut samples showing an increase in efficiency;
- to show the decreased sensitivity to the orientation of the fundamental beam polarization at high intensity;

The schematic of the set-up with a single BaF_2 situated between crossed polarizers is shown in Fig. 4.3. The derived system of two plane wave equations for the two interacting waves is:

$$\frac{dA(\zeta)}{d\zeta} = i\gamma_1 AAA^* + i\gamma_2 AAB^* + 2i\gamma_2 ABA^* + 2i\gamma_3 ABB^* + i\gamma_3 BBA^* + i\gamma_4 BBB^*, \tag{4.1a}$$

$$\frac{dB(\zeta)}{d\zeta} = i\gamma_5 BBB^* + i\gamma_4 BBA^* + 2i\gamma_4 ABB^* + 2i\gamma_3 ABA^* + i\gamma_3 AAB^* + i\gamma_2 AAA^*. \tag{4.1b}$$

where A and B denote the amplitudes of the fundamental and cross-polarized waves, respectively. The γ coefficients derived for both cuts are summarized in Tab. 4.5. The last line in the table I gives the orientations of input polarization β_{zero} for which the XPW signal is zero. These angles, derived from $\gamma_2(\beta) = 0$, are different for the two cuts and this can be used to test the correct orientation of the [011]-cut sample. The NLC used in the experiments are 2

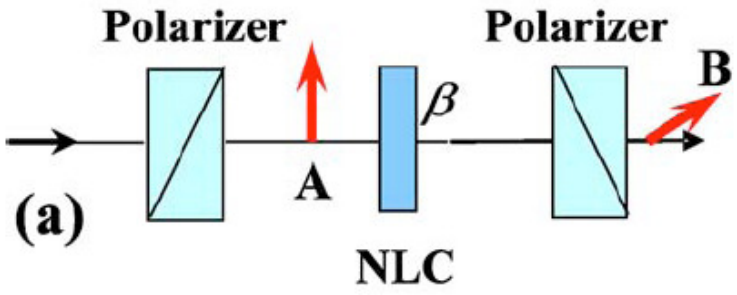

Figure 4.3: Schematic of the XPW generation experiment

mm thick z-cut and [011]-cut BaF_2 crystals. The BaF_2 sample is placed between two calcite Glan polarizers with an extinction ratio better than 4 orders of magnitude. Both the BaF_2

samples and the polarizers are un-coated. The β-dependence measurements were performed with the second harmonic of a Colliding Pulse Mode Locked (CPM) dye-laser (620 nm, 100 fs, 10 Hz-Salle Rose). The pulses with an energy up to 20 μJ were focused with a $f = 500$ mm lens into the NLC. Fig. 4.4 shows the experimental β dependence of XPW generation in the [011]-cut sample. The theoretical curves (lines) for Gaussian/Gaussian shapes for spatial/temporal modulation of the fundamental radiation are obtained by numerically solving the system 3.9. The agreement with experiment is good. The angles β_{zero} for which the XPW signal is minimal correspond to the values listed in Tab. 4.5. As predicted, the two main β position maxima for the holographic cut are insensitive to changes in input energy.

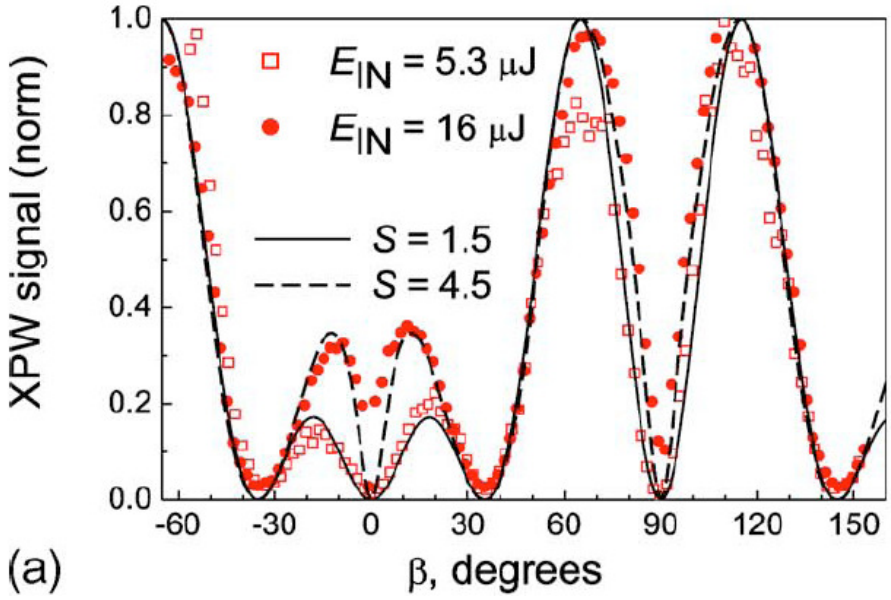

Figure 4.4: XPW signal as a function of angle β for [011] orientation for two different input energies. The lines are theoretical curves.

XPW generation efficiency measurements were done with a commercial femtosecond laser (Femtopower PRO CEP, Femtolasers GmbH) delivering up to 1 mJ, 30 fs pulses at 1 KHz. The fundamental beam spatial shape is very close to Gaussian as shown in the inset of Fig. 4.6. The pulse-to-pulse stability of the laser used in the experiment is below 1% ensuring a very small error (3%) in the efficiency measurements. Measured conversion efficiencies (without corrections for losses) for experiments with a single BaF_2 crystal are shown in Fig. 4.6. The pulses are focused with a $f = 500$ mm lens into the NLC. The efficiency with [011]-cut sample saturates at 11.4%. This value can be compared with the maximum efficiency of 10% measured with a single crystal (Fig. 4.6). Accounting for losses of the output Glan and the NLC, an internal efficiency of 15% is obtained. This efficiency saturates earlier than in the simulation because in the theoretical model we neglect diffraction and self-focusing. It is very important to note that the efficiency curve for the [001]-cut (circles) in Fig. 4.6 was obtained with reoptimization of angle β, while for experiment with the [011]-cut (squares) such a reoptimization was not necessary as predicted by the model.

	z-cut	Holographic cut
γ_1	$\gamma_0[1-(\sigma/2)\sin^2(2\beta)]$	$\gamma_0[D-(\sigma/4)\cos 2\beta]$
γ_2	$-(\gamma_0\sigma/2)\sin 2\beta\cos 2\beta$	$-(\gamma_0\sigma/8)\sin 2\beta(3\cos 2\beta-1)$
γ_3	$(\gamma_0/3)(4-\sigma)-\gamma_1$	$(\gamma_0/3)[D-(3\sigma/4)\cos 4\beta]$
γ_4	$-\gamma_2$	$(\gamma_0\sigma/8)\sin 2\beta(3\cos 2\beta+1)$
γ_5	γ_1	$\gamma_0[D+(\sigma/4)\cos 2\beta]$
β_{zero}	0°; 45°; 90°; 135°; 180°	0°; 35.3°; 90°; 144.7°; 180°

Figure 4.5: Nonlinear coupling coefficients both for z-cut and holographic cut. D stands for: $1+(3\sigma/16)cos4\beta-7\sigma/16$, $\gamma_0=6\pi\chi^{(3)}_{xxxx}/8n\lambda$

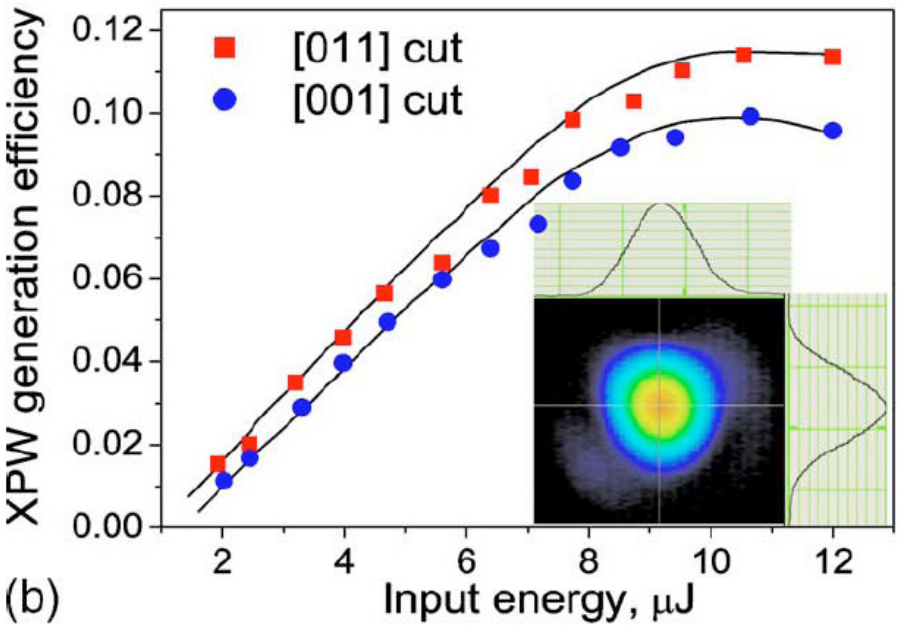

Figure 4.6: XPW generation efficiencies for the two cuts. Insets:input fundamental beam spatial shape.

As XPW filtering is useful at higher energy in a double CPA scheme, we also tested a two crystals scheme [1, 8] for XPW generation using two holographic cut BaF_2 crystals. The fundamental beam with a diameter of 7 mm was focused with a $f = 5$ m lens. The two crystals were set ≈ 50 cm apart, in accordance with the experimental dependence pointed out in [10]. The obtained XPW energy and efficiency are shown Fig. 4.7. The output spectrum has a near Gaussian shape with 80 nm FWHM (for an input width of 50 nm). The maximum obtained

efficiency of 29 % for a 190 μJ input pulse energy yields a 55 μJ XPW pulse energy. It is the highest XPW energy efficiency recorded so far with this kind of set up. This value is in fact 1.3 times higher than the previously published values obtained with z-cut crystals (see [8, ?, 9]) which is in accordance with the prediction of the model. Considering the output pulse shortening obtained via XPW generation this result corresponds to a 50% intensity conversion from one polarization to another. Highest efficiencies are obtained for an input energy just below the continuum generation threshold.

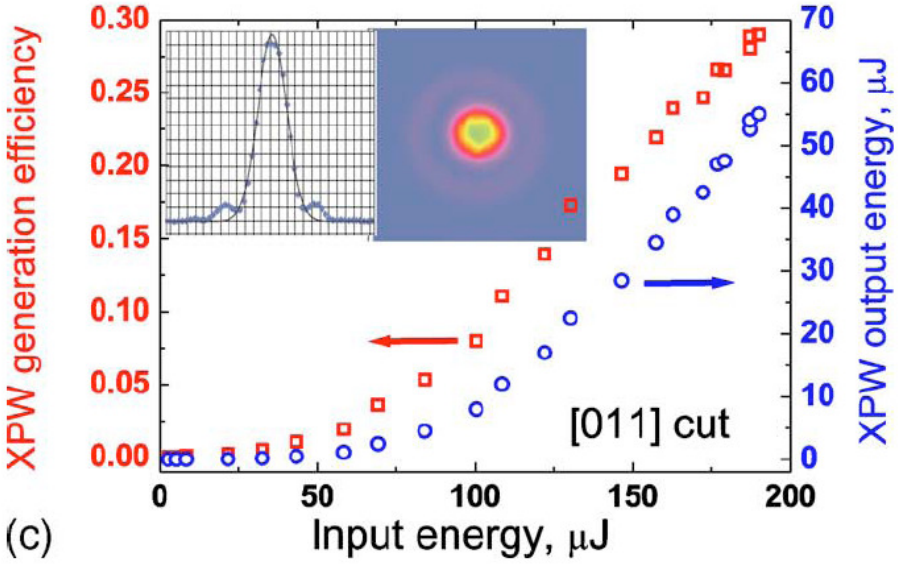

Figure 4.7: XPW generation energy (circle) and efficiency (square) for two crystal scheme with two holografic cut BaF_2 crystals. Insets: output XPW spatial shape

4.5 Conclusions

Record efficiencies for XPW generation using holographic ([011])-cut BaF_2 crystals (and Gaussian beams) have been demonstrated thereby confirming the theoretical predictions. I also demonstrated that when [011]-cut crystals are used for XPW generation, intensity dependent β compensation of the phase mismatch is not required. This feature makes the holographic cut easier to use for all XPW generation applications.

Bibliography

[1] A. Jullien, O. Albert, G. Cheriaux, J. Etchepare, S. Kourtev, N. Minkovski, S.M.Saltiel, Appl. Phys. B **84**, 409 (2006).

[2] V. Chvykov, P. Rousseau, S. Reed, G. Kalinchenko, and V. Yanovsky. Generation of 10^{11} contrast 50 TW laser pulses. *Opt. Lett.* **31**, 1456 (2006)

[3] N. Minkovski, G. I. Petrov, S. M. Saltiel, O. Albert, and J. Etchepare. Nonlinear polarization rotation and orthogonal polarization generation experienced in a single-beam configuration. *J. Opt. Soc. Am. B* **21**, 1659 (2004)

[4] Yu. P. Svirko and N. I. Zheludev, *Polarization of Light in Nonlinear Optics* (Wiley, New York, 1998).

[5] N.Minkovski, S.Saltiel, G. Petrov, O. Albert, J. Etchepare, Opt. Lett. **27**, 2025 (2002).

[6] M. Dabbicco, A. M. Fox, G. von Plessen, J. F. Ryan, Phys. Rev. B **53**, 4479 (1996).

[7] V. M. Gordienko, P. M. Mikheev, V. S. Syrtsov, Bulletin RAS: Physics **71**, 122 (2007).

[8] A. Jullien, O. Albert, G. Cheriaux, J. Etchepare, S. Kourtev, N. Minkovski, S. M. Saltiel , Opt. Express **14** , 2760 (2006).

[9] A. Cotel, A. Jullien, N. Forget, O. Albert, G. Ch´eriaux, C.L. Blanc, Appl. Phys. B **83**, 7 (2006).

[10] O. Albert, A. Jullien, J. Etchepare, S. Kourtev, N. Minkovski, S. M. Saltiel, Opt. Lett. **31**, 2990 (2006).

4.6 Effect of the spectral phase on XPW generation

In this section I present the first comprehensive study of the role of spectral phase on XPW generation using sub-30 fs laser pulses. For durations comprised between 30 and 10 fs the presence of residual uncompensated higher order spectral phase terms after the first compression can no longer be neglected and it is important to quantify their effect on the XPW spectrum and efficiency. For those short pulses, compression is achieved after measurement of the spectral phase with a SPIDER or a FROG. For a 30 fs pulse measurement precision is on the order of 100 fs^2 and 10000 fs^3 for the second and third order of the spectral phase [12, 13, 14]. As it will be demonstrated, within this range of residual spectral phase the XPW output spectrum can be significantly modified, especially with residual higher order spectral phase. I will also derive the maximum acceptable value of residual phase for a given initial pulse duration in order to efficiently drive the XPW process for pulse shortening and contrast improvement.

The XPW experimental setup is shown in Fig. 4.8. We use a commercial femtosecond laser (Femtolasers GmbH) delivering 1 mJ, 30 fs pulses at 1 kHz. The spectral phase of the compressed pulses was measured with an homemade SPIDER [20] and corrected using an acousto-optical programmable dispersive filter (AOPDF, Dazzler™ [21]) inserted into the chirped pulse amplifier. By doing so we have noticed that we removed $\varphi^{(4)} \sim -2.10^6\, fs^4$ and $\varphi^{(5)} \sim 50.10^6\, fs^5$. Furthermore, in order to test the effect of remaining spectral phase higher order terms, we can cancel the Dazzler correction and make experiment with known $\varphi^{(4)}$ and $\varphi^{(5)}$ values.

To study experimentally the effect of the spectral phase on the XPW process, I used a second AOPDF (25 mm TeO_2 crystal) as a versatile and precise way to tune the spectral phase on demand. This AOPDF is placed between the laser and the XPW setup. To avoid damaging the AOPDF, only 1 μJ is used from the total laser energy for our experiments. The diffracted output of the AOPDF is focused by a 40 mm focal length achromatic lens into a 1 mm thick BaF_2 crystal, the XPW beam is selected through a polarizer and focused onto the entrance slit of a spectrometer (Avantes). Both AODPF and spectrometer were synchronized with the laser pulses. The spectral phase from the laser was considered flat, except for the cases when we deliberately introduce the known higher order residual phase. The AOPDF was first set to compensate both its own dispersion and that of the focusing lens in a static way. We then use the AOPDF to add to the optical pulse some user-defined spectral phase. In the experiments presented we added the following spectral phases:

$$\delta\varphi(\omega) = \varphi^{(2)} (\omega - \omega_0)^2 /2 + \varphi^{(3)} (\omega - \omega_0)^3 /6 \tag{4.2}$$

Both coefficients $\varphi^{(2)}$ and $\varphi^{(3)}$ were automatically scanned between -2000 fs^2 and +2000 fs^2 for $\varphi^{(2)}$ (32 points) and between -60000 fs^3 and +60000 fs^3 for $\varphi^{(3)}$ (16 points). For each $\delta\varphi(\omega)$, a different acoustic wave was loaded into the AOPDF generator and the XPW spectrum was recorded and processed. With this setup, a systematic experimental analysis of the effect of cubic spectral phase on the XPW spectrum and efficiency was made possible.

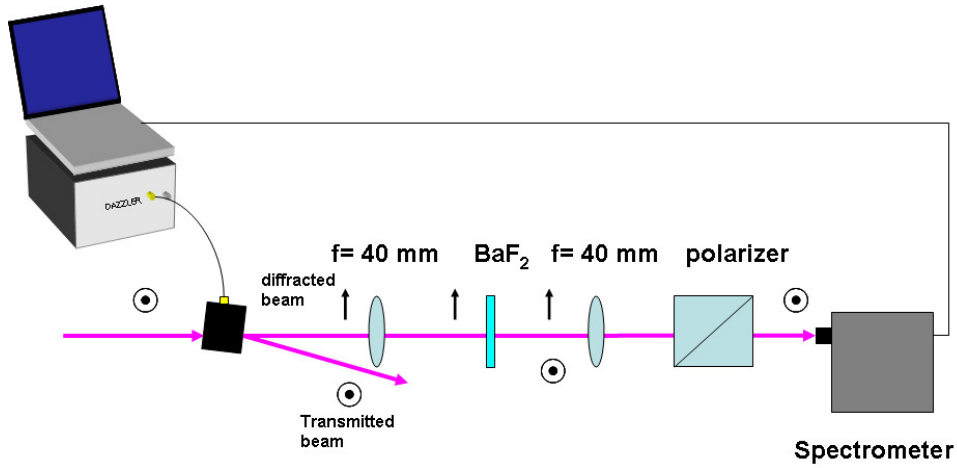

Figure 4.8: Experimental setup.

4.6.1 XPW efficiency

The first dependence considered is the influence of spectral phase on XPW efficiency. As the input energy is constant, the XPW efficiency is proportional to the XPW output energy. Therefore, the XPW efficiency is obtained by integrating every acquired XPW spectrum over the whole spectral range. Fig. 4.9 shows the obtained experimental efficiency map that should be compared with the theoretical map shown in Fig. 3.15. In both cases there is a global maximum of the efficiency corresponding to $\varphi^{(2)} = \varphi^{(3)} = 0$. This is due to the fact that XPW (as all nonlinear effects) is highly sensitive to peak intensity and the highest peak intensity is obtained for a pulse with a flat spectral phase. Fig. 4.10 presents cross sections of this map for $\varphi^{(3)} = 0\, fs^3$ and for $\varphi^{(2)} = 0\, fs^2$. The theoretical curves are obtained from the same cross sections of Fig. 3.15. As predicted, the efficiency decreases with second order phase with a Lorentzian dependence. In particular the experimental $\varphi^{(2)}_{\mathrm{cr,Energy}} = +350\, fs^2$ corresponds to the theoretical one. As a reminder $\varphi^{(2)}_{\mathrm{cr,Energy}}$ is the value of the second order dispersion for which the XPW efficiency is equal to half of the maximum conversion efficiency. The variation of the XPW efficiency with third order spectral phase fits also with the numerical calculation. The difference between the two curves is due to the imprecision of the measurement and correction from high order spectral phase terms.

In the case of a laser pulse with a residual spectral phase ($\varphi^{(4)} \sim -2.10^6\, fs^4$ and $\varphi^{(5)} \sim 50.10^6\, fs^5$) the efficiency dependence on $\varphi^{(2)}$ and $\varphi^{(3)}$ becomes asymmetric (Fig. 4.11.a). This behavior can be reproduced numerically (Fig. 4.11.b). To center the map, both coefficients $\varphi^{(2)}$ and $\varphi^{(3)}$ were scanned between -1500 fs^2 and +4000 fs^2 for $\varphi^{(2)}$ and between -80000 fs^3 and +80000 fs^3 for $\varphi^{(3)}$. The asymmetry can be explained intuitively. When $\varphi^{(2)}$ reaches a value corresponding to the opposite of the residual $\varphi^{(4)}$ value, the effect of both phase terms mutually

compensate, yielding better efficiency. When $\varphi^{(2)}$ and $\varphi^{(4)}$ have the same sign the effect of both phase terms sum up. This gives the vertical asymmetry in Fig. 4.11.a,b. The horizontal asymmetry is due to the same combination of effects between $\varphi^{(3)}$ and $\varphi^{(5)}$. Furthermore, maximum efficiency (which is less than in the case of a perfect flat phase) is reached at a non-zero [$\varphi^{(2)}$,$\varphi^{(3)}$] where the input spectral phase is the flattest.

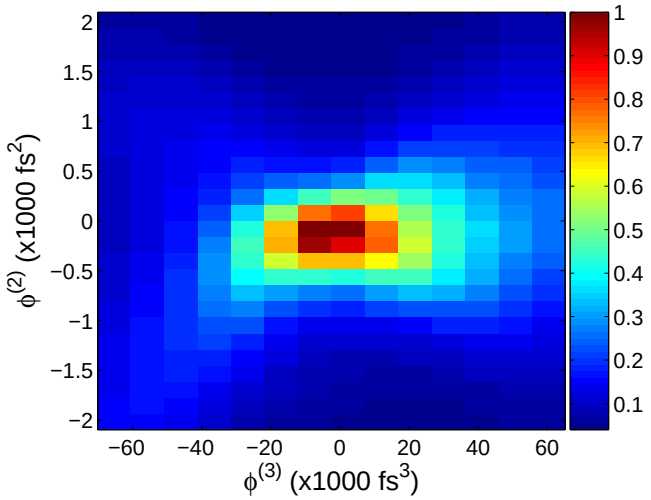

Figure 4.9: Experimental 2D plot of the normalized XPW efficiency versus $\varphi^{(2)}$ and $\varphi^{(3)}$ after compensation of the higher order spectral phase terms. The maximum signal corresponds to an XPW efficiency of 5%.

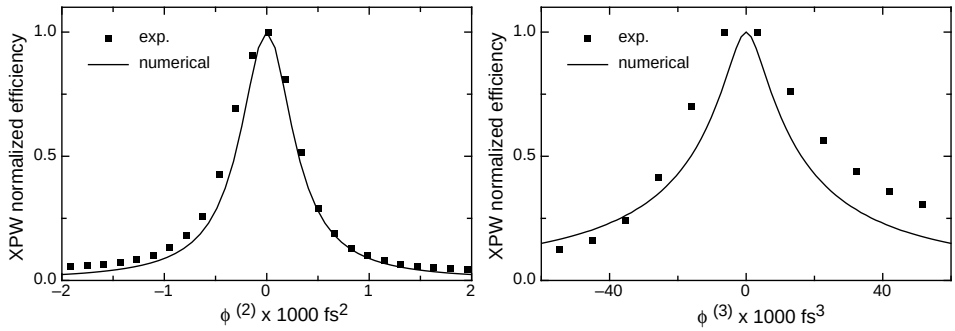

Figure 4.10: Left: normalized experimental (points), (dashed line) and theoretical Lorentzian (solid line) XPW efficiency as a function of $\varphi^{(2)}$ for $\varphi^{(3)} = 0$. Right: normalized experimental points and theoretical (solid line) XPW efficiency as a function of $\varphi^{(3)}$ for $\varphi^{(2)} = 0$

4.6.2 Spectral width

Fig. 4.12 shows the map displaying the spectral width of the previously acquired spectra. These data have been obtained with a laser pulse uncorrected for higher order spectral phase terms, so the theoretical curve in Fig. 4.12 is calculated using $\varphi^{(4)} \sim -2.10^6\, fs^4$ and $\varphi^{(5)} \sim 50.10^6\, fs^5$.

It can be noticed again that there is a global maximum of the spectral width when the total spectral phase is almost flat since both the efficiency and the spectral width reach their

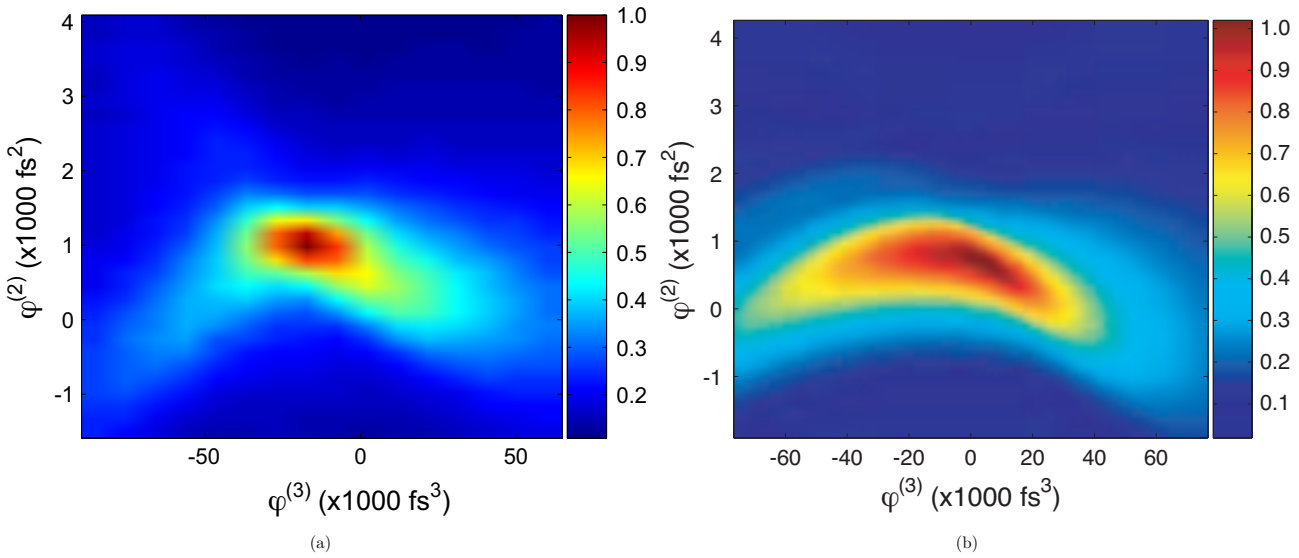

Figure 4.11: Experimental (a) and theoretical (b) 2D plot of the normalized XPW efficiency versus $\varphi^{(2)}$ and $\varphi^{(3)}$ with known residual $\varphi^{(4)}$ and $\varphi^{(5)}$.

maximum for the same ($\varphi^{(2)}$,$\varphi^{(3)}$). The asymmetry of the maps 4.12 is very similar to that already discussed for the efficiency map. As previously presented this can be explained by the presence of residual higher order spectral phase. These experiments confirm the sensitivity of the XPW spectral width to the initial spectral phase. In particular there is spectral broadening of the XPW spectrum compared to the fundamental spectrum for a limited range of $\varphi^{(2)}$,$\varphi^{(3)}$. These values for $\varphi^{(2)}_{\mathrm{cr,Width}}$ and $\varphi^{(3)}_{\mathrm{cr,Width}}$ derived experimentally are comparable to the numerical prediction.

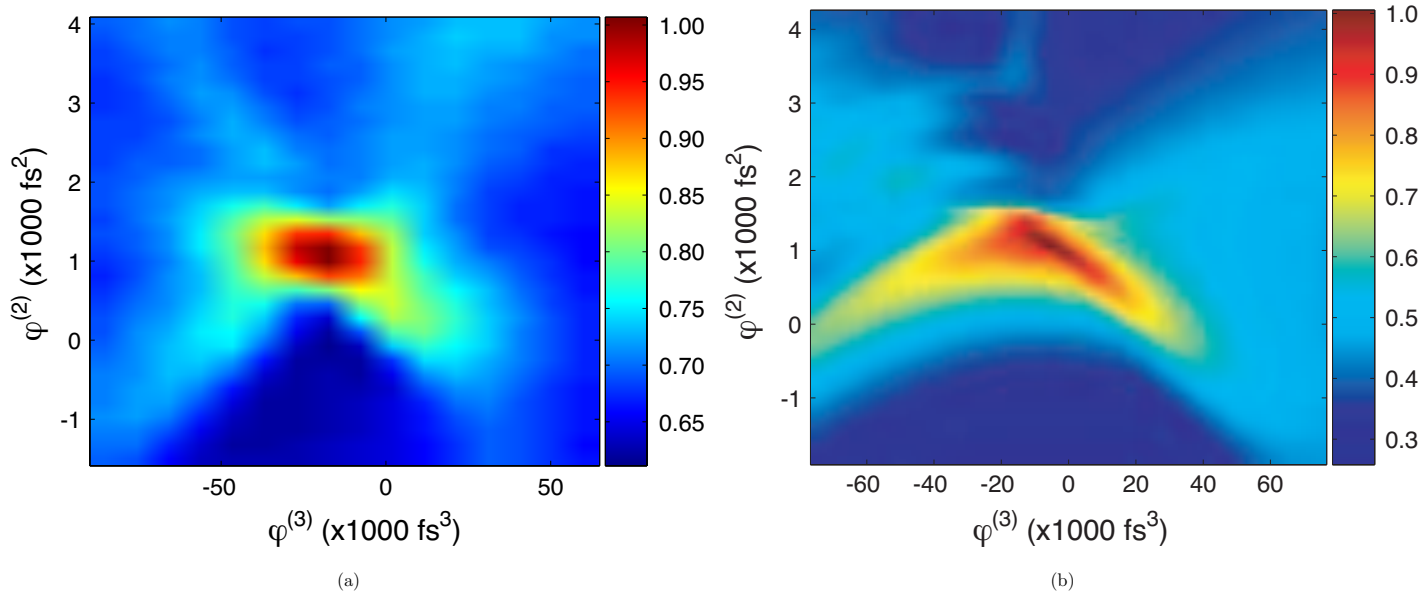

Figure 4.12: Experimental (a) and theoretical (b) 2D plot of the XPW pulse spectral width versus $\varphi^{(2)}$ and $\varphi^{(3)}$. The spectral width values are normalized to the maximum (best compression of the input pulse) of the 2D plot.

4.6.3 Spectral shift

The last parameter considered is the shift of the center of mass of the XPW spectrum. Fig. 4.13(a) shows the center of mass shift of the XPW spectrum as a function of [$\varphi^{(2)}$, $\varphi^{(3)}$] in the case of uncompensated higher order spectral phase terms. This map is in agreement with the hyperbolic parabola derived in the case of a pure $\varphi^{(2)}$, $\varphi^{(3)}$ scan. The analytical model derived in the theoretical section shows that for a residual $\varphi^{(2)}$ and $\varphi^{(3)}$ the spectrum becomes asymmetric. It also indicates that for a fixed and large value of $\varphi^{(3)}$, the center of mass shifts linearly with $\varphi^{(2)}$. The sign of the slope of this curve depends on the sign of $\varphi^{(3)}$. This is confirmed by experiments (Fig. 4.14) in the zone where this approximation is valid. It can also be noticed that this linear shift does not continue indefinitely for larger values of $\varphi^{(2)}$. By changing the input cubic spectral phase a global shift of the center of mass is obtained which is at maximum 1/3 of the spectral bandwidth. The shift of the XPW spectral center of mass function of $\varphi^{(2)}$ for two symmetrical values of $\varphi^{(3)}$ is not perfectly symmetric (for example Fig. 4.14) due to the higher order residual phase terms.

Comparing Fig. 3.16(a) and fig. 4.13(a) around the zone of optimum input pulse compression (center of the map, saddle point) it is visible that the experimental map has an additional shift towards shorter wavelengths (the color is light blue) compared to the theoretical one (where the color is yellow (Fig. 3.16a)). Simulations with the residual $\varphi^{(4)}$ and $\varphi^{(5)}$ spectral phase mentioned previously, reproduce this spectral shift as shown in Fig. 4.13(b). The center of mass of the XPW spectrum is visibly influenced by the higher order spectral phase also near $\varphi^{(2)} = \varphi^{(3)} = 0$ with a shift towards shorter wavelengths when $\varphi^{(4)}$ and $\varphi^{(5)}$ are of opposite sign and towards longer wavelengths when they are of the same sign. Therefore, higher order spectral phase terms have an influence on the XPW signal for any values of [$\varphi^{(2)}$,$\varphi^{(3)}$]. They shift the central wavelength, and influence the XPW efficiency and spectral width for higher values of $\varphi^{(2)}$ and $\varphi^{(3)}$.

4.7 Practical experimental conditions for XPW generation

This systematic theoretical and experimental analysis gives a general idea of the role of the spectral phase on the XPW nonlinear process. In particular it is possible to extract experimentally the maximum tolerable values of residual spectral phase for an input pulse of 30 fs. I have demonstrated that it is fundamental to compensate at least a pure second order spectral phase to a residual value lower than $\pm 325\, fs^2$ and the pure third order phase to a residual value lower than $\pm 17500\, fs^3$ to obtain half of the maximum XPW efficiency. In this range the XPW spectrum is broadened and the center of mass is shifted at maximum by 4 nm compared to the fundamental which is perfectly adapted for amplification in a Ti:Sa amplifier. These values of spectral phase are slightly increased ($\pm 500\, fs^2$and $\pm 25000\, fs^3$) when residual higher

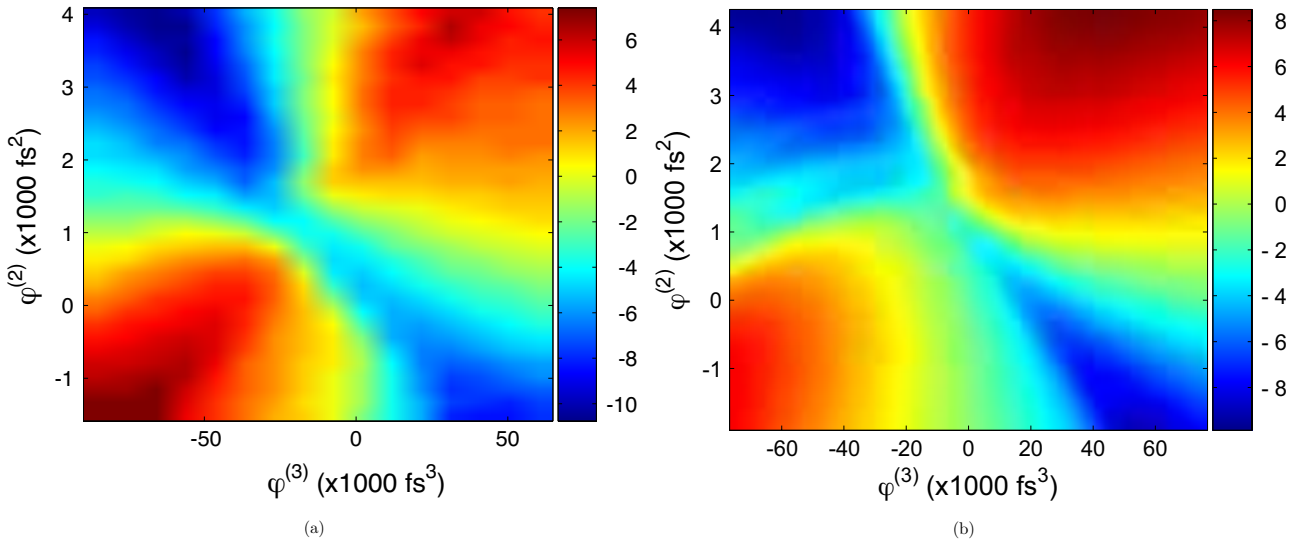

Figure 4.13: Experimental (a) and theoretical (b) 2D plot of XPW spectra center of mass shift (in nm) versus $\varphi^{(2)}$ and $\varphi^{(3)}$ with known residual $\varphi^{(4)}$ and $\varphi^{(5)}$.

order spectral phase terms are present. This can be understood as, for a spectral phase with some residual higher order terms, the XPW signal is lower than the one obtained for a perfectly compressed pulse. Those spectral phase higher order terms can be compensated by a wide combination of second and third order terms. Therefore, it broadens the region for which the XPW efficiency is kept above half of the maximum efficiency. In this case there is a shift of the center of mass even with perfect compensation of $\varphi^{(2)}$ and $\varphi^{(3)}$ terms. These values agree with the numerical simulations.

For a given stretcher compressor system, those $\varphi^{(2)}$ and $\varphi^{(3)}$ values can be correlated to a range of acceptable grating spacing variation and a range of incident angle variations that preserve an efficient XPW generation. Those ranges can also be seen as the degree of precision needed for the given stretcher compressor system to allow an efficient XPW generation.

As this range of $\varphi^{(2)}$ and $\varphi^{(3)}$ values for efficient XPW generation is of the same order of magnitude as the measurement precision obtained with a FROG or a SPIDER, the best approach is to tune the stretcher compressor system to the optimum and then tune the compressor slightly to optimize the XPW generation efficiency without spectral shift.

We can next generalize this analysis to shorter input pulse durations. This is important as it allows to know in general, when the input pulse can be defined as "Fourier limited" with respect to the XPW generation process. Fig. 4.15 (a) shows the [$\varphi^{(2)}$,$\varphi^{(3)}$] area for which efficiency is reduced by less than half calculated for 30, 20 and 10 fs pulses. The elongated peanut shape of these areas is due to partial compensation between $\varphi^{(2)}$ and $\varphi^{(3)}$ which induces a partially flat

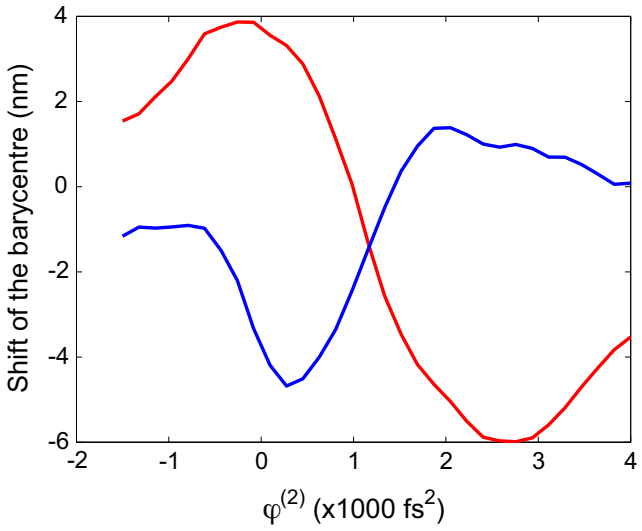

Figure 4.14: Shift of the XPW spectra center of mass as a function of $\varphi^{(2)}$ for $\varphi^{(3)} = -20000\, fs^3$(red) and $\varphi^{(3)} = +20000\, fs^3$(blue). These curves are obtained from cross-sections of Fig. 4.13(a)

spectral phase preventing excessive stretching of the pulse. Higher order phase terms break the symmetry of these plots and can also be evaluated theoretically. This figure confirms how fast the acceptable area decreases decreasing input pulses duration.

As demonstrated in [10] the chirp of the generated XPW pulse is reduced up to nine times compared to the incident pulse chirp. This improvement is less increasing input chirp and reaches a value equal to the input one for large values of input chirp. This behavior can be extended for higher order phase terms as has been done for second order nonlinearities [19]. Therefore we can predict that the spectral phase of the XPW pulse is flattened for the values of $\varphi^{(2)}$ and $\varphi^{(3)}$ yielding good XPW efficiency (i.e. in the area defined by Fig. 4.15 (a)). This area is the one typically used for contrast improvement with XPW, and corresponds to the area where XPW also improves the coherent contrast of the pulse [4]. Outside this area the XPW spectral phase corresponds to the input pulse spectral phase.

Fig. 4.15 (b) shows the [$\varphi^{(2)}$,$\varphi^{(3)}$] area that preserves the initial spectral width of the laser for the same input pulse durations. This area is broader than the area for efficient XPW generation (Fig. 4.15 a). XPW spectra generated for a couple [$\varphi^{(2)}$,$\varphi^{(3)}$] at the border of this area are modulated by the coupling of the input pulse spectral phase to the spectral amplitude of the XPW through the nonlinear process. This effect could allow approximate spectral tailoring in some coherent control experiments. This is emphasized by the fact that the main feature of the tailoring using the spectral phase is a controllable central wavelength shift.

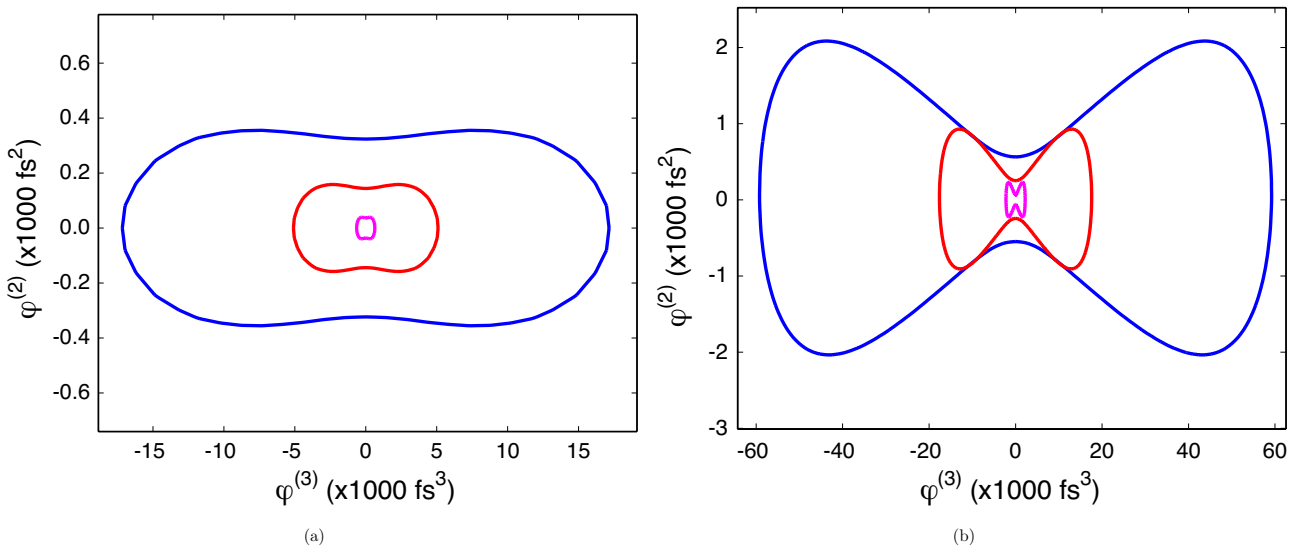

Figure 4.15: (a) Contour line representing the maximum values of $\varphi^{(2)}$and $\varphi^{(3)}$ to obtain half of the maximum XPW efficiency for respectively 30 fs (blue), 20 fs (red) and 10 fs (purple) input pulse duration. (b) Contour line representing the maximum values of $\varphi^{(2)}$and $\varphi^{(3)}$ to obtain $\Delta\lambda_{XPW} = \Delta\lambda_{laser}$ for respectively 30 fs (blue), 20 fs (red) and 10 fs (purple) input pulse duration (b). The range of both axis is different for the two figures i.e. the areas on (a) are broader that the corresponding areas on the (b).

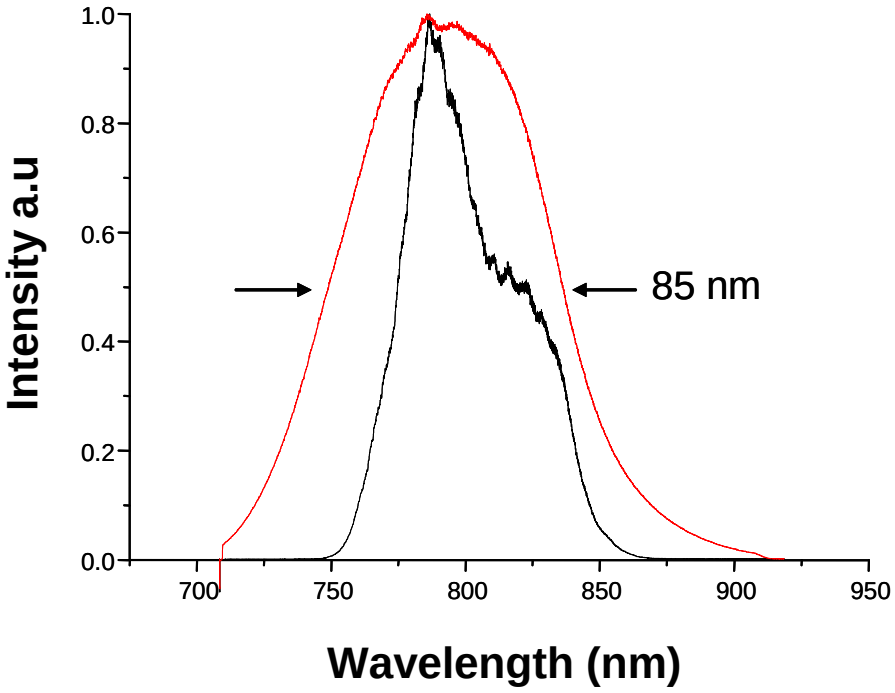

Figure 4.16: Spectrum of the input pulse (black) and of the XPW generated pulse (red). The XPW spectrum is Gaussian, broadened by a factor $\sqrt{3}$ and centered at the same wavelength than the input pulse giving a FWHM of about 85 nm. The input pulse is optimally compressed with a Dazzler.

4.8 Conclusions

In this section I demonstrate the importance of controlling the spectral phase of the input pulse for a correct generation of Cross-Polarized Wave with sub-30 fs pulses and how to optimize the pulse compression after the first CPA directly with the nonlinear effect of the XPW filter. With this control the XPW filter maintains all its benefits (increasing of ns and ps temporal contrast, spectral broadening) for pulses as short as 10 fs.

Fig. 4.16 shows a 85 nm XPW spectrum obtained from a 47 nm input spectrum. The compression of the input pulse was optimized with the Dazzler to obtain a transform limited pulse. The XPW spectrum is Gaussian, broadened by a factor $\sqrt{3}$ and centered at the same wavelength as the input pulse. Following the discussion presented in this section this demonstrates the optimal compression of the input beam. It is important to notice that, due to the spectral filtering, the XPW spectrum is Gaussian even with a modulated input spectrum. This feature can be very useful for sub-10 fs and is discussed in the next section.

Bibliography

[1] N. Minkovski, G. I. Petrov, S. M. Saltiel, O. Albert, and J. Etchepare. Nonlinear polarization rotation and orthogonal polarization generation experienced in a single-beam configuration. *J. Opt. Soc. Am. B* **21**, 1659 (2004)

[2] A. Jullien, O. Albert, F. Burgy, G. Hamoniaux, J.-P. Rousseau, J.-P. Chambaret, F. Augé-Rochereau, G. Chériaux, J. Etchepare, N. Minkovski, and S. M. Saltiel. 10^{-10} temporal contrast for femtosecond ultraintense lasers by cross-polarized wave generation. *Opt. Lett.* **30**, 920 (2005)

[3] V. Chvykov, P. Rousseau, S. Reed, G. Kalinchenko, and V. Yanovsky. Generation of 10^{11} contrast 50 TW laser pulses. *Opt. Lett.* **31**, 1456 (2006)

[4] L. Canova, M. Merano, A. Jullien, G. Chériaux, R. Lopez-Martens, O. Albert, N. Forget, S. Kourtev, N. Minkovsky, and S. M. Saltiel. Coherent contrast improvement by cross-polarized wave generation. *I*n Conference on Lasers and Electro-Optics/Quantum Electronics and Laser Science Conference and Photonic Applications Systems Technologies **JThD131** (2007)

[5] M. Kalashnikov, K. Osvay, and W. Sandner. High-power Ti:Sapphire lasers: Temporal contrast and spectral narrowing. *Laser and Particle Beams* **25**, 219 (2007)

[6] M. P. Kalashnikov, K. Osvay, I. M. Lachko, H. Schönnagel, and W. Sandner. Suppression of gain narrowing in multi-tw lasers with negatively and positively chirped pulse amplification. *Appl. Phys. B*, **81**, 1059 (2005)

[7] T. Oksenhendler, D. Kaplan, P. Tournois, G. M. Greetham, and F. Estable. Intracavity acousto-optic programmable gain control for ultra-wide-band regenerative amplifiers. *Appl. Phys. B*, **83**, 491 (2006)

[8] H. Takada and K. Torizuka. Design and construction of a tw-class 12-fs ti:sapphire chirped-pulse amplification system. *Selected Topics in Quantum Electronics, IEEE Journal of*, **12**, 201 (2006)

[9] I. Pastirk, B. Resan, A. Fry, J. MacKay, and M. Dantus. No loss spectral phase correction and arbitrary phase shaping of regeneratively amplified femtosecond pulses using miips. *Optics Express*, **14**, 9537 (2006)

[10] A. Jullien, L. Canova, O. Albert, D. Boschetto, L. Antonucci, Y.-H. Cha, J. P. Rousseau, P. Chaudet, G. Chériaux, J. Etchepare, S. Kourtev, N. Minkovski, and S. M. Saltiel. Spectral broadening and pulse duration reduction during cross-polarized wave generation: influence of the quadratic spectral phase. *Appl. Phys. B* **87**, 595 (2007)

[11] M. P. Kalashnikov, E. Risse, H. Schönnagel, and W. Sandner. Double chirped-pulse-amplification laser: a way to clean pulses temporally. *Opt. Lett.* **30**, 923 (2005)

[12] M. E. Anderson, L. E. E. de Araujo, E. M. Kosik, and I. A. Walmsley. The effects of noise on ultrashort-optical-pulse measurement using spider. *Appl. Phys. B* **70**, S85 (2000)

[13] D. N. Fittinghoff, K. W. DeLong, R. Trebino, and C. L. Ladera. Noise sensitivity in frequency-resolved optical-gating measurements of ultrashort pulses. *J. Opt. Soc. Am. B* **12**, 1955 (1995)

[14] G. Stibenz, C. Ropers, C. Lienau, C. Warmuth, A. S. Wyatt, I. A. Walmsley, and G. Steinmeyer. Advanced methods for the characterization of few-cycle light pulses: a comparison. *Appl. Phys. B*, **83**, 511 (2006)

[15] E. Sidick, A. Dienes, and A. Knoesen. Ultrashort-pulse second-harmonic generation. non-transform-limited fundamental pulses. *J. Opt. Soc. Am. B* **12**, 1713 (1995)

[16] A. C. L. Boscheron, C. J. Sauteret, and A. Migus. Efficient broadband sum frequency based on controlled phase-modulated input fields: theory for 351-nm ultrabroadband or ultrashort-pulse generation. *J. Opt. Soc. Am. B*, **13**, 818 (1996)

[17] K. Osvay and I. N. Ross. Broadband sum-frequency generation by chirp-assisted group-velocity matching. *J. Opt. Soc. Am. B*, **13**, 1431 (1996)

[18] G. Veitas and R. Danielius. Generation of narrow-bandwidth tunable picosecond pulses by difference-frequency mixing of stretched pulses. *J. Opt. Soc. Am. B*, **16**, 1561 (1999)

[19] P. Baum, S. Lochbrunner, and E. Riedle. Generation of tunable 7-fs ultraviolet pulses: achromatic phase matching and chirp management. *Appl. Phys. B* **79**, 1027 (2004)

[20] C. Iaconis and I. A. Walmsley. Spectral phase interferometry for direct electric-field reconstruction of ultrashort optical pulses. *Opt. Lett.* **23**, 792 (1998)

[21] F. Verluise, V. Laude, Z. Cheng, Ch. Spielmann, and P. Tournois. Amplitude and phase control of ultrashort pulses by use of an acousto-optic programmable dispersive filter: pulse compression and shaping. *Opt. Lett.* **25**, 575 (2000)

4.9 XPW sub-10 fs pulses

4.9.1 Introduction

From the results presented in section 4.6 it is evident that, with correct control of the input spectral phase, the XPW pulses are not only spectrally broadened but also spectrally cleaned compared to the input pulses. Sub-10 fs pulses often present poor coherent temporal quality. A pedestal, whose relative intensity can reach 10^{-3} on a picosecond timescale, surrounds the main pulse [7, 8]. As discussed in section 2.2.2 degraded coherent contrast is partly due to imperfect compensation of high-order spectral phase, but also to strong modulations and sharp features of the spectral amplitude. This last characteristic is typical of ultra-broadband spectra generated through hollow-fiber and filamentation compression techniques [14, 22], or amplified in either saturated or non-saturated OPCPA stages. Even with ideal flat phase compression, modulated spectra lead to broad wings in the temporal domain [10]. It is therefore interesting to demonstrate the capability of XPW generation to clean the strong modulations of ultra-broad spectra. These experiments were done in collaboration with the former "Etudes des Lasers Femtosecondes" (ELF) group in LOA. The results are compared to the theoretical predictions presented in section 3.4.6.

4.9.2 Experimental setup and results

The experimental setup is shown in Fig. 4.17.

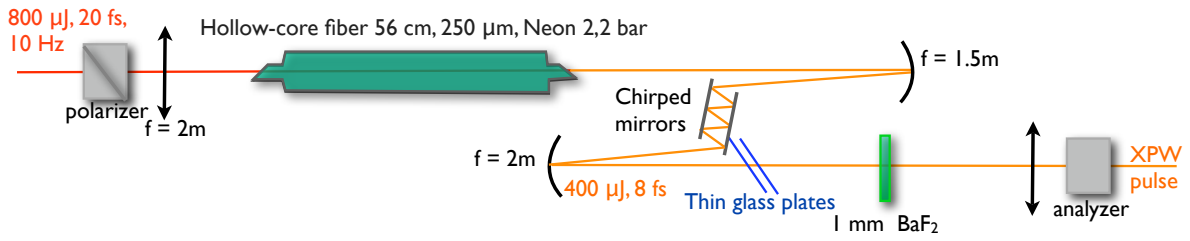

Figure 4.17: Experimental setup

The laser source is a Ti:Sa laser generating 1 mJ pulses, with a duration of 20 fs at 10 Hz repetition rate. To obtain pulse compression in the sub-10 fs range, 800 μJ pulses are focused to a hollow-core fiber (56 cm length, 250 μm inner diameter) filled with neon (2.2 bar) [14]. The transmission of the fiber is 50%. After propagation in the nonlinear medium, the spectrum is significantly broadened (600 nm - 950 nm) and exhibits strong modulations inherent to SPM and self-steepening processes (Fig. 4.18(a)). Chirped mirrors then provide adequate dispersion compensation($-200\,\mathrm{fs}^2$). A FROG measurement estimated the pulse duration to 8 fs (Fig. 4.18(b)) [15] which is close to the Fourier transform limit. These ultra-short pulses are sent in the XPW filter device, composed of one thin (1 mm) BaF_2 crystal ([101]) [16]) placed between crossed Glan polarizers. The first polarizer is placed at the entrance of the hollow fiber, where its intrinsic dispersion can be easily pre-compensated by the laser compressor adjustment. The

analyzer follows the nonlinear crystal to discriminate between the fundamental and XPW waves. The XPW filter contrast enhancement has been shown to be limited by the whole polarizing setup. We obtain 10^{-3} in our experiment. The BaF_2 crystal is placed close to the focus of a 2 m focal length mirror. When focused, the beam emerging as a single-mode from the hollow fiber presents an excellent spatial quality (Fig. 4.18(c)) which is favorable to get high XPW conversion efficiency. Moreover, the seeded energy of the 8 fs-pulses is reduced to 170 μJ to avoid additional nonlinear effects in air. This experiment is therefore a proof of principle.

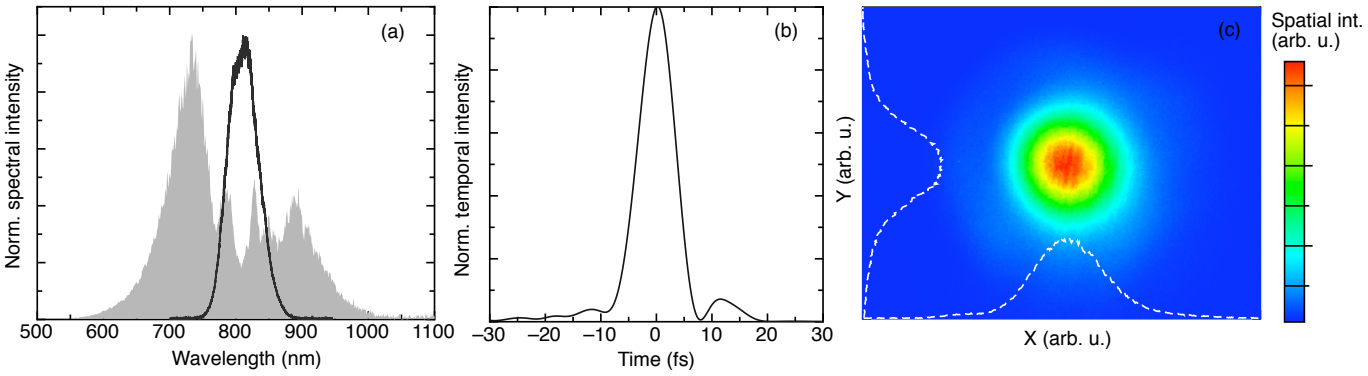

Figure 4.18: (a) Initial laser spectrum (black line) and spectrum measured after propagation in the hollow fiber (shaded area). (b) Pulse duration measurement after the hollow fiber by FROG technique (∼8 fs). (c) Spatial beam profile measured in the BaF_2 crystal plane (∼300 μm FWHM).

Filtering more energetic pulses would require the use of a vacuum or He-filled chamber. For such short pulses, one has to take into account the linear dispersion introduced by air and by the nonlinear crystal itself (380 fs^2/cm). For this reason, the chirp is over-compensated at the output of the fiber by two additional bounces on the chirped mirrors (total introduced dispersion:−300 fs^2). Thin BK7 plates (700 μm and a variable number of 150 μm plates) are inserted to optimize the degree of pulse compression for the XPW process.

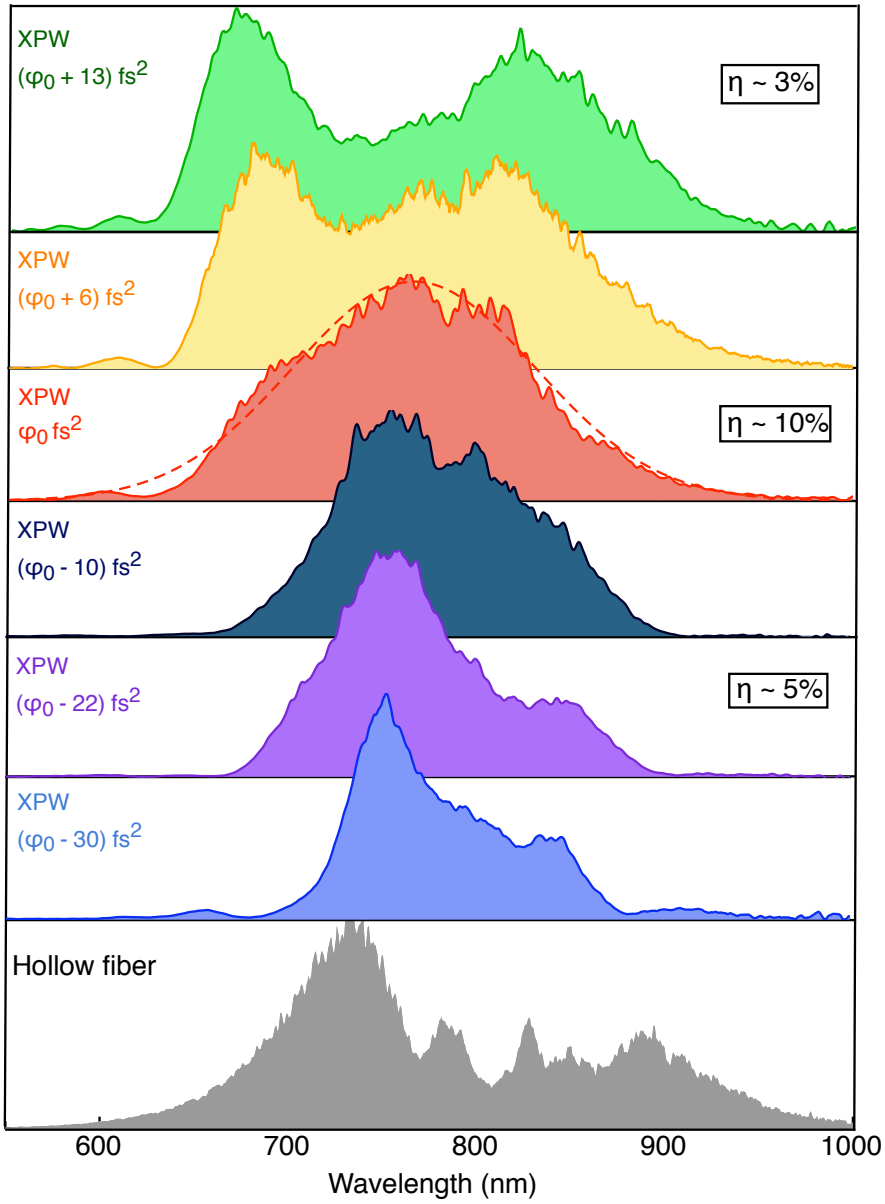

Figure 4.19: Experimental XPW spectra measured for various values of the residual chirp at the entrance of the crystal (values are relative to each other). The spectrum registered at the output of the hollow fiber is shown for comparison (grey area, lower panel). φ_0 is the residual input chirp, absolute value unknown, leading to the highest transmission efficiency of the process (10%) and providing a clean spectral quality. The corresponding output spectrum (red area) is fitted by a Gaussian shape (260 nm at $1/e^2$, dashed red line). The efficiency values are uncorrected from losses on the nonlinear crystal.

4.9.3 Analysis of the results

The experimental XPW spectral behavior as a function of residual second-order spectral phase is summarized in Fig. 4.19. The chirp compensation yielding the highest conversion efficiency is considered as the optimal pulse compression state accessible under our experimental conditions. The transmission of this single-crystal scheme is then slightly higher than 10% (uncorrected

for energy losses on the uncoated crystal faces). The residual input chirp in that case cannot be experimentally determined with accuracy and is simply labeled φ_0. The theoretical analysis presented in section 3.4.6 suggests that this residual input chirp corresponds to a slightly negative chirp ($-25f^2$). The optimized configuration also reveals the remarkable spectral cleaning effect of the process, as illustrated by the experimental output XPW spectrum plotted in Fig. 4.19 (XPW $\varphi_0\,\mathrm{fs}^2$). The input spectral bandwidth is preserved and the output spectrum has a smooth nearly-Gaussian shape. All the sharp features and fast modulations are eliminated.
XPW spectra registered for variable residual chirp (relatively to φ_0) at the entrance of the crystal show that the window for optimized compression is extremely narrow ($< 16\,\mathrm{fs}^2$, $\sim 40\,\mu$m of glass) (Fig. 4.19). They also show an asymmetry between the behavior for positive and negative input chirp. This asymmetry is correlated to the pulse dispersion during propagation in the crystal and was predicted theoretically in section 3.4.6. When the residual chirp is negative compared to φ_0, the available spectral bandwidth is narrower than that of the fundamental wave (Fig. 4.19 (XPW $(\varphi_0 - 10)\,\mathrm{fs}^2$, XPW $(\varphi_0 - 22)\,\mathrm{fs}^2$ and XPW $(\varphi_0 - 30)\,\mathrm{fs}^2$)), which is prohibitive. This is due to the fact that most of the conversion occurs with a negatively chirped pulse. The conversion efficiency in this regime is around 5%. On the other hand, if the residual chirp is positive compare to φ_0, the transmission becomes very weak (a few %). Despite being broader, the output spectrum is strongly modulated with sharp edges and a double-humped structure similar to the input spectrum (Fig. 4.19 (XPW $(\varphi_0 + 6)\,\mathrm{fs}^2$ and XPW $(\varphi_0 + 13)\,\mathrm{fs}^2$)). As predicted by the numerical simulations, in this case the conversion starts early in the crystal, and by the middle of the crystal the spectrum is very broad and smooth. Subsequent conversion takes place with a positively chirped pulse, leading to the evolution of a double humped output spectrum. These experimental results agree with the theory presented in section 3.4.6. We can then conclude that for this duration, (8 fs), the SVEA approximation is still acceptable.

4.9.4 Conclusion

With these experiments we have demonstrated the possibility of XPW filtering for sub-10 fs pulses. The energy conversion is acceptable for a single-crystal scheme (10%) and could be improved by using a two crystals configuration. We have also confirmed the influence of the dispersion in the non linear crystal. Very thin ($< 100\ \mu m$) or less dispersive (CaF_2, LiF) crystals are needed to generate spectrally cleaned and broadened XPW pulses.

Bibliography

[1] M. Hentschel, R. Kienberger, C. Spielmann, G. A. Reider, N. Milosevic, T. Brabec, P. Corkum, U. Heinzmann, M. Drescher, and F. Krausz, Attosecond metrology, Nature **414**, 509 (2001).

[2] M. Uiberacker, T. Uphues, M. Schultze, A. J. Verhoef, V. Yakovlev, M. F. Kling, J. Rauschenberger, N. M. Kabachnik, H. Schroder, M. Lezius, K. L. Kompa, H. G. Muller,

M. J. J. Vrakking, S. Hendel, U. Kleineberg, U. Heinzmann, M. Drescher, and F. Krausz, Supplementary information - attosecond real-time observation of electron tunnelling and multi-electron dynamics in atoms, Nature **446**, 627 (2007).

[3] C. Thaury, F. Quere, J. P. Geindre, A. Levy, T. Ceccotti, P. Monot, M. Bougeard, F. Reau, P. D'Oliveira, P. Audebert, R. Marjoribanks, and P. Martin, Plasma mirrors for ultrahigh-intensity optics, Nature Physics **3**, 424 (2007).

[4] G. D. Tsakiris, K. Eidmann, J. M. ter Vehn, and F. Krausz, Route to intense single attosecond pulses, New Journal of Physics **8** (2006).

[5] N. M. Naumova, C. P. Hauri, J. A. Nees, I. V. Sokolov, R. Lopez-Martens, and G. A. Mourou, Towards efficient generation of attosecond pulses from overdense plasma targets, New Journal of Physics **10**, 025,022 (2008).

[6] F. Tavella, A. Marcinkevicius, and F. Krausz, Investigation of the superfluorescence and signal amplification in an ultrabroadband multiterawatt optical parametric chirped pulse amplifier system, New Journal of Physics **8**, 219 (2006).

[7] F. Tavella, K. Schmid, N. Ishii, A. Marcinkevicius, l. Veisz, and F. Krausz, High-dynamic range pulse-contrast measurements of a broadband optical parametric chirped-pulse amplifier, Applied Physics B **81**, 753–756 (2005).

[8] N. Forget, A. Cotel, E. Brambrink, P. Audebert, C. L. Blanc, A. Jullien, O. Albert, and G. Chériaux, Pump-noise transfer in optical parametric chirped-pulse amplification, Optics Letters **30**, 2921–2923 (2005).

[9] C. Dorrer and J. Bromage, Impact of high-frequency spectral phase modulation on the temporal profile of short optical pulses, Opt. Express **16** (2008).

[10] K. Osvay, M. Csatari, I. N. Ross, A. Persson, and C. G. Wahlstrom, On the temporal contrast of high intensity femtosecond laser pulses, Lasers and Particle Beams **23**, 327 (2005).

[11] A. Jullien, O. Albert, F. Burgy, G. Hamoniaux, J.-P. Rousseau, J.-P. Chambaret, F. Augé-Rochereau, G. Chériaux, J. Etchepare, N. Minkovski, and S. M. Saltiel, 10^{-10} temporal contrast for femtosecond ultraintense lasers by cross-polarized wave generation, Opt. Lett. **30**, 920–922 (2005).

[12] A. Jullien, O. Albert, G. Chériaux, J. Etchepare, S. Kourtev, N. Minkovski, and S. M. Saltiel, Highly efficient temporal cleaner for femtosecond pulses based on cross-polarized wave generation in a dual crystal scheme, App. Phys. B **84**, 409–414 (2006).

[13] V. Chvykov, P. Rousseau, S. Reed, G. Kalinchenko, and V. Yanovsky, Generation of 10^{11} contrast 50 TW laser pulses, Opt. Lett. **31**, 1456–1458 (2006).

[14] M. Nisoli, S. D. Silvestri, and O. Svelto, Generation of high energy 10 fs pulses by a new pulse compression technique, Appl. Phys. Lett. **68**, 2793 (1996).

[15] S. Akturk, C. D'Amico, and A. Mysyrowicz, Measuring ultrashort pulses in the single-cycle regime using frequency-resolved optical gating, J. Opt. Soc. Am. B **25**, A63 (2008).

[16] L. Canova, S. Kourtev, N. Minkovski, A. Jullien, R. B. Lopez-Martens, O. Albert, and S. M. Saltiel, Efficient generation of cross-polarized femtosecond pulses in cubic crystals with holographic cut orientation, Appl. Phys. Lett. **92**, 231,102 (2008).

[17] F. Tavella, Y. Nomura, L. Veisz, V. Pervak, A. Marcinkevicius, and F. Krausz, Dispersion management for a sub-10-fs, 10 tw optical parametric chirped-pulse amplifier, Optics Letters **32**, 2227 (2007).

[18] H. Wang, Y. Wu, C. Li, H. Mashiko, S. Gilbertson, and Z. Chang, Generation of 0.5 mj, few-cycle laser pulses by an adaptive phase modulator, Opt. Express **16**, 14,448–14,455 (2008).

[19] A. Jullien, L. Canova, O. Albert, D. Boschetto, L. Antonucci, Y.-H. Cha, J. P. Rousseau, P. Chaudet, G. Cheriaux, J. Etchepare, S. Kourtev, N. Minkovski, and S. M. Saltiel, Spectral broadening and pulse duration reduction during cross-polarized wave generation: influence of the quadratic spectral phase, App. Phys. B **87**, 595 (2007).

[20] L. Canova, O. Albert, N. Forget, B. Mercier, S. Kourtev, N. Minkovski, S. M. Saltiel, and R. Lopez-Martens, Influence of spectral phase on cross-polarized wave generation with short femtosecond pulses, App. Phys. B (2008).

[21] A. Jullien, O. Albert, G. Cheriaux, J. Etchepare, S. Kourtev, N. Minkovski, and S. M. Saltiel, A two crystal arrangement to fight efficiency saturation in cross-polarized wave generation, Opt. Express **14**, 2760–2769 (2006).

[22] C.P. Hauri, W. Kornelis, F.W. Helbing, A. Heinrich, A. Couairon, A. Mysyrowicz, J. Biegert, and U. Keller. Generation of intense, carrier-envelope phase-locked few-cycle laser pulses through filamentation. *Applied Physics B: Lasers and Optics*, 79(6):673–677, October 2004.

4.10 XPW in UV

In all previous sections XPW generation has been studied in the visible/infrared region. In this section, I present an experimental investigation of the efficiency of XPW generation in the near UV region. These experiments have been done in collaboration with S. Kourtev and N. Minkowki from the Sofia University "St. Kliment Ohridski" (Bulgaria).

There are several motivations to extend the XPW process to shorter wavelength:
first femtosecond excimer laser amplifiers are being developed as ultra-intense femtosecond UV laser sources and they could be advantageous in many applications (material processing, biomedicine, laser fusion, etc.). Contrast improvement of these sources is of importance since ASE in the UV is directly absorbed during laser–matter interaction. Avoiding pre–plasma formation requires the ASE level in the UV region to be kept even lower than in the infrared.
Second XPW generation can be used as the nonlinear effect in diagnostics for the characterization of UV short pulses (section 2.3.4). It complies with the requirements of a useable nonlinear effect: it is efficient, achromatic, presents intrinsic phase matching, generates a measurable signal wavelength (identical to the input one) easily discriminated from the input pulses through its polarization. So it should be compared to several other methods used to measure the temporal profile or the temporal contrast of UV pulses (two-photon fluorescence in alkali-earth fluoride crystals [6, 7], self-diffraction or cross-phase modulation). A first demonstration of an XPW FROG in the visible (400nm) is reported in [8].
The last motivation is that few-cycle pulses consist of an ultra-broad spectrum spanning from the IR down to the U.V. Until now I have always assumed that the $\chi^{(3)}$ tensor is constant with wavelength. This is not verified anymore for photon energies approaching half the crystal band-gap. In this section, I present an experimental investigation of the efficiency of XPW generation in the near UV region (310 nm). By comparing XPW efficiency at 310 and 620 nm an estimate of the dispersion of $\chi^{(3)}$ in BaF_2 is obtained.

4.10.1 Experimental setup

The experimental setup is shown in Fig. 4.20. The pumping source is a CPM dye laser frequency-doubled in a 3 mm type I KDP crystal ($\lambda = 310$ nm after the doubling, $\tau \approx 100$ fs, repetition rate 10 Hz). The pulses are focused (f = 300 mm) into a 2 mm z-cut BaF_2 crystal placed between crossed, high extinction ratio, calcite UV grade polarizers (transparency range 0.22-2.3 μm). BaF_2 is highly transparent in the UV as it presents a cut-off at 150 nm and the losses due to two-photon absorption (TPA) are small (Fig. 4.21). To compare XPW generation in the UV with XPW generation behavior in the visible, measurements are also performed at the fundamental laser wavelength $\lambda = 620$ nm by removing the KDP doubling crystal and UV filter and using a focal length of 450 mm.

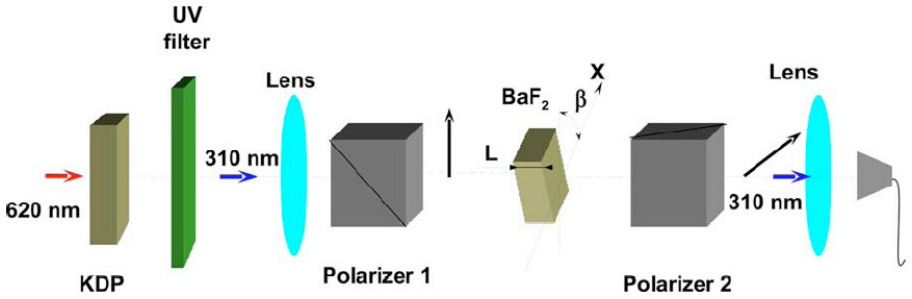

Figure 4.20: Schematic of the XPW experiment in UV region. BaF_2 it's a z-cut sample. β is the angle between the x-axis of the crystal and the polarization plane of the input beam.

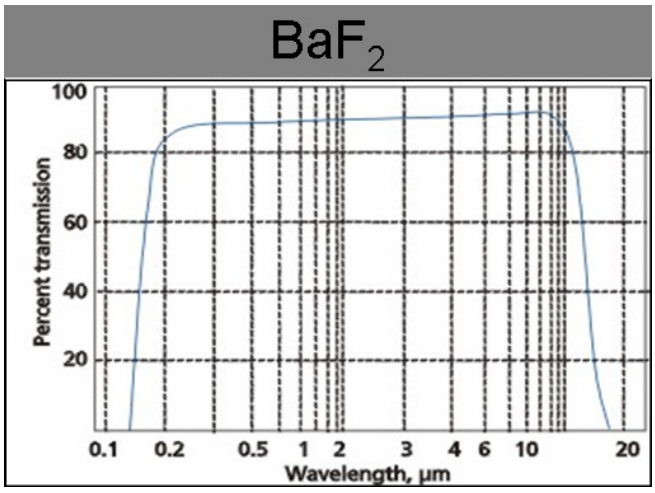

Figure 4.21: Transmission of BaF_2 crystal function of the wavelength λ (Saint-Gobain.)

4.10.2 Experimental results

XPW experiments in the UV immediately prove that XPW generation is not only possible at those wavelength but also that it is more efficient than in visible. To quantify the increase in XPW generation efficiency in the UV we did two type of experiments. We measured, both in the UV and the visible, the XPW intensity as a function of input intensity and crystal orientation. This gives two independent methods to measure the efficiency increase in the UV, which can then be compared to a theoretical model.

XPW generation efficiency measurements as a function of input intensities and wavelength are presented in Fig. 4.22. To estimate the input intensity, the spot surfaces of the input beams

(UV and VIS) were carefully measured. The ratio of spot surfaces (VIS/UV) was found to be 2.17 . Furthermore, the pulse durations were found to be identical for both wavelengths due to second harmonic generation (SHG) experimental conditions. The KDP crystal thickness is such that the difference in group velocities causes narrowing of the SHG spectrum that counterparts the $\sqrt{2}$ broadening due to the SHG process.

The slope of the XPW generation efficiency as a function of the input pulse intensity follows a quadratic law as it should be for any cubic nonlinear process. For a given input intensity, XPW efficiency is 6 times higher in UV than in visible when XPW generation is unsaturated. As seen from Fig. 4.22 in the saturation regime, XPW efficiency is the same in the visible and in the UV.

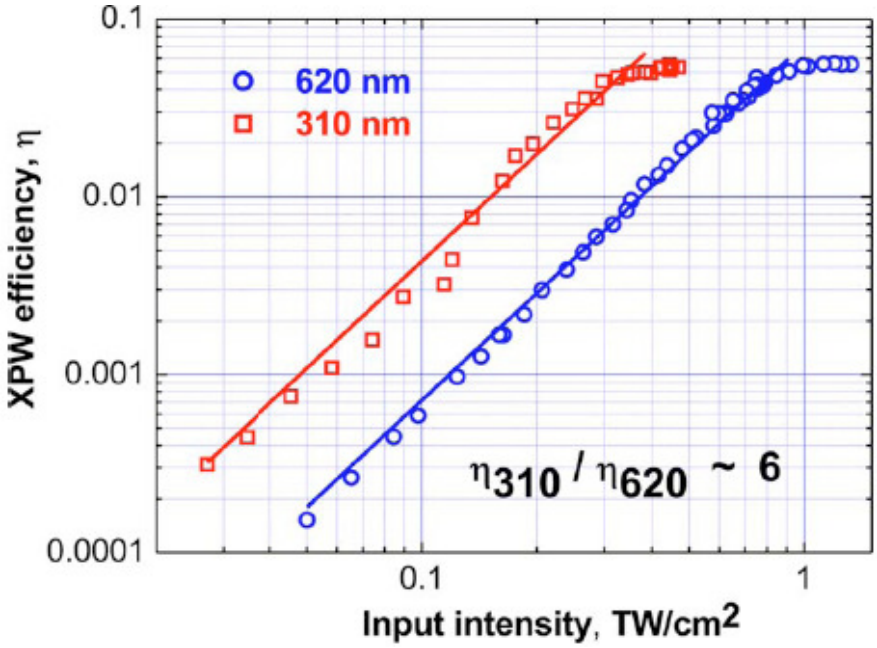

Figure 4.22: Comparison of XPW efficiencies at 310 nm and 620 nm. The solid lines represents quadratic dependence.

XPW efficiency being linked to $\chi^{(3)}$ anisotropy, it is strongly dependant on crystal axes orientation with respect to the input pulse polarization. The measured angular dependence of the XPW efficiency at λ=310 nm and λ=620 nm (pulse energies of 15.5 μJ and 56 μJ respectively) are presented in Fig. 4.23. β is the angle between the input polarization plane and the crystal axis x. The two energies correspond to intensities of 465 GW/cm^2 $\pm$ 10% at 310 nm and to 780 GW/cm^2 $\pm$ 10% at 620 nm, respectively.

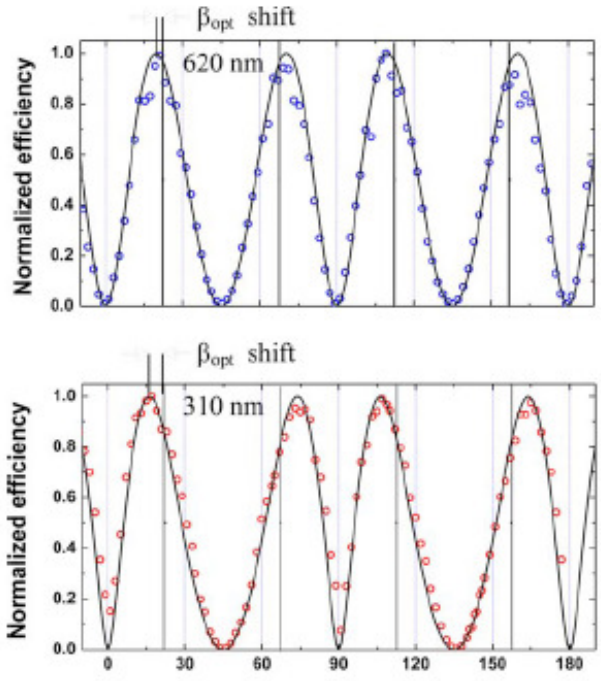

Figure 4.23: XPW generation efficiency as a function of angle β for (a) 620 nm and (b) 310 nm fundamental wavelengths. Each of the experimental curves is normalized to the average value of the maxima. The lines are theoretical curves for Gauss/Gauss shapes for spatial/temporal modulation of the fundamental radiation for (a) F=3.6 and (b) F=5.76. The theoretical model used takes into account SPM and depletion of the fundamental wave. The vertical solid lines indicate optimal β position for low input intensities when $F << 1$

4.10.3 Analysis of the results

From the results shown on Fig. 4.22 and 4.23 we can estimate the increase in third order nonlinearity at 310 nm with respect to 620 nm. In the undepleted regime the XPW efficiency η is given by:

$$\eta = \frac{I_{XPW}}{I_0} = \frac{2}{\epsilon_o cn}[(\sigma/4)\gamma_o I_o sin(4\beta)L]^2 \tag{4.3}$$

where I_0 is input intensity, $\gamma_0 = 6\pi\chi^{(3)}_{xxxx}/8n\lambda$; L is the crystal length; σ is the anisotropy of $\chi^{(3)}$ -tensor $\sigma = (\chi^{(3)}_{xxxx} - 3\chi^{(3)}_{xxyy})/\chi^{(3)}_{xxxx}$. Therefore, η varies with λ for two reasons. First it presents a $1/\lambda^2$ dependance due to the dispersion of γ_0. Second it is sensitive to the dispersion of $\chi^{(3)}$. As there is no data on the dispersion of σ we are able to measure the dispersion of $|\sigma\chi^{(3)}_{xxxx}|$ and assume that the dispersion of σ is negligible compare to the dispersion of $\chi^{(3)}$.

From measurements presented in Fig. 4.22, and using Eq. (4.3), we obtain a value of $|\sigma\chi^{(3)|}_{xxxx}$ which is 1.22 times higher at 310 nm than at 620 nm.

This is confirmed by the β scan analysis. XPW generation with high efficiency presents a β dependency that varies with $F = (2/\epsilon_o cn)\sigma\gamma_o I_o L$. The F parameter is the S parameter already defined multiplied by the anisotropy. When $F << 1$ the position of the maxima are at $\beta_{opt} = m.22.5^o$ with m integer. These positions are marked with vertical solid lines in Fig. 4.23.

At higher values of F the maxima are shifted from the low intensity positions. The bigger is the F parameter the bigger is the shift of β_{opt} from its low intensity position. Using F as a fitting parameter theoretical dependencies are plotted on Fig. 4.23. The corresponding F fitting parameters for both β experimental curves are $F_{620} = 3.6$ for the 620 nm experiment and $F_{310} = 5.76$ for the 310 nm experiment. Using the ratio $F_{310}/F_{620} = 1.60$ and the ratio $I_{o,310}/I_{o,620} = 0.60$ we obtain that the product $|\sigma(\chi^{(3)}_{xxxx}|$ is 1.33 times higher at 310 nm than that at 620 nm.

The main source of error in both intensity and beta dependence measurements is the input intensity measurement uncertainty. We then may conclude that the two estimations for the ratio $(\sigma\chi^{(3)}_{xxxx})_{310}/(\sigma\chi^{(3)}_{xxxx})_{620}$ are in accordance with each other giving an overall:

$$\sigma\chi^{(3)}_{xxxx})_{310}/(\sigma\chi^{(3)}_{xxxx})_{620} = 1.28 \pm 0.10 \tag{4.4}$$

$\chi^{(3)}_{xxxx}$ dispersion of BaF_2 as a function of the wavelength has been previously experimentally investigated by De-Salvo et al [9] using a Z-scan measurement at 1064 nm, 532 nm, 355 nm and 266 nm. Interpolating data in ref [9] one can estimate $\kappa = (\chi^{(3)}_{xxxx})_{310}/(\chi^{(3)}_{xxxx})_{620} \approx 1.4$. This ratio is comparable to the one reported in this section. Furthermore, we can also conclude that the dispersion of σ, the anisotropy of $\chi^{(3)}$, in the spectral range investigated is small and does not exceed the dispersion of $\chi^{(3)}_{xxxx}$.

Theoretical model

The method of Boling-Glass-Owyoung [10] is frequently used to theoretically derive the cubic nonlinearities of materials from their optical index. Furthermore, using the Sellmeier equation for optical index dispersion with this model, the dispersion of $\chi^{(3)}_{xxxx}$ for BaF_2 is given by:

$$\chi^{(3)}_{xxxx}(\lambda) = \chi^{(3)}_{xxxx}(\lambda_o)\frac{n(\lambda)[n(\lambda)^2+2]^2[n(\lambda)^2-1]^2}{n(\lambda_o)[n(\lambda_o)^2+2]^2[n(\lambda_o)^2-1]^2} \tag{4.5}$$

Applying this equation (4.5) to the wavelengths relevant to this experiment we obtain $\kappa = (\chi^{(3)}_{xxxx})_{310}/(\chi^{(3)}_{xxxx})_{620} \approx 1.17 \pm 0.20$ This estimation is also consistent with the measured value from this section enforcing the hypothesis that σ presents little dispersion with wavelength.

4.10.4 Conclusion

In conclusion, with these experiments we have demonstrated XPW generation in UV region and that this process, outside saturation, is 6 times more efficient than in the visible. Efficiency dependence with input wavelength from λ_o to λ, in the visible and near UV region, can be described by the following relation:

$$\eta(\lambda) = \eta(\lambda_o)(\kappa\frac{\lambda_o}{\lambda})^2 \tag{4.6}$$

The value reported here for κ is in accordance with what has been previously reported. The results presented here will be useful for extending the XPW nonlinear filter in the UV region and

for developing new applications as, for example, pulse characterization and temporal contrast filtering of femtosecond UV pulses. Similar results obtained with LiF crystal at 310 nm shows that XPW can be extended to wavelength as low as 266 nm (cut-off frequency at 100 nm).

Bibliography

[1] A. Jullien, O. Albert, F. Burgy, G. Hamoniaux, J.- P. Rousseau, J.-P. Chambaret, F. Auge-Rochereau, G. Cheriaux, J. Etchepare, N. Minkovski, and S. Saltiel. 10^{-10} temporal contrast for femtosecond ultraintense lasers by cross-polarized wave generation. *Opt. Lett.* **30**, 920-922 (2005).

[2] V. Chvykov, P. Rousseau, S. Reed, G. Kalinchenko, and V. Yanovsky. Generation of 10^{11} contrast 50 TW laser pulses. *Opt. Lett.* **31**, 1456 (2006)

[3] S. S. Bulanov, A. Brantov, V. Yu. Bychenkov, V. Chvykov, G. Kalinchenko, T. Matsuoka, P. Rousseau, S. Reed, V. Yanovsky, K. Krushelnick, D. W. Litzenberg and A. Maksimchuk. Accelerating protons to therapeutic energies with ultra-intense ultra-clean and ultra-short laser pulses. *Med. Phys.* **35**, 1770 (2008).

[4] A. Cotel, A. Jullien, N. Forget, O. Albert, G. Ch´eriaux, C.L. Blanc, Appl. Phys. B **83**, 7 (2006).

[5] N. Minkovski, G. I. Petrov, S. M. Saltiel, O. Albert, and J. Etchepare. Nonlinear polarization rotation and orthogonal polarization generation experienced in a single-beam configuration. *J. Opt. Soc. Am. B* **21**, 1659 (2004

[6] K. Osvay, I.N. Ross, C.J. Hooker, J.M.D. Lister. Laser-excited nonlinear properties of BaF_2 and its application in a single-shot spatially insensitive autocorrelator. *Appl. Phys.* B 59, 361 (1994).

[7] K. Osvay, M. Csataria, A. Gaal and I. N. Ross. Temporal Contrast of High Intensity Femtosecond UV Pulses. *Journal of the Chinese Chemical Society* 47, 855 (2000).

[8] N. Forget, S. Coudreau, F. Lepetit, O. Albert, T. Oksenhendler. Achromatic and Single-beam Pulse Characterization Technique for Visible-UV Pulses based on direct UV Pulse Shaping and Cross- polarized Wave Generation. *Lasers and Electro-Optics*, 2007. CLEO 2007.Page(s):1 - 2,CMA3.

[9] R. DeSalvo, A. A. Said, D. J. Hagan, E.W. Van Stryland, M. Sheik-Bahae,"Infrared to ultraviolet measurements of two-photon absorption and n_2 in wide bandgap solids. *IEEE Journal of Quantum Electronics* 32, 1324 - 1333 (1996).

[10] N. Boling, A. Glass, A. Owyoung. Empirical relationships for predicting nonlinear refractive index changes in optical solids. *IEEE Journal of Quantum Electronics*, 14, 601 (1978).

4.11 High energy XPW

4.11.1 Introduction

I have previously shown that, working in a double, holo-cut crystal configuration, XPW generation efficiency close to 30 % in energy can be reached (Fig. 4.7). In this configuration the first crystal is placed in the far field (at the focus) to have a good spatial profile and the position of the second crystal is optimized to maximize the overall efficiency. With this solution we obtained 55 μJ for an input energy of 190 μJ.
Today the most common front-ends of high intensity laser systems deliver mJ level, $\approx$ 30 fs pulses. This is for example the case of the LOASIS laser system presented in chapter 5 and of the "salle noire" laser system (the front-end is a commercial Femtopower CEP from Femtolasers GmbH) presented in chapter 6. The Femtopower system is also used as the front-end of the 100 TW laser system produced by Thales Laser (Alpha 10). The only solution at the moment, for implementing an XPW filter after the front-end is to decrease the input pulse energy. The consequence is that only several tens of μJ of XPW signal are obtained and an additional booster stage may be necessary before injecting into the low gain amplifiers. Furthermore, with the constant increase in focused intensity on target (PetaWatt class lasers), pulses with a temporal contrast higher than 10 orders of magnitude are needed. This implies injecting > 100 μJ, ultra high contrast pulses into the second CPA. There is therefore a big interest in trying to extend the high efficiency demonstrated at the hundreds of μJ level to higher input energy and, in particular, to the mJ level.
Several difficulties limit this extension. First, working in the far field and increasing the input energy (keeping the intensity on the crystal below the white-light generation threshold ($10^{12} W/cm^2$)), implies using very long focal lengths. The focal length for filtering 200 μJ, with an input beam diameter of 7 mm, is already 4 meters. The second problem is linked to the two-crystal configuration. Fig. 4.24 shows the optimal distance between the two crystals as a function of the focal length squared. The input beam diameter is 5 mm. The distance between the crystals increases linearly with the square of focal length and so with the input energy.

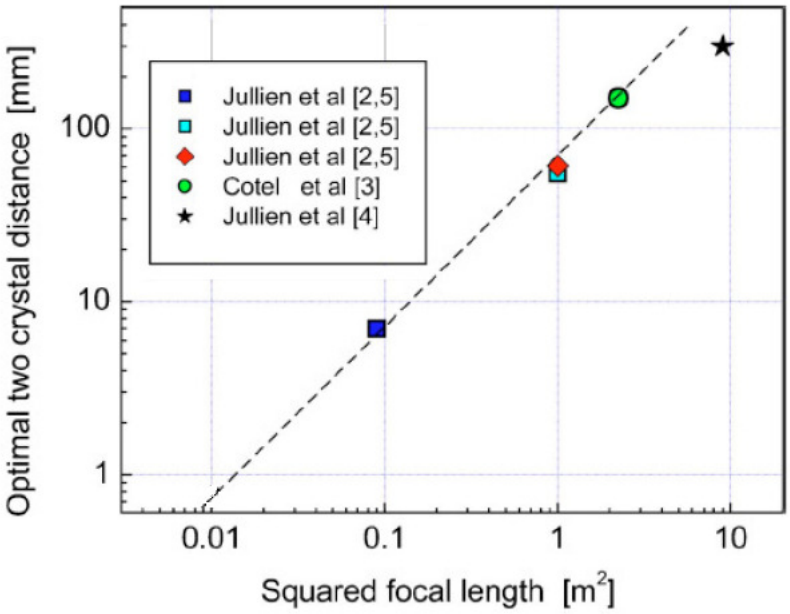

Figure 4.24: Summary of published optimal distances with two crystal schemes for XPW generation obtained with different focusing of the fundamental beam on the two crystal setup. The dashed lines corresponds to the theoretically predicted slope of 1.

Just as an example, in order to filter 1 mJ, 30 fs pulses, in the double crystal configuration, the second crystal needs to the located at more than 1 meter from the first. This also implies that several meters of propagation need to be put under vacuum to avoid any temporal and spatial distortion caused by SPM. These distances can be reduced by entering with a smaller beam size but this complicates the beam propagation and implies re-expanding the beam to avoid damaging the output polarizer.
The simplest solution to bypass these scaling effects consists in using a relatively short focal length (for example 1 m) and putting the crystal in the near field (out of focus). To circumvent the problem of poor spatial quality in the near field, a hard aperture can be placed in the focus to act as a spatial filter. The first results with this configuration were obtained after the-front end of a commercial 200 TW laser system (Amplitude Technologies) and are presented in the next section. This type of front-end was chosen because, thanks to the amplification in a regenerative amplifier, the M^2 is very close to 1 and the good spatial profile is maintained out of focus. Furthermore pulses with an energy higher than 10 mJ are available. With a conversion efficiency of 10 % in a single crystal configuration, XPW pulses approaching the 1 mJ level can be expected. This also makes it possible to measure, with high dynamic range, the temporal contrast directly after the XPW filter.

4.11.2 Experiments at Amplitude Technologies

The 200 TW Pulsar laser system (from Amplitude Technologies, France) is a CPA femtosecond laser source providing more than 5 J pulse energy at 10Hz repetition rate, with a peak power of 200 TW. It consists of a fully integrated Ti:Sa oscillator with a diode pumped solid state pump

laser, a stretcher, a regenerative amplifier, three multi-pass amplifiers pumped by Nd:YAG lasers and a vacuum compressor. The experiments described here were performed using the front-end only, limiting the energy and allowing pulse compression in air. With the gain narrowing control performed with an Acousto-Optic Programmable Gain Control Filter (AOPGCF, Mazzler) [2], spectra as wide as 80 nm are typically generated, only limited by the stretcher and mirrors bandpass. Due to the square shape of those spectra, the corresponding measured pulse durations is < 25 fs. The system overall spectral phase is carefully and actively controlled using a feedback loop between a spectral phase retrieval device, a commercial APE Spider, and the Dazzler. Using this technique, deviations from a flat spectral phase of less than 0.5 rad are achievable over about 100 nm spectral range.

To test the new XPW configuration the $\approx 25fs$, multi-mJ pulses, compressed after the front-end, pass through a variable neutral density filter for energy tuning and are focused with a 1 meter focal lens onto a 300 μm iris. The focal spot matches the sizes of the iris. A single BaF_2 1 mm, [101]-cut crystal is placed after the focus at a correct distance to stay just below the white-light generation threshold. The iris and the crystal are placed under vacuum in a plexiglass tube (Fig. 4.25). The transverse position of the iris and the longitudinal position of the crystal can be optimized by keeping the system under vacuum. The position of the single crystal is optimized to saturate the XPW effect without distortion of the spectrum. The generated XPW beam is selected with a, high extinction ratio, calcite Glan polarizer. The maximum output XPW energy we obtained is $\approx$ 1 mJ for an input of 10 mJ yielding an overall efficiency of 10 % (considering the losses through the iris) and a good spatial quality. The measured spectrum (Fig. 4.27 black line) is well fitted by a Gaussian and has a FWHM larger than 100 nm corresponding to sub-10 fs Fourier transform pulses. The actual temporal duration is $>$ 100 fs due to the dispersion (550 fs^2) added by the output Glan polarizer. This dispersion can be compensated with multiple bounces on broadband chirped mirrors. These mirrors were not available for the current experiment. The XPW spectrum is broadened and not shifted compared to the fundamental. As explained in section 4.6 this is an indication of the good compression of the input beam. The XPW energy stability function of time is shown in Fig. 4.26 while Fig. 4.28(black line) shows the high dynamic temporal contrast of the filtered pulses measured with a third order correlator (Sequoia, Amplitude Technologies). The dispersion added by the output window of the vacuum tube and the thick Glan polarizer is not compensated. The Sequoia measurement dynamic range is close to 12 orders of magnitude for a 1 mJ input pulse. To make the increase in temporal contrast clearly visible we started with the laser with a low temporal contrast ($< 10^5$ red line). An increase in temporal contrast of 5 orders magnitude is visible in the ns (ASE) and ps (coherent contrast) zone. This enhancement is determined by the ratio between the two components of the input linear polarization. These experiments confirm the resulted presented in [1] but with a scaling of the output energy by almost a factor 10.

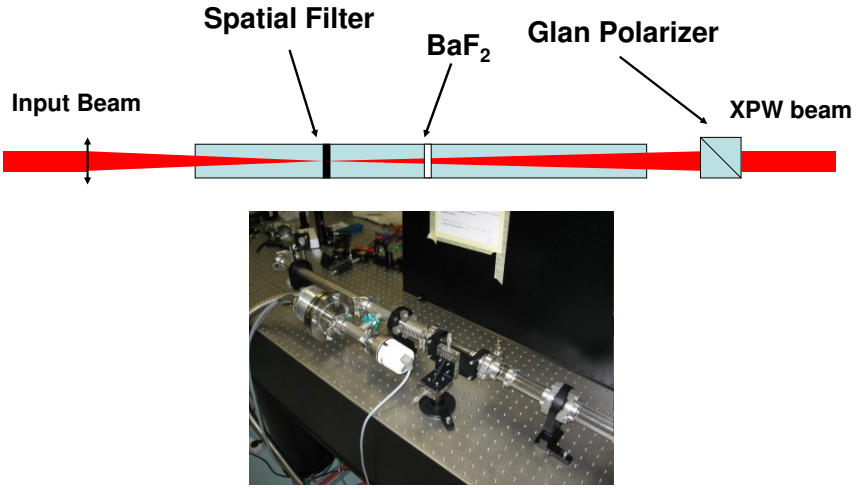

Figure 4.25: Schematic of the setup. An iris is placed in the focus to act as a spatial filter. The position of the crystal is optimized to have a good efficiency without distortion of the generated XPW spectrum. A maximum output energy of 850 μJ has been obtained.

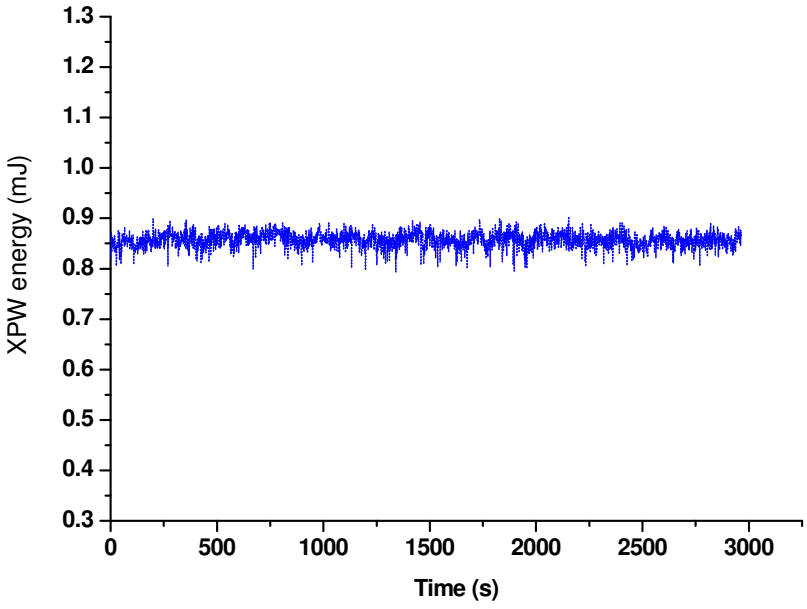

Figure 4.26: Energy of the XPW pulses function of time

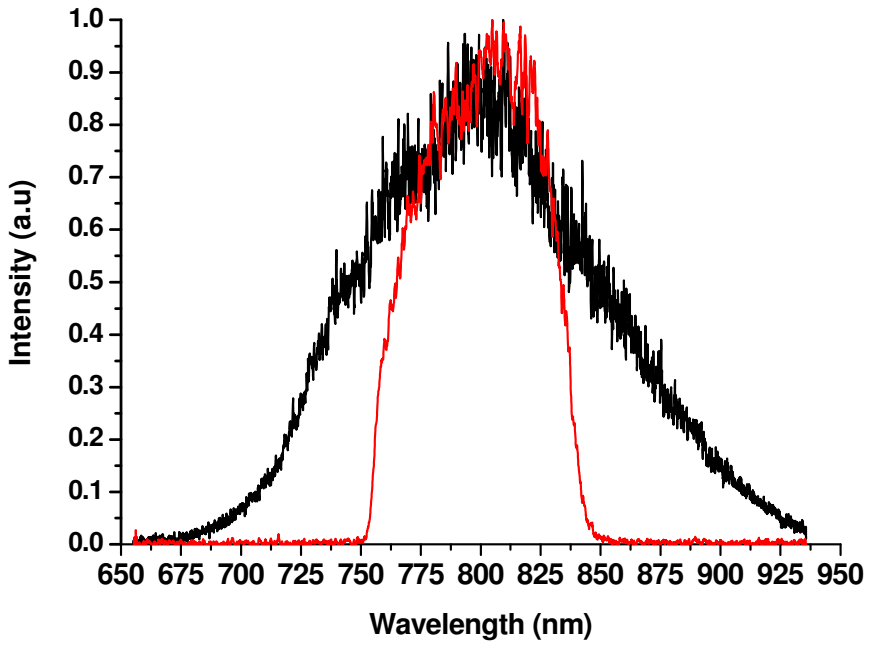

Figure 4.27: Spectrum of the converted XPW pulses(black line) and of the fundamental (red line)

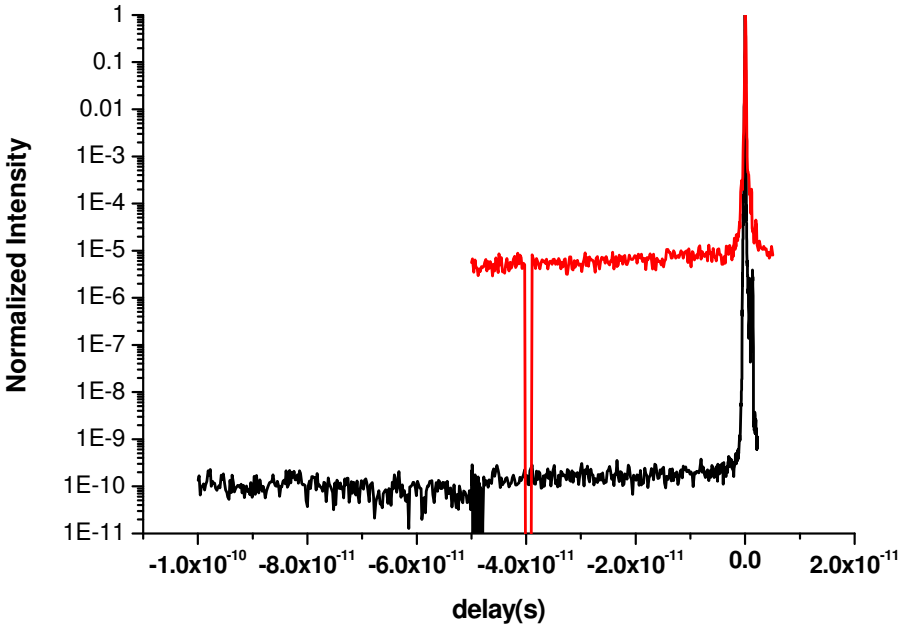

Figure 4.28: Third order correlator (Sequoia, Amplitude Technologies) measurement of the temporal contrast of initial laser (red line) and after the XPW filter (black line). The energy of the XPW beam was 850 μJ

4.11.3 Conclusion

In conclusion the results of these preliminary experiments are very promising. The possibility of obtaining 1 mJ, spectrally cleaned and broadened pulses was demonstrated. Starting with high contrast input pulses (10^{10} for a typical Amplitude Technologies system) opens the possibility for generating sub-20 fs pulses with a temporal contrast higher than 14 orders of magnitude.

Bibliography

[1] A. Jullien, O. Albert, F. Burgy, G. Hamoniaux, J.-P. Rousseau, J.-P. Chambaret, F. Augé-Rochereau, G. Chériaux, J. Etchepare, N. Minkovski, and S. M. Saltiel. 10^{-10} temporal contrast for femtosecond ultraintense lasers by cross-polarized wave generation. *Opt. Lett.*, 30(8):920–922, 2005.

[2] T. Oksenhendler, D. Kaplan, P. Tournois, G.M. Greetham, and F. Estable. Intracavity acousto-optic programmable gain control for ultra-wide-band regenerative amplifiers. *Applied Physics B: Lasers and Optics*, 83(4):491–494, June 2006.

Chapter 5

Implementation of an XPW filter at the LOASIS laser system

5.1 Introduction

In the third and fourth chapter of this manuscript the nonlinear process of XPW generation has been introduced theoretically and experimentally. In the present chapter all the results and conclusions that have been reached so far are used for the practical implementation of an XPW contrast filter to improve the temporal contrast of the Lasers, Optical, Accelerator Systems Integrated Studies (LOASIS) laser facility at the Lawrence Berkeley National Laboratory (LBNL) in Berkeley (Ca, USA). This work was done in collaboration with O. Albert who spent one year as a visiting scientist in the LOASIS group lead by Dr. Wim Leemans. My collaboration with LOASIS was part of my Ph.D grant (Bourse Monge, Ecole Polytechnique). This grant involves spending 6 weeks as a visiting scientist in a foreign laboratory.

5.2 Influence of the temporal contrast on electron acceleration

In chapter 2 I explained the importance of a high temporal contrast for avoiding pre-ionization of matter, in particular for high order harmonic generation on solid target. Solid targets are also used for proton acceleration and a high temporal contrast of the pulses is needed for efficient acceleration with thin targets [4]. The temporal quality of the pulses is also important in the interaction of a high intensity pulse with a gas jet as is the case for electron acceleration [8, 5]. Laser-based wakefield electron accelerators recently become the subject of vigorous investigation in many laboratories, mostly because of their potential as compact sources of high energy electron beams and bright, ultra-short pulse light sources for fundamental studies [1, 3, 7, 2, 6]. It has been revealed that the fine details of the optical properties of the driving laser pulses, such as pulse shape [5] and pre-pulse contrast [8], have significant effects on the properties and usability of the generated electron beams. In particular, the forward-running part of a high

intensity, ultrashort laser pulse, (pre-pulse or ASE pedestal) could start ionizing (or at least start modifying the index of refraction) the interaction medium in a plasma accelerator and eventually disturb the plasma wake generation process.

As presented in section 2.2.2, pulses with a temporal (ns) contrast of 6-7 order of magnitude with possible pre-pulses are typical in most CPA laser systems. Therefore, in order to improve the stability of laser plasma accelerators, there is a strong need to improve the contrast of the driver laser pulses. The solution selected for improving the contrast of the LOASIS laser facility is the implementation of an XPW contrast filter in a double CPA configuration.

5.3 Implementation of the XPW filter at the LOASIS laser system

The first implementation of an XPW filter in a double CPA configuration was realized at the Laboratoire d'Optique Appliquée. The XPW filter was designed to filter 1 mJ pulses in a double crystal configuration (two [100] BaF_2 crystals of 2 mm, first crystal in the focus), with an expected output energy of several hundreds of μJ. These filtered pulses are then stretched and amplified in several multi-pass amplifiers up to the joule level. The schematic of this filter is shown in Fig. 5.1. The practical realization of this filter has demonstrated several limitations in daily operation. First, the distance between the two crystals to avoid white-light generation or damaging in the second crystal was underestimated. Therefore, to keep the distance between the crystals acceptable for the vacuum chamber, the input energy is limited to 300 μJ with an output of just some tens of μJ. The distance between the crystals for filtering 1 mJ at 30 fs with the current input beam size is 1 meter. Second the size of the vacuum chamber (all the system is under vacuum) and the weight of the cover make the system not easy for daily alignment. Starting with these considerations it was decided, for the implementation in the LOASIS laser, to limit the input energy to 300 μJ and to work in air. Working in air is favorable in this case due to the relatively long duration of the pulses (45 fs) injected into the filter. A single double-passed [101]-cut BaF_2 crystal located in the focus is used for maximizing the efficiency and to make the system more robust to variations of the input intensity.
The LOASIS laser before the upgrade is presented in Fig. 5.2 top. The inclusion of the XPW pre-pulse filter required the installation of 4 new building blocks into the existing CPA laser chain (Fig. 5.2 bottom):

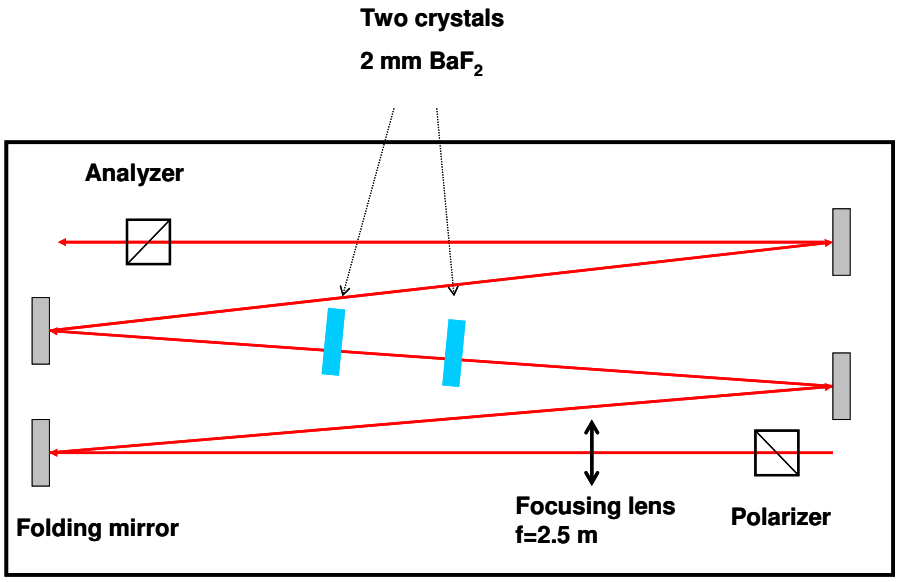

Figure 5.1: Schematic of the XPW filter installed at LOA (salle jaune) for the contrast enhancement in a double CPA configuration

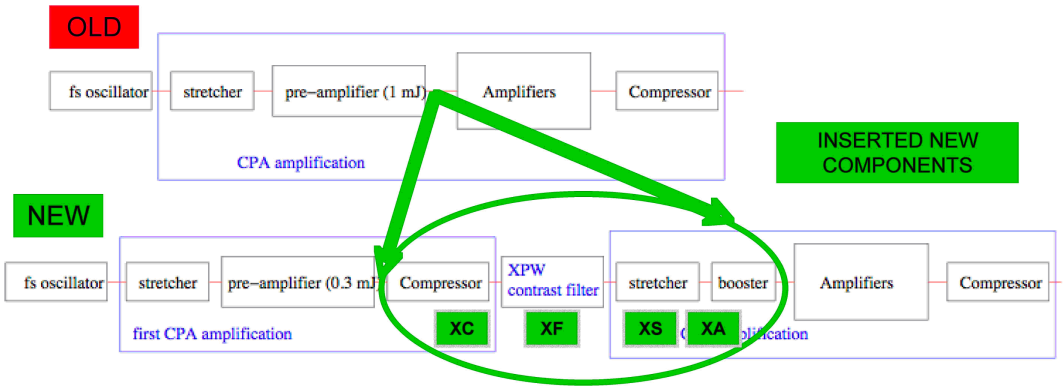

Figure 5.2: Front end of the LOASIS CPA system with the new components (see text for details)

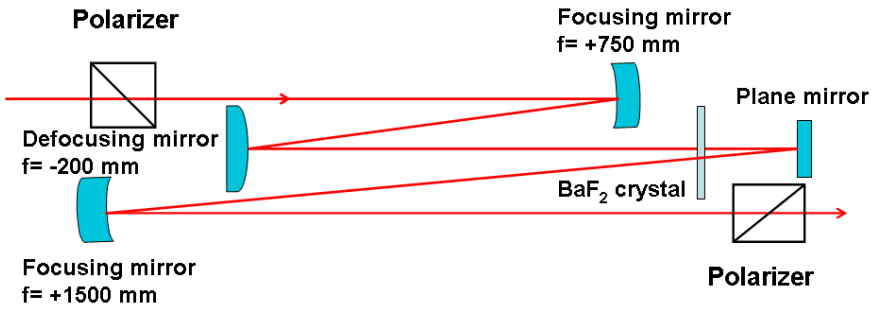

Figure 5.3: Schematic of the XPW filter implemented at the LOASIS laser facility. It comprises of the two, high extinction ratio (10^5) crossed polarizers, three curved optics forming a 4 m focal length focusing telescope in order to appropriately match the beam size in the BaF_2 nonlinear crystal, and a folding mirror to provide double path in the nonlinear crystal and also helping to maintain a compact foot-print (1.5 x 0.2 m2) for the whole setup. All components are situated in air

- XC: XPW compressor. For the correct functioning of the filter the normally stretched pulse (220 ps) needs to be compressed. A compressor part of a commercial (Newport/Spectra Physics) Stretcher/Compressor system with 1500 line/mm groove density and with a matched angle of incidence to the LOASIS CPA system was used.

- XF: The XPW filter itself (Fig. 5.3). It consists of two, high extinction ratio (10^5), calcite crossed polarizers, two curved optics forming a 4 m focal length focusing telescope in order to appropriately match the beam size in the BaF_2 nonlinear crystal (located in the focus), and a folding mirror to provide double passing of the nonlinear crystal and also help maintain a compact foot-print (1.5 x 0.2 m^2) for the whole setup. After the second pass in the crystal the beam is collimated with a f=+1500 mm focusing mirror

- XS: XPW stretcher. The filtered pulse has to be stretched again back to 220-250 ps to be ready for further amplification in the CPA chain. Here we used the stretcher part of a commercial (Newport/Spectra Physics) Stretcher/Compressor system with 1100 line/mm groove density and matched angle of incidence to the LOASIS CPA system.

- XA: XPW amplifier. This is a multipass booster amplifier, that makes up the losses in the previous three components, and brings back up the energy of the pulses from 30 μJ to 1 mJ, the same energy level, as before the insertion of the XPW filter system. In order to preserve the achieved contrast enhancement in the XF and to avoid ASE build-up

during the amplification process, the pump fluence in the Ti:Sa amplifier crystal is kept below 1.4 J/cm^2 and the number of passes was also kept low. A balanced 4-pass system was designed using the Frantz-Nodvik laser amplifier model. A flashlamp pumped and intracavity doubled, 10 Hz, 300 mW average power Nd:YAG laser ('ULTRA' from Big Sky Lasers) was used as the pumping source. The actual pump fluence was controlled by an external polarizer/waveplate setup.

The cleaned pulses are re-amplified to 40 mJ, then split to seed three independent amplifiers forming a multiple second CPA. The beam energy of the first power amplifier reaches 1 J, while the second amplifier's output (0.9 J) is split again to provide independently compressed beams for multi-beam plasma channel experiments. The third, cryo-cooled power amplifier produces 3.8 J/pulse at 10 Hz repetition rate, and propagates in vacuum tubes to the radiation shielded experimental area for final compression (35 fs). This beam is used in a capillary discharge plasma target area

The summary of the energy and spectral parameters of the laser beam measured after the installation of the XPW filter are:

- input/output energy to/from XPW filter (XF): 250-300 μJ/ 30-70 μJ.

- input/output optical spectrum FWHM at XPW filter: 46 nm/53 nm (Fig. 5.5a).

The contrast enhancement factor, at different time regions before the arrival of the main pulse, was measured using a commercial third-order cross-correlator device ('Sequoia' from Amplitude Technologies, Inc.). The first measurement (Fig. 5.4) was performed inside the laser chain after the booster amplifier (energy 1 mJ). To make this measurement possible the stretched beam (220 ps) is roughly compressed in a gratings compressor. The second measurement (Fig. 5.5b) was performed at the output of the 100 TW system. In the first measurement an increase in incoherent contrast by at least 3 orders of magnitude is visible. This is less than the extinction ratio of the crossed polarizers. We believe that this is due to a stress induced linear birefringence in the BaF_2 crystal. From the correlation trace the coherent pedestal due to the imperfect compression is also clearly visible. The coherent contrast is cleaned just after XPW and this residual spectral phase is due to the rough compression. This coherent contrast can be reduced by an accurate compression and by measuring accurately the spectral phase at the end of the laser chain and, with a feedback loop, compensate it with a pulse shaper. This issue will be addressed in section 6.3. At the output of the laser chain (Fig. 5.5b) the contrast enhancement is from 10^{-6} to 10^{-9} for the pedestal region, and from 10^{-4} to 10^{-8} for the prepulses at -5 ps time delay. The decrease in incoherent contrast compared to the measurement inside the laser system is due to the further amplification to the joule level.

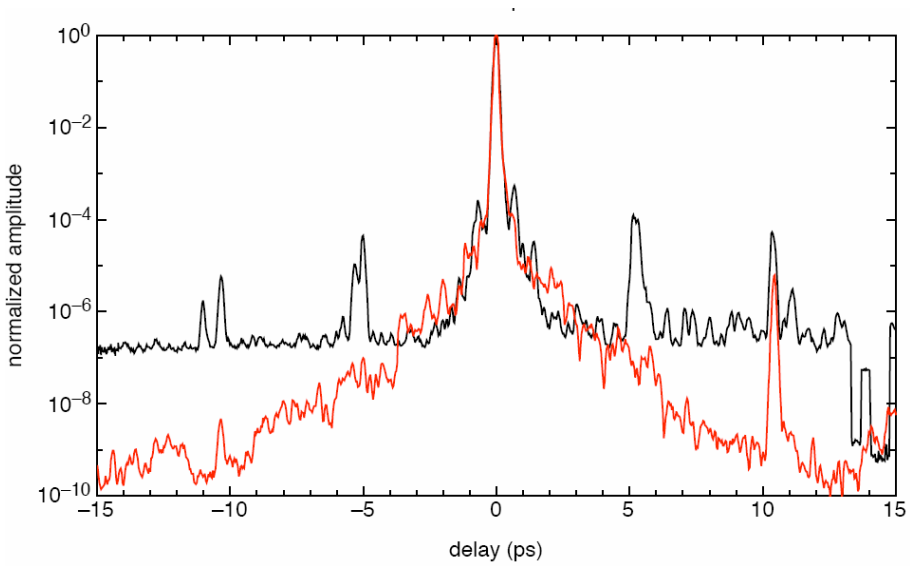

Figure 5.4: Sequoia measurement just after the XA amplifier and a rough recompression

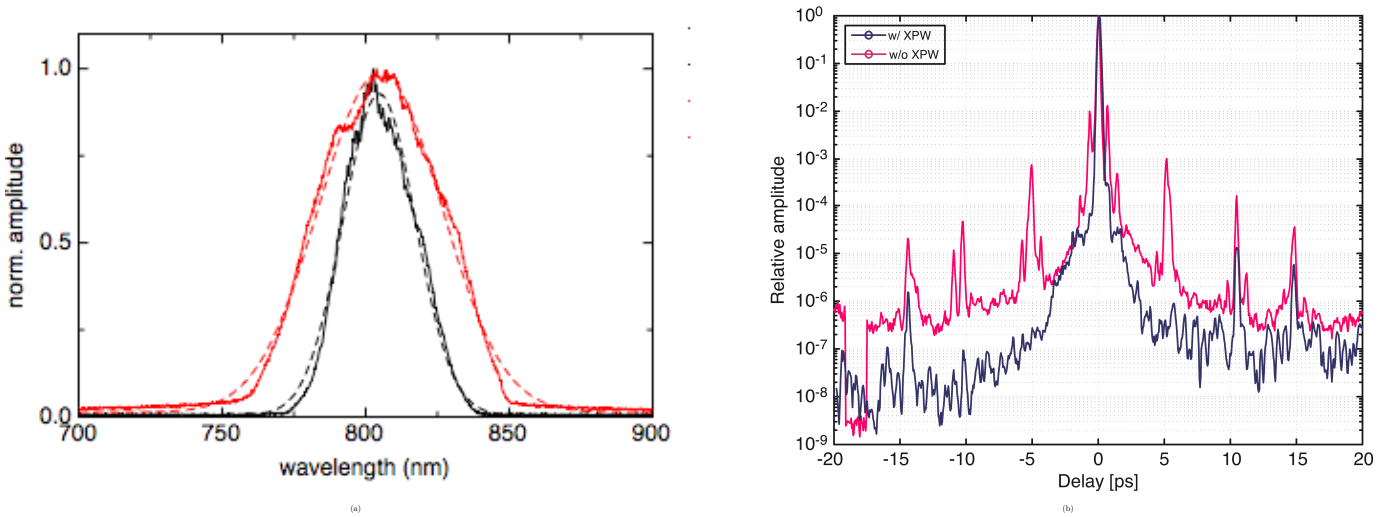

Figure 5.5: (a): Optical spectrum measured by an Ocean Optics 4000 USB spectrometer. The narrow, black curve is the input, and the broader, red curve represents the output of the XPW filter. Dashed lines are Gaussian fits to determine FWHM values. (b): Sequoia measurement data. The upper, red curve is the input, and the lower, blue curve represents the output of the XPW filter.

5.4 Improvements after the installation of the XPW filter

After the installation of the XPW filter, significant improvements of various characteristics of the laser beam along the amplifier chain and that of the generated electron and secondary radiation beams have been observed. Here I present two particular examples:

- enhanced yield and more stable THz emission from gas jet e-beam/THz experiments performed at the 10 TW laser beam line

- improved pointing and amplitude stability of the main 100 TW laser ('TRex') beam line used to generate GeV electron beams in capillary guided laser plasma accelerator experiments

5.4.1 Improvements of THz emission

As one of the potential future applications of laser wakefield accelerators, LWFAs, and also as a useful diagnostic tool for the accelerated electron bunches of these same LWFAs, the LOASIS group has extensively studied the intense THz emission phenomenon observed at the exit boundary of the plasma region in a typical gas-jet style LWFA experiment [9]. The laser pulses interacting with the plasma create accelerated electrons, which upon exiting the plasma emit THz pulses via transition radiation. Because these electron bunches are ultrashort (<50 fs), they can radiate coherently (coherent transition radiation - CTR) over a wide bandwidth (1 - 10 THz) yielding high intensity THz pulses [9]. In addition to providing a non-invasive bunch-length diagnostic and thus feedback for the LWFA, these high peak power THz pulses are suitable for high field (MV/cm) pump-probe experiments. In order to further understand the physical processes taking place in the interaction region, stable laser and electron beams are necessary for detailed parameter-scan experiments. For example, a typical, widely used scan is the "compressor scan", in which the grating separation of the last compressor is changed to tune the temporal duration of the compressed pulses. Fig. 5.6 shows an example of this scan where the total electron bunch charge is measured as a function of the grating separation. The two curves correspond to before (red) and after (blue) the installation of the XPW filter. An increase (4 times) of the total electron bunch charge is visible after the installation of the filter. Furthermore, the relative fluctuation of the charge (represented by the error bars) has also improved, resulting in dramatic improvements in the THz signal amplitude stability. The shot-to-shot variation, which were at the 100 % level prior to XPW implementation, decreased to the 10 % level. Similar improvements were observed for the gamma and neutron yields, constantly monitored during the experiments for radiation protection purposes.

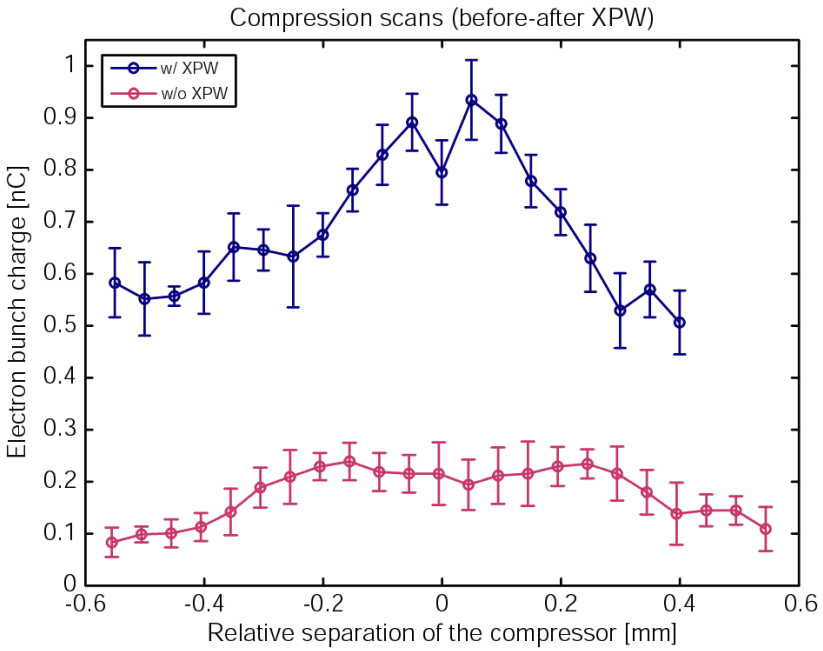

Figure 5.6: Comparison of total emitted bunch charge in a LWFA experimental compressor scan before (lower, red curve) and after (upper, blue curve) the installation of the XPW prepulse filter

5.4.2 Laser beam stability improvements

Since the XPW filtering process effectively improves both the spatial mode profile and spectral stability one can expect an overall improvement of the statistical parameters of the CPA laser. The amplitude and pointing stability variations of the laser beam have been recorded in the TRex (nominal 100 TW) laser beam line. A 3% RMS. energy variation was measured in a set of 200 shots at 1.5 J average energy on target in each pulse, and 2.5 μrad RMS pointing stability in a f = 2 m focusing geometry with 25 μm focal spot (Fig. 5.7). (Previous values were 5% energy stability and 10 μrad r.m.s pointing stability.) These improvements are crucial for production of stable GeV electron in capillary discharges.

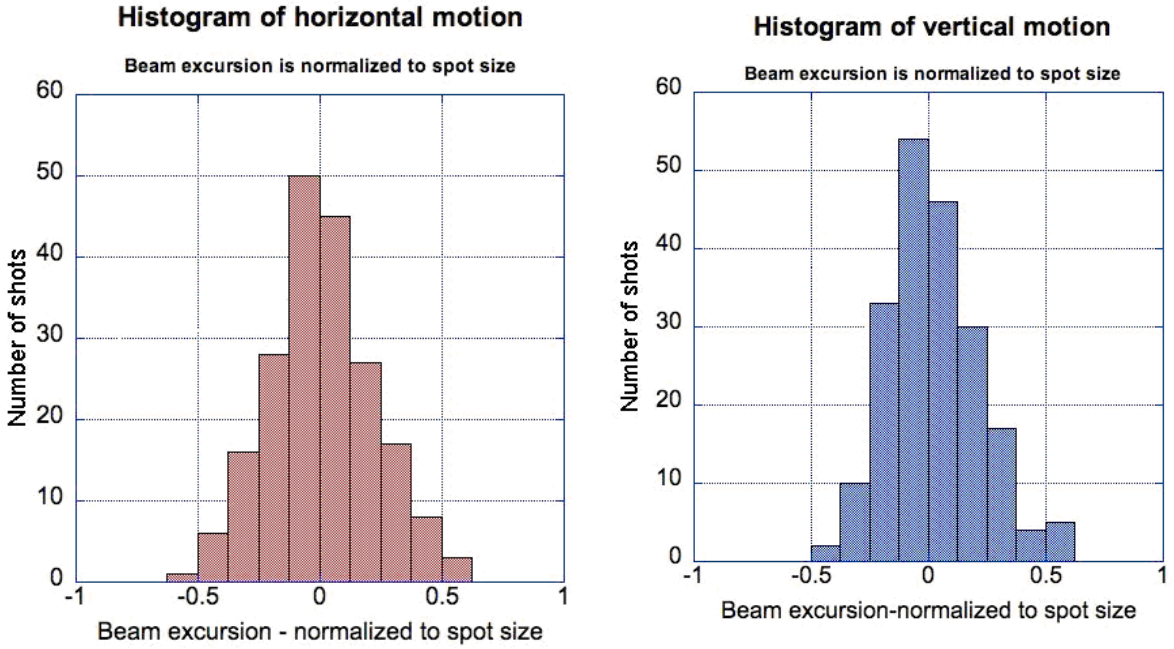

Figure 5.7: Horizontal (a) and vertical(b) pointing stability of the 100 TW beam line after installation of the XPW filter

Bibliography

[1] J. Faure, Y. Glinec, A. Pukhov, S. Kiselev, S. Gordienko, E. Lefebvre, J.-P. Rousseau, F. Burgy, and V. Malka. A laser-plasma accelerator producing monoenergetic electron beams. *Nature*, 431(7008):541–544, September 2004.

[2] J. Faure, C. Rechatin, A. Norlin, A. Lifschitz, Y. Glinec, and V. Malka. Controlled injection and acceleration of electrons in plasma wakefields by colliding laser pulses. *Nature*, 444(7120):737–739, December 2006.

[3] C. G. R. Geddes, Cs. Toth, J. van Tilborg, E. Esarey, C. B. Schroeder, D. Bruhwiler, C. Nieter, J. Cary, and W. P. Leemans. High-quality electron beams from a laser wakefield accelerator using plasma-channel guiding. *Nature*, 431(7008):538–541, September 2004.

[4] M. Kaluza, J. Schreiber, M. I. K. Santala, G. D. Tsakiris, K. Eidmann, J. Meyer-ter Vehn, and K. J. Witte. Influence of the laser prepulse on proton acceleration in thin-foil experiments. *Phys. Rev. Lett.*, 93(4):045003–, July 2004.

[5] W. P. Leemans, P. Catravas, E. Esarey, C. G. R. Geddes, C. Toth, R. Trines, C. B. Schroeder, B. A. Shadwick, J. van Tilborg, and J. Faure. Electron-yield enhancement

in a laser-wakefield accelerator driven by asymmetric laser pulses. *Phys. Rev. Lett.*, 89(17):174802, Oct 2002.

[6] W. P. Leemans, B. Nagler, A. J. Gonsalves, Cs. Toth, K. Nakamura, C. G. R. Geddes, E. Esarey, C. B. Schroeder, and S. M. Hooker. Gev electron beams from a centimetre-scale accelerator. *Nat Phys*, 2(10):696–699, October 2006.

[7] S. P. D. Mangles, C. D. Murphy, Z. Najmudin, A. G. R. Thomas, J. L. Collier, A. E. Dangor, E. J. Divall, P. S. Foster, J. G. Gallacher, C. J. Hooker, D. A. Jaroszynski, A. J. Langley, W. B. Mori, P. A. Norreys, F. S. Tsung, R. Viskup, B. R. Walton, and K. Krushelnick. Monoenergetic beams of relativistic electrons from intense laser-plasma interactions. *Nature*, 431(7008):535–538, September 2004.

[8] S P D Mangles, A G R Thomas, M C Kaluza, O Lundh, F Lindau, A Persson, Z Najmudin, C-G Wahlstrom, C D Murphy, C Kamperidis, K L Lancaster, E Divall, and K Krushelnick. Effect of laser contrast ratio on electron beam stability in laser wakefield acceleration experiments. *Plasma Physics and Controlled Fusion*, 48(12B):B83–B90, 2006.

[9] J. van Tilborg, C. B. Schroeder, C. V. Filip, Cs. Toth, C. G. R. Geddes, G. Fubiani, R. Huber, R. A. Kaindl, E. Esarey, and W. P. Leemans. Temporal characterization of femtosecond laser-plasma-accelerated electron bunches using terahertz radiation. *Physical Review Letters*, 96(1):014801, 2006.

Chapter 6

Development of 1 kHz, few-cycle, mJ level CEP stabilized laser source

6.1 Introduction

In this chapter I present the development of a laser system (Salle Noire) delivering CEP stabilized, 1 mJ, few-cycle pulses at 1 kHz repetition rate. In order to generate such pulses, a multi-mJ, CEP-stable front-end laser system, providing relatively short pulse duration (sub-30 fs), is necessary due to the current limitations of post-compression techniques used to get into the few-cycle regime (section 6.11). The high energy few-cycle pulses can then be used to drive attosecond pulse generation on solid target. At the beginning of my Ph.D there were no commercially available systems having the required characteristics. In particular the CEP stabilization was guaranteed for pulses with an energy lower than 1 mJ. Achieving a long term stabilization of the CEP at the multi-mJ level imposes various constraints on the design of laser system. Furthermore we wanted to build a laser source with a simple and robust architecture for daily operation.
The chosen configuration was:

- a broadband oscillator, CEP stabilized
- a stretcher composed of a block of glass and an AOPDF
- a first commercial mJ amplifier
- a second home-made amplifier for boosting the energy up to several mJ
- a hybrid compressor (prisms + chirped mirrors) or (transmission gratings + chirped mirrors)
- a hollow fiber for the compression down to the few-cycle regime
- a commercial device for stabilizing CEP at the kHz repetition rate.

We decided not to build the oscillator and the first amplification stage. The purchased front-end is a Femtopower Compact Pro CEP (Femtolasers GmbH) commercial system. This system delivers 1 kHz, CEP stabilized pulses with a temporal duration < 30 fs and a compressed energy of 1 mJ. The CEP is stabilized with a commercial stabilizing device (Menlo-system GmbH). We modified the system to accommodate an AOPDF pulse shaper between passes 4 and 5 to control dynamically the spectral phase of the system. The output of this first amplifier is injected into a home made three-pass amplifier boosting the energy up to the multi-mJ level. A single pump laser is used for pumping both amplification stages. The pulses are finally compressed in a hybrid compressor. The first configuration we tested was a combination of a prism compressor and chirped mirrors. Although pulses as short as 22 fs with an energy of 4 mJ was obtained with this configuration, we observed a substantial degradation of the spatial profile after compression due to inhomogeneities in the prisms. Furthermore CEP measurement of the output pulses has underlined the impossibility in achieving CEP stabilization in this configuration. For these reasons we tested a second hybrid compression scheme using a transmission gratings compressor and chirped mirrors. In this configuration we obtain daily 25 fs, 2.2 mJ, CEP stabilized pulses.

6.2 22 fs, 4 mJ 1 kHz source

I will now review more specifically the main components of the laser source starting with the configuration using the prism compressor and chirped mirrors.

6.2.1 CEP stabilized oscillator

The oscillator is a Kerr lens mode locking Rainbow CEP type (femtolasers GmbH) [1]. It delivers pulses with an energy of 2.5 nJ at a repetition of 80 MHz. The schematic of the cavity is presented in Fig. 6.1. The spectrum emitted by the oscillator is shown in Fig. 6.2. The FWHM is 220 nm corresponding to a transform limited duration of 6.8 fs. A nonlinear interferometer is implemented after the oscillator for the stabilization of the CEP with a fast loop. The pulses are focused with a concave mirror in a PPLN (Periodically Poled Lithium Niobate) crystal. The intensity in the crystal is high enough to broaden the spectrum by SPM and to generate intra-pulse difference frequency generation (DFG) between the high frequency and low frequency part of the spectrum [2]. Interference between lower frequencies of the fundamental spectrum and the difference frequency signal yields a beating at the frequency f_{ceo}. This signal is directed with a dichroic mirror to a frequency meter and a feedback electronic loop for the stabilization of the CEP (section 2.2.1). When the feedback loop is activated the electronic part of the stabilizing system controls an acousto-optic modulator that modulates the pump power of the oscillator. The resulting variation in intensity of the pulse inside the cavity forces f_{ceo} to be equal to $f_{rep}/4$. Forcing the two signals to oscillate in phase gives $\Delta\varphi_0 = 2\pi/4$, so that every 4 pulses exiting the cavity have identical CEP φ_0. For the correct operation of the system the frequency f_{ceo} must be detected with a signal to noise ratio (SNR) higher than 30 dB.

The oscillator pulses then go through an optical isolator and are stretched in a 20 cm block of glass (SF7).

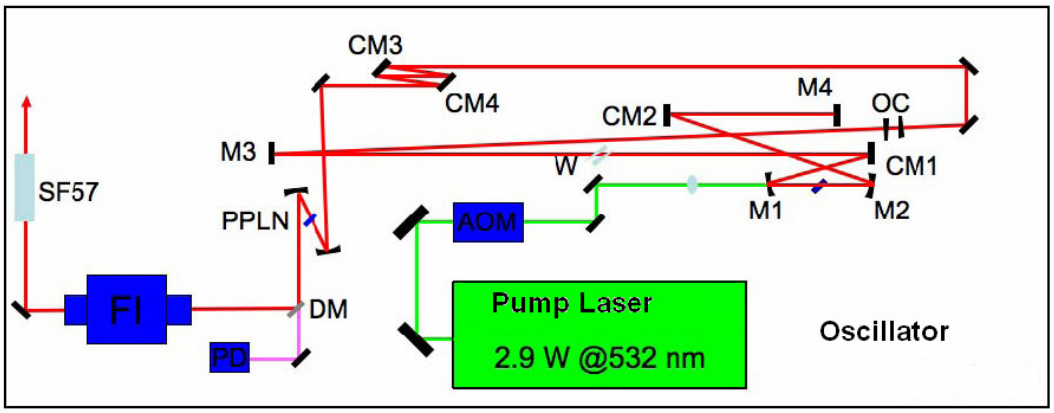

Figure 6.1: Schematic of the Rainbow CEP (Femtolasers GmbH). M1-M2 sub-cavity mirrors. CM1-CM2 chirped mirrors for the compensation of the intra-cavity GVD.

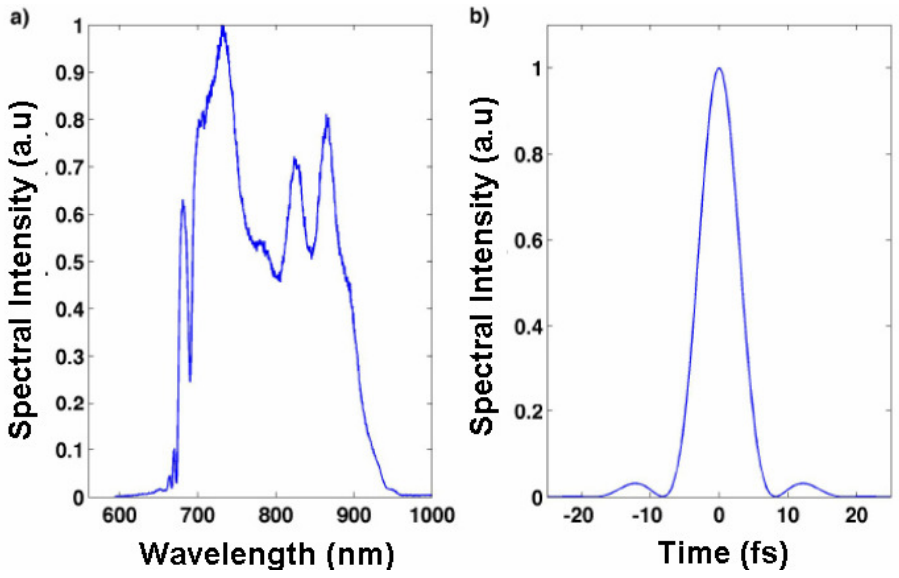

Figure 6.2: (a) Output spectrum of the oscillator (FWHM 220 nm), (b) corresponding Fourier transform temporal profile (temporal duration 6.8 fs).

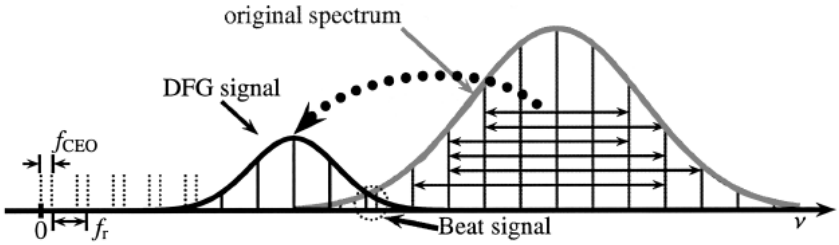

Figure 6.3: Schematic of the principle for the generation of the beat signal at the frequency f_{CEO} with a device using the difference frequency generation in a PPLN crystal. The pulse is focused in the crystal. new spectral components are generated by SPM. In this crystal there is a nonlinear process of difference frequency generation (DFG) between the high frequency and low frequency part of the spectrum [2]. Interference between low frequency of the fundamental spectrum and the DF signal yields a beating at the frequency f_{ceo}

6.2.2 Multi-pass amplifier

The commercial multi-pass amplifier (10 passes) delivers pulses with an energy of 2 mJ at 1 kHz (Fig. 6.4). The pump laser is a Nd:YLF (PI, Photonics Industries) delivering 1 kHz, 50 mJ (50 W) pulses at 527 nm. Only 11 W are used for pumping this amplification stage. In the first 8 passes the energy goes from few nJ to 400 μJ. After the fourth pass the beam goes through the AOPDF (HR800) and a Pockels cell for the selection of a train of pulses at 1 kHz. These pulses are further amplified to an energy of 2 mJ. The ASE level estimated by blocking the injection in the amplifier is around 40 μJ. The choice of the location of the AOPDF in the amplifier is original. We chose this configuration because, due to the gain narrowing in the first 4 passes, the spectral bandwidth injected into the the AOPDF is reduced compared to the case where it is placed after the oscillator. As a consequence, the diffraction efficiency of the AOPDF is higher, and thus the pulses can be amplified to the mJ level in the following passes while maintaining a good temporal contrast (10^8 at the output of the Femtopower).

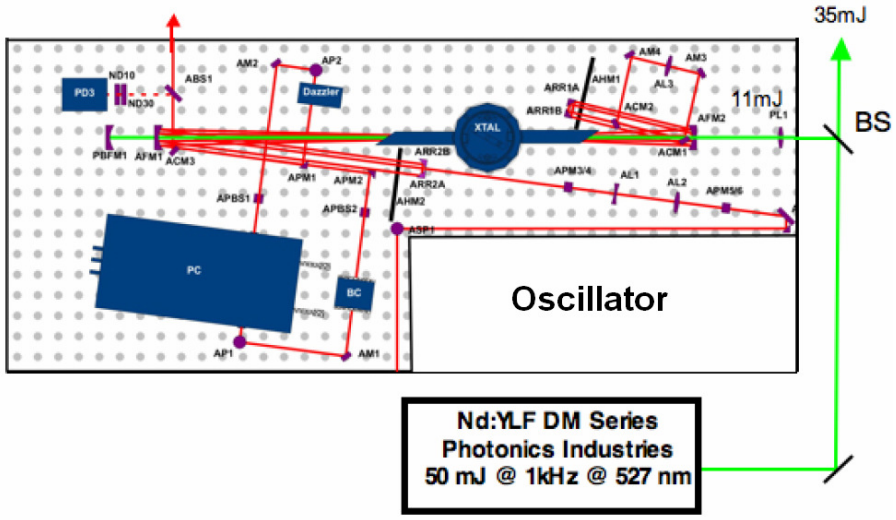

Figure 6.4: Schematic of the commercial amplification system. It is a ten-pass amplifier with an output pulse energy of 2 mJ at 1 kHz repetition rate(uncompressed). The crystal is pumped with 11 W (at 527 nm) and cooled at 193 K with a cryostat (XTAL). The Dazzler and the pockels cell are placed after the fourth pass.

6.2.3 AOPDF (Dazzler)

During all my Ph.D I used several times the AOPDF [3] for the pulse shaping and characterization. I give here a brief introduction of this device. It is constituted of a TeO_2 crystal which is optically and acoustically birefringent. An acoustic wave is launched by a transducer excited by an electronic signal. The acoustic wave propagates with a velocity V along the z axis and hence reproduces spatially the temporal shape of the rf signal. Two optical polarization modes can be coupled efficiently by the acousto-optic interaction only when some phase matching condition is achieved. If there is locally only one spatial frequency in the acoustic grating, then only one optical frequency can be diffracted at a position along z. The incident optical short pulse is initially in mode 1. Every frequency ω travels a certain distance before it encounters a phase-matched spatial frequency of the acoustic wave. At this position z(ω), part of the energy is diffracted into mode 2. The pulse leaving the device in mode 2 will be made up of all the spectral components that have been diffracted at various positions z(ω). Since the velocities of the modes are different, each frequency will experience a different time delay. The amplitude of the output pulse, or diffraction efficiency, is controlled by the acoustic power at position z(ω). The optical output $E_{out}(t)$ of the AOPDF is a function of the optical input $E_{in}(t)$ and of the electric signal H(t). More precisely, it has been shown to be proportional to the convolution of the optical input and the scaled electric field:

$$E_{out}(t) \propto E_{in}(t) \otimes H(t/\alpha) \tag{6.1}$$

where the scaling factor, $\alpha = \Delta n(V/c)$, is the ratio of the speed of sound to the speed of light times the index difference between the ordinary and extraordinary polarizations. α is the ratio of the acoustic frequency. Relation (6.1) can be written in the frequency domain as:

$$\tilde{E}_{out}(\omega) \propto \tilde{E}_{in}(\omega) H(\alpha\omega) \tag{6.2}$$

In this formulation H(t/α) appears as the impulse response of a filter applied to the input optical pulse. By generating a proper function S(t) one can achieve any arbitrary convolution with a temporal resolution given by the inverse of the available filter bandwidth.

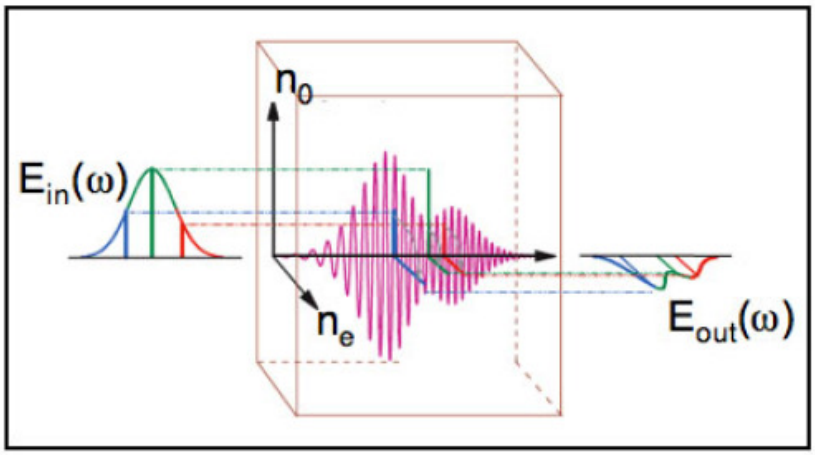

Figure 6.5: Schematic representation of the Acousto-Optic Dispersive Programmable Filter

6.2.4 Home made amplifier

The second amplifier is a home made three-pass amplifier. A schematic of this amplifier is shown in Fig. 6.6. The Ti:Sa crystal, cut at Brewster angle, is under vacuum and cooled at 195 K. The pump beam is down collimated by a (3:1) telescope and is then focused with a lens (L2) on the crystal. The power of the pump is 25 W. The absorbtion of the crystal is 75 % and the transmitted beam is refocused with a concave mirror (M1). The injection beam passes through an optical isolator to avoid any return into the first amplifier. A mirror telescope and a focusing lens (L1) are used to achieve the correct beam size on the crystal. After each pass the beam is re-imaged using concave dielectric mirrors (M2-M3) in order to have for each pass the correct beam size on the crystal. The diameter at $1/e^2$ in intensity of the infrared beam is roughly 1 mm for each pass. The geometrical focus for each pass is located before the crystal to have a slightly divergent beam to compensate the thermal lens in the crystal. The beam focus is inside the vacuum chamber to avoid any nonlinear effects in air. The output energy is 6 mJ. The total gain of the amplifier is 7.5.

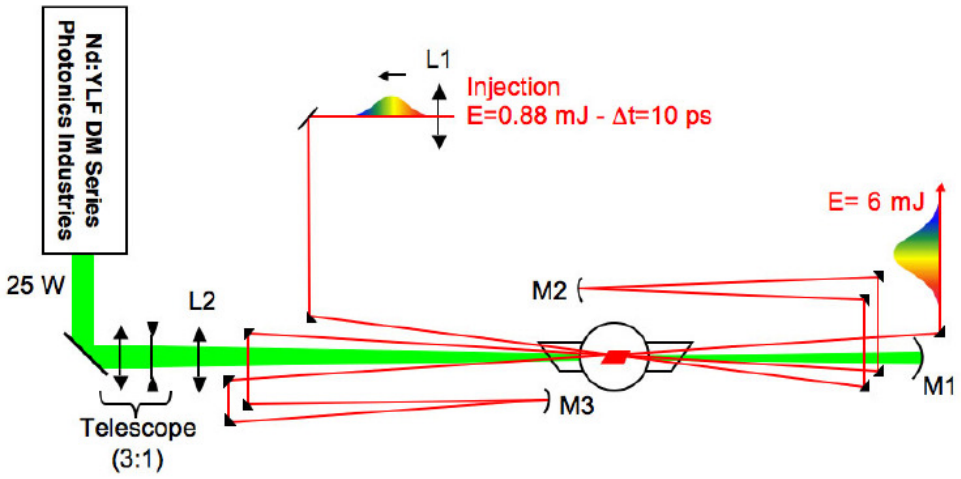

Figure 6.6: Schematic of the home made amplifier. L1:converging lens f=1500 mm. L2:converging lens f=700 mm. M1: dielectric mirror treated for 527 nm

The number of passes in this amplifier is limited to three due to the high B integral value (1.35 rad). This value needs to be added to the 3.5 radians already accumulated in the first amplifier. A total B integral higher than 4 radians is typically considered too high for the correct functioning of a CPA laser. As shown in the next section, the DazScope technique enables to measure and pre-compensate this nonlinear phase and therefore to achieve near perfectly compressed pulses. The high B integral of this chain originates from the small pulse stretching (10 ps). This choice is motivated by the fact that a small stretching factor enables the use of prism or very compact gratings compressors with increased insensitivity to dispersion fluctuations. This is of fundamental importance for achieving a good CEP stability.

6.2.5 Hybrid compressor: prism + chirped mirrors

The calculations for the design of the prism compressor were made by A. Trisorio from the PCO group. The values of dispersion added by this compressor are shown in Tab.1 together with the overall dispersion of the laser system Tab.2. The picture of the prisms and a schematic of the prism compressor are shown in Fig. 6.9 and Fig. 6.10

Incidence angle	d	λ_0	$\Delta\lambda$	$\varphi^2(\omega)$ fs^2	$\varphi^3(\omega)$ fs^3	$\varphi^4(\omega)$ f4
55.6°	30 mm	800 nm	750-850 nm	-64090	-95760	-262710

Figure 6.7: Parameter and dispersion introduced by the prisms

Optical elements	$\varphi^2(\omega)$ (fs^2)	$\varphi^3(\omega)$ (fs^3)	$\varphi^4(\omega)$ (fs^4)
Stretcher (20 cm of glass type SF57)	44206	31000	6730
Faraday isolator	5291	2693	-12
Pockels cell + Polarizers	2473	1478	810
Ti: saphir crystal (10*8 mm)	4853	3360	-1245
Dazzler (crystal dispersion of 45 mm)	22320	14580	8955
Dazzler (dispersion added by the acoustic-wave)	-17000	30000	200000
Calcite Polarizers type CVI CPAS (3*19.4 mm)	2270	1222	-58
Faraday rotator	3854	1895	352
silica lenses	782	552	-211
Ti: saphir crystal (10*8 mm))	1441	1008	-373
TOTAL	**70490**	**91064**	**214954**

Figure 6.8: Dispersion introduced by the different elements of the laser chain. This dispersion corresponds to 10 ps stretched pulses

Figure 6.9: Picture of the prisms used in the hybrid compressor.

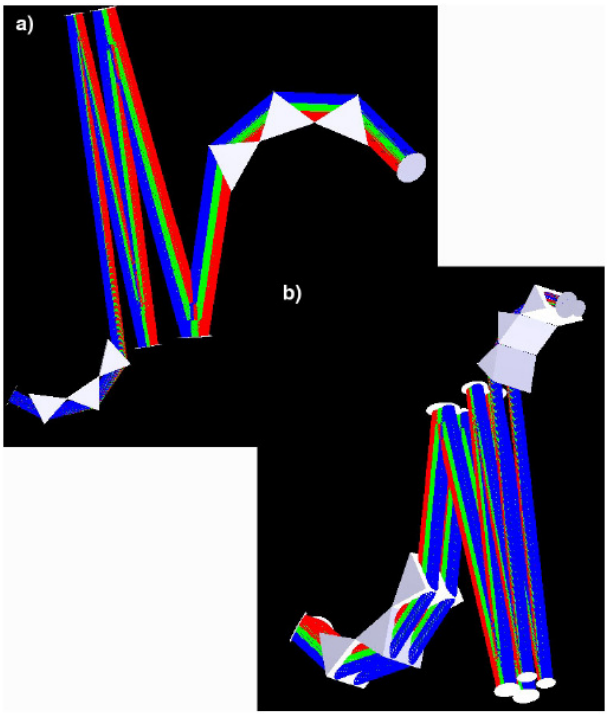

Figure 6.10: 3 D modeling of the prism compressor with Zeemax.

To limit SPM in the last prism, the temporal compression is ended by 32 reflections on two negatively dispersive chirped mirrors (Fig. 6.11). The characteristics of these chirped mirrors are:

- reflectivity higher than 99.5 % for a spectral range between 760 and 840 nm
- a damage threshold of 400 mJ/cm^2

- a second order dispersion of -200 fs^2 per bound with an angle of incidence of 15°

The pulse duration after the prism compressor is roughly 1 ps and is reduced to 22 fs after the 32 reflections (The total dispersion introduced by the chirped mirrors is -6400 fs^2).

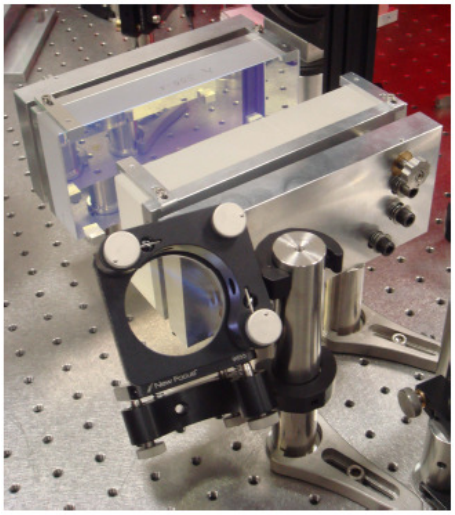

Figure 6.11: Photos of the chirped mirrors used in the hybrid compressor. The pulses are reflected 32 times on the mirrors to end the compression

The temporal duration has been optimized using a closed feedback loop (Dazscope), that is presented in the next section, and measured with a home made SPIDER. The compressed pulse energy is 4 mJ with an efficiency of the compressor of 67 %. The temporal contrast has also been measured in order to access the temporal quality of the pulses. This is shown in Fig. 6.12. The contrast is $5 * 10^5$ at a delay of 3 ps and $3 * 10^7$ for a delay of 15 ps. The ASE level is 10^7 at 40 ps. With a fast photodiode and a digital oscilloscope we measured the energy stability of the output pulses. The standard deviation of the energy fluctuations is 2.6 % over 10 minutes. This is due to the fact that the second amplifier is not saturated.
To test the quality of the beam we measured with a CMOS camera the far field spatial profile (f=1.5 m) at different z positions on either sides of the beam waist. From this measurement the M^2 factor can be calculated. In particular we obtain $M_x^2 = 1.9$ for the x axis and $M_y^2 = 2$ for the y axis. The spatial quality is not excellent and this is due to the relatively high B integral of our laser and to degradation of the spatial profile in the prism compressor. This is not too problematic because the spatial profile is cleaned with the propagation in the hollow-core fiber. Pre-compensation of nonlinear spectral phase with the pulse shaper and spatial cleaning in the hollow fiber enable us to avoid the main problems of a high B integral.

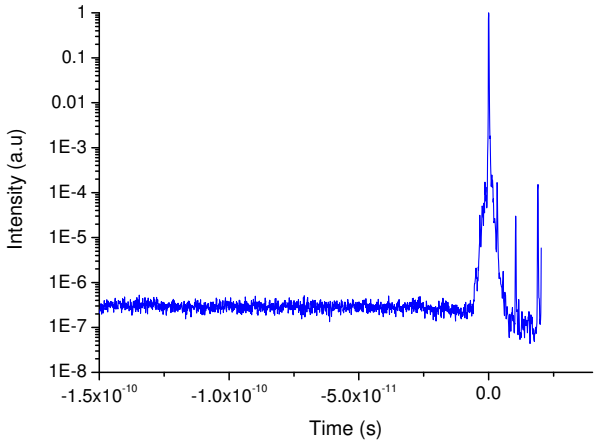

Figure 6.12: High dynamic range third order correlation (Sequoia, Amplitude Technologies) measurement of the pulses compressed in the hybrid compressor (prisms+chirped mirrors).The contrast is $5 * 10^5$ for a delay of 3 ps and $5 * 10^7$ for a delay of 15 ps.

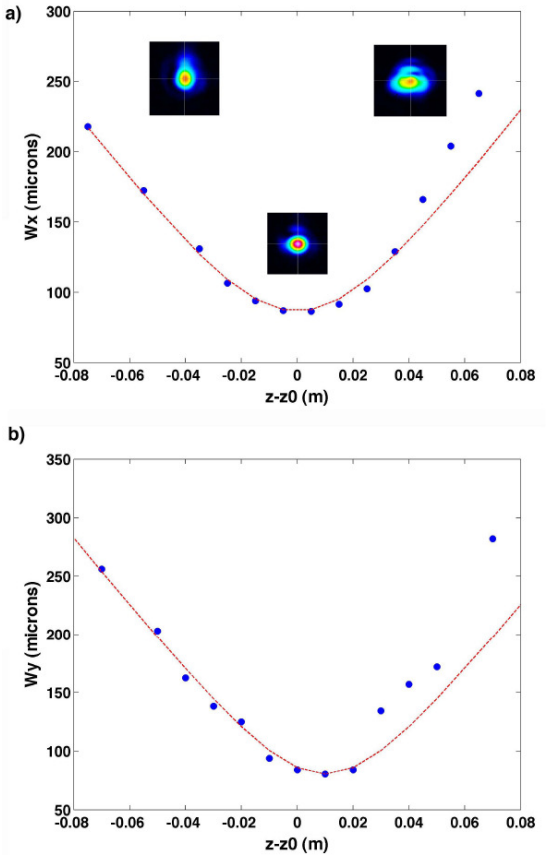

Figure 6.13: Measurement of the intensity profile focused with a f=1.5 m concave mirror for different position before and after the waist. (a) Radius at $1/e^2$, W_x in intensity measured along the x axis and fitting curve from the formula. (b) Radius at $1/e^2$, W_y in intensity measured along the y axis and fitting curve from the formula.

Bibliography

[1] T. Fuji, A. Unterhuber, V.S. Yakovlev, G. Tempea, A. Stingl, F. Krausz, and W. Drexler. Generation of smooth, ultra-broadband spectra directly from a prism-less ti:sapphire laser. *Applied Physics B: Lasers and Optics*, 77(1):125–128, August 2003.

[2] T. Fuji, A. Apolonski, and F. Krausz. Self-stabilization of carrier-envelope offset phase by use of difference-frequency generation. *Opt. Lett.*, 29(6):632–634, 2004.

[3] F. Verluise, V. Laude, Z. Cheng, Ch. Spielmann, and P. Tournois. Amplitude and phase control of ultrashort pulses by use of an acousto-optic programmable dispersive filter: pulse compression and shaping. *Opt. Lett.*, 25(8):575–577, 2000.

6.3 DazScope

6.3.1 Introduction

In this chapter I present the local spectral compression technique for the closed-loop optimization of the temporal duration, commercialized under the name DazScope™. I developed this technique in collaboration with FASTLITE. The starting point of this development was the study of the effect of the spectral phase on the XPW generation presented in section 4.6. From the results presented in this section there is a clear correlation between the shape of the XPW spectrum and the spectral phase of the input pulse. In particular, I have shown how the combination of second and third order spectral phase shifts the barycenter of the spectrum generated by the nonlinear process. This is even more evident using second harmonic generation (SHG) as the nonlinear effect. Fig. 6.14 shows for example the evolution of the SH spectrum function of $\varphi^{(2)}$ (x axis $\pm 2500 fs^2$) for different fixed values of $\varphi^{(3)}$ ($\pm 35000 fs^3$). The first figure on the left of the first line (figure 1) corresponds to $\varphi^{(3)} = -35000 fs^3$. The second figure of this line (figure 2) corresponds to $\varphi^{(3)} = -30625 fs^3$. The last figure on the right of the last line (figure 16) corresponds to $\varphi^{(3)} = 35000 fs^3$. From the different scans it is easy to see that the third order spectral phase passes through $\varphi^{(3)} = 0$ between picture 8 and 9 (respectively last figure of the second line and first figure of the third line) where the barycenter function of $\varphi^{(2)}$ changes the sign of the slope. For a single scan there is an absolute maximum of the SHG energy when $\varphi^{(2)} = 0$. Starting with this consideration it is important to see if, looking at the spectrum generated in the nonlinear process for different values of an added $\varphi^{(2)}$, enables the extraction of the spectral phase of the input pulses. This is demonstrated theoretically in the next section. The experimental results are then presented.

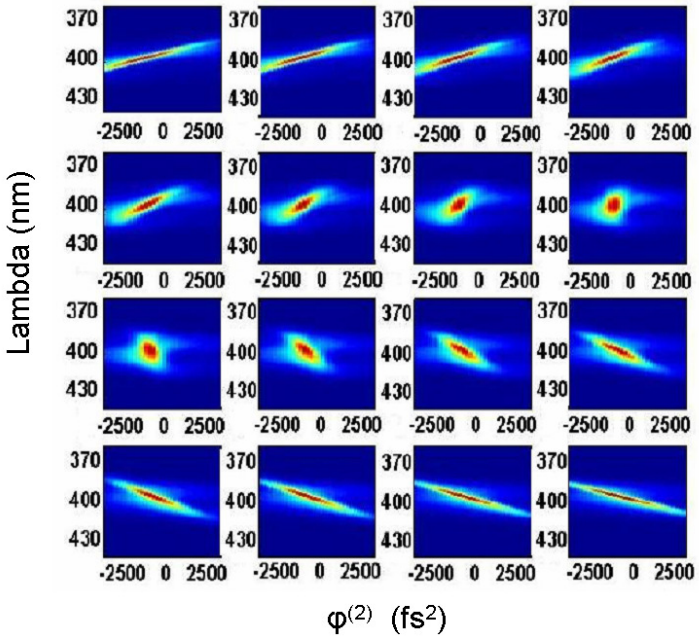

Figure 6.14: Evolution of the SH spectrum (y axis 370 nm<λ<430 nm) function of $\varphi^{(2)}$ (x axis $\pm 2500 fs^2$) for different fixed values of $\varphi^{(3)}$ ($\pm 35000 fs^3$). This graph needs to be read following the lines from the top two the bottom (like a text). The first figure on the left of the first line (figure 1) corresponds to $\varphi^{(3)} = -35000 fs^3$. The second figure of this line (figure 2) corresponds to $\varphi^{(3)} = -30625 fs^3$. Between each figure there is a fixed increment of the third order spectral phase $\varphi^{(3)} = +4375 fs^3$. The last figure on the right of the last line (figure 16) corresponds to $\varphi^{(3)} = 35000 fs^3$.

6.3.2 Theoretical introduction

The starting point of this analysis is the equation:

$$I_B(\omega) \propto \frac{I_A(\omega)^3}{|\phi''(\omega)|^2} \tag{6.3}$$

that has been derived for XPW generation using the stationary phase approximation. This formula, valid for sufficiently chirped pulses ($|\phi''(\omega)| > 1/\Delta\omega^2$, $\Delta\omega$ spectral bandwidth), states that the intensity of the spectrum of the cross-polarized wave $I_B(\omega)$ can be linked to the intensity of the spectrum of the fundamental pulse $I(\omega)$ and its spectral phase second order derivative $\phi''(\omega)$. The corresponding expression for second harmonic generation is:

$$I_{SHG}(2\omega) \propto \frac{I^2(\omega)}{|\phi''(\omega)|} \tag{6.4}$$

The validity of (6.4) can be confirmed by recording the SHG spectrum of a near Fourier-transform limited pulse to which a purely parabolic phase $\varphi^{(2)}(\omega - \omega_0)^2/2$ is added. In this case, the asymptotic expression of the SHG spectrum is a hyperbolic function of the second order phase $\varphi^{(2)}$ since the expected SHG spectrum is, according to (6.4):

$$I_{SHG}(2\omega) \propto \frac{I^2(\omega)}{\varphi^{(2)}} \tag{6.5}$$

Fig. 6.15 shows some typical experimental SHG signal recorded, at a given pulsation, as a function of the second order phase. A Lorentzian fit confirms the validity of (6.4), hyperbolic at large chirps.
When a set of purely linear chirps, $\varphi^{(2)}$, is added to the the spectral phase, $\varphi(\omega)$, of an input pulse, the total spectral phase becomes $\phi(\omega) = \varphi(\omega) + \varphi^{(2)}(\omega - \omega_0)^2/2$ and equation (6.4) predicts, for a given frequency, symmetric and hyperbolic decays of the SHG intensity with large positive and large negative $\varphi^{(2)}$ values, these decays being symmetric with respect to $\varphi''(\omega)$. The algorithm consists in finding the optimal hyperbolic fit at large chirps and returning, for every frequency, the value of $\varphi''(\omega)$ (the local chirp). The pulse spectral phase is then retrieved by a double integration.

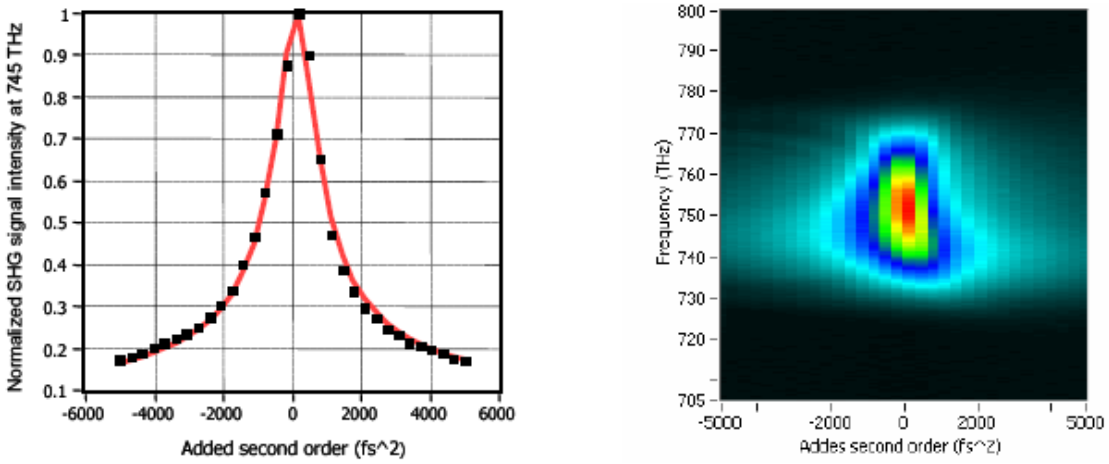

Figure 6.15: Left:typical Lorentzian fit (solid line) to the experimental data (dotted line)at a given wavelength. Right: map of the SHG spectra as function of frequency and added second order phase coefficient.

6.3.3 Examples

To illustrate the efficiency and accuracy of this method I have simulated the SHG spectrum obtained for a chirp scan from $-3000fs^2$ to $+3000fs^2$ for four different input pulses:
- Fourier transform (6.16.a),
- pure second order phase of $+1000fs^2$(6.16.*b*),
- pure third order phase of $+50000fs^3$(6.17.a)
- sinusoidal phase (6.17.b).

The pictures also show the fitted value of $\varphi''(\omega)$ (the local chirp) with a white dotted line. In

the case of a pure second order phase, $\varphi''(\omega) = const$; the constant giving the value of the initial chirp. For the purely third order spectral phase pulse, the image corresponds to linear chirp optimization vs wavelength, as the local chirp of a third order is linear. For a more complex phase, the image is distorted but still gives for each wavelength the local chirp.

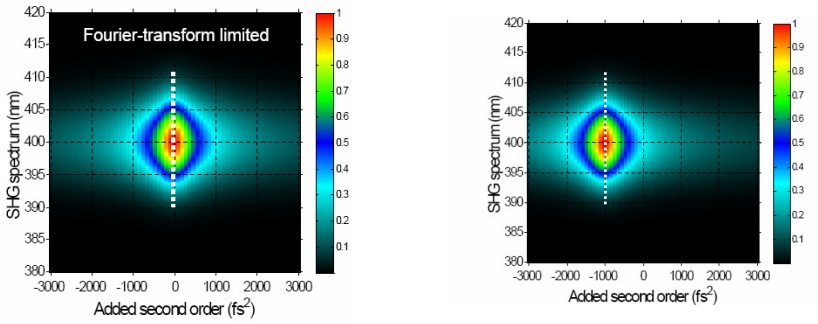

Figure 6.16: SHG spectrum obtained for a chirp scan from $-3000fs^2$ to $+3000fs^2$ for a Fourier transform limited input pulse (a), for an input pulse with a pure Chirp (b)

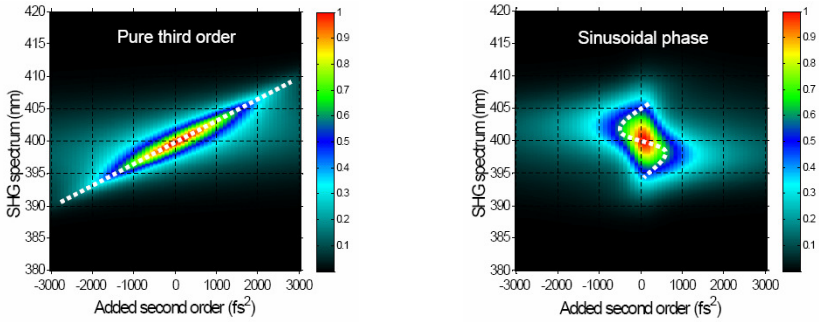

Figure 6.17: SHG spectrum obtained for a chirp scan from $-3000fs^2$ to $+3000fs^2$ for an input pulse with pure third order (a), and for an input pulse with a SPM oscillatory phase (b)

6.3.4 Experimental results

In the previous section it is demonstrated theoretically how the spectral phase can be measured using a $\varphi^{(2)}$ scan. This scan is experimentally done with an AOPDF. This measured phase can then be automatically compensated with the same AOPDF. Therefore, both phase measurement and correction are done in a single AOPDF. This closed-loop optimization has been implemented for the first time in the the "salle noire" laser system. I have previously shown that, due to the small stretching factor, the B integral of this source is quite high (B > 3). I now demonstrate that the AOPDF can be used to measure the spectral phase induced by SPM and then compensate for the measured phase distortion. For the pulse measurement, a small fraction of the output energy (< 1 μJ) is selected with a beam splitter and focused with a f=500 mm focal length lens into a 50 μm type-I BBO crystal. The generated SHG is separated from the fundamental and collected with a commercial spectrometer (AvaSpec-3648 from Avantes). Fig. 6.18a,b and Fig. 6.19c,d show the SHG spectra versus chirp traces together with the extracted local chirp function (white line) for four states: initial state at low energy (Fig. 6.18a),

optimized pulse at low energy (Fig. 6.18b), pulse at high energy with the same phase settings (Fig. 6.19c), optimized pulse at high energy (Fig. 6.19d).

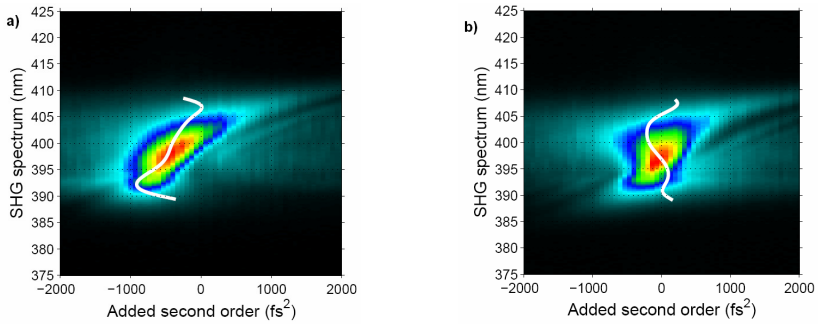

Figure 6.18: Chirp scan of a non compressed pulse (a), Chirp scan after optimization of the polynomial phase (b)

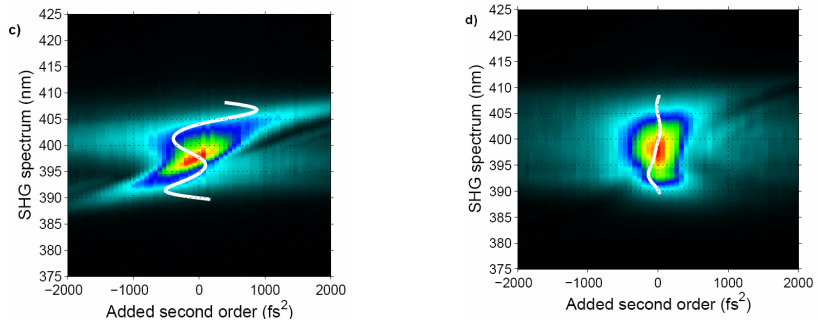

Figure 6.19: Chirp scan under the same conditions then Fig. 6.18b but with increased seed energy into the second amplifier (c), Chirp scan after correction of the nonlinear phase at high energy (d)

Fig. 6.18a shows an input spectral phase mainly dominated by a residual second and third order spectral phase resulting from imperfect optimization of the compressor. This phase is automatically compensated after a polynomial fit to the third order. The resulting trace after this compensation is shown in Fig. 6.18b. From this measurement it is visible that the remaining phase is oscillatory and can not be fitted with a low order polynomial. Fig. 6.19c clearly indicates that, changing the seeding of the second amplifier from 600 to 900 μJ, dramatically changes the spectral phase of the amplified pulses, in particular increasing the amplitude of the oscillations of the local chirp. Due to the small stretching of our pulse (10 ps) the B-integral of our laser system is estimated to be about 4-5 rad for the high energy seed. When a pulse is sufficiently chirped as in a CPA stretcher, the temporal profile corresponds to the spectral profile and so the nonlinear phase corresponds to the the spectral shape: $\varphi_{nl} \propto n_2 I(t) \propto n_2 I(\omega)$ (where $I(\omega)$ is typically a Gaussian). When we compensate the polynomial spectral phase of the stretcher/compressor pair the residual phase comes from nonlinear effects in the amplification crystal and the local chirp is then the second order derivative of a Gaussian function. This correspond to the oscillatory trace measured in Fig. 6.18b, Fig. 6.19c. In particular at high energy there is a large oscillation of period 50nm (12.5nm on the SHG

spectrum) with amplitude of about $\pm 900 fs^2$. As predicted theoretically in [1], this phase can be pre-compensated numerically with the pulse shaper. Naturally this assumes that the non linear phase is small compared to the stretching factor and this is still valid in our case. Fig. 6.19d shows experimentally the effect of the pre-compensation. The residual phase measured after optimization is less than 0.5 rad which corresponds to the typical measurement precision of SPIDER[3] or FROG[4] devices. The pulse temporal duration, measured with an home made SPIDER, is shown in Fig. 6.20.

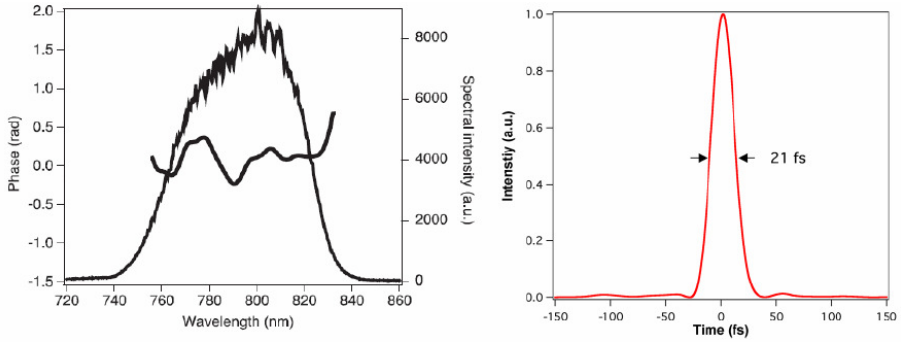

Figure 6.20: Temporal measurement and spectrum and phase after DazScope optimization.

6.3.5 Discussion

Compared to standard pulse measurement technique like FROG or SPIDER, the DazScope technique is a phase-only method and strictly speaking, is not a pulse measurement technique. For example a double structure pulse will not be measured. As a phase-only technique it can be compared to the Multiphoton Intrapulse Interference Phase Scan (MIIPS) [2, 5, 6, 7]. The DazScope technique is really adapted for the characterization and optimization of the output pulses of a CPA laser where an AOPDF is present. In these cases it has several advantages: the traces are very visual and in particular any residual linear chirp translates to a relative shift to the zero added second order phase. There is no ambiguity on the sign of this chirp. This technique is also very sensitive to the high order terms of the spectral phase. We have seen previously how it has been used for measuring and pre-compensating the non linear phase induced by SPM during amplification. We have also discussed in the introduction how the residual spectral phase affects the temporal quality of pulses at the output of a CPA laser and is responsible for the coherent (ps) contrast. Finally the measuring setup is extremely simple consisting of just a BBO crystal and the spectrometer. It can be placed as close as possible to the experiment even inside the interaction chamber.

Bibliography

[1] A. Braun, S. Kane, and T. Norris. Compensation of self-phase modulation in chirped-pulse amplification laser systems. *Opt. Lett.*, 22(9):615–617, 1997.

[2] Y. Coello, V. V. Lozovoy, T. C. Gunaratne, B. Xu, I. Borukhovich, C. Tseng, T. Weinacht, and M. Dantus. Interference without an interferometer: a different approach to measuring, compressing, and shaping ultrashort laser pulses. *J. Opt. Soc. Am. B*, 25(6):A140–A150, 2008.

[3] C. Iaconis and I.A. Walmsley. Spectral phase interferometry for direct electric-field reconstruction of ultrashort optical pulses. *Opt. Lett.*, 23(10):792–794, 1998.

[4] B. Kohler, V. V. Yakovlev, K. R. Wilson, J. Squier, K. W. DeLong, and R. Trebino. Phase and intensity characterization of femtosecond pulses from a chirped-pulse amplifier by frequency-resolved optical gating. *Opt. Lett.*, 20(5):483–485, 1995.

[5] V. V. Lozovoy, B. Xu, Y. Coello, and M. Dantus. Direct measurement of spectral phase for ultrashort laser pulses. *Opt. Express*, 16(2):592–597, 2008.

[6] I. Pastirk, Bojan Resan, Alan Fry, John MacKay, and M. Dantus. No loss spectral phase correction and arbitrary phase shaping of regeneratively amplified femtosecond pulses using miips. *Opt. Express*, 14(20):9537–9543, 2006.

[7] I. Pastirk, X. Zhu, R. M. Martin, and M. Dantus. Remote characterization and dispersioncompensation of amplified shaped femtosecondpulses using miips. *Opt. Express*, 14(19):8885–8889, 2006.

6.4 CEP

Up to now I have demonstrated the generation of 4 mJ, 21 fs pulses at 1 kHz. I have also presented how the pulses at the output of the oscillator are CEP stabilized. This is not enough for having CEP stable pulses at the output of the laser. All the optical elements after the oscillator introduce some phase fluctuations $\Delta\varphi_0$. The fluctuations in the multi-pass amplifier are caused by variations of the non linear index of the crystal. These variations are induced by fluctuations in the intensity of the pulses due to the fluctuations of the pump intensity. The CEP fluctuations in the strecther/compressor originate from dispersion fluctuations caused for example by a variations of beam pointing or beam path. The CEP noise thus originates from the oscillator, laser amplifiers and the compressor. In particular the main contribution comes from the oscillator. In the oscillator the repetition rate is 80 MHz compared to the kHz of the amplified pulses. There is therefore an accumulation of the variations of $\Delta\varphi_0$ over a period of 1 ms. In conclusion, to build a CEP stabilized system, it is necessary to have:

- a device for fixing the value $\Delta\varphi_0$. This is realized using two wedges inside the oscillator cavity. These wedges can be finely moved.
- a first feedback loop after the oscillator for actively stabilizing $\Delta\varphi_0$.
- a second feedback loop just at the end of the laser chain.

Although the measurement of $\Delta\varphi_0$ for the both loops is based on nonlinear interferometry, they are different because the first uses MHz low energy pulses from the oscillator and the second uses the amplified high energy, kHz pulses. The first loop is called fast loop and the second is called slow loop. In the commercial Menlo-system the two feedback loops generate two error signals that are treated to generate a single error signal. The feedback control is based on the modulation of the non linear dispersion of the Ti:Sa crystal of the oscillator. This is tuned by changing the intensity of the pump laser with an acousto-optical modulator. I have already discussed the scheme for measuring $\Delta\varphi_0$ after the oscillator (section 2.2.1). I now present the setup for measuring the slow changes of the CEP. This device is named an f-2f interferometer. The schematic is reported in Fig. 6.21. A beam splitter selects low energy pulses that are focused in a sapphire plate. This step is needed for broadening the spectrum to one octave. They are then focused on a BBO crystal, phase matched for converting the infrared side of the spectrum. The SHG and the fundament signal are cross-polarized and have a certain delay τ_0. These two signals pass then through a polarizer with the transmission axes at 45 degrees compared to the polarization signal of the two beams to make them interfere. The signal measured with the spectrometer presents many spectral fringes (Fig. 6.22). The CEP drift is extracted by the shift of these fringes as a function of time. In particular the spectrometer signal is given by the equation:

$$I(\omega) \propto \left| \int_{-\infty}^{+\infty} [E_F(t+\tau_0) + E_{SH}(t)]\, exp(-i\omega t) dt \right|^2 \tag{6.6}$$

that can be expressed in the form:

$$I(\omega) \propto I_F(\omega) + I_{SH}(\omega) + 2\sqrt{I_F(\omega)I_{SH}(\omega)}cos\left[((\varphi_0 + \Phi_{SH}(\omega) - \Phi_F(\omega) + \omega\tau_0)\right] \tag{6.7}$$

where $I_F(\omega)$ and $I_{SH}(\omega)$, ($\Phi_{SH}(\omega)$ and $\Phi_F(\omega)$) are the respective spectral intensity (spectral phases) of the fundamental and the SH. φ_0 is the input CEP phase. The argument of the cosine is extracted with the Fourier Transform Spectral Interferometry (FTSI) algorithm. As it was presented in the case of a SPIDER measurement this algorithm consists of making a Fourier transform to get into the time domain, to apply a band pass filter around τ_0 and to make another Fourier transform back in the frequency domain. It is then possible to measure the CEP variation between successive pulses. A tension signal proportional to the CEP variation is then sent to the acousto-optic RF driver for the CEP stabilization.

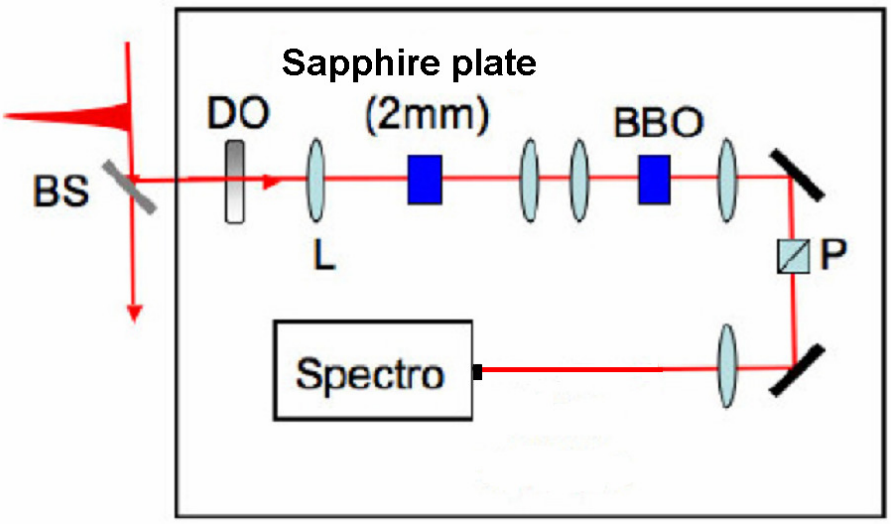

Figure 6.21: f-2f interferometer for measuring the CEP shift of the pulses at the output of the laser chain

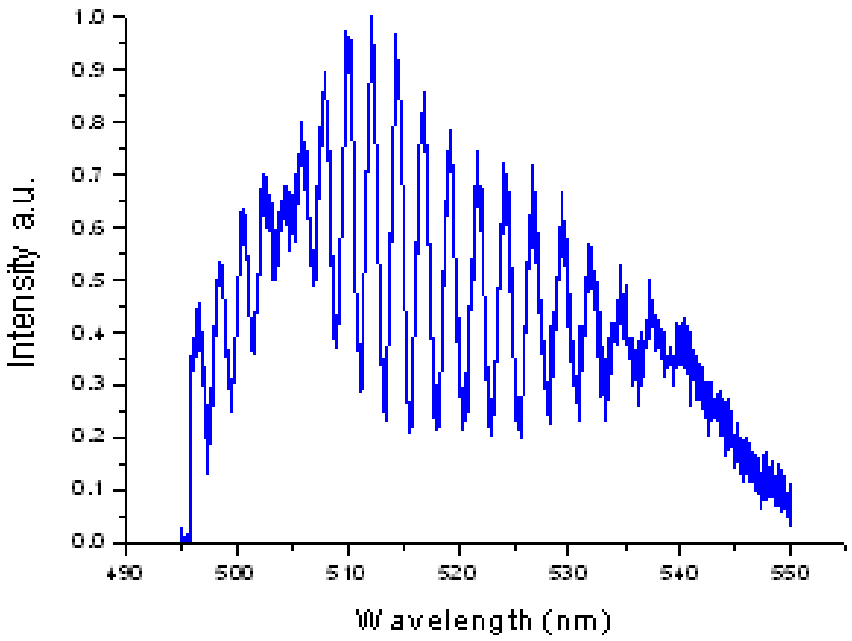

Figure 6.22: Typical spectrum measured after the f-2f interferometer. The CEP drift is extracted by the shift of these fringes as a function of time.

6.5 CEP after prism + chirped mirrors compressor

The commercial Femtopower front-end of the laser system is CEP stabilized. The initial CEP drift with the fast and slow feedback active was measured to be 176 mrad for a time of 30 minutes. The integration time on the spectrometer was 1 ms, 20 consecutive spectra are averaged for CEP measurement. After reducing the jitter of the acoustic wave of the AOPDF in the laser system (see next section) we decreased this noise to 100 mrad for a measurement of several hours Fig. 6.23.

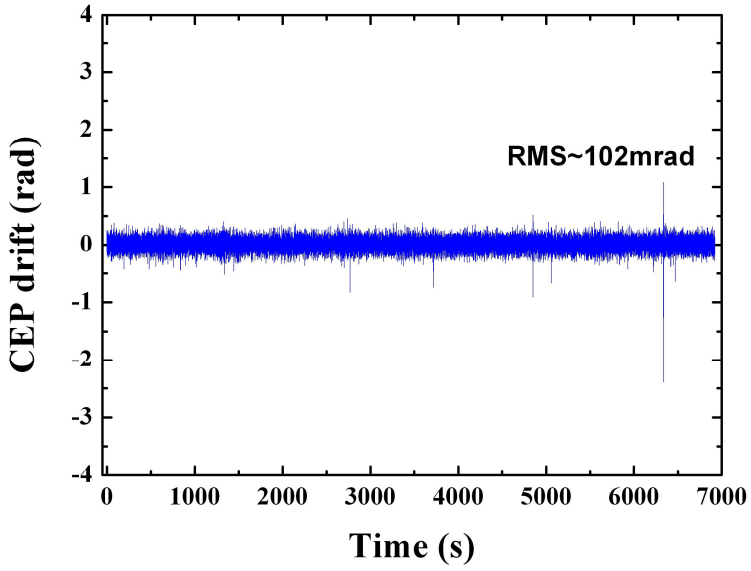

Figure 6.23: Measurement of the CEP drift at the output of the Femtopower. The integration time for each acquisition is 1 ms, 20 consecutive spectra are averaged for CEP measurement.

The same measurement was repeated to characterize the CEP drift between the 4 mJ pulses with the fast loop activated. The measurement trace presented frequent random jumps of the CEP and it was impossible to stabilize the CEP drift with the slow feedback loop. These random variations of the CEP between pulses can not be compensated with the slow feedback loop. We believe that this CEP drift was added by the compressor and in particular by the prisms (the chirped mirrors have been tested separately after the Femtopower without degradation of the CEP). Due to its large dimension (3 meters between the two triplets of prism) the compressor was not sufficiently isolated from the dispersion fluctuation caused by the movement of air between the prism. Probably with a correctly designed cover this problem can be solved. We did not continued in this direction because the propagation in the prisms also strongly degrades the spatial quality of the beam and thus its M^2. We thus tried a second configuration where the amplified pulses are compressed in a hybrid compressor consisting of transmission gratings and chirped mirrors. The good CEP stabilization we obtained in this configuration and its robustness convinced us to adopt this solution.

6.6 Transmission grating + chirped mirror compressor

The laser setup with the transmission gratings + chirped mirrors compressor is shown in Fig. 6.24. The compressor is composed of two 600 lines/mm, fused silica holographic gratings (Wasatch Photonics). Substituting the prisms with the gratings implies some changes in the laser configuration, primarily due to the fact that the stretcher and compressor are not matched anymore. The prism compressor introduces negative third order dispersion ($-95760 fs^3$) and this compensates the positive third order dispersion of the bulk stretcher and the material in the amplifier ($91064 fs^3$). In the case of a grating compressor, the third order dispersion is positive and it is therefore added to the value of the stretcher and the material in the amplifier. Furthermore the value of the third order dispersion is directly proportional to the value of the second order dispersion. We decided to compensate all the third order phase with the Dazzler. This is possible only making a trade-off with the negative chirp introduced by the compressor. With a distance between the gratings of 70 mm for an angle of incidence of 13.9 °, the spectral phase added by the compressor is $\varphi^{(2)} = -50000 fs^2$ and $\varphi^{(3)} = 70000 fs^3$. Again the final compression is then achieved after 32 bounces through the negatively chirped mirrors pair. The pulses are thus initially stretched to 7 ps. Decreasing the pulse stretching compared to the previous configuration limits the output pulse energy to 4 mJ. The spectral phase added by the Dazzler in the two compression configurations is reported in Tab. 6.25. The overall transmission of the compression stage is 53 % (60 % for the gratings compressor). Using grooved gratings instead of holographic gratings this efficiency can be increased to 83 %. Temporal and spectral characterization of the 2.1 mJ output pulses was achieved using an home made SPIDER, Fig. 6.26(a),(b), after a DazScope optimization. The spectrum does not exhibit any significant distortions over 100 nm bandwidth. The measured spectral duration is 25 fs, close to the Fourier transform limit. Furthermore, the proposed compression scheme preserves a good spatial quality. ($M^2 = 1.2$). The Gaussian spatial intensity distribution of the focused beam is represented in Fig. 6.26(c).

A few μJ are split off and sent into the collinear f-2f interferometer APS 800, Menlo System to monitor the relative CEP drift of the amplified pulses. Fig. 6.27(a) represents single shot fringe pattern registered at the output of the interferometer (2000 shots, the integration time of the spectrometer is 1 ms). No feedback loop is activated for this acquisition. The visible and well-contrasted interference figure demonstrates the effective CEP stabilization of the laser pulses. This observation is corroborated by the measurement of the corresponding CEP drift on a short time scale (one minute) (Fig. 6.27(b)). The parameters of the APS are: acquisition time=1 ms, cycle loop time =100 ms, 20 consecutive spectra are averaged for CEP measurement. To evaluate the long term stability, the slow drift introduced by the amplifier is then pre-compensated by a feedback loop to the oscillator locking electronics using the measured CEP. Fig. 6.27(c) shows the typical CE phase stabilization of the system with feedback control. The RMS phase error over tens of minutes is 250 mrad. Furthermore we discovered that part of this noise was added by the jitter of the acoustic-wave of the Dazzler (section 6.9). The added CEP noise is in fact linearly proportional to the acoustic wave jitter. In this first configuration the acoustic

rms jitter was measured to be 180-300 ps with a corresponding added CEP noise of 120-220 mrad. Decreasing the acoustic rms jitter to 70 ps noise reduces the added rms phase noise to less than 50 mrad. In this second configuration the measured RMS phase error is 180 mrad (Fig. 6.28) for a measurement of several (3) hours. Comparing this result to the measurement just after the Femtopower (after the Dazzler upgrading) we see that an additional CEP noise close to 80 mrad is added by the second amplifier and the grating compressor.
Small distance between the gratings reduces the sensitivity to beam pointing and air currents in the compressor. In our case, the reduced groove density of gratings and the lower incident angle decrease CEP fluctuations associated with variations of gratings separation (thermal of mechanical drift). Previous studies have theoretically and experimentally demonstrated that the CEP drift stabilization in gratings-based setup may require interferometric control of the effective gratings separation, which nevertheless this introduce additional experimental complexity. In our configuration we overcome this limitation.

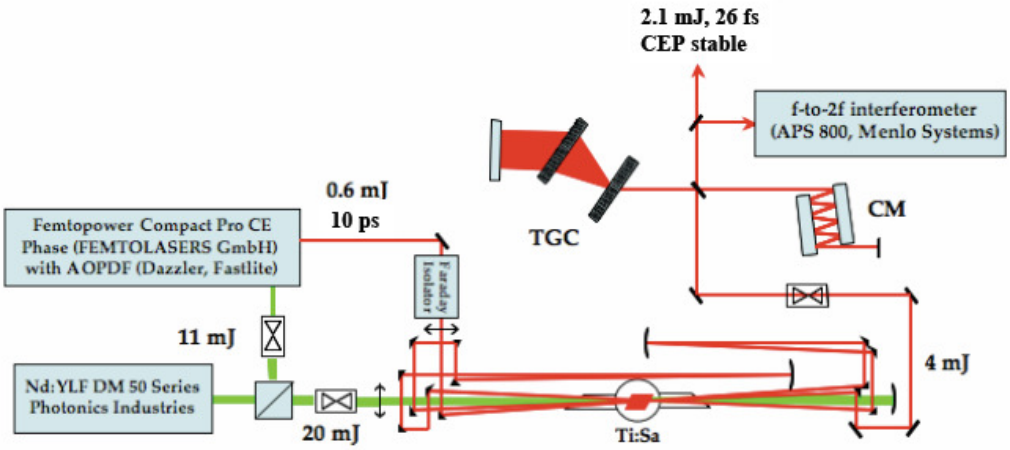

Figure 6.24: Schematic of the 2 mJ, 25 fs, 1 kHz, CEP stable CPA system with transmission gratings and chirped mirror compressor

	Prism compressor +chirped mirrors	Grating compressor + chirped mirrors
$\varphi^{(1)}$ fs	6916	10869
$\varphi^{(2)}$ fs^2	-18464	-30760
$\varphi^{(3)}$ fs^3	25000	-142795
$\varphi^{(4)}$ fs^4	-30000	2280

Figure 6.25: Spectral phase added by the Dazzler for the two compressions schemes

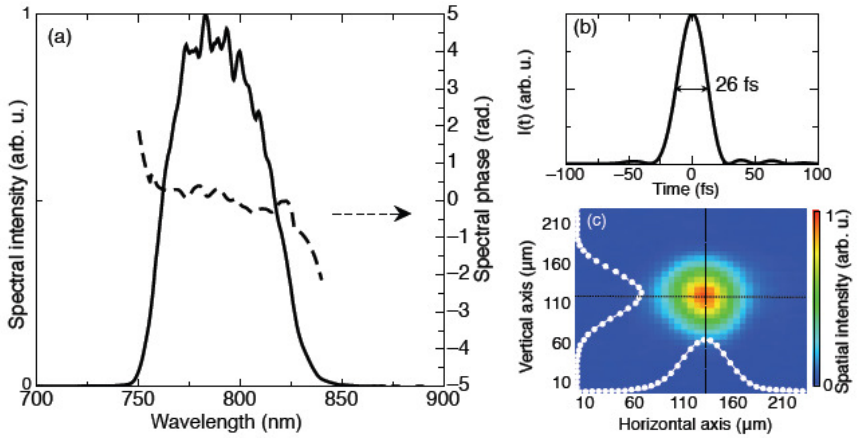

Figure 6.26: Temporal and spatial characterization of the compressed 2.1 mJ pulses. (a) Spectral intensity (solid line) and phase (dashed line) obtained from SPIDER measurement. (b) Temporal intensity profile (SPIDER measurement). (c) Spatial intensity distribution in the far-field (the 7 mm-diameter output beam is focused by a 1 m lens). Vertical and horizontal profiles are fitted by a Gaussian distribution (white lines). The measured value of M^2 factor is about 1.2

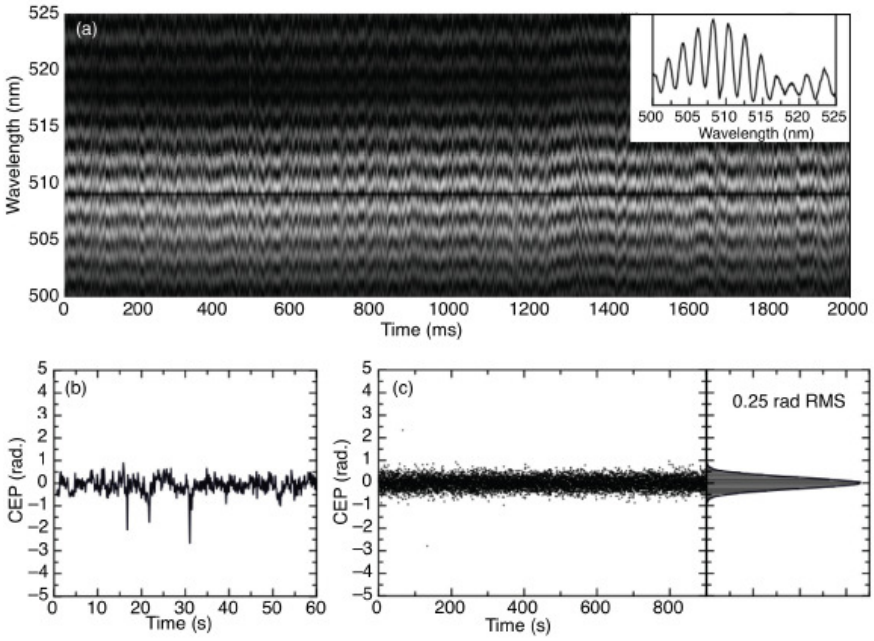

Figure 6.27: CEP stability measurements (spectrometer integration time: 1 ms). (a) Single shot fringe pattern from the collinear f-2f interferometer for 2000 consecutive shots. For illustration one shot is shown in the inset. (b) Measured relative CEP drift of amplified pulses without feedback loop. (c) Measured stabilized CEP drift of amplified pulses with feedback control over 15 minutes (250 mrad RMS). The stabilization of the CEP over an hour has been measured with a RMS error of 290 mrad

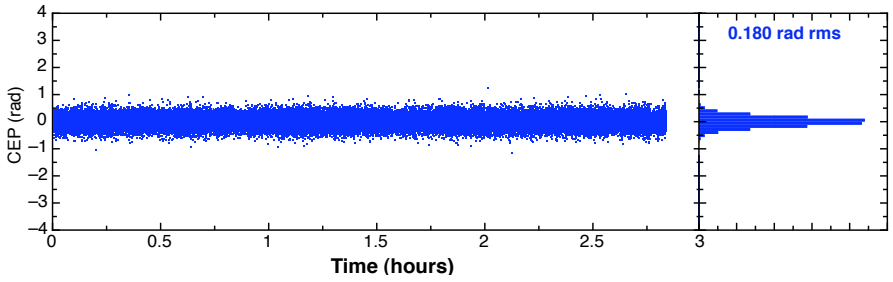

Figure 6.28: Measured stabilized CEP drift of amplified pulses after reduction of the jitter of the acoustic wave of the Dazzler.

6.7 Influence of the B integral on the CEP

The drawback of the small stretching factor of the pulses in the laser system, is the accumulation of a nonlinear phase induced by SPM during amplification. This nonlinear phase is evaluated measuring the B integral of the laser chain. I have shown in section 6.3 how the AOPDF can be used to measure and pre-compensate this spectral phase (DazScope) to avoid its adverse effect on the pulse compression. The B integral is also correlated to the added CEP noise. The intensity fluctuation of the amplified pulse shifts the CEP due to the nonlinear refractive index change. This shift can vary randomly from pulse to pulse and therefore can not be

compensated with an active phase stabilization loop. The refractive index change due to the nonlinear refractive index ($\Delta n = n_2 I$) is $n = n_0 + n_2 I$. The length corresponding to a 2π shift of the CEP is given by:

$$L_{2\pi,nl} = 1/(d\Delta n/d\lambda) = 1/((dn_2/d\lambda)I). \tag{6.8}$$

To make the situation simpler, we assume the intensity I constant over the length L; then the product of the intensity and the length is given by IL=$\lambda\ n_0 B_{tot}/2\pi n_2$. Where B_{tot}, the B integral, is given by expression $B_{tot} = 2\pi/(\lambda n_0)\int_0^L n_2 I dz$. In this case, the CEP shift due to the nonlinear index is given by:

$$\delta\theta_{nl} = 2\pi L/L_{2\pi,nl} = \frac{\lambda n_0}{n_2}\left(\frac{dn_2}{d\lambda}\right) B_{tot}. \tag{6.9}$$

The intensity fluctuation of ΔI results in the fluctuation of the CEP shift of $\Delta\varphi_0 = \delta\theta_{nl}\Delta I$. The list of n_0, n_2, $\frac{dn_2}{d\lambda}$ and $\delta\theta_{nl}$ at $B_{tot} = 1$, and the CEP fluctuation for a 1 % intensity fluctuation, is given in Tab. 6.29. For 1 % intensity fluctuation, the CEP fluctuation is on the order of 10^{-3} rad at $B_{tot} = 1$.

Material	n_0 at 800 nm	n_2 (m^2/W)	$dn_2/d\lambda$ (m/W)	$\delta\theta_{nl}$ (rad)	$\delta\theta_{nl}\Delta I$ (rad)
Fused silica	1.45	3.3×10^{-20}	-0.98×10^{-14}	−0.34	-3.4×10^{-3}
Sapphire (n_e)	1.76	3.0×10^{-20}	-1.03×10^{-14}	−0.48	-4.8×10^{-3}

Figure 6.29: List of the parameters related to the CEP shift due to intensity fluctuations

It is thus interesting to effectively measure the B integral of our chain in order to evaluate its contribution on the total CEP noise.

6.8 Measuring the B integral

The B integral of a laser chain can be measured by injecting the amplifier with two delayed pulses and measuring the output replicas of these pulses with a high dynamic range correlator. To understand how two pulses can generate several replicas after amplification and compression

I first give here a short theoretical introduction.

The most intuitive way to understand this temporal "diffraction" is to consider it as a four-wave mixing (FWM) process [2]. As shown in Fig. 6.30, the delay between pulses is chosen so that the pulses partially overlap after the stretching. At any particular position in the overlapped part of the two pulses the instantaneous optical carrier frequencies are ω_1 and ω_2 ($\omega_1 > \omega_2$). Since the pulses are stretched, the instantaneous carrier frequencies are $\omega_1(\tau) = \omega_0 + b(\tau + t_d/2)$ and $\omega_2(\tau) = \omega_0 + b(\tau - t_d/2)$, where t_d is the relative delay. The frequency difference is then $\delta\omega = \omega_1 - \omega_2 = bt_d$. The third order nonlinear polarization,

$$P_{NL} = \chi^{(3)} \left[\tilde{E}_1(\omega_1) + \tilde{E}_2(\omega_2)\right] \left[\tilde{E}_1^*(-\omega_1) + \tilde{E}_2^*(-\omega_2)\right] \times \left[\tilde{E}_1(\omega_1) + \tilde{E}_2(\omega_2)\right] \tag{6.10}$$

gives FWM, SPM and XPM. In particular, the terms $\tilde{E}_1(\omega_1)\tilde{E}_2^*(-\omega_2)\tilde{E}_1(\omega_1)$ and $\tilde{E}_2(\omega_2)\tilde{E}_1^*(-\omega_1)\tilde{E}_2(\omega_2)$ are the FWM process of interest, giving the new frequencies $2\omega_1 - \omega_2$, and $2\omega_2 - \omega_1$. We see that $2\omega_1 - \omega_2 = \omega_1 + bt_d$, so it is constantly blue shifted from $\omega_1(\tau)$. Likewise, $2\omega_2 - \omega_1 = \omega_2 - bt_d$ is red shifted from $\omega_2(\tau)$. When the chirped pulses are recompressed in the compressor, $\omega_1 + \delta\omega = \omega_1 + bt_d$ is advanced by t_d relative to the ω_1. Because the unshifted frequencies ω_1 collapse to $\tau = 0$ to form the compressed pulse, the blue shifted frequencies will collapse at $\tau = -t_d$ to form the pre-pulse. The same applies to the red shifted post-pulse. The partial overlap causes the bandwidth of the new pulses to be narrower, indeed no time casuality is violated.

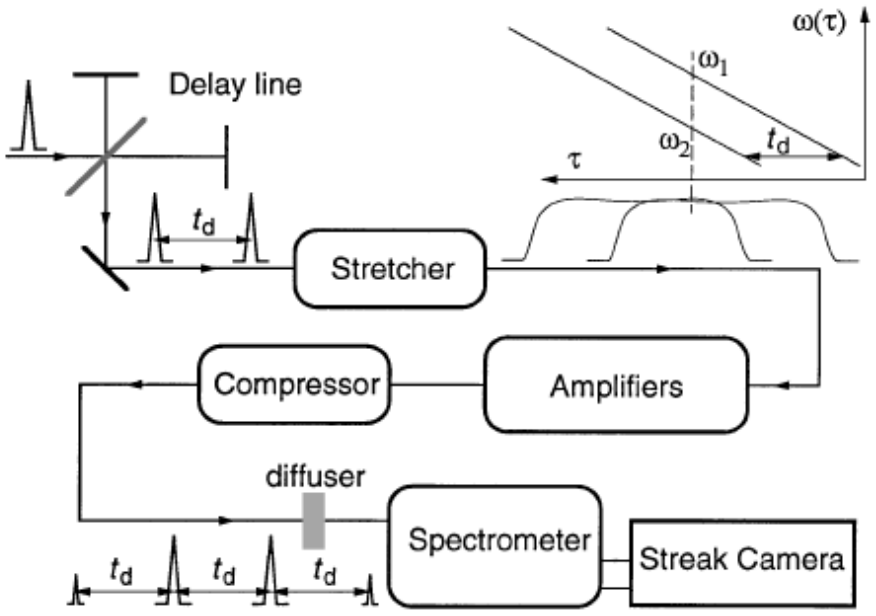

Figure 6.30: Experimental arrangement of nonlinear pulse shaping in a CPA amplifier. Reprinted from [2]

Another valid approach to understand the process is to look at the process as non linear propagation of the composite pulse, which contains the beat pattern. In this picture the new frequencies are generated as a result of SPM. The new frequencies are defined by: $\delta\omega \propto dI(\tau)/d\tau$.

Because of the many rapid intensity oscillations due to the beating, new frequencies are generated efficiently. In particular blue shifted frequencies are generated in the rising fronts and red shifted frequencies in the decreasing front. All the new frequencies generated will interfere in the compressor to give the additional pulses. In particular the amplitude of these replicas compared to the main peak depends of the amount of B integral of the chain. A fit algorithm can then searches for a B integral parameter that minimizes a least-square error function calculated for the temporal sidebands.

In our case two delayed pulses with the same amplitude are generated using the Dazzler present in the first amplifier (so strictly speaking we measure the B integral accumulated after the fourth pass of the first amplifier). The transfer function for generating these pulses is the same as that the one introduced in section 2.3.4 discussing the Phazzler. To measure the output replicas with sufficient dynamic range we used a third order correlator (Sequoia, Amplitude Technologies). In the absence of B-integral, the simulated third order cross correlation shows only three peaks and the energy ratio between the two pulses drives the symmetry of the resulting trace. This point is an important experimental control element; in particular, the relative injection-efficiency of the pulses into the amplifier, whose accurate control is experimentally challenging, can be evaluated that way. In the fit, the energy split ratio is adjusted numerically to fit any experimental asymmetry. In the presence of B-integral, side bands appear and the number and magnitude of the sidebands is adjusted to match the experimental data, using B as fit parameter. A typical measured trace is shown in Fig. 6.31. The multiples replicas separated by the temporal delay T_d are clearly visible. An unexpected asymmetry is visible in the recorded traces. A possible explanation relies on the theory presented previously and is confirmed by the simulation of the replication process. When the spectrum of each individual pulse is numerically isolated, one sees that there is a sizeable frequency shift of the replicas when the pulse-to-pulse delay is comparable to the stretched-pulse width. Experimentally, the delay between the pulses was set to 1 ps, which leads to a frequency shift of 15 nm between the two first replicas at the two side of the main pulses. Such a frequency shift certainly impacts on the conversion efficiency of the measurement setup because of the finite spectral acceptance of the thick frequency mixing crystals in the cross-correlator. The fitted B integral in this case is 1.5 radians. The output energy was reduced in this measurement to avoid any damages in the Ti:Sa crystal. We can then estimate a B-integral of 3 radians at full energy. From Tab. 6.29, the contribution to the CEP noise considering an intensity fluctuation of 2 % is then < 50 mrad.

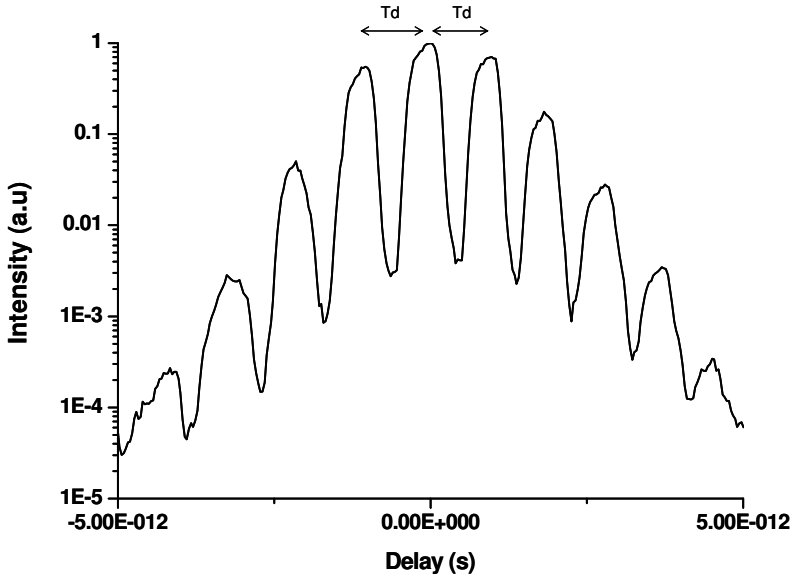

Figure 6.31: Measured high dynamic range correlation (Sequoia) injecting the CPA system with two temporally delayed (T_d) pulses

6.9 Control of the CEP with the Dazzler

Without feedback loop, the CEP drift of the amplified pulses was small enough over several minutes to demonstrate, for the first time, that CEP control could also be performed using the AOPDF inserted in the Femtopower. We do this by controlling the CEP of the acoustic waves in the AOPDF. This first experiment was done before the reduction of the jitter of the acoustic-wave.

The physics of AOPDF is based on a stringent acousto-optic phase-matching relationship between the acoustic and optical wave vectors. As for any phase-matching relationship, this relationship has its counterpart in terms of spectral phase and the acoustic and optical spectral phases are directly linked by the expression :

$$\varphi_{opr,in}(\omega_{opr}) + \varphi_{acc,in}(\omega_{acc}) - \varphi_{opr,diff}(\omega_{opr}) = \pi/2 \tag{6.11}$$

where, $\varphi_{opr,in}$ and $\varphi_{opr,diff}$ are the spectral phase of the input and diffracted optical pulses, and $\varphi_{acc,in}(\omega_{acc})$, is the spectral phase of the acoustic pulse. In this configuration, the electronic generator of the AOPDF is able to control the absolute phase of the acoustic wave within 160 mrad (rms time jitter between the trigger and the RF clock), which translates into the optical domain as follows: the CEP of the diffracted pulse can be changed with respect to the CEP of the input pulse by an arbitrary amount with 160 mrad (π /20) accuracy. Fig. 6.32 shows the effect of successive CEP jumps of -π, +π, -π, +$\pi/2$, +$\pi/2$, +$\pi/2$, +$\pi/2$ applied by the AOPDF, thereby demonstrating the ability of the AOPDF to exert control over the output CEP. Note here, that the feedback control was turned off to avoid automatic correction of the CEP jumps

by the oscillator locking electronics. These phase steps were performed at a low repetition rate, i.e. not limited by the refresh rate of the AOPDF. By pre-computing and pre-loading a set of RF waves with different CEP values (e.g. 64 waves covering the 0-2π interval) in SRAM memories, the RF generator is able to change the CEP phase drift at high repetition rate. A demonstration of this achievement is shown in Fig. 6.33 which shows the CEP measured function of time. The word "LOA-ENSTA" was written changing the CEP between successive shots. The vertical segments were obtained by choosing random values of CEP. The baseline (-2.5rad) shows the low CE phase drift of the system during this experiment. This control of the CEP opens the path to closed-loop CEP drift corrections at high repetition rates without any moving parts or retroaction on the oscillator. This is the subject of the next section.

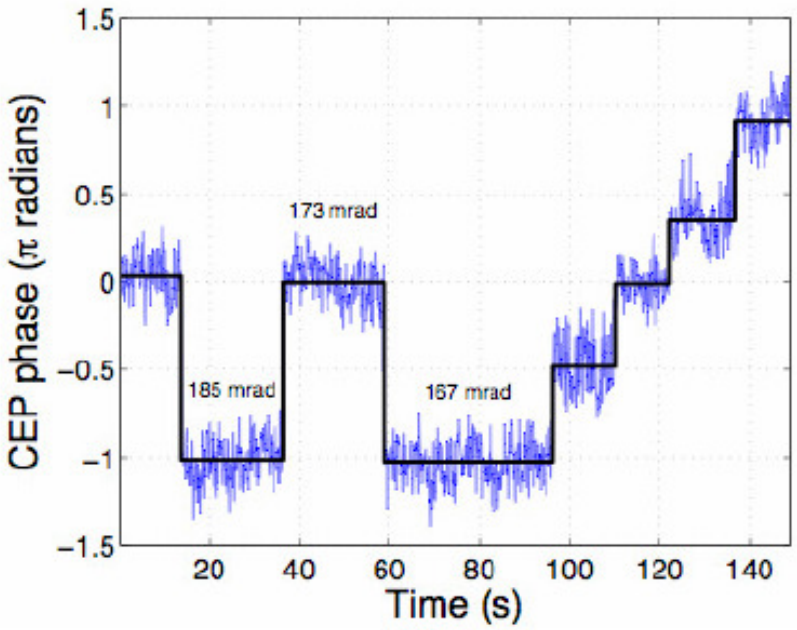

Figure 6.32: Measured CEP (red line) of amplified pulses and successive phase steps applied by the AOPDF (black line). No slow loop feedback was applied

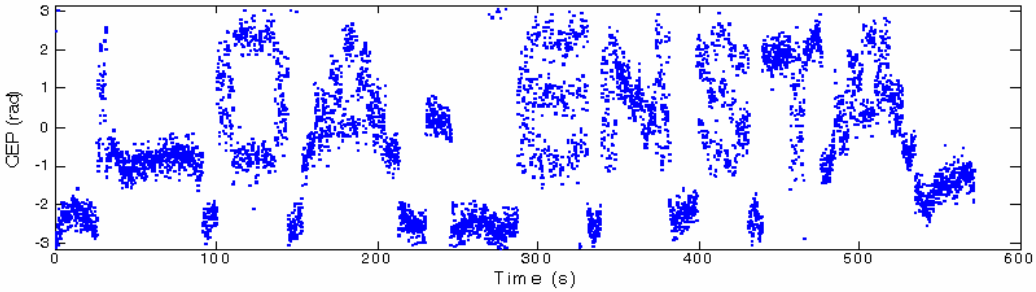

Figure 6.33: Measured CEP function of time. The CEP is changed with the AOPDF at high repetition rate to compose the word "LOA-ENSTA

6.10 Feedback of the CEP phase with the Dazzler

In the discussion about the CEP stabilization I have explained that, for a correct stabilization of the CEP drift, two feedback loops are needed. A fast feedback loop just after the oscillator and a slow feedback loop at the output of the system for compensating the slow CEP drift caused by the amplifier and the compressor. In the commercial Menlo system both feedback loops act, via an acousto-optical modulator, on the pump intensity of the oscillator. Applying two feedback signals with different time scales on the same actuator is suspected to increase the measured RMS noise on the CEP. This can cause the lock to break earlier than in the undisturbed case producing spikes in the CEP measurement. It is thus interesting to try to separate the two loops. A solution proposed by C.Li et al [1] is to use the signal measured with the f-2f of the slow loops to act with a piezoelectric transducer, changing the distance in the telescope grating of the stretcher. Another solution is to replace the sensitive grating adjustment by the introduction of dispersive material. In particular the CEP of the ultra-short amplified pulses can be controlled by slightly changing the dispersion in the pulse stretcher or compressor, without significantly changing the output pulse duration. In the previous section we have demonstrated how the CEP of the output pulses can be controlled with the AOPDF. This device can then be used to stabilize the CEP after the measurement of the slow drift. The advantage of this solution is the separation of the two loops without any additional elements into the laser chain. The development of this solution has been done in collaboration with Fastlite.

For the CEP stabilization with the AOPDF, like in the commercial APS800 Menlo system, the information from the f-2f fringes is extracted using the FTSI technique. After choosing a target CEP, the correction phase is applied with a proportional-integral (PI) feedback controller with the Dazzler. As discussed previously by pre-computing and pre-loading a set of RF waves with different CEP values in SRAM memories, the RF generator is able correct for any CEP phase drift at high repetition rates. The stabilization repetition rate is in fact determined by the overall loop time. In the case of AOPDF feedback loop this time is 60 ms (10ms of data acquisition, 30ms of data transfer and computation, 20ms of data transfer to RF generator) corresponding to a mean stabilization repetition rate >15Hz. Fig. 6.34 shows the CEP measured with the f-2f interferometer (averaged on 5 shots) before the activation of the AOPDF feedback (firsts 10 seconds) and after the stabilization (64 acoustic wave were loaded). The effect of the feedback is clearly visible. The target of the stabilization was also changed (0,+1,-1,0) to demonstrate the control of the CEP in closed loop. Fig. 6.36 shows the phase noise (dB, rad^2/Hz) for the open loop measurement (blue curve) and after the stabilization with the AOPDF(red curve). The effect of the correction is clearly visible(the intersection of the two curves). The rms CEP stability obtained with the AOPDF feedback loop is 144 mrad (334mrad FWHM) that needs to be compared with the result obtained using the standard APS800 Menlo system loop (131mrad (290mrad FWHM)). The two results are comparable. The large discretization level (98mrad for 64 waves loaded) of the CEP correction in the AOPDF loop is suspected to contribute to the slightly higher rms noise with the AOPDF loop. Future developments will enable a direct hardware feedback on the AOPDF and an increased number of memories (256), allowing both faster (500Hz) and finer (<25mrad) feedback.

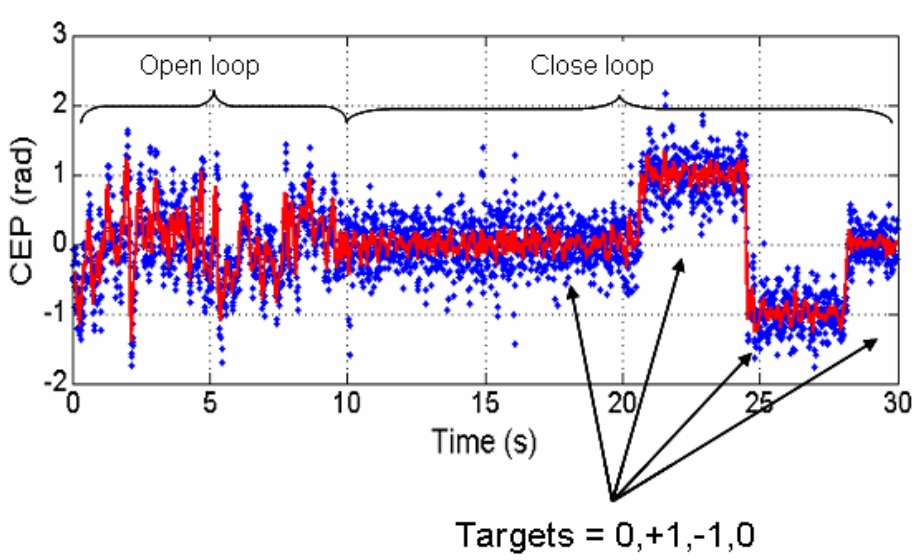

Figure 6.34: Single shot CEP measured with the f-2f interferometer before the activation of the AOPDF feedback (firsts 10 seconds) and after the stabilization. The effect of the feedback is clearly visible. The target of the stabilization was also changed (0,+1,-1,0) to demonstrate the control of the CEP in closed loop

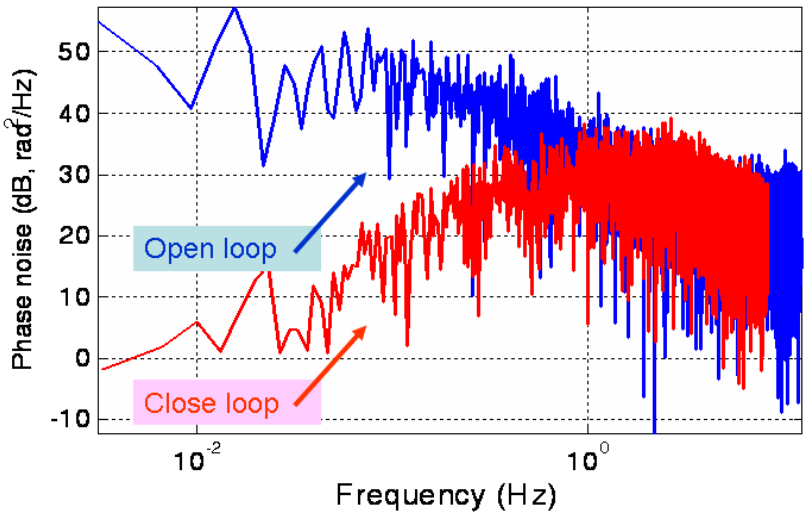

Figure 6.35: Phase noise (dB, rad^2/Hz) for the open loop measurement (blue curve) and after the stabilization with the AOPDF(red curve). The effect of the correction is clearly visible to a frequency of 4 Hz (the intersection of the two curves).

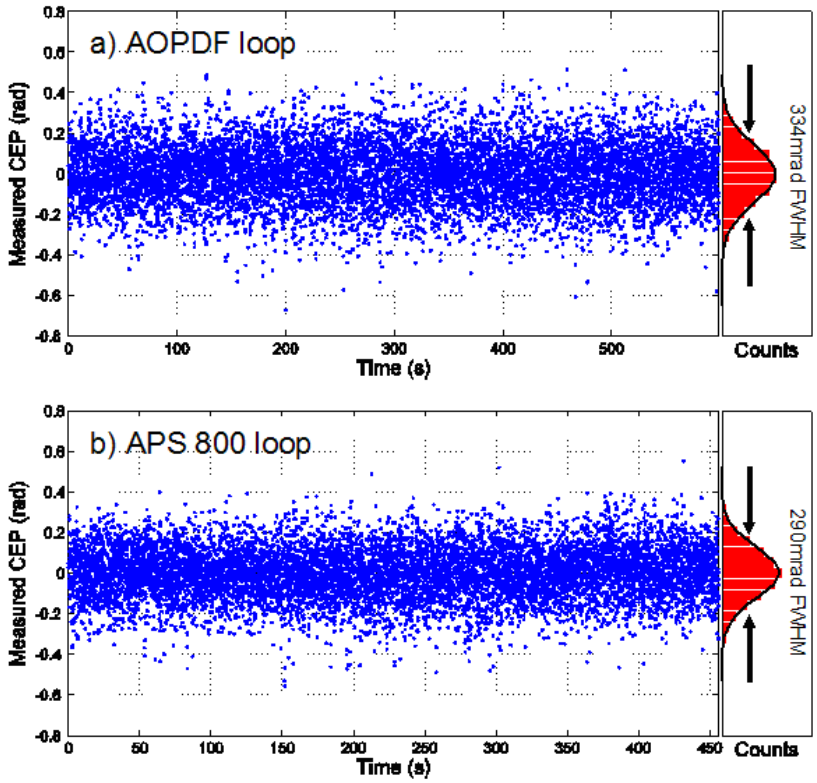

Figure 6.36: Comparison between closed loop operation using the AOPDF (a) or the Menlo loop (b) to correct for the CEP drift. Dots: CE phase values used for correction feedback.

Bibliography

[1] C. Li, E. Moon, and Z. Chang. Carrier-envelope phase shift caused by variation of grating separation. *Opt. Lett.*, 31(21):3113–3115, 2006.

[2] X. Liu, R. Wagner, A. Maksimchuk, E. Goodman, J. Workman, D. Umstadter, and A. Migus. Nonlinear temporal diffraction and frequency shifts resulting from pulse shaping in chirped-pulse amplification systems. *Opt. Lett.*, 20(10):1163–1165, 1995.

6.11 Hollow Fiber

6.11.1 Introduction

The temporal duration of the pulses that can be generated in a CPA laser system is limited to approximatively 18 fs [15, 7, 22, 20], for mJ level pulses. This limitation is mainly due to the gain narrowing during amplification. To balance this spectral narrowing several spectral shaping techniques have been tested. These solutions make it possible to reach temporal duration shorter than 15 fs. To generate pulses in the few-cycle regime post-compression spectral broadening techniques are necessary. The two most common are the propagation in a hollow-core fiber filled with noble gas [11] and filamentation [9]. Although a higher transmission efficiency and the possibility of self-compression has been claimed for filamentation [17, 8], the main drawback of this technique is that the compressed temporal duration varies radially across the beam [6, 21]. This implies that, in order to obtain a sub-10 fs pulse, only the central part of the beam needs to be selected with a corresponding substantial reduction of the usable energy. Furthermore 5 fs pulses can not be generated in a single filamentation stage. The solution chosen for the "salle noire" laser system is spectral broadening in a hollow fiber.

6.11.2 Hollow fiber

Few-cycle pulses can be generated by extra-cavity compression techniques, in which the pulses are spectrally broadened upon propagation in a suitable nonlinear waveguide and subsequently compressed in a carefully designed optical dispersive delay line. Spectral broadening of laser pulses by self-phase modulation in a single mode optical fiber is a well-established technique: pulses down to 6 fs were obtained in 1987 from 50-fs pulses generated in a mode locked dye laser [5]. More recently 13-fs pulses from a cavity-dumped Ti:sapphire laser were compressed to 5 fs with the same technique [1]. However, the use of a single-mode fiber limits the pulse energy to a few nanojoules. A powerful pulse compression technique based on spectral broadening in a hollow fiber filled with noble gas has demonstrated the capability of handling high energy pulses (sub-mJ range) [11, 12]. This technique presents the advantages of a guiding element with a large diameter mode and a fast nonlinear medium with a high threshold for multiphoton ionization. The theoretical principles of the propagation in a hollow fiber are briefly presented in the next section. In section 6.11.4 I present results about the generation of few-cycle pulses (4.3 fs) with an energy of 1 mJ. The CEP stabilization of this pulses is also demonstrated.

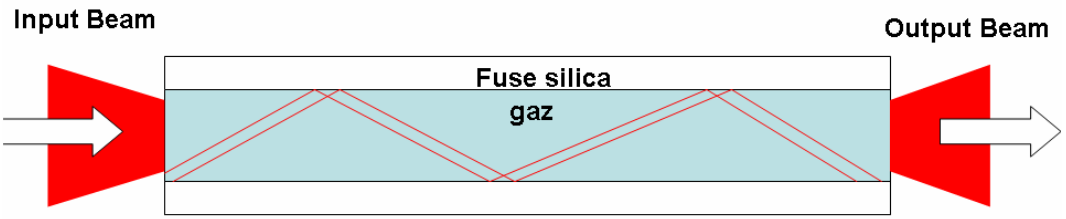

Figure 6.37: Schematic of the propagation in a hollow-core fiber.

6.11.3 Propagation modes and losses in hollow fibers

The use of hollow fibers permits the exploitation of spatially uniform SPM and overcomes the limitation imposed on the pulse energy by the small core diameters of single mode fibers. Owing to the large and scalable mode size, this technique can handle much higher pulse energies than traditionally used single-mode optical fibers. Wave propagation along a hollow waveguide can be thought of as occurring by grazing incident reflections at the dielectric inner surface. Since the losses caused by these multiple reflections discriminate against higher order modes, only the fundamental mode will be transmitted through a sufficiently long fiber. This offers the potential for using a large channel diameter without compromising the quality of the output beam. The modes of hollow cylindrical fibers with diameter much larger than the wavelength were considered by Marcantili and Schmeltzer. These fibers support three types of modes: transverse circular electric (TE_{0m}), in which the electric field lines are transverse concentric circles centered on the propagation axis. Transverse circular magnetic (TM_{0m}), with the electric field directed radially, and hybrid mode EH_{pm} ($|p| \geq 1$) with all the electric and magnetic components present. For fused silica gas-filled fibers the lowest-loss mode is the EH_{11} hybrid mode, whose intensity profile as a function of the radial coordinate r is given by:

$$I(r) = I_0 J_0^2(2.405r/a) \tag{6.12}$$

where I_0 is the peak intensity, J_0 is the zero-order Bessel function and a is the capillary radius. Fig. 6.38 shows the transmission of the fundamental mode EH_{11} at 780 nm as a function of hollow fiber length for different values of the capillary radius.

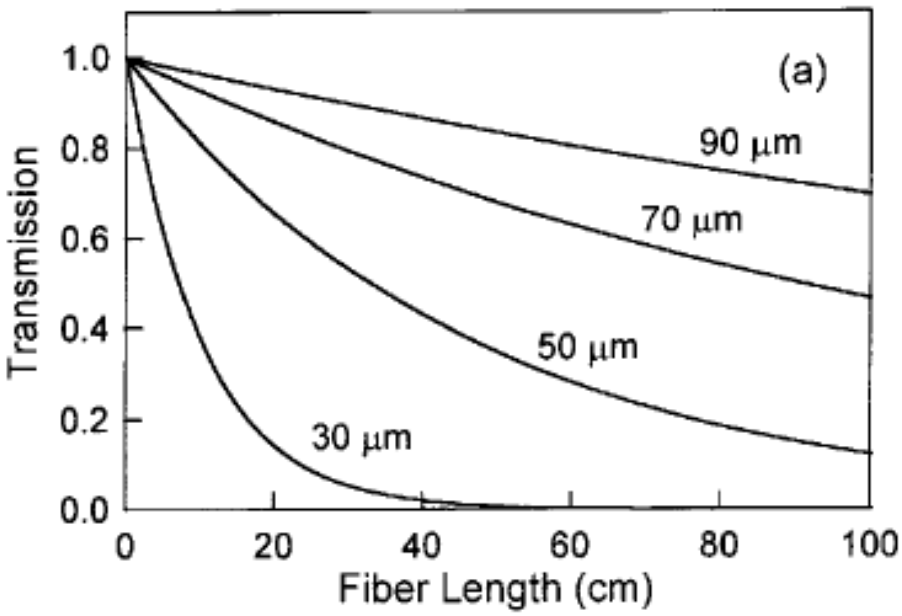

Figure 6.38: Transmission of the fundamental mode EH_{11} at 800 nm function of the fiber lengths and for different internal radius of the fiber. Reprinted from [12].

Another important point is the coupling efficiency of the input power in the fundamental mode EH_{11}. For maximizing this parameter the size of the beam at the input of the fiber needs to match the mode we want to couple. A theoretical coupling efficiency of 90 % has been theoretically demonstrated for a radius between 0.49a and 0.84a. If the modes are not matched the losses increases and more energy is coupled in the higher order modes. This decreases the throughput of the fiber and affects the output spatial quality. Working with a correct coupling, the fiber acts like a spatial filter and the output beam has a very good spatial quality.

The propagation in a hollow fiber is described by the propagation equation I have derived in the SEWA approximation (section 3.4.6). The two main phenomena governing the propagation are SPM and GVD. SPM induces the spectral broadening and introduces a nonlinear spectral phase. The influence of SPM is evaluated defining the non linear length:

$$L_{nl} = \frac{1}{\gamma P_0} \tag{6.13}$$

where P_0 is the peak power of the pulse and γ is the non linear coefficient. γ is defined as:

$$\gamma = \frac{n_2 \omega_0}{c A_{eff}} \tag{6.14}$$

where ω_0 is the laser pulsation, c the speed of light, n_2 the non linear index of refraction of the gaz and A_{eff} the effective area of the mode.
The influence of the GVD is estimated defining the dispersion length L_d:

$$L_d = \frac{T_0^2}{|\beta_2|} \tag{6.15}$$

where T_0 is the duration (at $1/e^2$ in intensity) of the input pulse and $\beta_2 = \frac{\partial^2 \beta}{\partial^2 \omega}$ is the dispersion of the group velocity. These two parameters quantify the physical length for the

contributions of SPM and dispersion. In particular for a good compressibility of the spectrally broadened pulses there should be an equilibrium between the two phenomena. The optimal regime is given for a fiber length: $L_{opt} \geq \sqrt{6 L_{nl} L_d}$.

6.11.4 Experimental results

Recently, Cavalieri *et al.* have demonstrated sub-4 fs pulses with 400 μJ energy via HCF compression of 1 mJ, sub-23 fs pulses [4]. Additional efforts have been made to push the output energy up to $\sim$1 mJ by safely coupling higher energy seed pulses into the fiber [19, 10]. For a HCF filled with a static gas pressure, however, the achievable output energy becomes quickly limited by self-focusing and plasma formation due to ionization of the gas, which degrade beam coupling into the fiber and result in significant energy losses. The use of longer and larger fiber cores with a pressure gradient helps delay these effects until the pulses are coupled well into the fiber, thereby making it possible to scale few-cycle pulse production beyond the mJ level [18, 13, 2].

Spectral broadening in a HCF is strongly dependent on the input pulse parameters such as duration and energy. A much less explored experimental parameter, however, is laser polarization [16]. Changing the polarization state of the laser from linear to circular provides a simple way of coupling more energy into the fiber since it reduces both the Kerr nonlinearity [3] and ionization [14] of the gas at equivalent intensities. The solution we tested to increase the energy out of a statically filled HCF was therefore to seed it with circularly polarized laser pulses. With this technique, we generated 4.3 fs, 1 mJ pulses, compressed from 2.5 mJ, 22 fs seed pulses. A comparison between linear (LP) and circular polarization (CP) shows that the energy throughput and the long-term spectral stability of the output pulses is significantly enhanced for CP.

The high-energy seed pulses in our experiments were generated using the "salle noire" laser at first with prisms + chirped mirrors compressor. The CEP stability after the hollow fiber for this high energy seeding has been confirmed after the installation of the transmission gratings + chirped mirrors compressor.

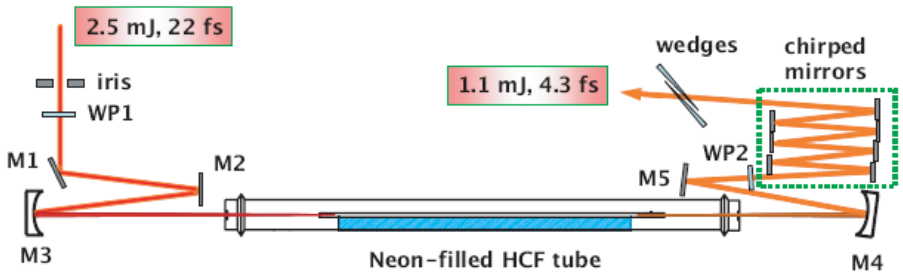

Figure 6.39: Schematic of the statically filled HCF setup seeded with circularly polarized pulses. WP1,2: broadband zero order quarter wave plates.

In the HCF compression setup, shown in Fig. 6.39, the input beam can be changed from LP to CP using a zero-order quarter wave plate (WP1). The beam is then loosely focused into the HCF by a $f = 1.5\,\mathrm{m}$ focusing mirror. The HCF is 1 m long with an inner diameter of 250 μm and rests inside a tube filled with a static pressure of Neon gas. The output beam can then be changed from CP back to LP for measurements downstream using a broadband zero-order quarter wave plate (WP2). Residual pulse dispersion is finely compensated by a set of broadband chirped mirrors (CMs) (Femtolasers GmbH) and a pair of fused silica wedges.

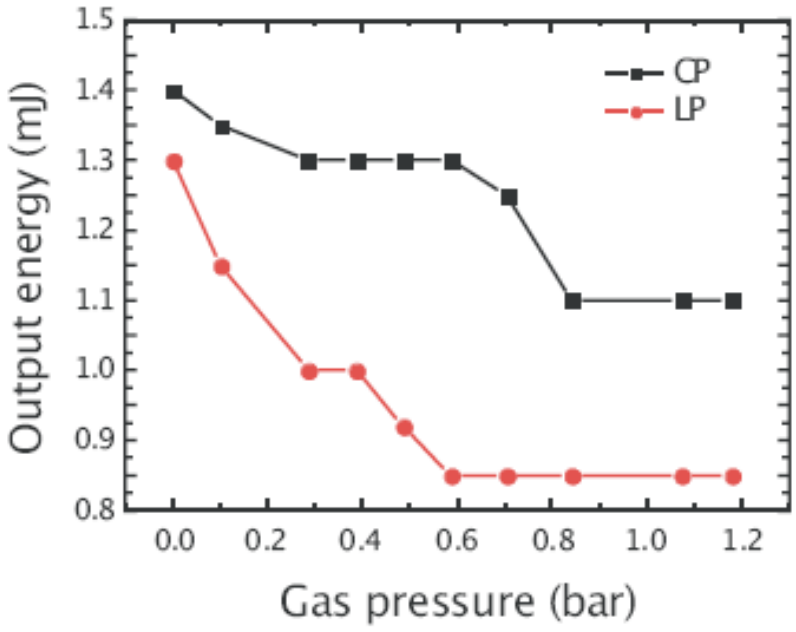

Figure 6.40: HCF output pulse energy for CP (black line) and LP (red line) as a function of Neon pressure, for an input pulse energy of 2.5mJ.

In the experiment, the difference in output pulse energy and spectral broadening between LP and CP was measured for the 2.5 mJ, 22 fs seed pulses. Fig. 6.40 shows the output pulse energy after the HCF as a function of gas pressure. A throughput enhancement is already quite visible for CP even in the case where the remnant gas pressure is very low ($<<1$ mbar). For both CP and LP, the output energy decreases with increasing gas pressure but the energy throughput remains higher for CP. Reduced self-phase modulation due to a diminished Kerr effect for CP means that spectral broadening is less pronounced for CP at pressures below ~ 1 bar. At higher pressures, however, pulse broadening for CP becomes comparable to that for LP, which can be explained by higher ionization losses for LP due to stronger ionization. At an optimum pressure of ~ 1.1 bar, the 1.1 mJ output energy measured for CP is almost 30 % higher than the 0.85 mJ measured for LP. Fig. 6.41 shows the spectral broadening recorded for CP and LP at the optimum pressure of 1.1 bar. A careful comparison of the two cases reveals that for CP (black line) a more homogeneous pulse broadening occurs around the central wavelength (780 nm) together with a clear extension of the spectrum towards shorter wavelengths, which is more adapted for obtaining cleaner compressed pulses.

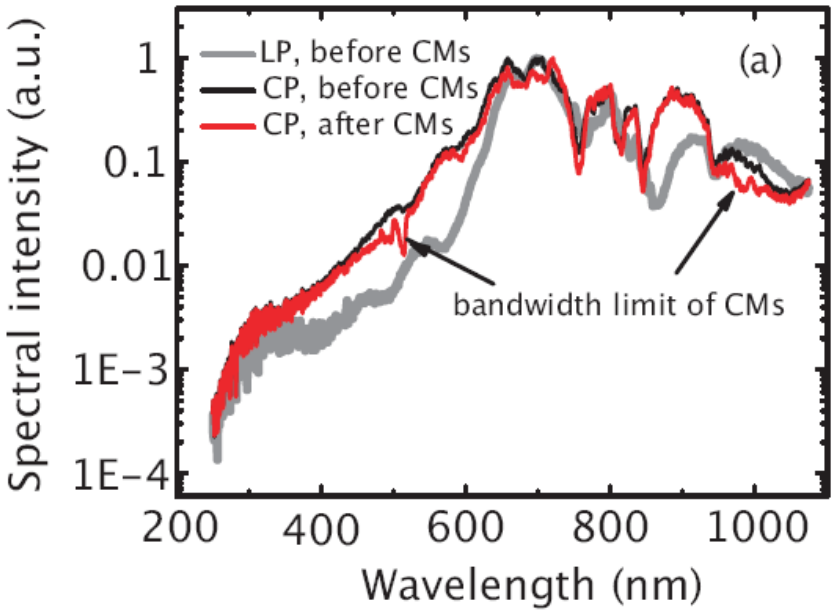

Figure 6.41: Broadened HCF spectrum before (black line) and after (red line) the chirped mirrors for CP and LP before the chirped mirrors (grey line).

At the optimum pressure of ~ 1.1 bar, the broadened spectrum (Fig. 6.41) for CP can support 3 fs transform-limited pulses. The compressed pulse duration is measured after fine compensation of pulse chirp using a commercial second-order autocorrelator (Femtolasers GmbH) suited for sub-5 fs pulse characterization. A typical optimized compression result for CP is shown in Fig. 6.42, showing a very good agreement with the theoretical autocorrelation trace for a 4.3 fs sech^2 pulse at a central wavelength of 780 nm (red filled circle in Fig. 6.42). This pulse duration corresponds to ~ 1.6 cycles of the carrier wavelength. The background oscillations present in the experimental autocorrelation trace are most likely due to satellite pulses resulting from the

combined effects of residual uncompensated spectral phase and the sharp modulations in the broadened spectrum. In addition, spectral clipping due to the bandwidth limit of the chirped mirrors was observed, as shown in Fig. 6.41 (red line), meaning that the compressed pulses could be shorter. Here, it is worth mentioning that the bandwidth of the zero-order quarter wave plate after the HCF is broad enough such that no spectral effects were observed.

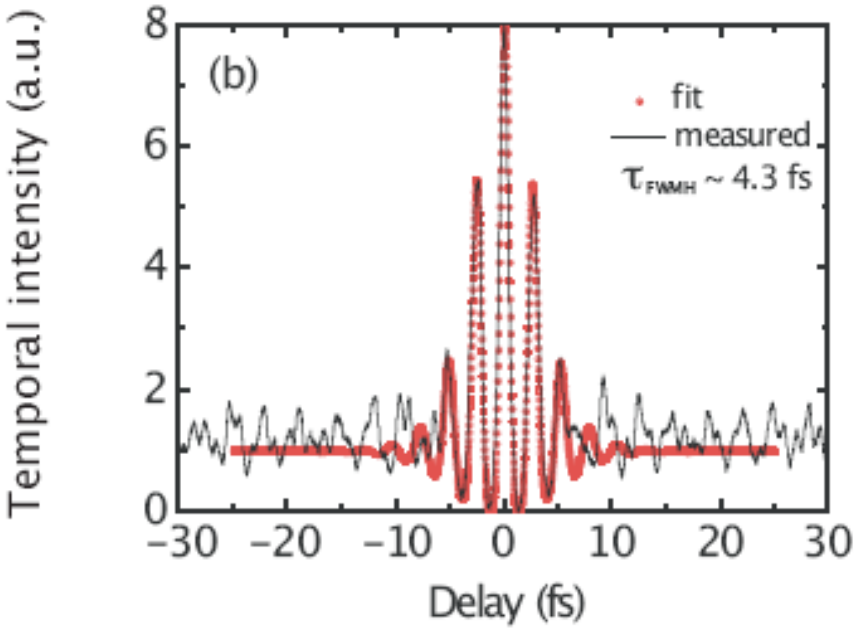

Figure 6.42: Measured (black line) and fitted (red filled circles) second order autocorrelation traces of the compressed pulses for CP. The seed energy is 2.5 mJ and the Neon pressure is 1.1 bar.

Although no obvious differences were observed in beam pointing for both polarization states, we did however observe that CP yields a more stable output spectrum over time. Fig. 6.43 shows density plots of the output spectra for CP and LP made from 20000 successive shots at the optimum pressure of 1.1 bar. Here, we observe a significant improvement in stability for CP, especially at the extremities of the spectrum.

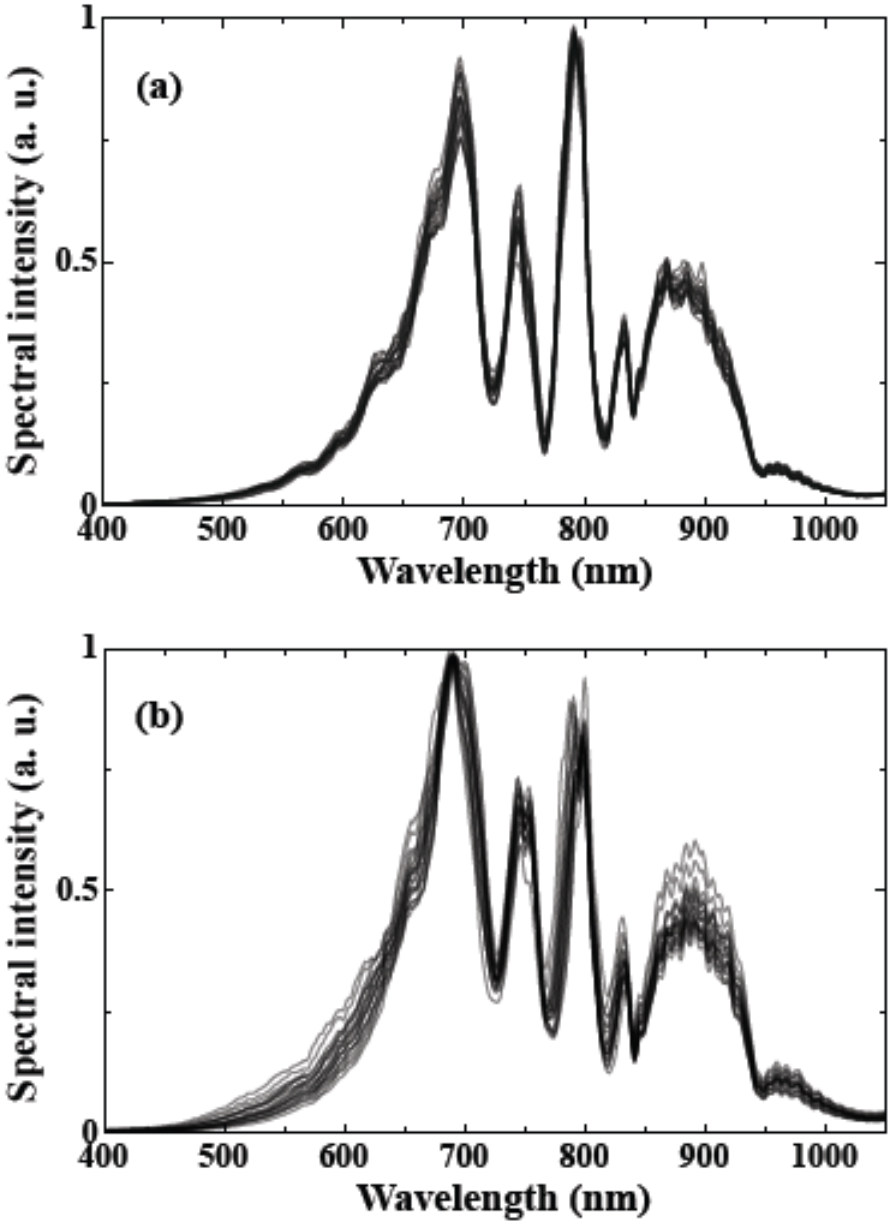

Figure 6.43: Density plot of the output spectrum of the HCF for CP (a) and LP (b) for a seed pulse energy of 2.5 mJ and Neon pressure of 1.1 bar. The fluctuations of the spectrum are the highest where the curve is the broadest

The CEP drift of the compressed pulses was measured with the f-2f interferometer, after the installation of the transmission gratings + chirped mirrors compressor. In this configuration we inject the fiber with 2 mJ with an output of 1.1 mJ. The gas pressure in CP is 1.5 barr. The measured FROG trace of the compressed pulses together with the reconstructed temporal shape is shown in Fig. 6.44. After the fiber the spectrum is already sufficiently broad to be doubled directly in the BBO crystal without passing in the sapphire plate. We measured an RMS CEP drift of 230 mrad (acquisition time 1 ms, averaging on 20 shots) (Fig. 6.45). This corresponds to an additional noise of 50 mrad compared to the results directly after the hybrid compressor. This additional noise is due to the intensity fluctuations that are coupled to CEP

fluctuations by the nonlinear index in the HCF.

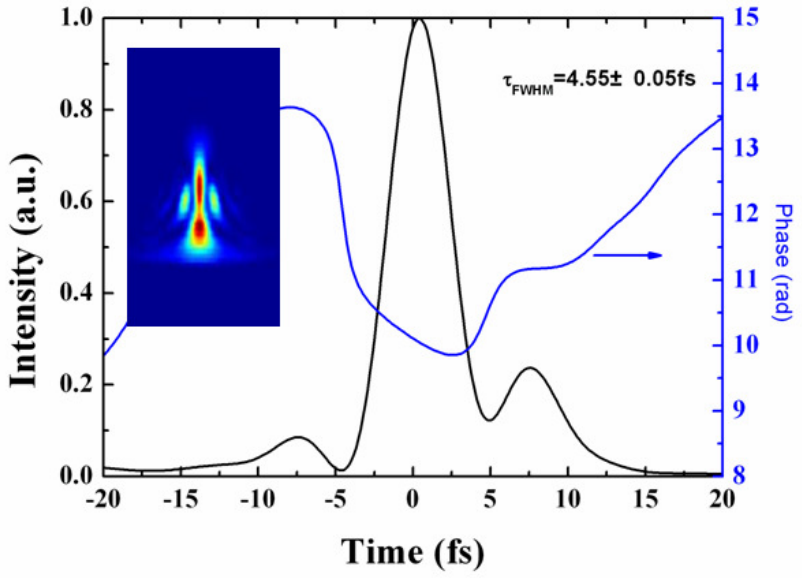

Figure 6.44: FROG trace and temporal reconstruction of the compressed pulses after the hollow-core fiber.

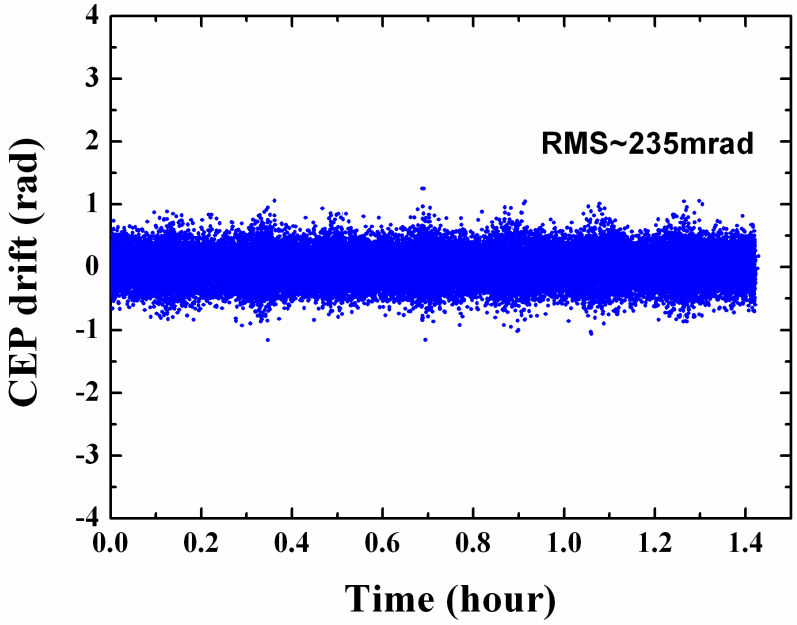

Figure 6.45: Closed loop CEP drift after spectral broadening in a hollow-core fiber and recompression.

6.11.5 Conclusions

In conclusion seeding the hollow fiber with circularly polarized pulses is a good solution to obtain a significant enhancement in energy throughput together with a notably improved spectral stability for circularly polarized seed pulses. Using this approach, 1 mJ, sub-5 fs pulses could be

generated, compressed from 2.5 mJ, 22 fs. Seeding larger core fibers with circularly polarized pulses should provide a effective way for generating sub-5fs pulses with even higher (multi-mJ) energies. This solution is the one adopted in our system for the generation of the energetic few-cycle pulses. As presented in the introduction the goal of the laser development of my group is to build an efficient (solid target) single attosecond source at high repetition rate (1 kHz). To obtain this source it is necessary to dispose of mJ level, CEP stabilized, kHz, few-cycle pulses. We can now satisfy these requirements. The ASE temporal contrast of our system is 10^7 which is enough to avoid pre-ionization of the target at least in the sub-relativistic regime. If the beam is taken directly after the hybrid compressor we also have a multi-mJ, 25 fs, kHz laser source for experiments in the multi-cycle regime. In the next chapter, after an introduction of the different regimes of high order generation on solid target, I will present the first experiments of laser-matter interaction with the study of the plasma mirror. In the last chapter of this thesis I present the future development of a double CPA system using an XPW contrast filter for obtaining ultra-high contrast pulses.

ï»¿

Bibliography

[1] A. Baltuska, Z. Wei, M. S. Pshenichnikov, and D. A. Wiersma. Optical pulse compression to 5 fs at a 1-mhz repetition rate. *Opt. Lett.*, 22(2):102–104, 1997.

[2] S. Bohman, A. Suda, M. Kaku, M. Nurhuda, T. Kanai, S. Yamaguchi, and K. Midorikawa. Generation of 5 fs, 0.5 tw pulses focusable to relativistic intensities at 1 khz. *Opt. Express*, 16(14):10684–10689, 2008.

[3] R. W. Boyd. *NonLinear Optics*. Academic Press, Inc., 1992.

[4] A. L Cavalieri, E. Goulielmakis, B. Horvath, W. Helml, M. Schultze, M. Fiess, V. Pervak, L. Veisz, V. S. Yakovlev, M. Uiberacker, A. Apolonski, F. Krausz, and R. Kienberger. Intense 1.5-cycle near infrared laser waveforms and their use for the generation of ultra-broadband soft-x-ray harmonic continua. *New Journal of Physics*, 9(7):242, 2007.

[5] R. L. Fork, C. H. Brito Cruz, P. C. Becker, and C. V. Shank. Compression of optical pulses to six femtoseconds by using cubic phase compensation. *Opt. Lett.*, 12(7):483–485, 1987.

[6] L. Gallmann, T. Pfeifer, P.M. Nagel, M.J. Abel, D.M. Neumark, and S.R. Leone. Comparison of the filamentation and the hollow-core fiber characteristics for pulse compression into the few-cycle regime. *Applied Physics B: Lasers and Optics*, 86(4):561–566, March 2007.

[7] C. P. Hauri, M. Bruck, W. Kornelis, J. Biegert, and U. Keller. Generation of 14.8-fs pulses in a spatially dispersed amplifier. *Opt. Lett.*, 29(2):201–203, 2004.

[8] C. P. Hauri, A. Trisorio, M. Merano, G. Rey, R. B. Lopez-Martens, and G. Mourou. Generation of high-fidelity, down-chirped sub-10 fs mj pulses through filamentation for driving relativistic laser-matter interactions at 1 khz. *Appl. Phys. Lett.*, 89(15):151125, Oct 2006.

[9] C.P. Hauri, W. Kornelis, F.W. Helbing, A. Heinrich, A. Couairon, A. Mysyrowicz, J. Biegert, and U. Keller. Generation of intense, carrier-envelope phase-locked few-cycle laser pulses through filamentation. *Applied Physics B: Lasers and Optics*, 79(6):673–677, October 2004.

[10] H. Mashiko, C. M. Nakamura, C. Li, E. Moon, H. Wang, J. Tackett, and Z. Chang. Carrier-envelope phase stabilized 5.6 fs, 1.2 mj pulses. *Applied Physics Letters*, 90(16):161114, 2007.

[11] M. Nisoli, S. De Silvestri, and O. Svelto. Generation of high energy 10 fs pulses by a new pulse compression technique. *Applied Physics Letters*, 68(20):2793–2795, 1996.

[12] M. Nisoli, S. Stagira, S. De Silvestri, O. Svelto, S. Sartania, Z. Cheng, M. Lenzner, C. Spielmann, and F. Krausz. A novel-high energy pulse compression system: generation of multigigawatt sub-5-fs pulses. *Applied Physics B: Lasers and Optics*, 65(2):189–196, August 1997.

[13] M. Nurhuda, A. Suda, M. Kaku, and K. Midorikawa. Optimization of hollow fiber pulse compression using pressure gradients. *Applied Physics B: Lasers and Optics*, 89(2):209–215, November 2007.

[14] S. Petit, A. Talebpour, A. Proulx, and S. L. Chin. Polarization dependence of the propagation of intense laser pulses in air. *Optics Communications*, 175(4-6):323 – 327, 2000.

[15] S. Sartania, Z. Cheng, M. Lenzner, G. Tempea, Ch. Spielmann, F. Krausz, and K. Ferencz. Generation of 0.1-tw 5-fs optical pulses at a 1-khz repetition rate. *Opt. Lett.*, 22(20):1562–1564, 1997.

[16] S. Stagira, E. Priori, G. Sansone, M. Nisoli, S. De Silvestri, and Ch. Gadermaier. Nonlinear guided propagation of few-optical-cycle laser pulses with arbitrary polarization states. *Phys. Rev. A*, 66(3):033810, Sep 2002.

[17] G. Stibenz, N. Zhavoronkov, and G. Steinmeyer. Self-compression of millijoule pulses to 7.8 fs duration in a white-light filament. *Opt. Lett.*, 31(2):274–276, 2006.

[18] J.H. Sung, J.Y. Park, T. Imran, Y.S. Lee, and C.H. Nam. Generation of 0.2-tw 5.5-fs optical pulses at 1Â khz using a differentially pumped hollow-fiber chirped-mirror compressor. *Applied Physics B: Lasers and Optics*, 82(1):5–8, January 2006.

[19] A.J. Verhoef, J. Seres, K. Schmid, Y. Nomura, G. Tempea, L. Veisz, and F. Krausz. Compression of the pulses of a ti:sapphire laser system to 5 femtoseconds at 0.2 terawatt level. *Applied Physics B: Lasers and Optics*, 82(4):513–517, March 2006.

[20] K. Yamakawa, M. Aoyama, S. Matsuoka, H. Takuma, C. P. J. Barty, and D. Fittinghoff. Generation of 16-fs, 10-tw pulses at a 10-hz repetition rate with efficient ti:sapphire amplifiers. *Opt. Lett.*, 23(7):525–527, 1998.

[21] A. Zaïr, A. Guandalini, F. Schapper, M. Holler, J. Biegert, L. Gallmann, A. Couairon, M. Franco, A. Mysyrowicz, and U. Keller. Spatio-temporal characterization of few-cycle pulses obtained by filamentation. *Opt. Express*, 15(9):5394–5404, 2007.

[22] E. Zeek, R. Bartels, M. M. Murnane, H. C. Kapteyn, S. Backus, and G. Vdovin. Adaptive pulse compression for transform-limited 15-fs high-energy pulse generation. *Opt. Lett.*, 25(8):587–589, 2000.

Chapter 7

High order harmonic generation on solid target

7.1 Introduction

In this chapter, after an historical overview of the high harmonic generation (HHG) on solid targets, I give a theoretical introduction of the two harmonic generation mechanisms and of the possibility of obtaining attosecond pulses from these harmonics. I then introduce the plasma mirror interaction regime that occurs for intensities below the generation of harmonics. This plasma mirror interaction can be used to increase the temporal contrast of the laser pulses. The first experiments of laser-matter interaction in this regime are presented in the last section.

7.2 Historical overview

High harmonic generation from solid plasmas was first observed by using high-energy nanosecond pulses from CO_2 laser systems [5, 6, 7]. In these experiments pulses with an energy in the Joule level at 10.6 μJ with ns duration were focused to the intensity of $\backsim 10^{15}\ Wcm^{-2}$, and harmonics up to 46th order ($\backsim 230\ nm$) were observed. Theoretical studies attributed the harmonic generation mechanism to the nonlinear restoring force of the plasma and mode coupling into plasma oscillations [2]. They also predicted that there would be a cut-off in the harmonic spectrum, whose position is determined by the plasma density. Another decade was needed until the first observation of harmonics from plasma surfaces using femtosecond pulses produced by table-top Ti:Sapphire laser systems [25]. Typical parameters were $\backsim 100mJ$ of energy at $\backsim 800nm$ with $\backsim 100fs$ duration. Although the pulse energy was 3 orders of magnitude lower than that from CO_2 lasers, the pulse duration, being shorter by 4 orders of magnitude, allowed to achieve the intensity of $\backsim 10^{17}Wcm^{-2}$. On the other hand, since the relativistic amplitude scales as $a_L^2 \propto I\lambda^2$, higher intensity was compensated by shorter wavelength, i.e., the value of a_L was comparable to that of CO_2 lasers. Nevertheless, it was shown that surface harmonics can be generated with a much smaller, table top laser system. In the meanwhile, numerical simulations (particle-in-cell PIC simulation code) found that there is no cut-off in

the spectrum [10], which is in contrast with the prediction from previous studies. Harmonics beyond the predicted cut-off were also experimentally observed using a high power, picosecond Nd:glass laser with a focal intensity of $\backsim 10^{19} W cm^{-2}$ at 1053 nm [18]. A new theoretical model was proposed to explain these results, which is known as the oscillating mirror model [14]. The model predicts that the harmonics are generated from fast moving reflective surface [4]. The appearance of the cut-off in the previous mode-coupling picture was attributed to the low resolution PIC simulations [10]. The oscillating mirror model and the numerical simulations predicted that the harmonic generation could be extended well beyond the previously expected cut off by increasing the laser intensity to the relativistic regime [10]. This new prediction leads to growing interest into harmonic generation from plasma surfaces as a source of coherent XUV radiation. Many experimental studies have followed. Several investigations have found that the harmonic generation process is strongly dependent on the plasma scale length [26, 22]. Harmonic generation efficiency was found to have an optimal scale length above zero, and then drop rapidly as the scale length increases [26, 12]. In fact, improving the temporal contrast of the incident pulses was found to be beneficial to the harmonics generation process [15]. Angular distribution of the generated harmonics was also studied. For picosecond laser pulses, the angular distribution was found to be near isotropic rather than specular [18], which was attributed to surface rippling owing to the high ponderomotive pressure. On the other hand, XUV beam directed in the specular direction was observed for femtosecond laser pulses [22], where the interaction occurs faster than the plasma expands. The polarization dependence of the process was studied by several group [18, 22]. The harmonic generation efficiency was observed to be lower for s-polarization when femtosecond pulses were used [26, 22], which was consistent with the prediction of the oscillating-mirror model [14].

Theoretical work has pursued the possibility of the harmonic generation process as a source of attosecond pulses. It was pointed out that harmonics are inherently phase locked and that leads to a train of attosecond pulses [19]. Another work proposed to focus a few-cycle pulse into a spot as small as the fundamental wavelength (λ^3), which leads to the generation of an isolated single attosecond pulse in a certain direction [16]. Analytical work similar to the oscillating-mirror model [11] has revealed that the harmonics spectra scales as a power law: $I_q \propto q^{-p}$, where q is the harmonic order and p is the scaling parameter p$\backsim$ 2.5. From this slow power-law decay, they predicted that even a train of zeptosecond pulses could be produced. This scaling was verified by experimental observation of the harmonic spectrum scaling law. It was also predicted that the cut-off position should scale as $\backsim \gamma^3$, where γ is the relativistic γ-factor. This means that the highest harmonics generated from this process scales up very rapidly when the intensity of the incident field is increased. This scaling of the cut-off was also confirmed experimentally [8]. One more important thing to be mentioned are the studies on of harmonic generation in non relativistic regime [20]. They found that there is a harmonic generation process efficient with non-relativistic intensity, which they named as coherent wake emission (CWE). The results predicted from their model are similar to the prediction from very early theoretical models, for example, the observation of the cut-off.

7.3 Harmonic generation mechanism

Harmonic generation mechanism from solid surfaces is categorized into two different regimes depending on the incident laser intensity: relativistic regime and non-relativistic regime. The former is known as relativistic oscillating mirror (ROM) model [14, 25], while the latter is named as coherent wake emission (CWE) [20].

7.3.1 Relativistic oscillating mirror

To understand the physical mechanism of harmonic generation from solid target, we can consider an electromagnetic wave incident on the surface composed of a number of electrons that can oscillate around an immovable ion background (Fig. 7.1). The plasma can be directly created from the solid target by the leading edge of the laser pulse. The plasma electrons are accelerated along the polarization direction by the electric field and acquire a velocity that is proportional to the normalized filed amplitude a_L:

$$a_L = \frac{eE_L}{\omega_L mc} \tag{7.1}$$

where E_L and ω_L are the electric field and the laser frequency respectively. As long as the laser intensity is such that $a_L << 1$, the magnetic field B does not play any relevant role, but it becomes relevant for $a_L \geq 1$. In such condition the Lorentz force $F_p \propto \overrightarrow{B} \backsim I_L \lambda_L^2 sin(2\omega_L t)$ tends to move the electrons parallel to the laser propagation direction inducing an oscillatory motion. The interplay between the Lorentz force and the restoring force due to the electrostatic field induced charge separation, determines an oscillatory motion. Since the incident electromagnetic pulse is reflected at the electron surface and this surface is moving relativistically, the incident field experience an extreme Doppler up shift up to:

$$\Omega_{max} \approx 4\gamma_{max}^2 \omega_L = 4(1 + a_L^2)\omega_L \tag{7.2}$$

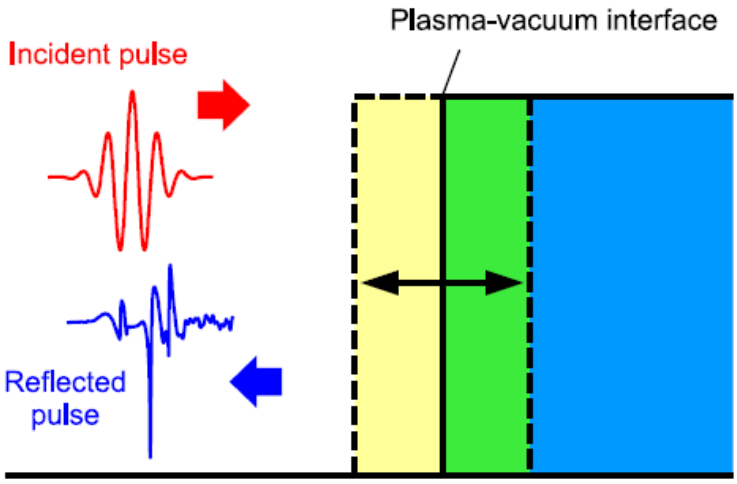

Figure 7.1: Schematic drawing of oscillating mirror. The electromagnetic field of the incident pulse drives the plasma-vacuum interface back and forth. The pulse experience a huge Doppler shift upon reflection on the oscillating surface, which leads to the generation of high frequency components. Reprinted from [17]

7.3.2 The relativistic γ-spikes model

The oscillating mirror model offers a simple and intuitive picture of the harmonic generation process for solids, leading to a simple law for the cut-off frequency. However, recent experimental works have evidenced a different evolution of the cut-off frequency as a function of the maximum relativistic γ_{max}. The experimental data have been interpreted using a different theoretical analysis performed by Baeva et al.[1]. This theory allows one to recognize the different behavior between the plasma electrons and the plasma surface during the interaction with the relativistic laser pulse. Indeed, whereas the velocity of the electrons are close to the speed of light in all instants (with a component both normal p_n and parallel p_τ to the plasma surface), the plasma boundary behave in a quite different way. Its velocity v_s is not ultra-relativistic for most of the times but smoothly approaches c only when the tangential electron momentum vanishes (Fig. 7.2(a),(b)). The γ-factor of the surface γ_s also shows a specific behavior Fig. 7.2(c). It has sharp peaks at those times for which the velocity of the surface approaches c. Thus, while the velocity function v_s is characterized by its smoothness, the distinctive feature of γ_s are its quasi-singularities. When v_s reaches its maximum and γ_s has a sharp peak, high harmonics of the incident wave are generated and can be seen in the reflected radiation. The temporal width of this γ spike scale as $\Delta t \sim 1/\gamma_{max}$. In other words the duration of the emitted pulse scales accordingly. Since this pulse is compressed by Doppler shift by a factor $4\gamma_{max}^2$ and the emission of these harmonics is confined to a time interval $\Delta t/4\gamma_{max}^2 \sim 1/\gamma_{max}^3$ it thus contains frequencies up to $\sim \gamma_{max}^3$. This theoretical prediction is in agreement with experimental results. In particular it demonstrates way a universal harmonic spectrum (that does not depend on the particular surface motion) can be derived. Physically, only the time interval of γ-spiking is

responsible for harmonic generation. Consequently only region around the maximum velocity v_s corresponds to the harmonic spectrum. As a result, since all smooth functions resemble parabolas around their maxima, the harmonic spectrum is universal (Fig. 7.3). It contains two qualitatively different parts: a power low decay (to the spectral cut-off) and an exponential decay.

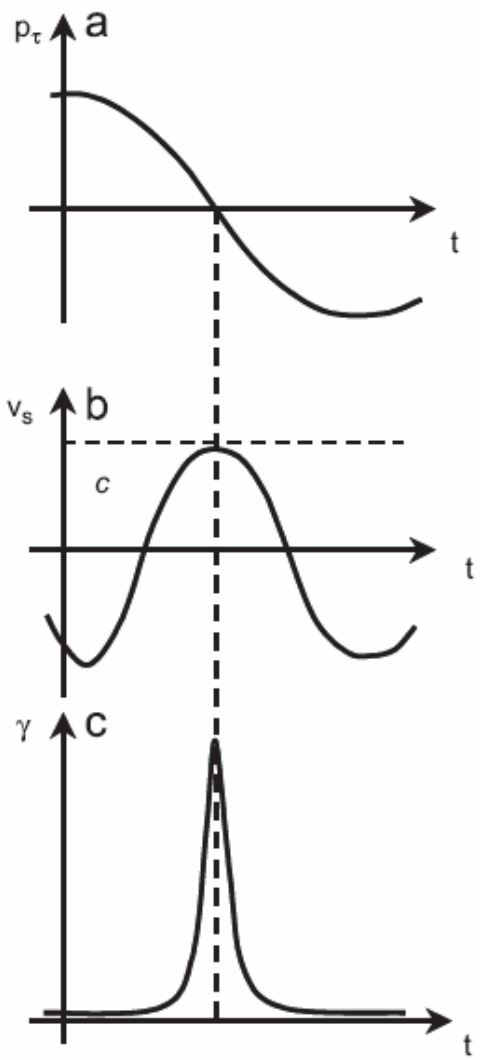

Figure 7.2: Schematic view of the principle of the γ spike model. (a) Electron momentum component parallel to the surface as a function of time; (b) velocity of the plasma surfaces and (c) γ factor of the surface. Reprinted from [1].

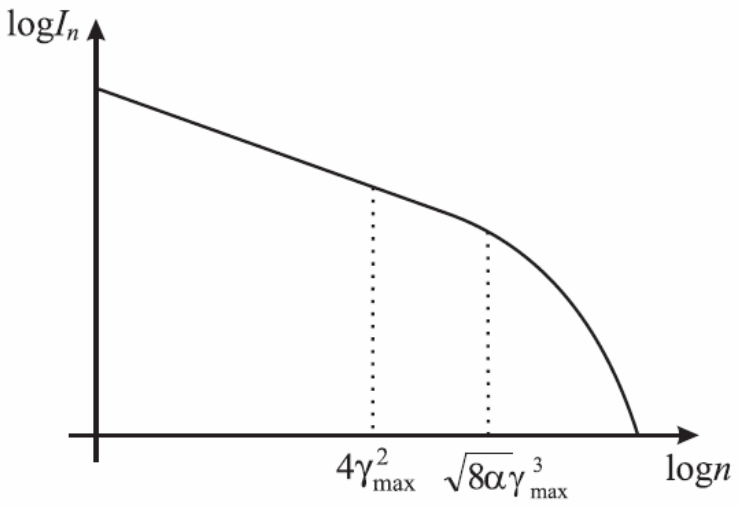

Figure 7.3: The universal high harmonic spectrum contains power law decay and exponential decay (plotted in log-log scale).

7.3.3 Coherent wake emission

When the intensity of the incident laser field is not relativistic,the oscillating mirror does not generate harmonic efficiently and CWE becomes dominant. Fig. 7.4 illustrates the process of CWE. The CWE is a process associated with plasma wake oscillation. This process occurs for a p-polarized incident electric field. When a pulse is incident on the surface of the plasma, the electric field of the pulse pulls electrons out from the plasma. Those electrons, named Brunel electrons, are driven back into the plasma by the same electric field and absorbed by the plasma, a process known as vacuum heating [3]. These electrons bunch in the plasma density gradient and constitute a density wave inside the plasma. As the density wave travels, it triggers plasma oscillations in its wake. These plasma oscillations are converted back to electromagnetic waves at the point where the wave front of the wake turn around [21]. As the generated electromagnetic wave travels along the density gradient, it refracts and comes out of the plasma in the specular direction of the incident beam. Since this occur within a fraction of cycle, each wave generated is in a form of a pulse shorter than one optical cycle, possibly sub-femtosecond. The CWE process has several interesting properties. As apposed to the ROM harmonic generation, this process is efficient down to the incident intensity of $I\lambda^2 \sim 4 \times 10^{15} W cm^{-2}$ [20], which corresponds to the normalized amplitude of $a_L \sim 0.05$. Therefore, CWE will be the dominant harmonic generation mechanism when the intensity is non relativistic. Another important feature of CWE is that the harmonic spectra shows a clear cut-off at the maximum plasma frequency ω_p, which is determined by the density of the plasma. The reason way no harmonics are generated above ω_p, is that the generation process relies on the density wave in the plasma. This is in contrast with the spectra of ROM harmonics, where it shows a slow roll-over around the frequency $\sqrt{8}\gamma^3_{max}$. The harmonics and a pulse train generated from CWE is chirped in two ways. One is a chirp generated within the density

gradient, because the higher frequency component is generated from the higher-density part in the plasma and hence needs to travel more to come out of the plasma. The other is a chirp coming from the velocity of the electrons pulled out into the vacuum. Since the velocity of the electrons is dependent on the intensity of the incident pulse, the time they require to re-collide with the plasma surface depends on the intensity. In other words it gains a chirp according to the intensity envelope of the pulse. The former introduces a chirp in a single attosecond pulse in a train, which is analogous to an chirp observed in gas HHG [24], while the latter changes the time spacing between individual pulses in a train, analogous to a harmonic chirp [24]. A typical CWE spectrum is shown in Fig. 7.5.

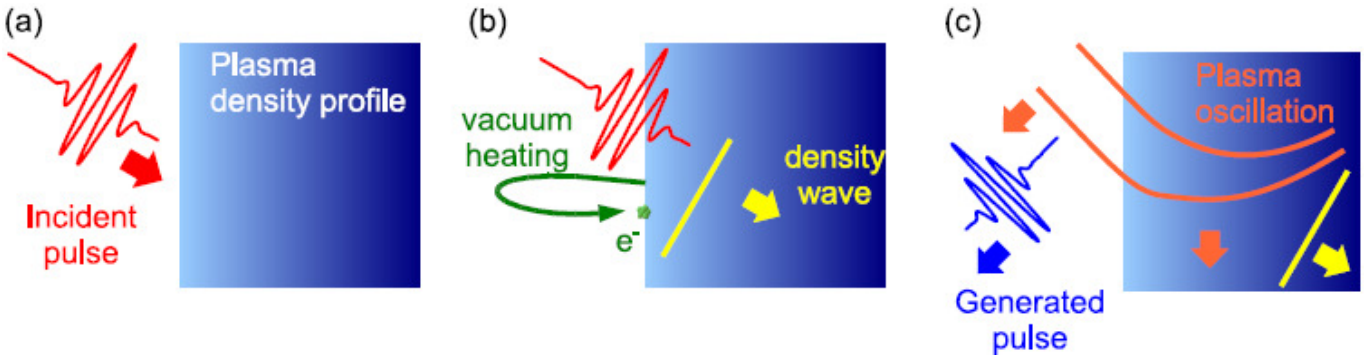

Figure 7.4: Schematic illustration of the coherent wake emission. (a) The pulse enter the plasma density gradient with an oblique incidence. (b) The electric field of the pulse pulls electrons out from the plasma into the vacuum and then drives them back into the plasma. The plasma gains the energy through the recollision (vacuum heating) and plasma density wave is generated. (c) Plasma oscillation in the wake of the density wave generates a pulse back into the vacuum. Reprinted from [17]

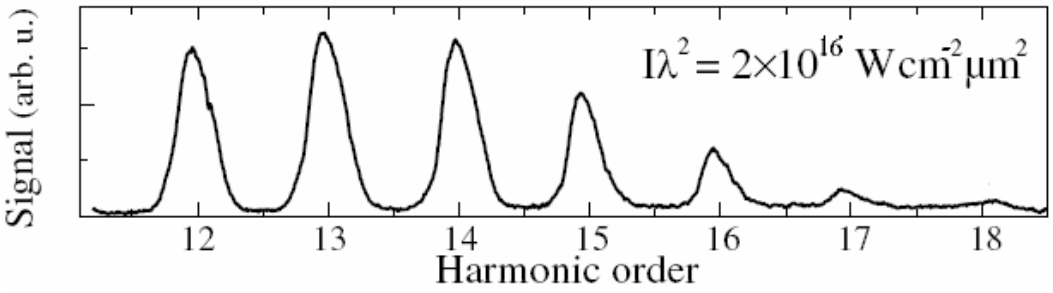

Figure 7.5: Typical raw harmonic spectrum

7.4 Route to intense attosecond pulses

One of the most appealing aspects of harmonic generation from solid surfaces is its potential to generate intense attosecond pulses [23]. In fact the predicted harmonic generation efficiency is several order of magnitude higher than that of gas HHG and thus attosecond with very high intensity are expected. According to theoretical studies, the surface HHG process is capable of generating a train of attosecond pulses [19] or an isolated attosecond pulse [23, 16].

7.4.1 Generation of a train of attosecond pulses

When several equidistant frequencies are phase-locked, superposing them will lead to a train of pulses much shorter than the cycle of the original frequencies. Applying this idea to the harmonics was proposed to generate a train of attosecond pulses [9]. One of the properties that makes harmonic generation process suitable for attosecond pulse generation is its broad spectral span of the generated harmonics. Even for harmonics from a monochromatic wave, the overall spectral bandwidth is as wide as $\triangle\omega \backsim 2N\omega$, where N is the number of the synthesized harmonics. The expected pulse duration after the Fourier synthesis is $\tau \backsim 1/\triangle\omega \backsim 1/2N\omega$. Note that the factor of 2 appears only for gas HHG, where only odd harmonics are generated. For example, when a 800 nm fundamental wave ($\omega = 2.35 \times 10^{15} Hz$) is used, synthesizing three harmonic of gas HHG (five for surface HHG) can lead to an attosecond pulse train, where each pulse is as short as $\sim 100as$. Above mentioned analysis assumed that the harmonics were phase locked which is not necessary the case in reality. In fact, it was found that the

individual atoms are not phase locked in the gas HHG process. On the other hand it was also found that the propagation in the atomic media will results in the phase locking of the harmonics, which allows the generation of a attosecond pulse train. This have been successfully experimentally demonstrated. Since the physical origin of harmonic generation from plasma surfaces is different from that of gas HHG, the same question arise as whether harmonics are phase locked and attosecond pulses can really be generated. Theoretical studies found that this is indeed the case and predicted that it is possible to generate a train of attosecond pulses [19].

7.4.2 Generation of isolated attosecond pulses

Although a train of attosecond pulses can be used for applications such as spectroscopy, the interpretation of the data will be a convolution of information from each pulse in the train. Therefore, an isolated attosecond pulse would be more desirable. It exists two solutions for generating these pulses derived from HHG in gases: using few-cycle pulses and polarization gating. For our system the first solution has been chosen. Fig. 7.6 illustrates the principle of this method. When the incident pulse is short enough, the highest frequency component is generated only at the middle of the pulse, where the intensity is significantly higher than the other part of the pulses. Filtering out that highest frequency part of the spectrum will lead to a single attosecond pulse. When the incident pulse is longer, on the other hand, the high frequency component is generated over several cycles, i.e filtering results in a train of attosecond pulses instead of a single attosecond pulse. It is also important to notice that a shorter incident pulse can lead to a shorter attosecond pulse, because the threshold intensity at the middle will be lower and thus the spectral region that can be used synthesize the attosecond pulse will be broader.

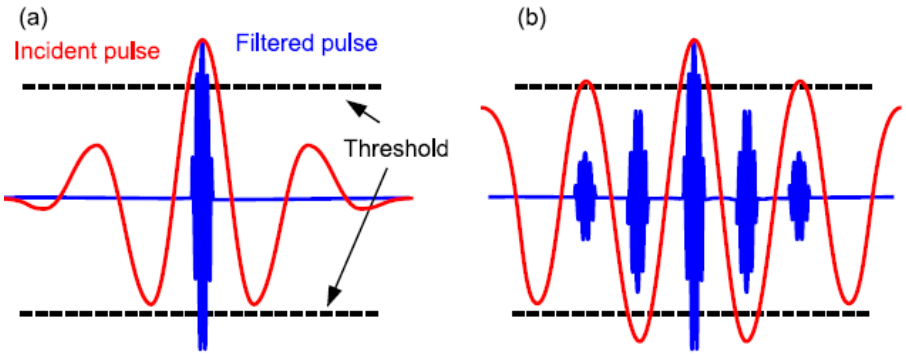

Figure 7.6: Principle of single attosecond pulse generation by a few cycle pulse. Dashed lines show the threshold intensity for generating the high frequency component of interest. (a) When the incident pulse is short, only one cycle contributes to the generation of high frequency component. (b) When the incident pulse is longer, where the high frequency components is generated over several cycles, a train of attosecond pulses is generated instead. These are symbolic drawing to show the idea. In reality, the generation timings of the attosecond pulses do not necessarily coincide the peaks of the field. Reprinted from [17]

It is possible to apply this method to the surface HHG process directly because the principle is the same. There is a small difference that the high frequency components is generated twice per optical cycle for gas HHG, while once per cycle for surface HHG. This difference is actually advantageous in practice because the condition on the pulse duration is slightly relaxed. One important thing to consider is the effect of the carrier envelope phase on the harmonic generation process. In gas HHG, a cosine pulse produces a single attosecond pulse, while a sine pulse produces two attosecond pulses (Fig. 7.7). For surface HHG, numerical simulations predict an analogous behavior. Therefore, as I have already introduced, it is necessary to control the CEP to control the generation of single attosecond pulses.

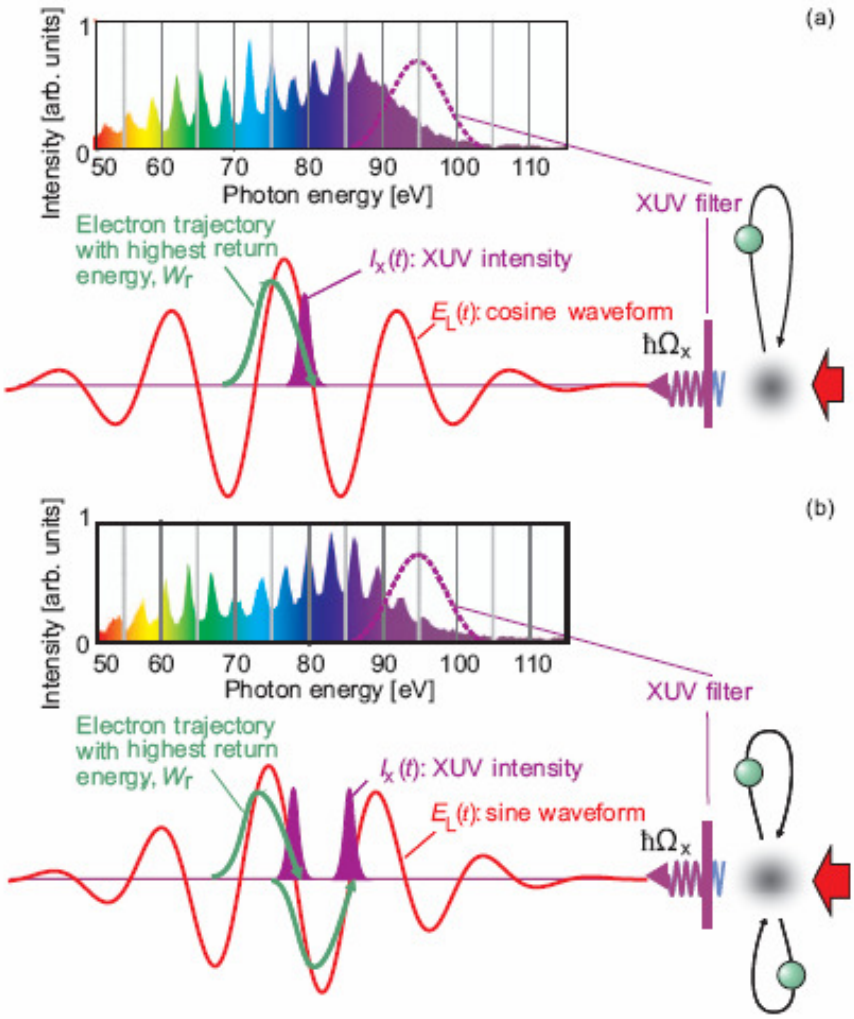

Figure 7.7: High order harmonic spectra obtained experimentally in gases with a few cycle laser. (a) cosine shaped and (b) sine shaped waveform. Reprinted from [13]

7.5 Plasma mirrors

7.5.1 Introduction

I have demonstrated that the "salle noire" laser system satisfies all the initial prescriptions for attosecond generation on solid target. The actual temporal contrast of 7 orders of magnitude in the ns regime is a limitation principally for the ROM harmonics where the highest focused intensity are needed. A solution to increase the temporal contrast without any major modification of the laser system consists of using the plasma mirror technique at the output of the laser. Studying plasma mirror is also very useful because the rotating/translating target for the

plasma mirror is the same that the one used for HHG generation and because this is the first regime of the laser-plasma interaction. Passing from the plasma mirror regime to HHG regime (CWE and then ROM) implies to increase the focused intensity.
Discussing the contrast filtering techniques I have shown that they are based on the nonlinearity on their response. The ionization of a dielectric material, a very nonlinear phenomena, is also a good candidate to be used in a contrast filter. Electric insulators have a large band-gap and are transparent for visible wavelength. However, if the intensity focused on the insulator is sufficiently intense, electrons are excited from the valence band to the conduction band. If the density of the excited electrons is higher than the critical density $N_c = \epsilon_0 m_e \omega_L^2 / e^2$, the dielectric will act like a plasma. In particular it will become highly reflective. The ionization phenomena is also very fast. It can now understood how a plasma mirror works for the contrast enhancement. If the intensity of the pedestal is below the ionization threshold of the target and the main pulse ionizes the target due to multi-photon absorbtion and is reflected, the contrast between the two is increased. This kind of interaction is named plasma mirror. The situation is depicted in Fig. 7.8.

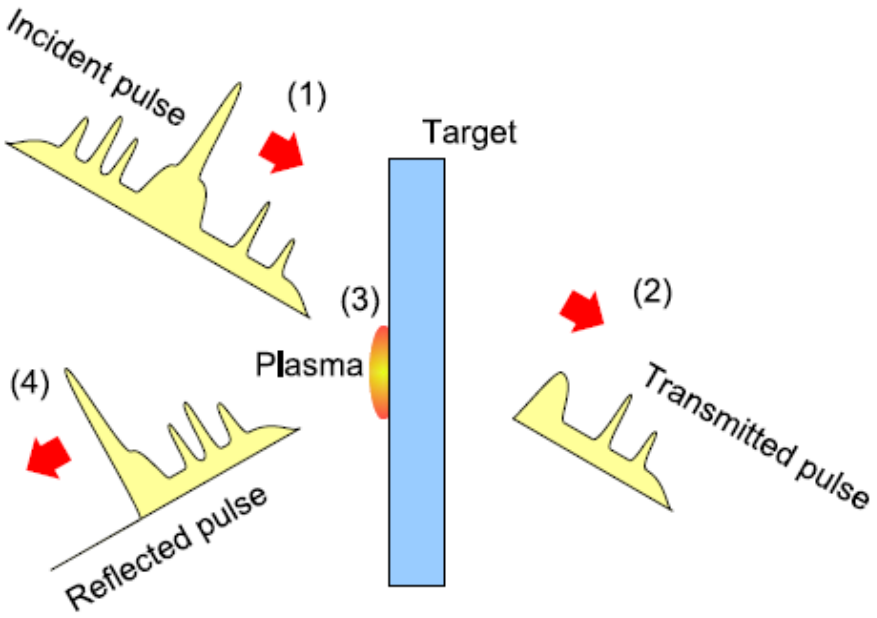

Figure 7.8: Principle of the plasma mirror (1) The incident pulse is focused onto a transparent target. (2) The prepulse/pedestal are transmitted through the material. (3) Plasma is generated by the leading edge of the main pulse. (4) The rest of the pulse is reflected by the generated plasma. Reprinted from [17]

To be more specific, the pedestal, even below the ionization threshold, will be slightly reflected. The contrast enhancement is then the ratio between the initial reflectivity seen by the pedestal and the reflectivity of the plasma generated by the main pulse. It is thus important to limit the initial reflectivity and to have a high plasma reflectivity for the main pulse. Another very important issue is that the plasma generated on the surface of the dielectric will cause a damage in this zone and the next shot needs to illuminate a different point of the target.

This is why, until now, the plasma mirror technique has been applied mainly in single shot configuration or at very low repetition rate. To extent this process to the kHz repetition rate implies working with a rotating and translating target. The development of the target has been done by A. Borot, another PhD member of the PCO group. A representation of the target inside the interaction vacuum chamber is shown in Fig. 7.9.

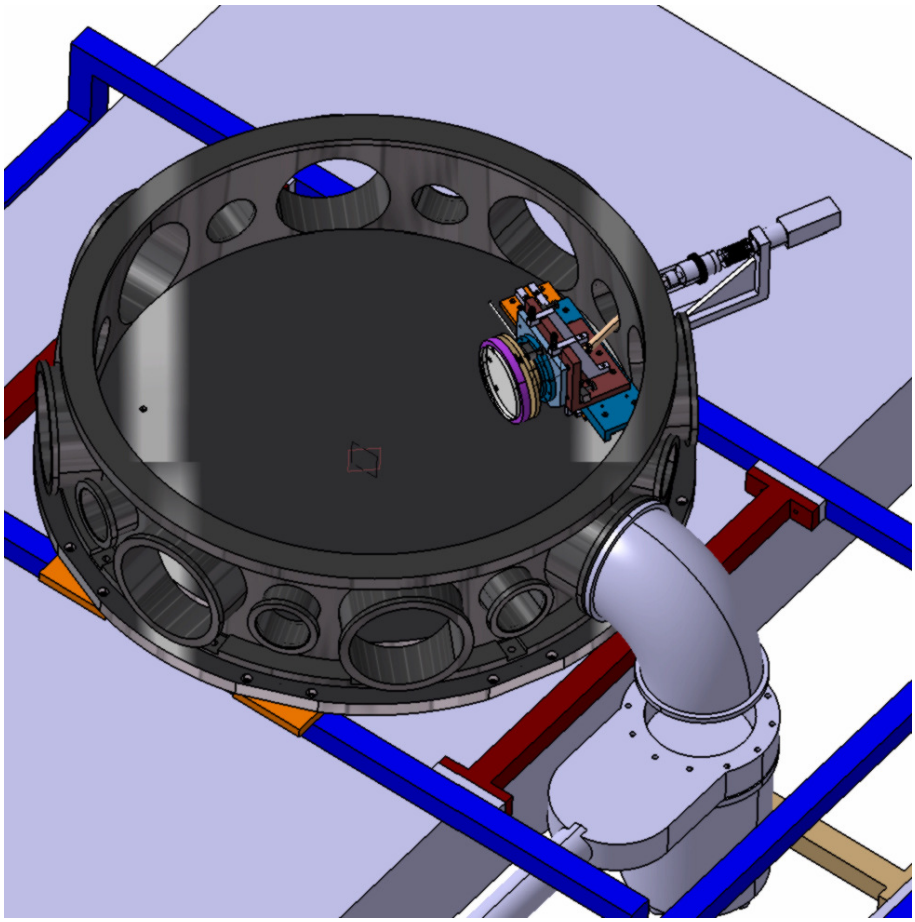

Figure 7.9: Translating/rotating target mounted inside the vacuum chamber. The target is made by fused silica

7.5.2 Experimental setup and results

For the plasma mirror experiments we used the 25 fs pulses compressed with transmission gratings + chirped mirrors. To further clean the spatial profile the output beam passes through the hollow fiber without any gas inside to act just as a spatial filter. The positive dispersion

of the windows is compensated by reflections on the already installed chirped mirrors. The beam is then expanded by a factor of two with a mirror telescope and passes through a $\lambda/2$ and a polarizer. These elements are used to finely tune the fluence on the target. A second $\lambda/2$ is used for changing the polarization state before entering the interaction chamber (under vacuum). Inside the chamber the beam is focused with a f=300 mm lens on the solid target with an incident angle of 45°. This super polished fused silica target has an RMS surface flatness of $\lambda/10$ and an anti reflecting coating at 800 nm.

Fig. 7.10 shows the measured time-and space-integrated reflectivity for s and p polarization function of the input fluence. The maximum fluence corresponds to an input energy of 450 μJ. The input and reflected beam were measured using two calibrated photodiodes and acquired digitally. The fluence is calculated by dividing the input energy by the FWHM of the focused beam which is the same for both polarizations (Fig. 7.11). The highest reflectivity (75 %) is reached with s-polarization. This is due to the absence of the losses due to resonance absorption and Brunel absorbtion [3]. These effects are acting with p-polarization and reduce the reflected energy. On the other hand the reflectivity is higher for s-polarization than for p-polarization (for p-polarization we are close to the Brewster angle).
In s-polarization we expect an increasing of the temporal contrast of 1 order of magnitude with a high transmission efficiency. The contrast enhancement can be increased to 2 orders of magnitude reducing the initial reflectivity with a better anti-reflecting coating.

Generating harmonics after cleaning the temporal contrast with a plasma mirror implies having two rotating targets. Due to the complexity of this setup at the kHz repetition rate and the loss in energy we decided, for the future HHG experiments, to start using the current laser source without any contrast filtering technique. The high contrast ($> 10^{10}$) pulses will be obtained integrating an XPW filter in the laser system in a double CPA configuration. The design of this system is the subject of the next, conclusive chapter.

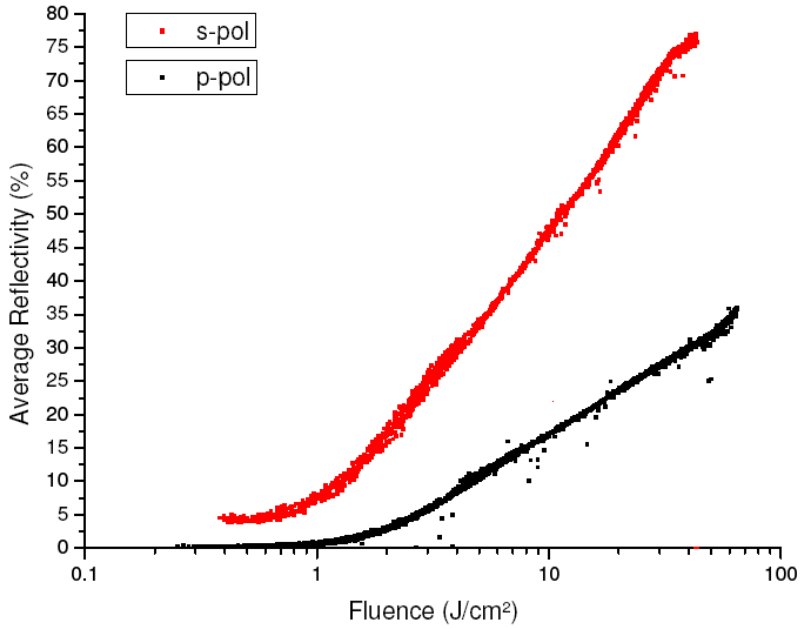

Figure 7.10: Measured time- and space-integrated reflectivity for s and p polarization function of the input fluence. The maximum input energy is 0.45 mJ

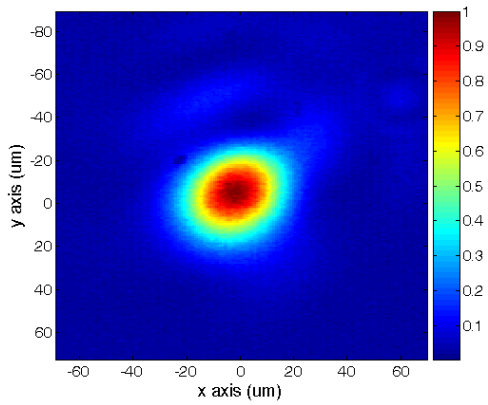

Figure 7.11: Focal spot on the target measured with a CCD camera

Bibliography

[1] T. Baeva, S. Gordienko, and A. Pukhov. Theory of high-order harmonic generation in relativistic laser interaction with overdense plasma. *Physical Review E (Statistical, Nonlinear, and Soft Matter Physics)*, 74(4):046404, 2006.

[2] B. Bezzerides, R. D. Jones, and D. W. Forslund. Plasma mechanism for ultraviolet harmonic radiation due to intense CO_2 light. *Phys. Rev. Lett.*, 49(3):202–205, Jul 1982.

[3] F. Brunel. Not-so-resonant, resonant absorption. *Phys. Rev. Lett.*, 59(1):52–55, Jul 1987.

[4] S. V. Bulanov, N. M. Naumova, and F. Pegoraro. Interaction of an ultrashort, relativistically strong laser pulse with an overdense plasma. *Physics of Plasmas*, 1(3):745–757, 1994.

[5] N. H. Burnett, H. A. Baldis, M. C. Richardson, and G. D. Enright. Harmonic generation in CO_2 laser target interaction. *Applied Physics Letters*, 31(3):172–174, 1977.

[6] R. L. Carman, D. W. Forslund, and J. M. Kindel. Visible harmonic emission as a way of measuring profile steepening. *Phys. Rev. Lett.*, 46(1):29–32, Jan 1981.

[7] R. L. Carman, C. K. Rhodes, and R. F. Benjamin. Observation of harmonics in the visible and ultraviolet created in CO_2 laser-produced plasmas. *Phys. Rev. A*, 24(5):2649–2663, Nov 1981.

[8] B. Dromey, S. Kar, C. Bellei, D. C. Carroll, R. J. Clarke, J. S. Green, S. Kneip, K. Markey, S. R. Nagel, P. T. Simpson, L. Willingale, P. McKenna, D. Neely, Z. Najmudin, K. Krushelnick, P. A. Norreys, and M. Zepf. Bright multi-kev harmonic generation from relativistically oscillating plasma surfaces. *Physical Review Letters*, 99(8):085001, 2007.

[9] G. Farkas and C. Tóth. Proposal for attosecond light pulse generation using laser induced multiple-harmonic conversion processes in rare gases. *Physics Letters A*, 168(5-6):447 – 450, 1992.

[10] P. Gibbon. Harmonic generation by femtosecond laser-solid interaction: A coherent "water-window" light source? *Phys. Rev. Lett.*, 76(1):50–53, Jan 1996.

[11] S. Gordienko, A. Pukhov, O. Shorokhov, and T. Baeva. Relativistic doppler effect: Universal spectra and zeptosecond pulses. *Phys. Rev. Lett.*, 93(11):115002, Sep 2004.

[12] A. Ishizawa, T. Kanai, T. Ozaki, and H. Kuroda. Enhancement of high-order harmonic generation efficiency from solid-surface plasma by controlling the electron density gradient of picosecond laser-produced plasmas. *Quantum Electronics, IEEE Journal of*, 37(3):384–389, Mar 2001.

[13] F. Krausz and M. Ivanov. Attosecond physics. *Reviews of Modern Physics*, 81(1):163, 2009.

[14] R. Lichters, J. Meyer ter Vehn, and A. Pukhov. Short-pulse laser harmonics from oscillating plasma surfaces driven at relativistic intensity. *Physics of Plasmas*, 3(9):3425–3437, 1996.

[15] P. Monot, G. Doumy, S. Dobosz, M. Perdrix, P. D'Oliveira, F. Quéré, F. Réau, P. Martin, P. Audebert, J-C. Gauthier, and J. P. Geindre. High-order harmonic generation by nonlinear reflection of an intensehigh-contrast laser pulse on a plasma. *Opt. Lett.*, 29(8):893–895, 2004.

[16] N. M. Naumova, J. A. Nees, I. V. Sokolov, B. Hou, and G. A. Mourou. Relativistic generation of isolated attosecond pulses in a λ^3 focal volume. *Phys. Rev. Lett.*, 92(6):063902, Feb 2004.

[17] Y. Nomura PhD manuscript

[18] P. A. Norreys, M. Zepf, S. Moustaizis, A. P. Fews, J. Zhang, P. Lee, M. Bakarezos, C. N. Danson, A. Dyson, P. Gibbon, P. Loukakos, D. Neely, F. N. Walsh, J. S. Wark, and A. E. Dangor. Efficient extreme uv harmonics generated from picosecond laser pulse interactions with solid targets. *Phys. Rev. Lett.*, 76(11):1832–1835, Mar 1996.

[19] L. Plaja, L. Roso, K. Rzazewski, and M. Lewenstein. Generation of attosecond pulse trains during the reflection of a very intense laser on a solid surface. *J. Opt. Soc. Am. B*, 15(7):1904–1911, 1998.

[20] F. Quere, C. Thaury, P. Monot, S. Dobosz, Ph. Martin, J.-P. Geindre, and P. Audebert. Coherent wake emission of high-order harmonics from overdense plasmas. *Physical Review Letters*, 96(12):125004, 2006.

[21] Z.-M. Sheng, K. Mima, J. Zhang, and H. Sanuki. Emission of electromagnetic pulses from laser wakefields through linear mode conversion. *Phys. Rev. Lett.*, 94(9):095003, Mar 2005.

[22] A. Tarasevitch, A. Orisch, D. von der Linde, Ph. Balcou, G. Rey, J.-P. Chambaret, U. Teubner, D. Klöpfel, and W. Theobald. Generation of high-order spatially coherent harmonics from solid targets by femtosecond laser pulses. *Phys. Rev. A*, 62(2):023816, Jul 2000.

[23] G. D Tsakiris, K. Eidmann, J. Meyer ter Vehn, and F. Krausz. Route to intense single attosecond pulses. *New Journal of Physics*, 8(1):19, 2006.

[24] K. Varju, Y. Mairesse, Carré B., M. B. Gaarde, P. Johnsson, S. Kazamias, R. Lopez-Martens, J. Mauritsson, K. J. Schafer, PH. Balcou, A. L'huillier, and P. Salières. Frequency chirp of harmonic and attosecond pulses. *Journal of Modern Optics*, 52(2):379–394, 2005.

[25] D. von der Linde, T. Engers, G. Jenke, P. Agostini, G. Grillon, E. Nibbering, A. Mysyrowicz, and A. Antonetti. Generation of high-order harmonics from solid surfaces by intense femtosecond laser pulses. *Phys. Rev. A*, 52(1):R25–R27, Jul 1995.

[26] M. Zepf, G. D. Tsakiris, G. Pretzler, I. Watts, D. M. Chambers, P. A. Norreys, U. Andiel, A. E. Dangor, K. Eidmann, C. Gahn, A. Machacek, J. S. Wark, and K. Witte. Role of the plasma scale length in the harmonic generation from solid targets. *Phys. Rev. E*, 58(5):R5253–R5256, Nov 1998.

Chapter 8

Conclusions and perspective

8.1 Introduction

My Ph.D work focused on the possibility of generating high contrast, ultra-short pulses for doing high repetition rate relativistic optics. In this manuscript I presented the study of the XPW contrast filter for obtaining the high contrast pulses and the development of a mJ level, few-cycle, CEP stabilized source. During this work several devices were developed in collaboration with the company FASTLITE. Two different hybrid compression schemes were tested and the solution based on transmission gratings and chirped mirrors was adapted. Some preliminary results were obtained using the source in laser-matter experiments in the sub-relativistic regime (plasma mirror regime). To efficiently generate harmonics in the relativistic regime a high temporal contrast is also needed. In particular recent experiments underline the importance of a high temporal contrast down to just a few picosecond before the main peak. This implies to control both the incoherent and coherent contrast. The XPW filter is the chosen solution that satisfies those requirements. The installation of a XPW filter in the laser system involves working in a double CPA configuration. The design of this solution is presented in the next sections.

8.2 Double CPA XPW

The front-end of the "salle noire" laser is a commercial system (Femtopower CEP) delivering CEP stabilized, 1 mJ, 30 fs pulses compressed in a prism compressor with a temporal contrast of 10^8. This is the first building block (CPA) of the future system. To generate few-cycle, high contrast pulses there are two possibilities:

- Implement an XPW contrast filter at the output of the Femtopower, seed the second CPA for re-amplification keeping the high contrast. Broaden the spectrum in the hollow-core fiber for the generation of few-cycle (high contrast) pulses. (I)

- Broaden the spectrum to the few-cycle regime in the hollow-core fiber directly after the Femtopower, clean the few-cycle pulses temporally and spectrally with an XPW contrast

filter and seed in the second CPA. (II)

After the developments done during my Ph.D on XPW generation, the two options above are feasible. The second solution is scalable to higher energy but will result in a longer pulse duration due to gain narrowing in the second CPA. Thanks to the XPW spectral cleaning after the hollow fiber, in the second configuration the spectrum will be less modulated but the temporal contrast, at least in the nanosecond regime, will be the same for both configurations (similar injecting energy in the second CPA). The contribution to the coherent contrast due to the residual spectral phase is defined by the second CPA and so should be the same in the two configurations. The contribution due to modulations of the spectrum will be smaller in the second configuration. An experimental implementation similar to the second possibility (except for the XPW filter) has already been tested [2, 3] with the generation of 3.4 mJ pulses with a sub-10 fs temporal duration. Implementing an XPW filter after an hollow fiber with a further amplification in an OPCPA system has also been tested by Tavella et al.

I believe that for our applications the first solution has several advantages in terms of cost, simplicity and robustness. The sensitivity of the XPW filter to the spectral phase has already been demonstrated for sub-10 fs pulses. In terms of daily operation (and also for the need of broadband optics) it is much easier to implement the XPW filter at the 30 fs duration, where the influence of the phase is less critical, followed by pulse broadening in the hollow fiber at the end of the system. This solution is the one designed in the following part.

As I have discussed in section 4.11 the two crystals configuration with the first crystal in focus is not easily scalable to high input energy and short pulse duration. With a reasonable input beam size, in order to avoid white light generation in crystals, a focal length of 10 meter is needed with a distance between the crystals of more than 1 meter to filter 1 mJ, 30 fs pulses (the output of the Femtopower). Furthermore in order to avoid SPM in air, a major part of the setup should be under vacuum. To dispose of a more compact and user-friendly filter there are two solutions:

- the first consists in decreasing the input energy to 200 μJ (with a spatial filter) and work in air with a standard two (holo- cut) crystal setup configuration. In this configuration we have demonstrated the possibility of generating around 50 μJ with a overall efficiency near 30 %. To seed the second CPA the beam needs to be stretched again and eventually passes through another Dazzler. With a 70 % transmission of the stretcher and a 40 % efficiency of the Dazzler there are 17 μJ to be amplified in the second amplifier.

- The second possibility is to try a high energy XPW configuration, using the whole energy and focusing it with a short focal length (1 m) in a vacuum chamber with an iris placed at the focus. The two BaF_2 are placed after the focus where the intensity is below the white light generation threshold. In this configuration a global efficiency (considering also the losses in the iris) of 10 % is expected with an output energy of 100 μJ. The spatial cleaning

in the focus is necessary due to the spatial quality of the beam after the Femtopower. 30 μJ are then injected in the second amplifier. In this case the iris for the spatial filtering and the crystals are placed under vacuum. Due to the limited amount of elements under vacuum a simple plexiglas tube can be used. The advantage of this configuration is its compactness and simplicity of alignment.

The increase in temporal contrast after a XPW filter is determined by the extinction ratio of the polarizers eventually degraded by some linear birefringence of the nonlinear crystals. To be conservative we can consider an increase in temporal contrast of 3 orders of magnitude. Furthermore in both the configurations the spectrum is broadened after the XPW filter and a FWHM >90 nm is expected. Tens of μJ pulses, with a temporal contrast higher than 10^{10} and compressible to 15 fs can then be seeded into the second CPA.
The second amplifier stage has been designed using Commod pro in collaboration with B. Mercier, another member of the PCO group. I assume the pulses stretched to 10 ps. The table with the energy after each pass for the two XPW filter options and for different sizes of the pump beam are shown in Tab. 8.1. This table also gives the accumulated B integral after each pass.

Diameter of the pump spot	800 µm	800 µm	900 µm	900 µm	1 mm	1 mm	
gain per pass	13	13	7.8	7.8	5.2	5.2	
passes	**Energy mJ**						**B integral**
0	0.016	0.032	0.016	0.032	0.06	0.032	radians
1	0.101	0.203	0.072	0.144	0.056	0.113	0.01
2	0.725	1.13	0.351	0.686	0.207	0.409	0.1
3	2.58	3.46	1.3	2.08	0.683	1.2	0.5
4	4.95	5.91	3.04	4.01	1.74	2.57	1.5
5	6.86	7.71	4.85	5.73	3.2	4.09	3.2
6	8.27	9	6.32	7.07	4.59	5.41	5.5

Figure 8.1: amplification for each pass

To obtain the desired energy a 5-pass amplifier is needed. Considering for example a diameter of the pump of 900 μm, pulses with an energy of 4.85 mJ are obtained injecting with 16 μJ (first solution for the XPW filter) and an energy of 5.73 mJ injecting with 32 μJ (second

solution for the XPW filter). The number of passes is limited to 5 to limit the additional B integral to 3.2 rad. The B integral accumulated is the first CPA is cleaned in the XPW filter. As discussed in section 6.3 the Dazscope optimization loop can be used to measure and pre-compensate the additional spectral phase induced by non linear effects during amplification. In the actual configuration of our laser system the stretcher and the compressor are not matched and all the third order spectral phase accumulated in our laser system in compensated by the AOPDF. The pulse can only be stretched to 7 ps and this limit the output energy. Designing the second CPA we can choose a gratings solution both for the stretcher and the compressor and stretch to 10 ps. Using the solution with the hybrid compressor consisting of transmission gratings and chirped mirrors (new grooved gratings with 83 % efficiency), pulses with energies > 3.5 mJ can be obtained and compressed to sub-20 fs. These pulses can then be compressed down to the few-cycle regime in a hollow fiber working with circular polarization. Getting in the few-cycle regime should be facilitated by the short input pulse duration. In section 6.11 I have demonstrated the possibility to generate 1 mJ pulses using a hollow fiber with a diameter of 250 μm. To inject more energy tests are planned using fibers with a 500 μm. The difficulty with a hollow fiber with a big core diameter is keeping a good spatial profile. Another possibility for increasing the input energy of the fibers is the use of a pressure gradient.
The CEP stabilization of the compressed few-cycle pulses at the output of the "salle noire" laser has been demonstrated in section 6.6. The CEP stability directly after the Femtopower has also been presented. The only new element that can affect the CEP stability of the system in the double CPA is the XPW filter. The demonstration that the XPW filter does not introduce significant CEP drift noise into the system is given in the appendix (section 9).

8.3 Conclusion

We can then conclude that, with the design presented in this last chapter, multi-mJ, CEP stabilized, high contrast ($> 10^{10}$), few-cycle pulses can be generated at the kHz repetition rate. A source with these specifications is not currently commercially available but it is realistic to expect that it will be available in the next years due to the importance of its applications. The pulses generated with this source, gently focused on a gaz jet or tightly focused on a solid target, can generate single attosecond pulses. A higher efficiency is expected for the generation on a solid target. The characterization and applications of these attosecond pulses in pump/probe experiments will be the subject of the research for the future years and in particular it will the subject of the experiments with the "Salle Noire" laser system in a near future. Using a deformable mirror to focus these pulses down to the limit of diffraction (λ^2) [1], intensities in the relativistic regime can be obtained and attosecond pulses can be generated with the relativistic oscillating mirror regime or in λ^3 regime. An eventual pre-pulse with controlled amplitude and delay can be added (for example with the AOPDF) to generate a particular plasma density gradient that maximize the harmonic emission.

Bibliography

[1] O. Albert, H. Wang, D. Liu, Z. Chang, and G. Mourou. Generation of relativistic intensity pulses at a kilohertz repetition rate. *Opt. Lett.*, 25(15):1125–1127, 2000.

[2] J. Seres, A. Müller, E. Seres, K. O'Keeffe, M. Lenner, R. F. Herzog, D. Kaplan, C. Spielmann, and F. Krausz. Sub-10-fs, terawatt-scale ti:sapphire laser system. *Opt. Lett.*, 28(19):1832–1834, 2003.

[3] A.J. Verhoef, J. Seres, K. Schmid, Y. Nomura, G. Tempea, L. Veisz, and F. Krausz. Compression of the pulses of a ti:sapphire laser system to 5 femtoseconds at 0.2 terawatt level. *Applied Physics B: Lasers and Optics*, 82(4):513–517, March 2006.

Chapter 9

Appendix

9.1 CEP after XPW

9.1.1 Carrier envelope phase after XPW

When the XPW filter is introduced in the laser system it is important to demonstrate that it does not deteriorate the CEP stability. This means to demonstrate that the relative CEP between the fundamental and the generated XPW pulse is constant between successive pulses. If successive pulses have the same CEP then this is true also for the generated XPW pulses. Considering again the relation:

$$\hat{B}(L,\omega) = -i\gamma_{\perp} L \iint_{\mathbb{R}^2} \hat{A}(\omega_1)\hat{A}(\omega_2)\hat{A}^*(\omega_1+\omega_2-\omega)d\omega_1 d\omega_2 \tag{9.1}$$

expressing the XPW four-wave mixing process (neglecting SPM and XPM), it results that for a generated angular frequency $\omega_4 = \omega_1 + \omega_2 - \omega$ there is the following relation between the CEP of the interacting waves :

$$\phi_{\omega_4} = \pi/2 + \phi_{\omega_1} + \phi_{\omega_2} - \phi_{\omega} \tag{9.2}$$

This expression describes the buildup of the frequency-independent part of the XPW pulse phase. The other processes that act together with XPW generation (SPM and XPM) induce an intensity-induced phase shift but, for a given intensity, the CEP difference between the fundamental and the XPW beam remain constant between successive pulses.

In the following part, I give a clear experimental evidence that the CEP is preserved upon the XPW process. These experiments were done in collaboration with K. Osvay group from Szeged (Hungary). This group have a long experience with the spectrally and spatially resolved interferometry (SSRI). SSRI has been proven to be a powerful technique for dispersion measurement of various materials and optical elements. It typically consists of a two-beam interferometer, where the phase fronts of the reference and sample beams are tilted with a small angle, and an imaging spectrograph. The interference pattern is imaged onto the input slit of the spectrograph, so that spatially (along the slit) and spectrally resolved interference fringes are formed on the CCD camera inserted at the output plane of the spectrograph (Fig. 8.1).

The slope and the curvature of the interference fringes are characteristic to the dispersion coefficients of the sample such as group delay (GD) or group delay dispersion (GDD). The absolute spatial position of the fringes is, however, directly and uniquely related to the relative carrier envelope phase of the sample and reference beams. If the detector is slow or its exposure time long enough, then it actually captures many subsequent interference patterns on top of each other. As a result, the visibility of the recorded interference pattern would be substantially degraded, if there is a change in relative CEP between sample and reference pulses. However, if there is no relative CEP drift, then the position of the fringes should be maintained and the visibility of the integrated fringe system is expected to be independent on the exposure time.

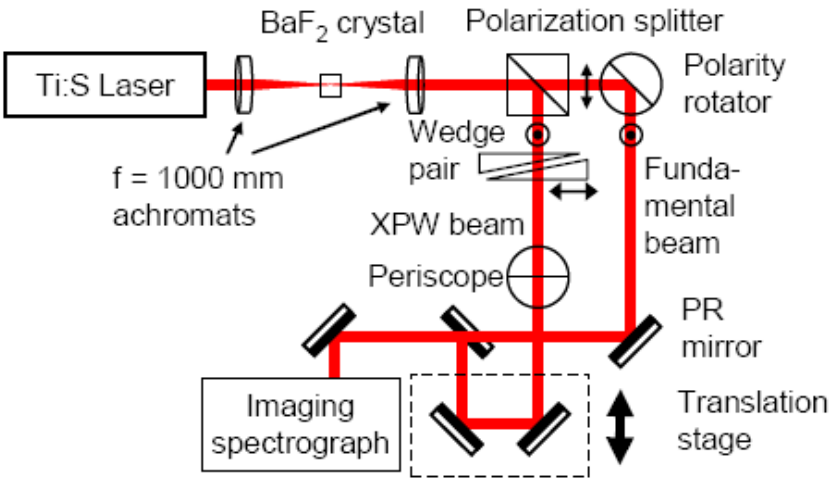

Figure 9.1: Experimental setup. The cross polarized pulses interfere with the fundamental beam in a Mach-.Zehnder interferometer

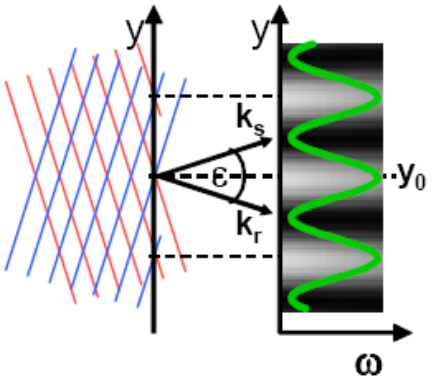

Figure 9.2: The spatial position y of the SSRI fringes is uniquely determined by the CEP difference between the sample (i.e. cross polarized) and the reference (i.e. fundamental) pulses.

Experiments CEP after XPW

In the experiment (Fig. 9.1) the laser source is the "salle noire" laser system. Due to the fact that we measure the relative CEP between the fundamental and the XPW beam (and not between successive pulses) the system does not need to be CEP stabilized. The pulse energy is considerably attenuated prior to the XPW generation stage that consisted of an f=1m focal lens and a BaF_2 crystal. The generated XPW beam and the rest of the fundamental pulses are collimated by a second lens. The orthogonally polarized XPW beam is split from the fundamental beam by a polarizing cube. After adjusting their relative polarization and timing appropriately, both beams are sent to the input slit of an imaging spectrograph. Two independent experiments were carried out to measure the relative change in CEP between XPW and fundamental beams. First the exposure time of the CCD camera was varied from 1 ms to 1000 ms to test the fringe stability over time. Fig. 9.3 shows spatial cross section of the fringes for three different wavelength function of the exposure time of the CCD camera. As is clear from the composed images at three different wavelengths, the vertical position of the fringes (relative CEP) is maintained over the large variation of the exposure time. Moreover, the position is also independent of the spectral position of the interferograms. This evaluation of the fringes is restricted to certain wavelengths. We can evaluate the whole interference pattern (i.e. for each spatial point and for each wavelengths) if we compute the visibility of the fringes for the entire interferograms. From the captured interferograms the visibility has been also evaluated, varying from 0.883 to 0.823 when the exposition time was increased from 1ms to 1s. This small change of visibility is attributed the unavoidable mechanical vibration of the optical components in the two arms of the interferometer.

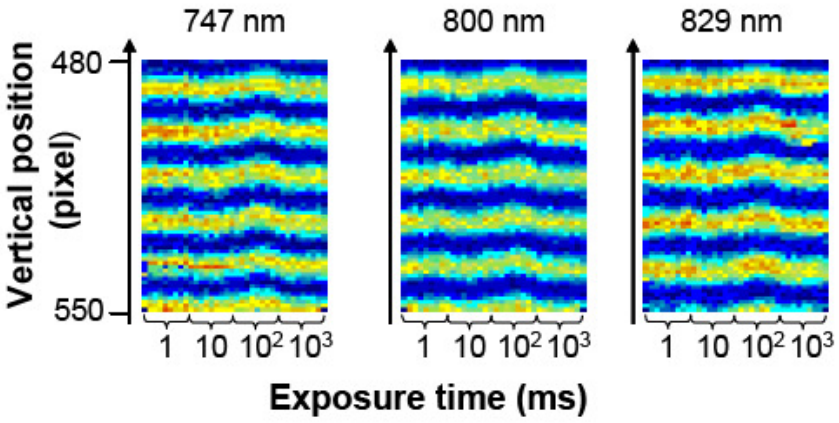

Figure 9.3: Spatial cross section of the fringes at three different wavelengths in the function of the exposure time of the CCD camera. At each exposure time the corresponding slice of nine independent interferograms are displayed

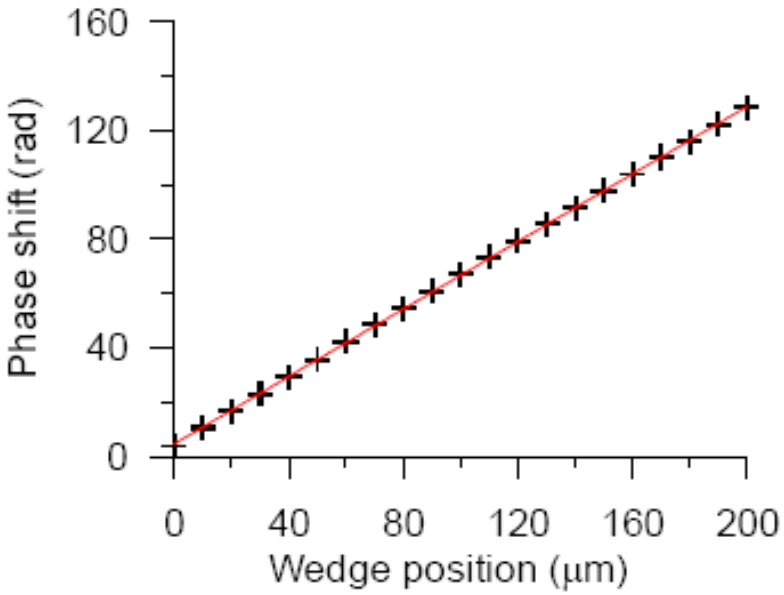

Figure 9.4: Change of total CEP of the XPW pulses relative to the sample pulses as a function of wedge insertion in the XPW beam.

The second experiment yielded an independent proof of CEP preservation during XPW generation. A pair of fused silica wedges with an apex angle of 10.3 was inserted into the XPW arm of the interferometer. The change in relative CEP between the XPW and fundamental beam was measured as a function of the material amount inserted into the XPW beam path through moving one of the wedges. Nine interferograms were captured at each position of the traveling wedge moved by a precision translator in 10 μm steps. The variation of the total spectral phase of the XPW pulses relative to the fundamental beam was calculated at each subsequent position of the wedge (Fig. 9.4). The rate of phase change for the XPW beam as a function of wedge insertion was hence measured as 644.6 rad/mm, which is in excellent agreement with the calculated value of 647.0 rad/mm.

These experiments using the spectrally and spatially resolved interferometry clearly demonstrate that the relative CEP is maintained between the fundamental and the XPW pulse. The last check is to measure the CEP drift between successive pulses after XPW. This has been realized measuring the CEP drift in open loop (just the oscillator stabilized) with the f-2f nonlinear interferometer placed after the XPW filter. This experiment was realized in collaboration with the O. Gobert and J.Hergott from the Centre Energy Atomic (CEA Saclay). No increasing CEP noise is measured after the filter compared to the output of the laser. We have even measured a slightly reduction of the CEP noise. We think that the spectral broadening and the cleaning of the spatial profile has as a consequence the reduction of the noise added by the white light generation in the bulk sapphire and thus on the measured CEP noise.

Bibliography

[1] O. Albert, H. Wang, D. Liu, Z. Chang, and G. Mourou. Generation of relativistic intensity pulses at a kilohertz repetition rate. *Opt. Lett.*, 25(15):1125–1127, 2000.

[2] J. Seres, A. Müller, E. Seres, K. O'Keeffe, M. Lenner, R. F. Herzog, D. Kaplan, C. Spielmann, and F. Krausz. Sub-10-fs, terawatt-scale ti:sapphire laser system. *Opt. Lett.*, 28(19):1832–1834, 2003.

[3] A.J. Verhoef, J. Seres, K. Schmid, Y. Nomura, G. Tempea, L. Veisz, and F. Krausz. Compression of the pulses of a ti:sapphire laser system to 5 femtoseconds at 0.2 terawatt level. *Applied Physics B: Lasers and Optics*, 82(4):513–517, March 2006.

List of publications

Bibliography

[1] **L. Canova**, S. Kourtev, N. Minkovski, R. Lopez-Martens, O. Albert and S.M. Saltiel. Cross-polarized wave generation in the UV region. *Opt. Lett.* **33**, 2299-2301 (2008)

[2] **L. Canova**, S. Kourtev, N. Minkovski, A. jullien R. Lopez-Martens, O. Albert and S.M. Saltiel. Efficient generation of cross-polarized femtosecond pulses in cubic crystals with holographic cut orientation. *Appl. Phys. Lett.* **92**, 231102 (2008)

[3] **L. Canova**, O. Albert, N. Forget, B. Mercier, S. Kourtev, N. Minkovski, S.M. Saltiel and R. Lopez-Martens. Influence of spectral phase on cross-polarized wave generation with short femtosecond pulses. *Appl. Phys. Lett.*: Lasers and Optics (2008)

[4] A. Jullien, **L. Canova**, O. Albert, D. Boschetto, L. Antonucci, Y.H. Cha, J.P. Rousseau, P. Chaudet, G. Chériaux, J. Etchepare, S. Kourtev, N. Minkovski and S.M. Saltiel. Spectral broadening and pulse duration reduction during cross-polarized wave generation: influence of the quadratic spectral phase. *Appl. Phys. B* **87**(4), 595-601 (2007)

[5] S. Kourtev,N. Minkovski, **L. Canova**, O. Albert, A. Jullien, J. Etchepare and S.M. Saltiel. Nonlinear filtering and beam shaping with $\chi^{(3)}$ nonlinear polarization interferometer. *Opt. Commun.* **281**, 3375-3380 (2008)

[6] **L. Canova**, X. Chen, A. Trisorio, A. Jullien, A. Assion, G. Tempea, N. Forget, T. Oksenhendler and R. Lopez-Martens. Carrier-envelope phase stabilization and control using a transmission grating compressor and an AOPDF. *Opt. Lett.* **34**, 1333-1335 (2009)

[7] X. Chen, A. Jullien, A. Malvache, **L. Canova**, A. Borot, A. Trisorio, O. Albert, C. Durfee and R. Lopez-Martens. Generation of 4.3 fs, 1 mJ pulses via compression of circularly polarized pulses in a gas-filled hollow-core fiber. *Opt.Lett.***34**, 1588-1590 (2009)

[8] A. Jullien, C. Durfee, A. Trisorio, **L. Canova**, J.P. Rousseau, B. Mercier, L. Antonucci, G. Cheriaux, O. Albert and R. Lopez-Martens. Nonlinear spectral cleaning of few-cycle pulses via cross-polarized wave (XPW) generation. *Appl.Phys. B.* **96**, 2-3 (2009)

[9] S. Kourtev, N. Minkowski, **L. Canova**, A. Jullien, O. Albert, and S.M. Saltiel. Improved nonlinear Cross-polarized wave generation in cubic crystals by optimization of crystal orientation. *JOSA B.* **26**, pp.1269-1275 (2009)

[10] F. Canova, A. Flacco, **L. Canova**, J.P. Chambaret, F. Plé, M. Pittman, T. Planchon, M. Silva, R. Benocci, G. Lucchini, D. Batani, E. Lavergne, G. Dovillaire, X. Levecq. Wavefront correction and aberrations pre-compensation in the middle of Petawatt-class CPA laser chains. *Laser and particle beam*, 25, 649-655 (2007)

[11] K. Osvay, **L. Canova**, A. Borzsonyi, K. Attila, C.P. Durfee, R. Lopez Martens. Preservation of the carrier envelope phase during Cross-Polarized Wave generation. *To be published in Optics Express*

[12] X. Chen, **L. Canova**, A. Malvache, A. Jullien, R. Lopez Martens, C.P. Durfee, D. Papadopoulos, F. Druon. 1 mJ, sub-5 fs carrier-envelope phase-locked pulses. *To be published in Applied Physics B:Lasers and Optics*

[13] N. Forget, **L. Canova**, X. Chen, A. Jullien, R. Lopez Martens. Closed loop carrier-envelope phase stabilization with an acousto-optic programmable dispersive filter. *To be published in Opt. Lett.*